

Inkjet Printing Digital Image Generation and Compensation for Surface Chemistry Effects

by
Juan Francisco Reyes Luna

Doctoral Thesis

Submitted to the University of Nottingham
for the degree of

Doctor of Philosophy

Department of Mechanical, Materials and Manufacturing Engineering
Faculty of Engineering

February, 2023

“If I have seen further it is by standing on the shoulders
of Giants.”

- Sir Isaac Newton

Abstract.

Additive manufacturing (AM) of electronic materials using digital inkjet printing (DIJP) is of research interests nowadays because of its potential benefits in the semiconductor industry. Current trends in manufacturing electronics feature DIJP as a key technology to enable the production of customised and microscale functional devices. However, the fabrication of microelectronic components at large scale demands fast printing of tight features with high dimensional accuracy on substrates with varied surface topography which push inkjet printing process to its limits. To understand the DIJP droplet deposition on such substrates, generally requires computational fluid dynamics modelling which is limited in its physics approximation of surface interactions. Otherwise, a kind of “trial and error” approach to determining how the ink spreads, coalesce and solidifies over the substrate is used, often a very time-consuming process. Consequently, this thesis aims to develop new modelling techniques to predict fast and accurately the surface morphology of inkjet-printed features, enabling the optimisation of DIJP control parameters and the compensation of images for better dimensional accuracy of printed electronics devices.

This investigation explored three categories of modelling techniques to predict the surface morphology of inkjet-printed features: physics-based, data-driven and hybrid physics-based and data-driven. Two physics-based numerical models were developed to reproduce the inkjet printing droplet deposition and solidification processes using a lattice Boltzmann (LB) multiphase flow model and a finite element (FE) chemo-mechanical model, respectively. The LB model was limited to the simulation of single tracks and small square films and the FE model was mainly employed for the distortion prediction of multilayer objects. Alternatively, two data-driven models were implemented to reconstruct the surface morphology of single tracks and free-form films using images from experiments: image analysis (IA) and shape from shading (SFS). IA assumed volume conservation and minimal energy drop shape to reconstruct the surface while SFS resolved the height of the image using a reflection model. Finally, a hybrid physics-based and data-driven approach was generated which incorporates the uncertainty of droplet landing position and footprint, hydrostatic analytical models, empirical correlations derived from experiments, and relationships derived from physics-based models to predict fast and accurately any free-form layer

pattern as a function of physical properties, printing parameters and wetting characteristics.

Depending on the selection of the modelling technique to predict the deformed geometry, further considerations were required. For the purely physics-based and data-driven models, a surrogate model using response surface equations was employed to create a transfer function between printing parameters, substrate wetting characteristics and the resulting surface morphology. The development of a transfer function significantly decreased the computational time required by purely physics-based models and enabled the parameter optimisation using a multi-objective genetic algorithm approach to attain the best film dimensional accuracy. Additionally, for multilayer printing applications, a layer compensation approach was achieved utilizing a convolutional neural network trained by the predicted (deformed) geometry to reduce the out of plane error to target shape. The optimal combination of printing parameters and input image compensation helped with the generation of fine features that are traditionally difficult for inkjet, improved resolution of edges and corners by reducing the amount of overflow from material, accounted for varied topography and capillary effects thereof on the substrate surface and considered the effect of multiple layers built up on each other.

This study revealed for the first time to the best of our knowledge the role of the droplet location and footprint diameter uncertainty in the stability and uniformity of printed features. Using a droplet overlap map which was proposed as a universal technique to assess the effect of printing parameters on pattern geometry, it was shown that reliable limits for break-up and bulging of printed features were obtained. Considering droplet position and diameter size uncertainties, predicted optimal printing parameters improved the quality of printed films on substrates with different wettability. Finally, a stability diagram illustrating the onset of bulging and separation for lines and films as well as the optimal drop spacing, printing frequency and stand-off distance was generated to inform visually the results.

This investigation has developed a predictive physics-based model of the surface morphology of DIJP features on heterogeneous substrates and a methodology to find the printing parameters and compensate the layer geometry required for optimum part dimensional accuracy. The simplicity of the proposed technique makes it a promising

tool for model driven inkjet printing process optimization, including real time process control and paves the way for better quality devices in the printed electronics industry.

Acknowledgements.

I would like to express my deepest gratitude to my academic supervisors Prof. Ian Ashcroft and Prof. Christopher Tuck for their guidance and support throughout the research. Their curiosity, leadership, and knowledge on every review, challenged my work to improve my understanding of the physics involved on additive manufacturing technologies. I would also like to thank Prof. Ricky Wildman for his advice and patience during the PhD annual progress reviews.

I am especially grateful to Dr. Yinfeng He for preparing the TPGDA ink to perform the experimental work and for helping me understand the subtleties of the inkjet printing process. I would also like to thank Dr. Jisun Im for the Dimatix printer training and guidance optimising TPGDA on samba cartridge, Dr. Christopher Strong for his support measuring droplet contact angles and his advice on printing stable tracks and Dr. Peng Zhao for his guidance using the high-performance computing system and insightful discussions about modelling of photo-polymerization phenomena.

A special thanks goes to Nathan Roberts from the Metrology group for conducting coherence scanning interferometry measurements of the printed films and Inês Barreiros for performing micro-CT scanning of the 3D artifacts used for model validation purposes.

I thank all technical, administrative and research members of the Centre for Additive Manufacturing for their help over the last few years. Special thanks to Mirela Axinte for facilitating seminars and keeping myself engaged in the PhD journey. I also finally like to thank my PhD peers for making my time at the University of Nottingham an enjoyable experience.

Special thanks to the University of Nottingham Industry Studentship and Texas Instruments for providing the funding for this course and to my industry supervisor, Sean Chang, for his invaluable recommendations on our research reviews.

Finally, I couldn't carry out this work without the endless love and support of my family, especially my mother for her constant encouragement, listening, and presence. Thank you all for staying close and sharing the PhD journey with me.

Publications.

Reyes-Luna, J. F., Chang, S., Tuck, C. J. and Ashcroft, I. A. A Surrogate Modelling Strategy to Improve the Surface Morphology Quality of Inkjet Printing Applications. *Journal of Manufacturing Processes*. 89 (June 2022) 458–471
<https://doi.org/10.1016/j.jmapro.2023.01.078>

Reyes-Luna, J. F., Chang, S., Tuck, C. J. and Ashcroft, I. A. Material jetting high quality components via an inverse problem framework. *Additive Manufacturing*. 73 (2023) 103667. <https://doi.org/10.1016/j.addma.2023.103667>

Reyes-Luna, J. F., Chang, S., Tuck, C. J. and Ashcroft, I. A. FE multiphysics framework for the prediction of the distortion of 3D inkjet-printed parts. *Additive Manufacturing*. In preparation for submission.

Reyes-Luna, J. F., Chang, S., Tuck, C. J. and Ashcroft, I. A. Prediction of the deformed geometry of 3D inkjet-printed components using a multiphysics stochastic framework. *Additive Manufacturing*. In preparation for submission.

Conference Presentations

Statistical Predictive Modelling of the Morphology of Inkjet-printed Tracks. XVIII Symposium of Mexican Studies and Students in the UK, Synergy-the link to the future. July 2021. University of Nottingham, UK.

An efficient surrogate-based model optimisation to predict the morphology of inkjet-printed dielectric tracks. 33rd Annual International Solid Freeform Fabrication Symposium an Additive Manufacturing Conference. July 2022. Austin, Texas.

Contents.

Abstract.....	iii
Acknowledgements.....	vi
Publications.....	vii
Contents.....	viii
List of Figures.....	xiv
List of Tables.....	xxi
Nomenclature: List of Symbols.....	xxii
Nomenclature: List of Acronyms.....	xxiii
1 Introduction.....	1
1.1 Background.....	1
1.2 Aim and objectives.....	2
1.3 Significance and novelty of the research.....	3
1.4 Research methodology.....	6
1.5 Thesis structure.....	7
2 Literature Review.....	11
2.1 Material jetting.....	11
2.1.1 Introduction.....	11
2.1.2 The inkjet printing process.....	13
2.1.3 Drop ejection and formation stage.....	14
2.1.4 Drop deposition and coalescence stage.....	16
2.1.5 Drop solidification stage.....	19
2.2 Dielectric materials compatible with AM.....	21
2.2.1 Inks.....	21
2.2.2 Substrates.....	23
2.2.3 Printers.....	25
2.3 Physics-based numerical methods.....	26
2.3.1 Classical methods.....	27
2.3.2 Particle-based methods.....	31
2.3.3 The lattice Boltzmann method.....	33
2.4 Optimisation methods.....	36
2.5 Data-driven compensation methods.....	40
2.6 Summary of literature and identified gaps in the knowledge.....	42

3	Materials and Experimental Methods.....	48
3.1	Materials.....	48
3.1.1	Ink formulation.....	48
3.1.2	Ink physical properties.....	49
3.1.3	Substrates.....	49
3.2	Experimental methods.....	50
3.2.1	Density.....	50
3.2.2	Surface tension.....	50
3.2.3	Viscosity.....	51
3.2.4	Artifacts design.....	51
3.2.4.1	2D.....	51
3.2.4.2	3D.....	52
3.2.5	Printing.....	54
3.2.6	Optical microscopy.....	56
3.2.7	Coherence scanning interferometry.....	56
3.2.8	Micro-CT scanning.....	56
3.2.9	Droplet volume.....	56
3.2.10	Determining droplet footprint diameter, position accuracy and precision.....	57
3.2.11	Determining theoretical static contact angle and layer thickness assuming a spherical cap shape and volume conservation.....	57
3.2.12	Determining printing parameters effect on the stability of single tracks and square films.....	58
4	Computational Methods.....	61
4.1	Physics-based prediction models.....	61
4.1.1	Modelling droplet impact, spreading and coalescing in inkjet printing. 62	
4.1.1.1	Governing equation.....	62
4.1.1.2	Model implementation.....	62
4.1.1.3	Numerical validation.....	63
4.1.1.4	Simulation of printing single tracks.....	64
4.1.1.5	Simulation of printing square films.....	67
4.1.2	Modelling the deformation of UV curable materials in inkjet printing. 67	
4.1.2.1	Governing equations.....	67
4.1.2.2	Model implementation.....	70
4.1.2.3	Mesh size determination.....	71

4.1.2.4	Simulation of printing rectangular cage.....	72
4.2	Data-driven prediction models.....	74
4.2.1	Shape from Shading surface reconstruction.....	74
4.2.1.1	Governing equations.....	74
4.2.1.2	Model implementation.....	75
4.2.1.3	Surface reconstruction of half sphere using synthetic image.....	77
4.2.2	Minimum-energy-shape method for surface reconstruction.....	77
4.3	Stochastic prediction model.....	79
4.3.1	Model derivation.....	79
4.3.1.1	Determination of droplet position and footprint size uncertainty and overlap map metric for film defect prediction.....	80
4.3.1.2	Determination of material overflow in single tracks and films.....	83
4.3.1.3	Determination of curing strain using photo-polymerisation model.....	86
4.3.1.4	Determination of optimal resolution, printing frequency and standoff distance for stable thin and thick film printing.....	86
4.3.1.5	Determination of stability diagram for films using stochastic thresholds..	88
4.3.2	Model implementation.....	90
4.4	Surrogate modelling approach.....	93
4.4.1	Model implementation.....	93
4.4.2	Definition of surrogate model for multiphase flow simulation.....	95
4.5	Optimisation models.....	98
4.5.1	Parameter optimisation using multi-objective genetic algorithm approach.....	98
4.5.1.1	Model implementation.....	98
4.5.1.2	Optimisation approach used in multiphase flow simulation of single tracks.	100
4.5.2	Geometry compensation using convolutional neural network approach.	101
4.6	Prediction and optimisation framework for inkjet-printed parts.....	103
4.7	Post-processing methods.....	105
4.7.1	Automatic extraction of surface morphology from CSI measurements.	105
4.7.1.1	MATLAB script implementation.....	106
4.7.2	Automatic extraction of footprint dimensions from Dimatix images.	108
4.7.2.1	MATLAB script implementation.....	109
4.7.3	Determining geometrical deviation of inkjet-printed parts.....	109
5	Surrogate model-based optimisation of printing parameters for the stability of single tracks.....	111

5.1	Introduction.	111
5.2	Methodology.	111
5.3	Results and discussion.	112
5.3.1	Surrogate model-based optimisation using lattice Boltzmann multiphase flow simulations.	112
5.3.1.1	Lattice Boltzmann multiphase flow simulation results.	112
5.3.1.2	Surrogate modelling results.	116
5.3.1.3	Optimisation results.	122
5.3.2	Surrogate model-based optimisation using experiments performed in Dimatix printer.	126
5.3.2.1	Experiments results.	126
5.3.2.2	Surrogate modelling results.	128
5.3.2.3	Optimisation results.	132
5.3.3	Differences of the surrogate model-based optimisation results using high-fidelity simulations against experiments.	135
5.4	Conclusions and summary.	138
6	Surrogate model-based optimisation of printing parameters for the stability of free form films.	140
6.1	Introduction.	140
6.2	Methodology.	140
6.3	Results and discussion.	141
6.3.1	Surrogate model-based optimisation using LB multiphase flow method. 141	
6.3.2	Surrogate model-based optimisation using Shape-from-Shading inverse problem approach.	143
6.3.2.1	Experiments results.	144
6.3.2.2	Prediction results.	145
6.3.2.3	Surrogate model results.	149
6.3.2.4	Optimisation and validation results.	155
6.4	Conclusions and summary.	159
7	Geometry prediction and compensation for the stability of 3D printed parts using machine learning approach.	162
7.1	Introduction.	162
7.2	Overall Methodology.	162
7.3	Results and discussion.	163
7.3.1	3D printed artifacts using optimal printing settings derived for films. 163	

7.3.2	Deformed geometry prediction model using a semi-empirical, semi-coupled photo-polymerisation and structural finite element approach.....	168
7.3.3	Geometry compensation and validation using a neural network trained with results from FE simulations.	173
7.3.4	Geometry compensation and validation using a neural network trained with experimental measurements.....	177
7.4	Conclusions and summary.....	182
8	Analytical model-based prediction and optimisation of the morphology of inkjet-printed parts.....	185
8.1	Introduction.	185
8.2	Methodology.	185
8.3	Results and discussion.....	186
8.3.1	Experimental results for analytical model calibration.	186
8.3.2	Break-up and bulging prediction and validation using overlap map.	190
8.3.3	Bulging frequency and volume prediction using viscous and capillary timescales.....	193
8.3.4	Experimental validation of the analytical prediction model for single tracks.	197
8.3.5	Prediction, optimisation, and validation of the surface morphology of single tracks.	202
8.3.6	Prediction and validation of the surface morphology of freeform films.	206
8.3.7	Prediction and compensation of the deformed geometry of 3D printed parts.	214
8.3.7.1	Deformed geometry prediction using stochastic model.....	214
8.3.7.2	Deformed geometry prediction using semi-empirical model.....	216
8.3.8	Computational inkjet printing implementation in MATLAB.	222
8.3.8.1	Digital image generation module.....	222
8.3.8.2	Analytical model prediction module.....	223
8.3.8.3	Surrogate model prediction module.....	225
8.3.8.4	Digital image compensation module.....	227
8.3.8.5	Shape validation module.....	229
8.4	Conclusions and summary.....	230
9	Discussion.....	233
9.1	Results discussion summary.....	234
9.1.1	Surface morphology prediction results.	234
9.1.2	Parameter optimisation results.	241
9.1.3	Deformed geometry generation and compensation results.	243

9.2	Benefits of the research to academia.....	248
9.3	Benefits of the research to industry.....	249
9.4	Novelty of the research.....	250
10	Conclusions and Future Work.....	253
10.1	Conclusions.....	253
10.2	Future work.....	259
10.2.1	Short term recommendations.....	259
10.2.2	Long term recommendations.....	261
	References.....	263
11	Appendices.....	286
11.1	Supplemental information on the lattice Boltzmann method.....	286
11.1.1	Mathematical formulation.....	286
11.1.2	Numerical validation.....	291
11.1.2.1	Evaluation of Thermodynamic Consistency.....	291
11.1.2.2	Evaluation of Laplace’s Law.....	292
11.1.2.3	Evaluation of spatial accuracy.....	293
11.1.2.4	Evaluation of contact angle.....	295
11.1.2.5	Evaluation of contact line pinning.....	296
11.2	Supplemental information on the image analysis technique validation for lines and freeform films.....	299
11.3	Supplemental information on MATLAB GUI and FORTRAN scripts....	303

List of Figures.

Figure 1-1 Research framework.....	7
Figure 1-2 Thesis layout.....	10
Figure 2-1 CIJ and DOD Inkjet printing schematic (Derby, 2010)	13
Figure 2-2 DoD inkjet printing process map and critical to quality factors for each process stage.....	14
Figure 2-3 Drop deposition process input-output diagram and critical to quality factors (Derby, 2010).	18
Figure 2-4 Drop spreading factor versus time (Wijshoff, 2018).....	21
Figure 2-5 Lattice Boltzmann methods map.....	34
Figure 2-6 LBM pseudopotential process map	36
Figure 2-7 Advantages and limitations of optimisation methods.	37
Figure 3-1 a) Jetting waveform and b) Jetted drops velocity measurement	54
Figure 3-2 Printing mechanism of a DIMATIX DMP-2830 Inkjet printer	55
Figure 4-1 Lattice Boltzmann implementation flowchart.....	63
Figure 4-2 Lattice Boltzmann benchmark tests. a. Analytical vs numerical coexisting densities. b. Validation of the capability to model density ratio up to 870 when parameter $\varepsilon = 0.319$. c. Laplace's law validation, model is capable to modify surface tension independently of density ratio by tuning parameter κ . d. Validation that model is second order accurate in space. e. Static contact angle varies linearly to the artificial wall density enabling the model to handle different wetting conditions. f. Analytical vs numerical static contact angle shows excellent agreement. g. Drop simulations for different wetting conditions. I. Lyophobic surface. II. Neutral surface. III. Lyophilic surface. IV. Two sequential drops with contact angle hysteresis included. V. Two sequential drops without contact angle hysteresis.	64
Figure 4-3 Single tracks modelling assumptions.	65
Figure 4-4 Boundary conditions schematic for single track simulation.	66
Figure 4-5 Square film. a. Modelling assumptions, b. Boundary conditions.....	67
Figure 4-6 Finite element implementation flowchart.....	70
Figure 4-7 Mesh convergence study: a. Boundary conditions; b. Displacements magnitude distribution; c. Displacements at region of interest for multiple element sizes; d. Von Mises stress at region of interest varying mesh size.	72
Figure 4-8 Printing strategy.	73
Figure 4-9 Mesh and boundary conditions of rectangular cage.....	74
Figure 4-10 Shape-from-shading implementation flow chart.....	76
Figure 4-11 Model validation using synthetic half sphere images. a. Ground truth surface: b. Synthetic images generated using the reflectance map parameters from Table 4-3; c. Reconstructed surface using Lax-Friedrichs scheme: $MAD = 3.18 \mu\text{m}$, $RMSE = 3.24 \mu\text{m}$, $CPU \text{ time} = 122 \text{ s}$	77
Figure 4-12 Spherical cap volume reconstruction schematic.	78
Figure 4-13 Minimum-energy-shape implementation flow chart.....	78
Figure 4-14 Droplet deposition representation: a. Without droplet position and size uncertainty; b. With droplet and position uncertainty.....	81
Figure 4-15 Example of overlap map metric to detect film defects.....	82

Figure 4-16 Surface morphology characterisation of single track: a. 3D view showing maximum height of printed feature; b. Top view defining average (ABW) and maximum (MBW) width; c. Front view defining average and maximum height.....	83
Figure 4-17 Single track prediction with transient flow effects.....	86
Figure 4-18 Methodology to introduce uncertainty to instabilities thresholds.	89
Figure 4-19 Example of film stability diagram.....	89
Figure 4-20 Analytical model flow chart.....	90
Figure 4-21 Analytical model outputs for the prediction of a square film: a. Printing parameters inputs. b. Printability diagram showing material is printable. c. Pattern bitmap illustrating start location and direction of printing. d. Overlap map of droplets including position and size uncertainty. Map shows no indication of film break-ups. e. Curing degree map based on UV accumulated dosage used to estimate film shrinkage. f. Film footprint edges capturing non-uniform surface morphology due to the use of multiple swaths, the width of the swath determined by the number of nozzles used while printing. g. Point cloud of the predicted film surface morphology. h. Stability diagram showing optimal printing parameters and thresholds for the onset of bulges and break-ups.	93
Figure 4-22 Surrogate modelling strategy implementation flow chart.....	94
Figure 4-23 Surrogate model development for high fidelity multiphase flow simulation.....	98
Figure 4-24 Optimisation methodology.....	101
Figure 4-25 Overview of geometry compensation methodology.	102
Figure 4-26 Convolutional neural network for geometry compensation: a. CNN training schematic; b. CNN compensation schematic.....	103
Figure 4-27 Hybrid physics-based and data-driven framework.....	104
Figure 4-28 Square film measurements report.....	106
Figure 4-29 Semi-automatic workflow for post-processing CSI measurements.	107
Figure 4-30 Square film image analysis report.....	108
Figure 4-31 Geometry deviation measurement methodology.....	110
Figure 5-1 Four sequential drops deposited at different drop spacings ($Re=16.52$, $We=32.2$, $dh=20$ and $\theta_a=60^\circ$): a) 2D Footprints, b) 3D Time evolution at $ds=70$.	114
Figure 5-2 Evolution of printed line dimensionless bead width and dimensionless thickness.....	115
Figure 5-3 Average width prediction: lattice Boltzmann model vs theoretical model (Stringer & Derby, 2010).....	116
Figure 5-4 Bead width measured at first droplet centre: a. Main effects; b. Statistically significant effects.	117
Figure 5-5 Bead width measured at first droplet centre: a) Residuals Normality, b) Percentage of error vs fit.....	118
Figure 5-6 Printed track prediction model goodness of fit results.....	121
Figure 5-7 Results comparison between a. High-fidelity lattice Boltzmann; b. Surrogate model.....	122
Figure 5-8 Simulation results mapped onto line formation regimes and the normalized central geometric moments error function.....	123
Figure 5-9 a) Pareto front and b) Validation run with optimal factor settings.....	125
Figure 5-10 Images of printed lines $L = 1$ mm following response surface methodology.....	126

Figure 5-11 CSI measurements used to generate surrogate model	127
Figure 5-12 Average width and thickness calculation.	127
Figure 5-13 Validation of the surface morphology prediction model for single tracks by comparing samples printed with printing parameters defined in matrix of experiments. a) Measured surface morphology of single track; b) predicted surface morphology built using surrogate model. c)-f) deviation assessment of the predictive models for the average width, maximum width, average thickness, and maximum thickness, respectively.....	129
Figure 5-14 Statistical analysis of predictive model. a) Average width; b) Maximum width.....	130
Figure 5-15 Statistical analysis of predictive model. a) Average thickness; b) Maximum thickness.	131
Figure 5-16 Measured vs predicted values of the fitness functions used to produce the most stable single track as function of the printing parameters. a)-c) effect of drop spacing; d)-f) effect of printing frequency; g)-i) effect of standoff distance and j)-l) effect of drop overlap on NCGM, waviness and roughness functions, respectively.	133
Figure 5-17 Surrogate model-based multi-objective optimisation results: a) Pareto front; b) Morphology prediction using optimal printing parameters.	135
Figure 5-18 Validation run on Dimatix printer using optimal printing parameters.	135
Figure 5-19 Effect of droplet overlap on NCGM error fitness function obtained from a) simulations and b) experiments.....	136
Figure 5-20 Effect of critical printing parameters on roughness fitness function. Droplet overlap effect on surrogate model based on a) simulations, b) experiments. Printing frequency effect on surrogate model based on c) simulations and d) experiments.	137
Figure 6-1 Simulation of square films using the lattice Boltzmann method varying the drop spacing only: a. Film evolution using a drop spacing of 20 μm depicting film bulging; b. Film evolution using a drop spacing of 33 μm yielding a stable film and c. Film evolution using a drop spacing of 47 μm showing film break-up and significant edge waviness. All schematics show the target square footprint as a dotted line.....	142
Figure 6-2 Comparison of LB model results and in-house experiments for validation purposes: a. Drop spacing = 20 μm and b. Drop spacing = 60 μm	143
Figure 6-3 Images of printed films following the matrix of experiments described in Table 3-5.	144
Figure 6-4 Surface morphology prediction of square films using the Shape from Shading approach.	146
Figure 6-5 Validation of prediction model using CSI measurements: a. Bulging film (ds=10 μm , pf=1 kHz and sd=0.5 mm); b. Stable film (ds=30 μm , pf=3 kHz and sd=1 mm) and c. Break-up film (ds=50 μm , pf=2 kHz, sd=1 mm).	147
Figure 6-6 Validation of the surface morphology prediction model for square films by comparing samples printed with printing parameters defined in matrix of experiments. a) Measured surface morphology of square film; b) reconstructed surface morphology using shape from shading approach. d)-i) deviation assessment	

of the predictive models for the average length, average width, average thickness, maximum length, maximum width, and maximum thickness, respectively.	151
Figure 6-7 Statistical analysis of prediction models: a. Average length, b. Average width and c. Average thickness.	152
Figure 6-8 Statistical analysis of prediction models: a. Maximum length, b. Maximum width and c. Maximum thickness.	153
Figure 6-9 Effect of printing parameters on NCGM and roughness fitness functions. a)-b) effect of drop spacing; c)-d) effect of printing frequency; e)-f) effect of standoff distance. Predicted vs measured values of NCGM and roughness fitness functions included in g) and h), respectively.	156
Figure 6-10 Multi-objective optimisation results. a. Optimal printing parameters and b. Film prediction using optimal printing parameters.	158
Figure 6-11 Printed free-form films using optimal parameters: a. Solid square film of side 1 mm; b. Ring film (outer diameter=1 mm, thickness=270 μm) and c. Hollowed square film of outer side=1 mm and thickness=250 μm . Target vs real Footprint overlay is included for each feature to illustrate the accuracy of the print.	159
Figure 7-1 3D inkjet-printed cuboid results including. CAD structure, Dimatix image, target vs real footprint and point cloud.	165
Figure 7-2 3D inkjet-printed cylinder results including CAD structure, Dimatix image, target vs real footprint and point cloud.	165
Figure 7-3 3D inkjet-printed cage results including CAD structure, Dimatix image, target vs real footprint and point cloud.	166
Figure 7-4 3D inkjet-printed H-structure results including CAD structure, Dimatix image, target vs real footprint and point cloud.	166
Figure 7-5 3D inkjet-printed I-structure results including CAD structure, Dimatix image, target vs real footprint and point cloud.	167
Figure 7-6 3D inkjet-printed TI sensor package results including CAD structure, Dimatix image, target vs real footprint and point cloud.	167
Figure 7-7 TPGDA material properties employed in FE simulation: a. Semi-empirical model of the degree of monomer consumption as function of UV dosage; b. Young's modulus as function of degree of monomer consumption assuming gel point at 0.42 and polymer Young modulus of 0.6 GPa; and c. Effective coefficient of thermal expansion (chemical contraction) assuming maximum chemical strain at 0.12.	169
Figure 7-8 Comparison of the degree of monomer consumption distribution for a square film with the printed sample for the optimal printing parameters.	169
Figure 7-9 FE Results for the cuboid artifact: a. Schematic showing part orientation, printing origin and direction; b. Z-displacements contour plot with 50 layers overlaid (magnification factor = 2); c. Shrinkage behaviour of cuboid surface from top to bottom section; and d. CAD vs predicted point cloud overlay.	171
Figure 7-10 FE simulation results. Target geometry, predicted geometry, overlay of target vs predicted point clouds and absolute deviations ordered by columns, respectively.	172
Figure 7-11 Neural network training process statistical analysis results including histogram of residuals and mean squared error convergence plots.	174

Figure 7-12 Geometry compensation framework results using FE simulation for neural network training process.	175
Figure 7-13 Neural network training process statistical analysis results including histogram of residuals and mean squared error convergence plots.....	179
Figure 7-14 Compensated geometry using experimental data for neural network training process.	180
Figure 7-15 Validation of geometry compensation framework by direct comparison to printed samples. Layer Schematic and Dimatix images included.	182
Figure 8-1 TPGDA printability diagram.....	187
Figure 8-2 Comparison of footprint diameter normal distribution: a) analytical model and b) measured data.....	189
Figure 8-3 Position error distributions: a) X-direction and b) Y-direction.....	189
Figure 8-4 Graphical representation of inkjet-printed droplets on a circular pattern considering a) constant and b) variable drop spacing.	190
Figure 8-5 Prediction of high probability break-up locations using Overlap Map and Monte Carlo simulation. a) Single pixel line (L=1 mm, ds=50 μ m, pf=1 kHz, sd=0.5 mm), b) Solid square pattern (side=1 mm, ds=50 μ m, pf=1 kHz, sd=0.5 mm), and c) Solid circle pattern (D=1.5 mm, ds=40 μ m, pf=1 kHz, sd=0.5 mm).....	191
Figure 8-6 Prediction of high probability bulging locations for a solid square pattern using Overlap Map and Monte Carlo simulation. a) Drop spacing set to 10 μ m and b) Drop spacing set to 30 μ m.	193
Figure 8-7 Effect of printing parameters, physical properties and wetting on the size and frequency of bulges. a) Contact angle, b) printing frequency, c) standoff distance, d) surface tension and e) dynamic viscosity.	195
Figure 8-8 Primary and secondary bulges prediction with different drop spacing. .	196
Figure 8-9 Example of model calibration grid and printed single track examples. .	198
Figure 8-10 Comparison of analytical model predictions and measured data for average and maximum width dimensions of single tracks. Printed tracks on Si-wafer with native droplet volume of 10 pL displayed in a. and b. Printed tracks on Si-wafer with native droplet volume of 2.4 pL displayed in c. and d.....	200
Figure 8-11 Comparison of analytical model predictions and measured data for average and maximum height dimensions of single tracks. Printed tracks on Si-wafer with native droplet volume of 10 pL displayed in a. and b. Printed tracks on Si-wafer with native droplet volume of 2.4 pL displayed in c. and d.....	201
Figure 8-12 Comparison of analytical model simulation and printed samples of single tracks varying drop spacing. a. 10 μ m, b. 20 μ m, c. 30 μ m, d. 40 μ m, e. 45 μ m, f. 50 μ m, g. 60 μ m and h. 70 μ m.....	203
Figure 8-13 Simulated lines L=1 mm vs printed samples varying drop spacing. a.10 μ m, b. 40 μ m and c. 60 μ m.....	203
Figure 8-14 Effect of printing frequency on lines printed using high resolution (drop spacing = 10 μ m). a. 1 kHz and b. 4 kHz.....	204
Figure 8-15 Stability Diagram for TPGDA printed on glass with cartridge model 11610. Optimal printing parameters shown are to achieve stable thinnest tracks. .	205
Figure 8-16 Analytical model simulation results compared to printed samples for freeform patterns. a. Solid square, b. Hollowed square, c. Ring, and d. Archimedean spiral.....	207

Figure 8-17 Comparison of simulated patterns using a. single and b. multiple nozzles.	208
Figure 8-18 Comparison of analytical model simulation of a square film with excessive overflow on pattern boundaries with experiments. a. Simulated morphology, b. Printed sample, c. Footprint overlay plot and d. Y-Z cross-section overlay plot at centroid of film.....	209
Figure 8-19 Simulated vs real surface morphology overlay and absolute deviation for a solid square film.	210
Figure 8-20 Experimental validation of optimal printing parameters using the proposed stability diagrams for: a. TPGDA on Si-wafer, V=2.4 pL, batch 1; b. TPGDA on Si-wafer, V=10 pL, batch 2; c. TPGDA on Si-wafer, V=2.4 pL, batch 2 and d. TPGDA on glass, V=10 pL with optimised parameters for thicker films.....	212
Figure 8-21 Comparison of printed samples with different substrate wettabilities against target dimensions: a. TPGDA printed on Si-wafer and b. TPGDA printed on a film of TPGDA.....	213
Figure 8-22 Analytical simulation results and comparison to target and printed samples.	216
Figure 8-23 Experiments performed to understand the effect of multiple layers on features' dimensions. Three simple patterns are printed with 5 layers each as follows: a. solid square side 1 mm, b. hollowed square side=1 mm, width=0.25 mm and c. ring diameter=1 mm, width = 0.27 mm.	217
Figure 8-24 Overlay plot of layer footprints to assess the impact of multilayer printing in overall features' dimensions.	218
Figure 8-25 Quantitative analysis results for the solid square part. a. Schematic of measured dimensions. b. Effect of multiple layers on length and width. c. Effect of multiple layers on thickness. d. Regression equations to model error on average dimensions.	219
Figure 8-26 Effect of multiple layers on the evolution of corner radii. a. Schematic with corner IDs. b. Regression analysis plot.....	220
Figure 8-27 Semi-empirical prediction model results comparison with printed samples.....	221
Figure 8-28 Pattern generation module interface. a. Single layer of simple shapes. b. Multiple layers from CAD files.	223
Figure 8-29 Prediction module interface.....	225
Figure 8-30 Surrogate model prediction module interface. a. Statistical analysis results. b. Predicted surface morphology as function of selected factors.	227
Figure 8-31 Digital image compensation module.....	228
Figure 8-32 Shape validation module interface post processing tools. a. Volume cross-sections viewer, b. Overlay plot and c. Deviations map with maximum deviations and mean square error.....	230
Figure 9-1 Comparison of the surface morphology of single tracks using different prediction models. a. Lattice Boltzmann of a line build from 4 drops. b. Surrogate model built from sample of LBM simulation results. c. Experiments measured using CSI. d. Surrogate model built from experiments. e. Shape from shading prediction built from image. F. MPSA single track prediction.	237
Figure 9-2 Comparison of the surface morphology of solid square films using different prediction models. a. Experiments measured using CSI. b. Shape from	

shading prediction built from image. C. Surrogate model built from experiments. d. Analytical model prediction. e. Deviation of SFS prediction from experiments. f. Deviation of analytical prediction from experiments.....	240
Figure 9-3 Samples printed with optimal printing parameters for validation purposes.	242
Figure 9-4 Geometry compensation framework results. a. Experiments measured using microCT scan. b. Target vs compensated geometry using data measurements. c. Deformed geometry predicted using FE simulation. d. Target vs compensated geometry from FE results. e. MPSA model prediction of deformed geometry vs target. f. MPSA model prediction with spherical cap assumption for simple 3D features.	247
Figure 11-1 Thermodynamic consistency validation.	292
Figure 11-2 Laplace's law validation.	293
Figure 11-3 Spatial accuracy validation.....	294
Figure 11-4 (a) Lyophobic surface; (b) Neutral surface; (c) Lyophilic surface.....	296
Figure 11-5 (a) Static contact angle vs ρ_w ; (b) Theoretical vs numerical spreading factor comparison.....	296
Figure 11-6 Footprint of sequential drops a) with and b) without contact angle hysteresis.	298
Figure 11-7 Comparison of image analysis vs CSI measurements of the footprints of single tracks.....	300
Figure 11-8 Comparison of dimensions measured using image analysis and CSI. a. Length, b. Average width, c. Maximum width and d. Average thickness.	301
Figure 11-9 Comparison of image analysis vs CSI measurements of the footprints of solid and hollowed films.	302

List of Tables.

Table 2-1 Drop formation input-output diagram and critical to quality factors.	16
Table 2-2 Classification of dielectric materials (Singh & Ulrich, 1999)	22
Table 2-3 Applications of polymer-based substrates (Hoffman, 2017).....	24
Table 2-4 Applications of glass-based substrates (Parthier et al., 2017).	24
Table 2-5 Advantages and limitations of discretization schemes for CFD applications.	28
Table 3-1 TPGDA physical properties.....	49
Table 3-2 2D testing artifacts dimensions.....	52
Table 3-3 3D artifacts dimensions	53
Table 3-4 Matrix of experiments for single tracks.....	59
Table 3-5 Matrix of experiments for square films	60
Table 4-1 Fluid properties, simulation parameters and relevant dimensionless numbers	65
Table 4-2 Fitted parameters for degree of curing estimation.	73
Table 4-3 Reflectance map parameters for synthetic images.....	77
Table 4-4 Critical printing parameters bounds.	88
Table 4-5 Design variables bounds.	96
Table 4-6 Central composite design of experiments.....	97
Table 5-1 Bead width transfer functions and measures of fit	118
Table 5-2 Bead thickness transfer functions and measures of fit.....	119
Table 5-3 Calculated fitness functions based on experimental results.	127
Table 5-4 Single objective optimisation using gradient based (local) approach.	134
Table 6-1 Optimal reflectance map parameters.	145
Table 6-2 Quantitative comparisons of predicted vs measured film morphology. ...	149
Table 6-3 Calculated fitness functions based on SFS prediction results.	149
Table 6-4 Surrogate model accuracy indicators.....	154
Table 6-5 Single objective optimisation using gradient based (local) approach.	157
Table 7-1 Comparison of real and target dimensions of printed artifacts.....	164
Table 7-2 FE parameters, simulation results and solution time.	173
Table 7-3 Comparison of the mean squared error before and after compensation. .	176
Table 8-1 TPGDA measured physical properties.	186
Table 8-2 Droplet footprint size and location statistics.	188
Table 8-3 Estimated values for droplet height and volume.	188
Table 8-4 Grid analysis results for analytical model calibration.	198
Table 8-5 Coefficient “A” determined using droplet characteristics from grid analysis and physical properties.....	199
Table 8-6 Prediction error observed in dimensions of single tracks.....	202
Table 8-7 Predicted morphology at optimal printing settings for thin and thick lines.	205
Table 9-1 Optimal printing parameters derived from different prediction models..	242
Table 11-1 Printing parameters for single tracks used in image analysis validation.	299

Nomenclature: List of Symbols.

A_{fp}	Footprint Area [m ²]	U_c	Capillary speed [m s ⁻¹]
Bo	Bond Number	U_{CL}	Contact line speed [m s ⁻¹]
Ca	Capillary Number	U_e	Ejection speed [m s ⁻¹]
DPU	Droplet Position Uncertainty [m]	U_T	Traverse speed [m s ⁻¹]
DSU	Droplet Size Uncertainty [m]	V_{drop}	Drop in-flight volume [m ³]
d_o	Drop in-flight diameter [m]	W	Width [m]
d_{fp}	Drop footprint diameter [m]	We	Weber Number
dh	Drop Spacing (vertical) [m]	Z	Printability Number
ds	Drop Spacing [m]	α	Statistical Significance Level
E	Young Modulus [Pa]	β	Spreading Factor
H	Height [m]	Γ	Shape Prior [m]
h	Spherical Cap Height [m]	γ	Surface Tension [N m ⁻¹]
h_t	Spherical Cap Max Height [m]	δ	Deviation [m]
L	Length [m]	ε	Strain
L_{thk}	Layer Thickness [m]	ζ	Volumetric Shrinkage [%]
N	Number of Drops	η	Kinematic Viscosity [m ² s ⁻¹]
N_l	Number of Layers	θ_a	Advancing Contact Angle [°]
N_n	Number of Nozzles	θ_e	Equilibrium Contact Angle [°]
n	Shininess Factor	θ_{js}	Jet Straightness [°]
Oh	Ohnesorge Number	θ_r	Receding Contact Angle [°]
pf	Printing Frequency [s ⁻¹]	θ_{th}	Spherical Cap Contact Angle [°]
s	Surface Roughness Factor	κ	Shape Wettability Factor
sd	Standoff Distance [m]	λ	UV Radiation Dosage [kg ^{0.5} s ^{-0.5}]
R	Radius of Gyration [m]	μ	Dynamic Viscosity [Pa s]
R_{DPI}	Resolution [DPI]	μ_n	Mean of n observations
Re	Reynolds Number	O	Droplet Overlap [%]
r	Spherical Cap Radius [m]	ρ	Density [kg m ⁻³]
T_p	Printhead Temperature [°C]	σ	Stress [Pa]
T_s	Substrate Temperature [°C]	σ_n	Standard Deviation in n direction
t	Time [s]	φ	Volumetric Factor
t_c	Capillary timescale [s]	χ	Degree of Monomer Consumption
t_f	Frequency timescale [s]	ψ	Diffusivity Factor
t_v	Viscous timescale [s]	ω_d	Diffuse Reflection Factor
t_{uv}	UV exposure time [s]	ω_s	Specular Reflection Factor

Nomenclature: List of Acronyms.

2D	2-Dimensional	MBW	Maximum Bead Width
3D	3-Dimensional	ML	Machine Learning
ABH	Average Bead Height	MOO	Multi-Objective Optimisation
ABW	Average Bead Width	MRT	Multi-Relaxation Time
AI	Artificial Intelligence	MPSA	Multi-Physics Stochastic Analytical
AM	Additive Manufacturing	MSE	Mean Square Error
BGK	Bhatnagar–Gross–Krook operator	NCGM	Normalised Central Geometric Moment
BMP	Bitmap file	NSE	Navier Stokes Equations
CAD	Computer Aided Design	OLED	Organic Light-Emitting Diode
CCD	Central Composite Design	PDE	Partial Differential Equation
CFD	Computational Fluid Dynamics	PDF	Probability Density Function
CIJ	Continuous Inkjet	PE	Printed Electronics
CNN	Convolutional Neural Network	PEN	Polyethylene Naphthalate
CPU	Central Processing Unit	PET	Polyethylene Terephthalate
CSI	Coherence Scanning Interferometry	PI	Polyimide
CT	Computed Tomography	PMMA	Polymethyl Methacrylate
CTQ	Critical To Quality factor	PVP	Poly (4–vinyl phenol)
DIJP	Digital Inkjet Printing	RF	Radio Frequency
DOD	Drop On Demand	RFID	Radio Frequency Identification
DOE	Design Of Experiments	RGB	Red-Green-Blue format
DPI	Drops Per Inch	ROI	Region Of Interest
DPE	Drop Position Error	RSM	Response Surface Method
DPU	Drop Position Uncertainty	RSME	Root Mean Square Error
FE	Finite Element	SCMP	Single Component Multi-Phase
GA	Genetic Algorithm	SFS	Shape from Shading
GBR	Gerber file	SLA	Stereolithography technology
GUI	Graphical User Interface	STL	Stereolithography file
HPC	High Performance Computing	TI	Texas Instruments
IA	Image Analysis	TPGDA	Tripropylene Glycol Diacrylate
IPC	Institute of Printed Circuits	TXT	Text file
LBM	Lattice Boltzmann Method	UV	Ultraviolet
LS	Level Set method	UMAT	User Material subroutine
MAD	Mean Absolute Deviation	VOF	Volume of Fluid
MBH	Maximum Bead Height		

1 Introduction.

1.1 Background.

Current technology trends indicate a growing interest in the development of highly integrated printed electronics to a broad range of industries. From healthcare to aerospace applications, the demand of thinner electronics and light-weight devices is in continuous expansion. Due to the increased development of smart and connected devices, the printed electronics worldwide market is projected to grow from 7.8 billion in 2020 to 20.7 billion (USD) by 2025 (Markets & Markets, 2020). Among different devices, OLEDs, conductive inks in photovoltaic applications and printed organic sensors are taking the lead in the market, while smart devices such as RFID tags and indicators are expected to spread with the entrance of 5G wireless band. As a result, printed electronics is considered one of the fastest growing technologies today.

As such, AM technologies are steadily evolving to fulfil the printed electronics demand by reducing costs and incorporating agile production of overly complex products. In particular, inkjet printing has proven to be a flexible and reliable manufacturing process for the printed electronics business (Saleh et al., 2017). Inkjet printing is an additive manufacturing technology associated with the material jetting family, featuring digital design integration, contactless deposition, and minimal material waste. The application of this process has made possible the miniaturization of various kinds of electronic systems such as multilayer RF capacitors (Cook et al., 2013), Lab-on-a-Chip microfluidic devices (Su et al., 2016), mm-wave wireless systems packaging (Tehrani et al., 2017), OLED displays (Amruth et al., 2019), and antennas (Tehrani et al., 2018) in a cost-effective way.

However, despite of all benefits brought by inkjet printing to the printed electronics business, there are still challenges worthy of discussion. Current electronic packaging applications demand uniform thickness to ensure adequate protection of critical components as well as high resolution of fine features from printed patterns such as corners or edges to prevent short circuits and increase printed quality. To achieve uniformity and stability of printed films requires fine-tuned inkjet printing parameters coupled with adequate physical properties of the ink and compatible substrate

wettability characteristics. This demands a trial-and-error approach with validation tests, that are often very time-consuming process. Therefore, this work concentrates on developing fast and accurate modelling methods to improve the accuracy of printed features considering inhomogeneous morphology, substrate capillary effects and multiple layers build-up interaction for printed electronics applications.

1.2 Aim and objectives.

The aim of this thesis is to develop new modelling techniques to predict fast and accurately the surface morphology of inkjet-printed features, enabling the optimisation of DIJP control parameters and the compensation of images for better dimensional accuracy of printed electronics devices. To achieve this, the following objectives are required:

1. Construct a high-fidelity model of the inkjet deposition process.
 - Develop a fundamental understanding of inkjet drop dynamics: impact, merging and wetting stages.
 - Predict droplet deposition during inkjet printing of functional dielectric materials based on literature survey.
 - Investigate the role of printing parameters and wetting characteristics on the feature stability.
 - Assess the capability of the model to simulate any size and pattern shape on a timely manner.
2. Validate high fidelity model.
 - Show model work for different inks and patterns (lines, corners, films) on non-porous substrates.
 - Extend validation to account for the morphology of the printed structure.
 - Show the effect of multiple layers built up on each other.
3. Develop and validate a predictive model.

- Find the optimal printing parameters that produce a stable film.
- Create methodology to compensate digital image to print fine features.
- Validate compensation methodology using complex 2D patterns and 3D artifacts.
- Incorporate an active control for the model to adapt towards dynamic behaviour of surface chemistry effects.

1.3 Significance and novelty of the research.

Although inkjet printing has proven to be a reliable and cost-effective method to fabricate certain electronics components, the effort to find the optimal parameters to obtain a uniform and stable film is still remarkably high. Computational fluid dynamics simulations have been extensively employed to build high-fidelity models of the inkjet printing processes using both classical and particle-based methods with good correlation to experimental data; however, the simulation time to determine drop impact and spreading dynamics is significantly high to be used within an optimization algorithm, rendering this method impractical. Surrogate models capable of fast execution without losing accuracy in the flow field prediction have not been thoroughly investigated to the best of our knowledge. Furthermore, evidence from the literature review shows that little analytic attention has been paid to the influence of substrate morphology on final deposition pattern for 3D inkjet printing applications. Finally, studies about error compensation techniques used in additive manufacturing technologies are still scarce. There are few articles providing insight of error compensation methods for VAT photopolymerisation and material extrusion technologies, but no scientific evidence was found for inkjet printing technologies.

Therefore, the novelty of this research lies in the development of a hybrid physics-based and data-driven modelling framework to predict and optimise the surface morphology of 3D inkjet-printed parts as a function of printing parameters, material physical properties and wetting characteristics. After reviewing the literature, this framework introduces for the first time to the best of our knowledge the following features in a single process:

Image Generation App. Produces ready-to-print bitmaps of patterns used in electronic packaging applications for any given size and position. Capable of reading and slicing STL files providing the desired resolution and layer thickness.

Prediction App. Simulates the inkjet printing deposition process of the target layer pattern given material properties, printing parameters, wetting characteristics, UV curing shrinkage and droplet landing location and size uncertainties using an analytical model. Based on the initial inputs, creates a printability diagram illustrating if the system meets droplet formation and impact requirements and produces a stability diagram depicting thresholds for bulging and break-up and optimal values for drop spacing, printing frequency and stand-off distance depending on the type of feature desired to print such as lines or films.

Optimisation App. Builds matrix parametric study based on a response surface design of experiments to create a surrogate model from the results of high-fidelity simulations, shape from shading volume reconstructions or actual measurements of printed features. Creates an input file to run the simulations in our lattice Boltzmann multiphase flow solver or our finite element chemo-mechanical solver (for lines or small square films only) or our PDE shape from shading solver (for any shape but constrained to high contrast images).

Compensation App. Trains a convolutional neural network (CNN) using the x, y and z coordinates of the 3D deformed geometry, which results from either our prediction models or from actual measurements. By providing the target shape coordinates, the CNN calculates the compensation required by the geometry to minimise the error to target shape. New geometry is sliced and bitmaps with compensated layer geometry are produced.

Validation App. Provides a set of post-processing tools to compare the results from the model predictions or actual measurements against target 2D patterns and 3D shapes. For example, allows the calculation of the mean square error (MSE) and mean absolute deviation between two surfaces, generates cross-section images at any given location of a geometry, overlaps and measures footprints to evaluate dimensional accuracy.

This investigation is significant since it has contributed to the advancement of the understanding of the complex fluid dynamics observed in inkjet printing: Some key contributions derived from this research are:

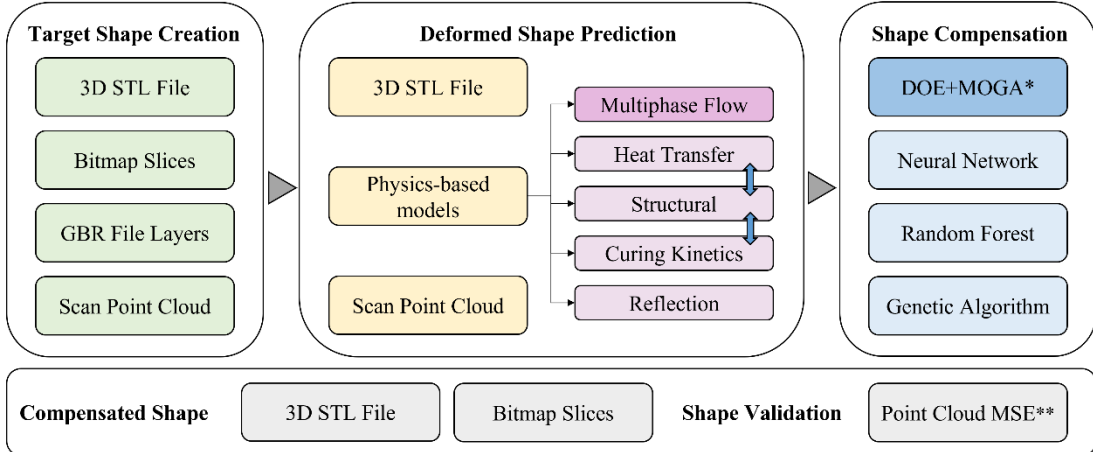
- An analytical model to predict the material overflow at edges of films employing the ratio of momentum diffusivity and capillary diffusion, which provides an insightful connection between physical properties, printing parameters and wetting behaviour.
- An analytical model to predict the centroid of the layer thickness utilising the ratio of the total volume of ink deposited and the square of the drop spacing, which offers a fast and accurate way to estimate the layer thickness assuming a spherical cap minimal energy shape.
- An analytical and experimental methodology to determine the droplet landing position and diameter uncertainty inherent to the printer motion system accuracy and precision which are critical to predict edge waviness and therefore, the optimal values of printing parameters.
- An analytical and experimental methodology to identify the size and location of partial curing in printed films, which provides a way to account for its effects in the predicted deformed geometry of layers and 3D printed artifacts.
- An analytical model to calculate the optimal traverse velocity as a function of the ratio between the ejection velocity and the capillary velocity and the contact line velocity, which is critical to determine the printing frequency and stand-off distance required for printing stable tracks and films.
- A droplet overlap map which provides a fast way to quantify statistically the number of defects such as bulges and break ups in tracks and films and helps determining a more realistic footprint edge than traditional simulation methods.
- A film stability diagram which illustrates the onset of bulging and separation for lines and films as well as the optimal drop spacing, printing frequency and stand-off distance considering the uncertainty of the equipment.

1.4 Research methodology.

Based on the objectives outlined, a research framework was proposed to foster the integration of predictive physics-based and data driven models with parameter optimisation and layer compensation techniques required to improve the dimensional accuracy of inkjet-printed parts. As illustrated in Figure 1-1, the framework consists of five modules: target shape creation, deformed shape prediction, parameter optimisation, shape compensation and model validation.

The research framework is initiated with the target shape creation module which investigates tools to produce bitmap files defining the desired pattern to print. Since the intention is to mimic how an actual inkjet printer works, this module enables the generation of simple bitmap patterns with desired resolution, size and location and ensures that any 3D target shape defined in STL, GBR or TXT format is sliced and converted to bitmap files suitable for the printer and prediction models. In addition, printing parameters, droplet characteristics, physical properties and wetting behaviour are defined and communicated to the prediction module in a “recipe” format. Then, to investigate the accuracy and suitability of the selected physics-based and data-driven models, a variety of simulation studies are performed to understand the effect of printing parameters, wetting characteristics and physical properties on the surface morphology of tracks and films during the inkjet printing process. Physics-based models are simplified using a surrogate model based on response surface equations to significantly reduce the simulation time. Alternatively, data driven models are developed to enable the surface morphology reconstruction of free-form shapes. Simulation results from physics-based models and surface reconstruction from data-driven models are employed to build a transfer function relating printing parameters and the predicted surface morphology. Subsequently, in the parameter optimisation module, a multi-objective genetic algorithm is used to find the printing parameters that minimise the error between the predicted surface morphology and the target pattern of single layers. For multi-layered parts, the shape compensation module follows, a convolutional neural network is utilized to compensate the 3D deformed geometry such that the error to target shape is reduced. Bitmaps of layers with optimised resolution and geometry are generated and validated by experiments and measurements from CSI or microCT scan are post-processed in the validation module.

This investigation aims at developing fast and accurate physics-based and data driven prediction models of the deformed geometry of inkjet printed components integrated with a process parameter optimisation framework to improve the surface morphology quality of printed parts.



* Design of Experiments + Multi-objective Genetic Algorithm
 ** Mean Square Error to nearest point neighbour

Figure 1-1 Research framework

1.5 Thesis structure.

A description of the contents for each chapter is presented below.

Chapter 1 provides a brief overview of the inkjet printing process, the advantages that this additive manufacturing technology brings for the fabrication of microelectronic devices and the current challenges it faces to be fully adopted in the semiconductor industry. Within this context, the aim and objectives of this investigation are laid out pointing out the novelty of the research. The chapter closes with a summary of the research framework and thesis layout setting a clear scope and direction for the investigation.

Chapter 2 presents a literature survey of the state of the art in modelling and optimisation of inkjet printing in the context of printed electronics applications. The chapter starts with an extensive review of the physics behind the inkjet printing technology, followed by a summary of previous research done using the materials, inks and substrates, under investigation. Then, the most relevant numerical and optimisation methods in inkjet printing are introduced in greater detail, along with non-traditional methods that have not yet been explored in this context. Finally, the knowledge gaps in the current state of research are identified.

Chapter 3 describes the experimental methods and materials used in this investigation. First, details on the material formulation, substrate characteristics and cleaning process are pinned down, followed by an explanation of the procedure to setup the printer before every experiment. Then, a design of experiments methodology is selected to establish the relationship of the parameters under investigation and benchmark artifacts for validation purposes are illustrated. Finally, the measurement techniques used to characterise the surface morphology of the printed features are examined.

Chapter 4 focuses on the computational and analytical methods implemented in this research. The chapter is divided in five sections: physics-based models, data-driven models, surrogate methods, optimisation techniques and hybrid approach. The lattice Boltzmann multiphase flow model and the finite element chemo-thermo-mechanical model formulation, problem definition and numerical validation are documented in the physics-based section. Shape from shading inverse problem and image analysis based on spherical cap assumptions methodologies to reconstruct the surface morphology of a printed feature are reported thoroughly in the data-driven section. Then, the proposed surrogate methods, one based on a response surface methodology and the other based on derived analytical models, are scrutinized to enable the optimisation of parameters under investigation. Finally, a hybrid methodology to perform the prediction of single and multilayer parts in a holistic manner is postulated.

Chapter 5 covers the results achieved from a study on the prediction and optimisation of single tracks created by inkjet printing. A set of in silico experiments using the lattice Boltzmann multiphase flow model to study the effect of drop spacing and contact angle hysteresis on the surface morphology of single tracks are documented. Then, investigations conducted using the finite element chemo-mechanical model to examine the effect of UV exposure time on the final geometry of printed tracks are reported. Finally, surrogate model results based on simulations and experiments are utilized to build a transfer function and find the optimal printing parameters to attain a stable track.

Chapter 6 documents the results achieved from a study of the prediction and optimisation of freeform films with fine features created by inkjet printing. Using the data driven approaches, a comprehensive parametric study to determine the influence of drop spacing, printing frequency and stand-off distance on the surface morphology

of freeform films is examined. Finally, recommendations on minimum achievable features and values of optimal parameters to fabricate stable films are outlined.

Chapter 7 reports the results achieved from a study of the prediction and optimisation of 3D inkjet-printed parts. First, the definition of the 3D artifact is illustrated, followed by the slicing procedure to generate the set of layers required to print component. Then, a series of studies, both experimental and computational, are performed to assess the effect of printing parameters on each layer, along with their corresponding optimal values. Subsequently, a layer compensation strategy based on a convolutional neural network is applied to reduce the error between the target shape and deformed geometry. Validation of the optimised printing parameters and layer compensation strategy is performed by quantifying the maximum absolute deviation between target and deformed geometry. Finally, recommendations on minimum achievable features and values of optimal parameters to fabricate 3D parts are outlined.

Chapter 8 presents the results of the multiphysics, stochastic, analytical model developed in this investigation to predict fast and accurately the surface morphology of inkjet-printed parts for any size and shape considering droplet size and position uncertainty, multi-nozzle printing, UV exposure time and chemical shrinkage. The analytical model represents the most significant contribution of the present work, since it leverages learnings from the physics-based and data-driven models and integrates creative algorithms and heuristics rules to drive AM part quality optimisation within a computational inkjet printing environment, which is considered the cornerstone of an inkjet printing digital twin.

Chapter 9 explains the implications and limitations of the key findings obtained from this research work. It shows how gaps from literature review are covered and highlights the research contribution to knowledge in the academic and industrial contexts.

Chapter 10 outlines the conclusions of this investigation and provides a summary of recommendations for future work.

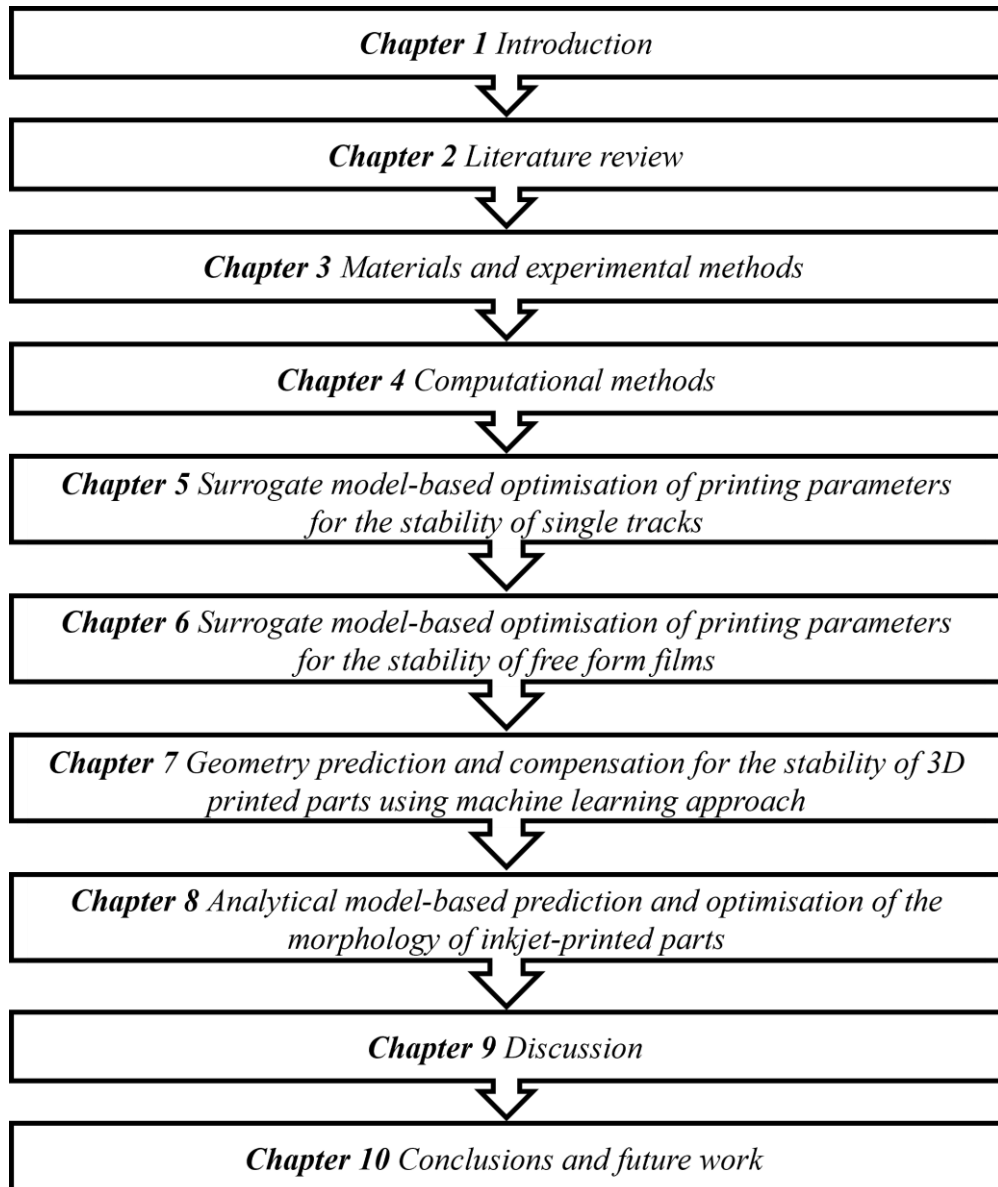


Figure 1-2 Thesis layout.

2 Literature Review.

The purpose of this chapter is to scrutinise current literature regarding modelling and optimisation techniques used in inkjet printing of electronic materials and to identify gaps in the knowledge that this research aims to fulfil. First, a detailed review of the drop on demand inkjet printing process is presented, including the most relevant dimensionless numbers, key printing parameters and limiting conditions on each phase of the process. Next, a survey in the areas of electronic materials compatible with Additive Manufacturing and inkjet equipment capability for industrial applications is examined. Then, an extensive survey of the numerical methods utilized to model inkjet is performed, along with related theory. Finally, research regarding optimisation algorithms and error compensation schemes employed to improve the dimensional accuracy of additive manufactured parts is studied. The gaps in the literature related to the modelling and optimisation of inkjet printing applied to printed electronics devices are pointed out at the end of the chapter.

2.1 Material jetting.

2.1.1 Introduction.

The concept of additive manufacturing dates to the early 80s in Japan. The idea behind the concept is simple, a flexible fabrication process of complex structures in which material is gradually layered until the desired form is reached. AM has become relevant due to the increased digitalization of manufacturing processes, bringing flexibility and efficiency into a broad range of industries. AM allows the fabrication of complex shapes providing a larger design space that ultimately impacts the product development cycle (Hague et al., 2003). Furthermore, additive systems can integrate additional features to customize products in a cost-effective way (Tuck et al., 2008) and fabricate components simultaneously for greater operation flexibility (Ruffo & Hague, 2007). Also, whether AM is used for production or prototyping, design lead times are frequently reduced. For example, lead times for jet engines parts have been reduced by a year or more (Han, 2017).

Material jetting is one of the seven types of AM technologies (ASTM, 2012). In material jetting, droplets of material are selectively jetted and cured using either ultraviolet light or heat to form a 3D object. The material can be jetted continuously or on-demand to create the parts. As with most AM technology machines, the deposition of the material is controlled by X, Y and Z movement to create the object in 3D space.

A comprehensive overview of AM technologies is given by Gibson et al. (2010). One contribution of this work is the description of eight key steps present in every AM technique, namely:

- Design conceptualization using CAD or 3D scanning and “point cloud” treatment (Tuck et al., 2008)
- Conversion to Stereolithography (STL) file format
- STL file manipulation and transfer to AM system
- Machine setup
- Object building
- Part clean-up and removal
- Post-processing
- Application

Although, AM technologies present multiple advantages in the fabrication of complex products, there are still limitations that have prevented their full industry adoption. Some of the biggest AM technological challenges are related to build speed, materials formulation and consistency, printing geometry data preparation, surface finish and dimensional accuracy (Abdulhameed et al., 2019). The issue of ensuring dimensional accuracy in printed parts, along with the bottleneck imposed by the printing files, which is assessed in the present work through the development of state-of-the-art prediction models coupled with error compensation schemes applied to digital objects in inkjet printing for AM applications.

2.1.2 The inkjet printing process.

Inkjet printing is a technology where multiple droplets are deposited onto a substrate in a certain pattern defined by a digital object. Based on the printhead configuration, as shown in Figure 2-1, there are two types of operation: continuous inkjet (CIJ) and drop-on-demand (DOD). CIJ technology was first introduced in the early 70s to commercial applications that demand high speed at the cost of less resolution. But the increasing need of precise prints evolved the technology into DOD which enables a better control of the ejected ink and thus, higher printing resolution and less waste. Nowadays, DOD is the most widely used printhead mode in commercial applications (Hoath, 2016). In this investigation, DOD inkjet printing technology and its applications to the printed electronics business is examined.

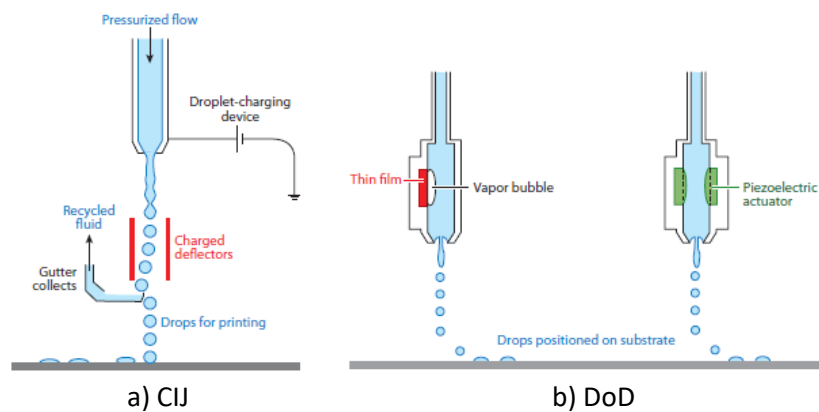


Figure 2-1 CIJ and DOD Inkjet printing schematic (Derby, 2010)

According to Derby (2010), the inkjet printing process encompasses 3 physical operations which define and constrain the accurate positional placement of microscale drops on arbitrary substrates: drop formation, drop/substrate interaction and drop solidification. In this study, we build upon this research and proposed a fourth process called layer interaction which considers 3D printing phenomena. Furthermore, a printability criterion is associated to each physical process output that are considered “fit and form” factors critical to the quality, namely CTQs, of the printing pattern. For printed electronics applications, the shape and uniformity of the printed pattern are paramount for the adequate product operation (Beedasy & Smith, 2020). Therefore, the high-level process map shown in Figure 2-2 includes a “function” criterion based on electrical and mechanical characterization of patterns.

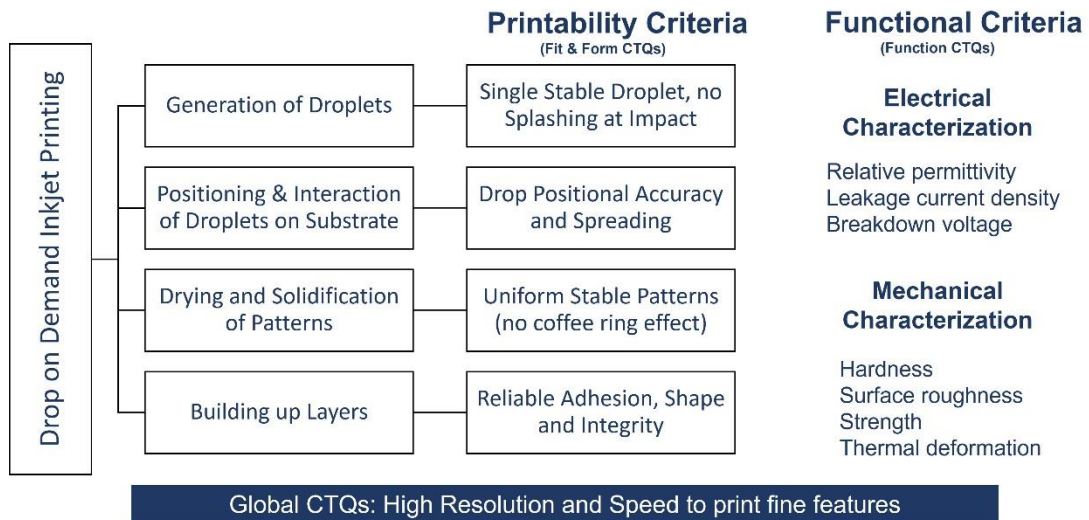


Figure 2-2 DoD inkjet printing process map and critical to quality factors for each process stage.

2.1.3 Drop ejection and formation stage.

In piezoelectric DOD, droplets are generated by a pressure wave that travels along the printhead ink channel, which is driven by the deformation of a piezoelectric actuator. The energy transfer process happens at the nozzle where the acoustic energy is transformed into kinetic and surface energy, shaping and driving the fluid droplets. Drop ejection speed and volume are controlled by the interaction of the electrical pulse shape and printhead geometry and structural stiffness (Wijshoff, 2004). The physical properties driving the drop formation process are ink density (ρ), surface tension (γ) and dynamic viscosity (μ). The latter is a key constraint to the inkjet printing process since typical commercial printheads can only handle viscosities less than 20 centipoise. Important developments in equipment design have enabled a higher ink viscosity range in 3D inkjet printing applications (Ledesma, 2018), although this is still an area under research.

To study the relationships between drop ejection velocity, drop volume and the physical properties of the ink, a series of dimensionless numbers have been historically defined. The purpose of the dimensionless numbers is to describe the interaction between inertia, surface and viscous forces which help to understand the stability of the inkjet printing process. First, the relationship between inertial and viscous forces is given by the Reynolds number (Re) which compares the density (ρ), drop ejection velocity (U_e) and in-flight droplet diameter (d_0) with the dynamic viscosity (μ),

$$Re = \frac{\rho U_e d_0}{\mu} \quad (1)$$

Similarly, the relationship between inertial and capillary forces is provided by the Weber number (We) which compares the density (ρ), drop ejection velocity (U_e) and in-flight droplet diameter (d_0) with the surface tension (γ),

$$We = \frac{\rho U_e^2 d_0}{\gamma} \quad (2)$$

Since both the Reynolds and Weber numbers depend on the velocity of the drop and in some circumstances a control parameter independent of inertial forces is desired, the Ohnesorge number (Oh) is defined as,

$$Oh = \frac{\sqrt{We}}{Re} = \frac{\mu}{\sqrt{\gamma \rho d_0}} \quad (3)$$

Additionally, to assess the effect of gravity in the inkjet printing process, the Bond number (Bo) is calculated by comparing gravitational to capillary forces, where g is the gravitational constant:

$$Bo = \frac{\rho g d_0^2}{\gamma} \quad (4)$$

In general, due to the microscale drop sizes observed in inkjet printing, the Bo is much less than 1 and hence, the effect of gravity is neglected (Derby, 2010).

Several authors have used these parameters in the form of a printability diagram to assess the stability of the drop formation process, showing bounds to prevent splashing, satellite formation or no drop ejection (Reis & Derby, 2000). The recommended range over which inks can be printed is $1 < Z < 10$, where Z is defined as the inverse of the Ohnesorge number. Although, other authors have suggested more appropriate ranges such as $2 < Z < 20$ (Liu & Derby, 2019), $1 < Z < 14$ (Kim & Baek, 2012), $4 < Z < 14$ (Jang et al., 2009). Drop filament break-up and satellite formation were thoroughly studied by Castrejón-Pita et al. (2012). Jetting of non-Newtonian fluids have been studied by Hoath et al. (2012), Planchette et al. (2019) and Yang et al. (2014). Other authors have suggested the inclusion of aerodynamic effects (Rodríguez-Rivero et al., 2015), nozzle defects (Castrejón-Pita et al., 2011), viscoelastic properties

(Morrison & Harlen, 2010) impact on jetting necking, stretching and break-up phenomena. Table 2-1 summarizes the drop formation process critical to quality factors found in the literature (Jang et al., 2009)(Lohse, 2021). In this work, we used the recommended range to achieve stable drops from the jet formation process developed by Derby (2010).

Table 2-1 Drop formation input-output diagram and critical to quality factors.

Suppliers	Inputs	Process	Outputs	Customers
Fujifilm Dimatix (DMC-11610)	Equipment Characteristics Nozzle Diameter (a) <i>(characteristic length)</i> Actuation mode Inkjet & Printhead type	Drop Formation Experiments Numerical Simulation	Drop Characteristics Velocity Volume Pinch-off time Filament length Time to Single Drop Length to Single Drop Filament Aspect Ratio	External Texas Instruments (TI)
Meyer & Burger (PIXDRO LP50)	Process Parameters Waveform type: Pulse Shape Voltage Frequency Stand-off distance	Dimensionless Parameters $Z = 1/Oh = (\sigma\rho a)^{1/2}/\mu$	Drop Ejection Stages 1. Filament Elongation (necking & pinch-off) 2. Filament Recoiling 3. Single Stable Droplet 4. Droplet coalescing with satellite(s) 5. Droplet + one satellite 6. Droplet + satellites	Internal Center for Additive Manufacturing (CfAM)
Sigma-Aldridge	Ink Properties Density (ρ) Surface Tension (σ) Dynamic Viscosity (μ) Relaxation time Shear rate Polymer concentration Molecular weight Solvent viscosity	Ohnesorge (Oh) Weber (We) Reynolds (Re) Capillary (Ca) *Bond (Bo) Froude (Fr) Weissenberg (Wi) Deborah (De)	Printability Phase Diagram We vs Z (Newtonian only) We based on jet velocity	Printability CTQs ➤ Single Stable Drop ➤ Max Positional Accuracy (highest resolution) ➤ Max Jetting Frequency (highest speed)

2.1.4 Drop deposition and coalescence stage.

The second physical operation in the inkjet printing process is the positioning and interaction of droplets on arbitrary substrates. The aim is that a spherical drop with no satellites is ejected with the right amount of energy to avoid splashing and minimal volume for better resolution. Key process parameters in this operation with direct impact on pattern accuracy are substrate placement, speed, temperature, and vibration (Jang et al., 2009). Since the subject of study is understanding the interaction between ink and substrate, the physical properties of both become relevant. Surface tension, viscosity and density of the ink and surface roughness, porosity, morphology and chemically treatments of the substrate define the wetting dynamics interaction. Reynolds, Weber, and Ohnesorge dimensionless parameters are used to discriminate between impact driven or capillary driven deposition and between almost inviscid to highly viscous flow drop behaviour. DoD inkjet printing applications are quoted as almost inviscid and impact driven (Derby, 2010). Experimental and numerical studies of the impact and spreading of viscoelastic fluids have been reported by Hoath (2016),

Jung et al. (2013) and Vega & Castrejón-Pita (2017). From this research, it has been found that three drop characteristics have a direct impact in the printed pattern resolution: contact angle, drop contact line footprint diameter and drop height. The contact angle (θ_e) is the angle between the surface tension tangent on the liquid–vapor interface (γ_{lv}) and the surface tension tangent on the solid–liquid interface at their intersection ($\gamma_{sv} - \gamma_{sl}$). It quantifies the wettability of a solid surface by a liquid via the Young equation given by,

$$\cos \theta_e = \frac{\gamma_{sv} - \gamma_{sl}}{\gamma_{lv}} \quad (5)$$

The transient behaviour of these characteristics is driven by the surface forces developed between ink and substrate interaction and therefore, understanding wetting dynamics theory is the natural next step.

Wetting dynamics theory has been widely researched by several authors (Starov & Velarde, 2007)(de Gennes et al., 2004). Their contributions provide the fundamental equations used to study spreading and wetting phenomena on dry/wet surfaces, curved interfaces, porous substrates, surfactants solutions and non-Newtonian fluids (Arjmandi-Tash et al., 2017). Computational based methods have made it possible to deepen our understanding of the drop pinning-depinning mechanisms (Zhang et al., 2019), and explain contact line dynamics under the influence of evaporation (Shanahan & Sefiane, 2010), dynamic contact line fluctuations (Fernández-Toledano et al., 2019) and fluid adhesion at an atomic scale (Fernandez-Toledano et al., 2017). Although, spreading and wetting dynamics has been developed largely in the last decade, it is still an active area of research. In particular, the development of accurate dynamic contact angle models is crucial to predict the final deposition pattern before solidification occurs.

To better describe the wetting phenomena, the interaction between drop and substrate is divided in five key phases: impact, spreading, relaxation, wetting and equilibrium. Yarin (2006) observed in experiments that at the impact stage, the drop spreading is dominated by the kinetic energy with a time span of less than 1 μ s. Fluid deformation dissipates the kinetic energy until reaching a maximum spreading at approximately 4 μ s where viscous and surface tension forces start coming into play. Viscous forces are responsible to damp drop oscillation at the relaxation phase which lasts to

approximately 50 μs , while capillary spreading picks up when surface tension dominates the flow in the wetting phase up to 5 s. Equilibrium phase is reached beyond 5 s of the experiment. Figure 2-3 summarizes the drop deposition process critical to quality factors found in the literature (Derby, 2010)(Lohse, 2021).

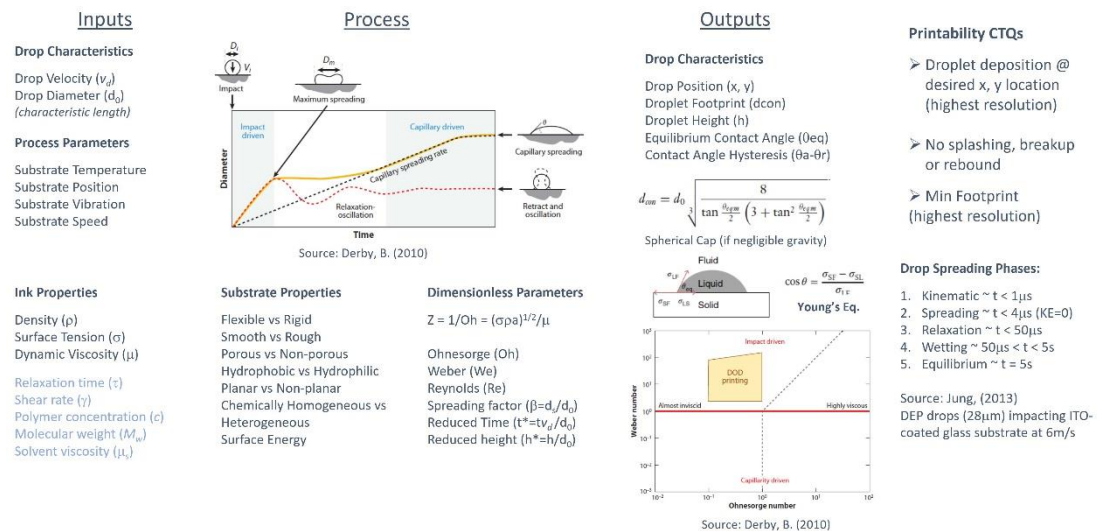


Figure 2-3 Drop deposition process input-output diagram and critical to quality factors (Derby, 2010).

The study of individual drops interacting with arbitrary substrates provide detail insight to the final footprint prediction, however, the aim of this project is to understand the behaviour of drops coalescing to form stable patterns. Previous theoretical studies have focused on understanding the physics behind the periodic instabilities observed when lines of fluid are formed (Davis, 1980). Periodic scallops, coins, bulges, and uniform lines were observed experimentally by Schiaffino & Sonin (1997) and confirmed Davis's stability theory. Several later works furthered our understanding of line morphologies and stability mechanisms (Duineveld, 2003) using conductive silver inks (Perelaer et al., 2006), polyurethane colloidal suspensions (van den Berg et al., 2007) and conductive polymer solvent based inks (Soltman & Subramanian, 2008).

In the work by Duineveld (2003), the spacing between deposited drops was identified as the main factor influencing line stability. Soltman & Subramanian (2008) build upon this premise by developing an analytical model based on volume conservation assumptions, which yielded four theoretical regimes depending on the amount of

overlap between deposited drops. They observed that bulges are formed when drop spacing is shorter than a certain length, due to the larger Laplace pressure of newly deposited droplet driving flow into bead main body. As the drop spacing increases, a scalloped shaped contact line emerges from the uniform pattern that eventually separates in pairs or isolated drops. As a result, a stability diagram relating non dimensional radius versus drop spacing was introduced with regime threshold transitions. Later, Stringer & Derby (2010) proposed a region for line stability defined by two limits emerging from the interaction of substrate transversal speed, drop spacing and advancing contact angle. Further studies demonstrated that a variable line spacing has a positive influence on film stability (Soltman et al., 2010)(Mu et al., 2017) and contact angle hysteresis plays a key role in final pattern accuracy (Soltman et al., 2013). Unfortunately, both models have the limitation of not including inertia effects nor considering bead morphology, which results in underpredicting the printed line width (Hsiao et al., 2014). Other studies have shown through numerical simulation and experimental data, the presence of a bulging instability regardless of drop spacing (Thompson et al., 2014). Although several studies have been reported in the literature to understand the role of critical printing parameters in the stability of inkjet-printed lines and films, little attention has been paid to fast and accurate prediction and parameter optimisation methods to improve the quality of printed features. Therefore, this study builds upon the work of Stringer & Derby (2010) to develop more accurate approach to identify the stability regime for single tracks and films.

2.1.5 Drop solidification stage.

The last physical operation in the inkjet printing process is drop solidification and attainment of the final deposition shape. Once the drops have coalesced, the mechanisms in which the liquid transforms to solid play a critical role in the final pattern morphology. Usually, this transition comes with an overall volume shrinkage, which could be acute depending on ink formulation. A key parameter of these process is the solidification time which has a direct influence on the deposited drop diameter, i.e., for faster solidification times the drop diameter is reduced, compromising drop spacing and ergo, pattern stability. There are three potential solidification mechanisms

based on the physical phenomenon driving the liquid-to-solid transition: evaporation, chemical reaction, and sintering.

Due to the low viscosity limits observed in inkjet printheads, common ink formulations must reduce solid particle content and tune viscosity by using solvents or other additives. Most solvents are volatile substances (present a high vapor pressure at room temperature), enhancing evaporation rates with increasing temperature and after full drying, leaving a thin layer of solid content material to adhere to the substrate. For details about droplet solidification via evaporation, theoretical models, experimental studies and influence of critical parameters on inkjet-printed feature's stability, the reader can consult (Deegan et al., 2000) (Popov, 2005) (Fukai et al., 2006) (Kim et al., 2006) (Yunker et al., 2011)(Dugyala & Basavaraj, 2014) (Eral et al., 2011) (Mampallil et al., 2015) (Seo et al., 2017) (Nguyen et al., 2017) for further reference.

In the case of reaction-based inks, which is the focus of this study, the solidification is triggered by an energy source which could be heat or UV radiation depending on the ink formulation. Typical UV curable inks are composed of monomers or oligomers, photoinitiator, diluents and other additives (He, 2016). The UV photo-polymerisation process consists of three stages: initiation, propagation, and termination. In free radical polymerization, a photoinitiator absorbs the energy from the UV light to generate free radicals, then chain propagation is initiated by the groups formed reacting with unreacted monomers/oligomers and finally the reaction reaches termination when no more unreacted groups are available (Pappas, 1980). Examples of successful printing of UV curable inks have been reported in microfluidic devices (Hamad et al., 2016), functional electromagnetic applications (Saleh et al., 2017), multi-material circuits (Ledesma, 2018).

Finally, the inkjet printing process involves a wide range of length and time scales, as shown in Figure 2-4 (Wijshoff, 2018). This impose a challenging situation when optimization of the overall process is required. Understanding each physical operation associated with these scales is key to define ink formulations, substrate wetting characteristics, solidification types and even what modelling techniques and assumptions are suitable to improve the printed pattern accuracy. Furthermore, an insight into the physics driving the fluid behaviour and potential coupling between operations is deducted from a multiscale analysis. Therefore, the next section

investigates inks and substrates used in printed electronics applications to in order select a simple, but relevant system to use as a model system for the numerical simulations in this work.

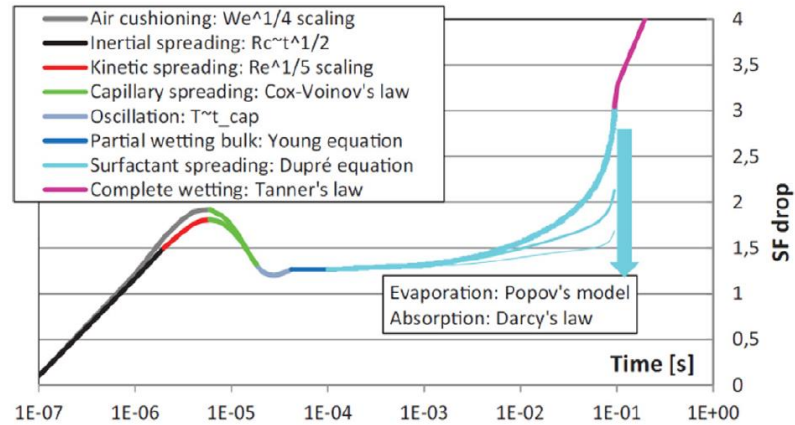


Figure 2-4 Drop spreading factor versus time (Wijshoff, 2018)

2.2 Dielectric materials compatible with AM

This section presents a brief overview of the state-of-the-art of dielectric materials, substrates characteristics and AM equipment for the printed electronics business using inkjet printing technology. Its intention is to provide the reader with current trends, standards and applications of dielectric materials used in inkjet printing technology. The scope of this investigation is limited to UV-curable dielectric inks deposited on non-porous flat substrates as this was determined to be the most relevant type of system for the intended applications of this work.

2.2.1 Inks.

A dielectric material is an electrical insulator that can be polarized by an electrical field, which controls the energy storage capacity of the material. An extensive list of more than 2000 dielectric materials has been reported by Sebastian (2008) along with their key properties and references. However, only a narrow subset of dielectric materials is used in inkjet printing applications. In general, most additively manufacturable materials are polymeric, with a dielectric constant that falls within the range of 2 to 6 (Booth et al., 2017). Nevertheless, some composite materials incorporating metals and ceramics provide enhanced dielectric constants that are

useful in microelectronic devices. For dielectrics, relative permittivity and loss tangent are critical for implementing microwave systems (Sebastian, 2008). Over the years, dielectric materials have been classified by their state of matter (solid, liquid or gas), chemistry composition (organic, inorganic, synthetic polymers), dipole moment activity (active or passive) and dielectric constant (low, high)(Poplavko, 2019). The latter classification is useful to identify suitable materials for applications in microelectronics as shown in Table 2-2 (Singh & Ulrich, 1999).

Table 2-2 Classification of dielectric materials (Singh & Ulrich, 1999)

	Material	Dielectric Constant	Application
High-k	PbMgNbO ₃ +PbTiO ₃	22,600	Capacitor dielectrics
	PbLaZrTiO ₃	1000	Capacitor dielectrics
	BaSrTiO ₃	300	Capacitor dielectrics
	TiO ₂	50	Gate dielectrics, Photoelectrochemical cells
	Ta ₂ O ₅	25	Gate dielectrics, Capacitor dielectrics
	CeO ₂	20	Gate dielectrics
	BaZrTiO ₃	17.3	Gate dielectrics for organic transistors on plastic
	Al ₂ O ₃	9	Capacitor dielectrics
	(Bz,Ca,Sr)F ₂	7.3	Epitaxial dielectrics
Low-k	SiO _x F _y	3.5	Capacitor, internal supports
	Hydrogen silsesquioxane	3	Photonic integrated circuits
	Polysiloxane	2.89	Intermetal dielectrics
	Fluoropolyimide	2.8	Optoelectronics
	Benzo-cyclo-butane	2.7	Integrated circuits
	Black diamond	2.7	Field effect transistors, Epitaxial dielectrics
	Polyethylene	2.4	Intermetal dielectrics
	Polypropylene	2.3	Intermetal dielectrics
	Fluoropolymer	2.24	Intermetal dielectrics
	Perylene	2.2	Thin film transistors
	Dupont PTFE-based copolymer AF 2400	2.06	Intermetal dielectrics, internal supports
	Xerogels	1.2	Flexible electronics

Several authors have presented examples of 3D inkjet-printed electronic components using dielectric inks. For example, Zhang et al. (2016) proposed a continuous method to fabricate stable polyimide insulator layers using inkjet printing technology. By increasing substrate temperature and setting line overlap to 30%, stable films were obtained, yielding uniform thickness and adequate dielectric properties for microelectronic devices. Tehrani et al. (2016) investigated the mechanical and electrical behaviour of thick layers of SU-8 polymer and thin layers of poly(4-vinylphenol)-based solutions and demonstrated a high-performance on-silicon RF capacitor. McCoul et al. (2017) proposed a high throughput method to print dielectric silicone elastomer actuators using DoD technology, showing better mechanical and

actuation properties in layers of 2 μm or less, resulting in lower driving voltages. Graddage et al. (2016) inkjet-printed capacitors using PVP based dielectric ink on PET substrate and transistors using DPP-Thieno[3,2-b] thiophene copolymer (PDBT-co-TT) showing thin and uniform layers by maximizing a coffee ring effect strategy. He et al. (2017) proposed a methodology to print simultaneously structure and support materials by inkjet printing Tripropylene Glycol Diacrylate (TPGDA) which allows the efficient fabrication of overhanging structures. Cho et al. (2018) inkjet-printed a metal-insulator-metal capacitor of SU-8 polymer layers as dielectric insulator on Liquid Crystal Polymer as substrate, proposing a soft-bake strategy at 60°C for 20 minutes to eliminate bubbles and ripples in the films. Furthermore, Mikolajek et al. (2019) developed a ceramic/polymer composite ink made from Ba_{0.6}Sr_{0.4}tio₃ (BSt) and poly(methyl methacrylate) (PMMA) to print insulator layers for capacitors demonstrating homogeneous films and increased permittivity with larger ceramic particle sizes. In conclusion, there are many studies found in the literature probing dielectric materials can be selectively deposited to form complex patterns and even create electronic components in a voxel by voxel approach. The interest of this work is to select the most stable dielectric ink suitable for electronic packaging applications using AM inkjet printing technology.

2.2.2 Substrates.

As with the formulation of inks, the most suitable substrate selection depends on the specific application requirements. Rigid substrates such as glass or silicon wafers are typically used in inkjet printing applications, but flexible substrates based on polymers are becoming more common due to the growing demand of stretchable electronics and thin film sensors. Two critical phenomena in the inkjet printing process are determined by the substrate surface characteristics: wetting and adhesion. Wetting affinity is measured by the contact angle formed between the drop fluid and substrate surface which depends on the substrate surface energy and its fluid surface tension. Adhesion force depends on the substrate roughness and the electro/chemical interaction at the contact surface of the solid/liquid interface. Hence, the accuracy and reliability of the printing process greatly depends on the observed ink-substrate system interactions. It is common practice to manipulate substrate surfaces using coatings, chemical

treatments, or geometry modifications (masking) for high-fidelity positional accuracy. Table 2-3 & Table 2-4 provides some key performance features and main applications for polymer-based substrates and silicon-based substrates, respectively.

Table 2-3 Applications of polymer-based substrates (Hoffman, 2017).

Polymer Substrate Type		Outstanding Properties	Typical Application
General-purpose polymers	HDPE/polyolefins	Low cost, food-safe	Packaging, imaging
	PVC	Outdoor resistance, low cost	Architectural, signage
	Plasticized PVC	Extrudable, low cost, outdoor resistant	Imaging, signage
Engineering polymers	PA-Nylon-6	Mechanical strength	Textiles, electrical
	Polycarbonate	Scratch resistance, puncture strength	Solar, packaging
	PET	Dimensional stability, tensile strength	Electronics, packaging
	PUR/PUR copolymer Elastan	Stretchable	Rubber, textiles
High performance plastics	PEEK	Chemical resistance	Automotive, electronic, medical
	PI, kapton	High-temperature resistance	Optoelectronics
	PPS, polyphenylene sulfide	Flame protection, heat resistance, gas barrier	Electrical, Electronic
	PTFE	Chemical resistance, low friction	Hostile environments, low friction

Table 2-4 Applications of glass-based substrates (Parthier et al., 2017).

Type	Composition	Key Properties	Typical Application	Commercial
Soda-lime glass	70-75% SiO ₂ 12-16% Na ₂ O 10-15% lime	Good flatness, low production cost available for large thickness ranges unlimited availability	Most common glass type Windows and containers	
Borosilicate glass	70-80% SiO ₂ 7-13% B ₂ O ₃ 4-8% Na ₂ O/K ₂ O 2-7% Al ₂ O ₃	High Chemical resistivity, high thermal shock and high temperature resistance	Glassware Laboratory glasses	AF 32® eco D 263® T eco MEMpax®
Lead glass	54-65% SiO ₂ 18-38% PbO 13-15% Na ₂ O/K ₂ O others	High-grade glass with high density higher refractive index, and high brightness (crystal glass)	Radiation shielding glasses, accessories	Zerodur® Foturan® II

Substrate materials are regulated by several industry wide standards such as IPC/JPCA-4921 which provides guidance on mechanical capability and compatibility of flexible and rigid base dielectric materials, ET-4101 that focuses on glass and polymer substrate materials (JEITA, 2020) and IPC-2292 which concentrates on design standards of printed electronics on flexible substrates (IPC, 2020). In addition, organizations such as ASTM and ISO provide standard tests methods to measure the

physical properties for both silicon and polymer-based substrates. Although, most manufactures and suppliers provide average properties of substrate materials, it is of utmost importance to have access to other references for comparison purposes. For further reference, a comprehensive summary of chemical, mechanical, thermal and optical properties for polymer-based substrates was given by Hofmann (2017) and for glass-based substrates by Parthier et al. (2017). The interest of this work is to use flat, non-porous substrates such as silicon wafers, to facilitate the modelling and simulation of the inkjet printing process and to cover a wide range of applications in the printed electronics industry.

2.2.3 Printers.

The purpose of this section is to report recent advances in inkjet printing technology, considering the hardware and associated software necessary to translate a digital object into a 3D structure. It is of the utmost importance to investigate what new commercial printers are offering to the market and how they are tackling current industrial challenges. Considering this perspective, new commercially available technology could be leveraged and enhanced by this PhD research project.

The increasing demand of higher production speeds and the best quality products at the lowest cost has pushed printed electronics' traditional manufacturing processes to their limits. Inkjet printing technology has helped seen increasing application in this field due to its ability to build multi-material complex structures with minimal waste.

An interesting recent development is the integration of Artificial Intelligence (AI) techniques with inkjet printing. For example, Inkbit Corporation® integrated a machine vision system that scans the morphology of each layer, corrects any deviation from geometry of subsequent layers in real time and uses this data to train a predictive model for each ink-substrate system used in the printer (Inkbit, 2020). No data could be found to validate the 100% accuracy claimed by the company; however, the method does demonstrate how AI enables 3D part reconstruction and quality tracking per part automatically. The printer system has an in-plane resolution of 50 μm , an out-plane resolution of 10-25 μm , deposits 2.75 L of material per hour, handles up to 8 different

epoxy resins or elastomer materials and could print up to 22 vertical millimetres per hour.

Another example was developed by Nano-Dimension Corporation® with its DragonFly LDM precision inkjet printing system for electronics. The DragonFly™ is a high precision R&D printer whose target is to reduce printed electronics design lead times and provide freedom to create multi-material complex structures. Nano-Dimension® partnered with SolidWorks® to develop an optimization algorithm for non-planar, multi-material electronics which enables a seamless connection between the SolidWorks design environment and DragonFly™ printer (Nano-Dimension, 2020). The algorithm takes as input a free-form object with embedded 3D electronics and prepares all files and scripts required to print automatically, cutting time, and eliminating error-prone tasks.

Printhead technology principles, configurations and capabilities have been reported for commercial brands such as Fujifilm Dimatix (Rosario, 2017), Minolta Konica (Corrall, 2017), Xaar (Brünahl et al., 2017), Hewlett-Packard (Simske, 2017) and Océ Technologies (Piatt et al., 2017). The printhead determines printing materials, processing speed and product resolution and it is one of the most important components in inkjet printing technology. Printheads are usually designed in conjunction with other printer hardware for efficient operation and therefore, migration to a different printer platform is not straightforward. The interest of this work is to evaluate two Fujifilm Dimatix printhead models which mainly differ on the droplet volume generation, 10 and 1 pL.

2.3 Physics-based numerical methods.

After reviewing the fundamental theory behind the inkjet printing process and the complex ink formulations, substrates, and equipment suitable for printed electronics, we can appreciate the challenges of studying the physics of drop formation, spreading and solidification using experiments alone. For instance, advanced visualization techniques are needed to accurately observe phenomena at length scales in the order of tens of microns at frequencies over a megahertz. Furthermore, repeatability, reproducibility and stability quality measures must be assessed to validate the

measurement system, adding time and resources to the experimental process. For these and other reasons, numerical simulations have been utilized to describe the flow dynamics of the inkjet printing process, usually hand-in-hand with laboratory investigations. Therefore, this section reviews the state-of-the-art in numerical methods for fluid dynamics applications, with an emphasis on inkjet printing simulations.

2.3.1 Classical methods.

Classical numerical methods solve partial differential equations (PDE) by discretizing the domain of interest using three main approaches: finite difference, finite volume, or finite element. From the conservation of mass and momentum laws applied to an infinitesimal control volume, a set of partial differential equations are obtained to describe in a continuous manner the behaviour of fluids, commonly called the continuity and Navier-Stokes (NS) equations, respectively. Other equations such as an energy equation, an equation of state and an interface tracking equation may be added depending on the physics of the problem. Analytical solution of the continuity and NS equations is extremely difficult for most cases due to the NS nonlinear nature and the complex geometry and complex boundary conditions usually present in fluid flow applications. This is where numerical methods become essential to determine the flow field, either by approximating the equations directly using regular grids (finite difference approach) or volumes (finite volume method) or approximating the solution of the equations (finite element approach). Regardless of the method used, a set of linear equations relating the solution variables, boundary conditions and source terms is generated, turning the problem to a linear algebra form for efficient computational solution. Some characteristics, advantages and limitations of the discretization methods are given in Table 2-5. The reader is referred to the finite difference approximation (Patankar, 1980), the finite volume method (Versteeg et al., 1995) and the finite element approach (Zienkiewicz et al., 2013) theory and applications to fluid problems for further explanation.

Table 2-5 Advantages and limitations of discretization schemes for CFD applications.

Approach	Characteristics	Advantages	Limitations
Finite difference (FD)	Regular grid Differential approach	Simple in principle	Mass & momentum may not be conserved Induce false diffusion Troublesome for complex geometries
Finite volume (FV)	Irregular grid Integral approach	Handles complex geometries Mass and momentum always conserved	Higher order methods difficult to implement
Finite element (FE)	Unstructured grid Integral approach	Higher order functions for better accuracy Handles complex geometries Grid adapts dynamically	Mass & momentum may not be conserved Increased complexity for implementation

In general, there is no single method that solves every type of physics-based problem. It is paramount, therefore, to clearly understand the phenomena and object of the study before launching a computational investigation. In our case, the inkjet printing process stages described in Section 2.1.2 belong to the free surface flow class of problems, which means that the shape and size of the deformable fluid is part of the flow field solution (Liggett, 1994). In this type of problems, special treatments to track the interface change in location and deformation are required.

Under the continuum assumption employed in classical methods, the surface of a drop, i.e. the liquid and air interface, is considered a “sharp” interface or surface with zero thickness (Gibou et al., 2019). Depending on the discretization approach, a “sharp” interface could be attained by applying specific models. For instance, using the finite element approach to simulate a drop spreading on a substrate, the mesh conforms to the free surface shape and evolves with it, but it requires the prescription of the contact angle as boundary condition (Zienkiewicz et al., 2013). An alternative approach known as “the interface formation model” was developed by Shikhmurzaev (2007) which allows the simulation of moving contact lines without imposing the contact angle as boundary condition. Shikhmurzaev’s model assumes Young’s equation holds for the computation of the dynamic contact angle using interfacial tensions arising when contact line is moving. The model requires an equation of state for the interface and an equation to balance the flow between fluid bulk and interface. Results from a drop impacting and spreading on a substrate with different wettabilities was reported by

Sprittles & Shikhmurzaev (2012) showing good correlation with previous numerical studies.

On the other hand, the finite volume approach utilizes two widely investigated methods to track and capture the interface: the volume of fluid (VOF) and the level set (LS) methods. The VOF method assumes a stationary mesh through which a free surface travels depending on the advection of a volume fraction function defined at each volume cell. The algorithm has proven to be a numerically efficient method of solving the NS equations, but at the cost of an accurate free surface shape, which is reconstructed using a piece-wise linear function. Several developments have improved the free surface reconstruction schemes needed in VOF and for this reason, it is one of the most popular methods used in both industry and academy. In contrast, the LS method more accurately represents the free surface shape using a level set or zero contour represented by a higher dimensional function. The evolution of the contour is then modelled by an advection equation, as with the volume fraction in VOF. This allows an accurate representation of the free surface shape, but with the downside that volume is not explicitly conserved (Katopodes, 2018). In an attempt to address this deficiencies, a coupled level set and volume of fluid (CLSVOF) approach was created by Sussman & Puckett (2000) to exploit the best of both methods, with numerous studies in the literature. For example, Xia & Kamlah (2022) developed an improved CLSVOF framework without explicit interface reconstruction for modelling micro-sized droplets with and without evaporation with good agreement between the numerical and corresponding analytical solutions. Meng et al. (2022) created an enhanced CLSVOF with an algebraic second-reconstruction step for simulating incompressible two-phase flows for the accurate representation of air-water interface validating simulations with experiments data.

For years, the classical methods have been the workhorses in the computational fluid dynamics arena. Several studies have been documented using the VOF and LS methods to model inkjet printing processes. For example, Kim et al. (2009) created a piezoelectric printhead CFD model based on the VOF approach to investigate the influence of nozzle geometry, pulse amplitude, and ink viscosity on droplet size, speed, and break-up characteristics. The VOF model was validated using a fabricated prototype of the printhead. Results showed a more stable nozzle meniscus when a buffer is included prior the nozzle; drop ejection speed is significantly influenced by

the waveform amplitude, whereas ink viscosity showed a negligible effect on drop size. Later, Guo et al. (2014) employed the CLSVOF approach to study the behaviour of a droplet impact on a liquid film. Crown formation, splashing and air entrainment were captured accurately and compared to previous experimental and numerical studies for validation purposes. Results showed good qualitative agreement with previous investigations. Then, Fu et al. (2019) studied in detail the competing behaviours observed in a drop spreading on a porous surface. Using the VOF approach the effects of the Darcy number, Bond number, equilibrium contact angle and spreading factor were determined to characterize the problem. Although, the results correlated well with previous numerical studies, the authors recommended to include a dynamic contact angle model for situations when drop impact is present. Furthermore, Amani et al. (2020) proposed a finite volume scheme based on the conservative level set method to assess the effect of rheological properties in drop impact deformation. Shear thinning, shear thickening and viscoelastic materials were modelled using unstructured grids to avoid classical numerical instabilities due to the small time-steps required. Results showed that mass is conserved using the conservative level set formulation and compared well with available data found in the literature. Finally, Florio (2018) used the finite volume method to model ejection, impact, and solidification of molten copper drops on steel. He employed the VOF approach to track the interactions between the steel, copper, and air, showing the method can capture drop deformation under the influence of viscous and surface tension forces. However, results showed a loss of mass in the copper material when the drop size was of the same order of the mesh size. In addition, it was noted that the model could not simulate the solidified drops sticking to the flow path surfaces, suggesting a particle agglomeration approach may be more suitable for this kind of phenomenon. This last recommendations from Florio, provides an excellent lead to our next section, where we will discuss how particle-based methods can be used to solve computational fluid dynamics problems, characteristics, advantages, and limitations.

Several investigations have used finite element simulations to model the solidification process of UV curable inks. For example, to better understand the photopolymerisation process that TPGDA undergoes when exposed to UV light, several studies have been reported concerning the simulation of the curing process of

polymers. Goodner & Bowman (2002) developed a comprehensive free radical photopolymerisation model incorporating heat and mass transfer effects in thick films and Ruiz et al. (2006) optimized the injection moulding of a resin by simulating a curing kinetics model. Bowman & Kloxin (2008) modelled and experimentally validated the complex spatially dependent polymerization kinetics and network heterogeneity applied to SLA microdevice fabrication. More specific studies to understand the role of oxygen inhibition, viscosity, and dynamic light intensity in the free radical photopolymerisation were performed by Lin et al. (2019) and a detailed methodology to model and simulate epoxy resins using finite element analysis was proposed by Leistner et al. (2020). An alternative approach was presented by Sarkar & Lin-Gibson (2018) where instead of solving classically the curing kinetics system of equations, developed a stochastic simulation of polymerization to accelerate the design of polymeric materials with targeted physical properties for specific applications. Finally, Zhao et al. (2021) created a predictive model to simulate inkjet based 3D printing process considering the influence of UV curing strategies to optimize the process. These references provide a solid baseline to understand the physics behind UV curing processes with the aim to couple this with a material constitutive model for shrinkage prediction.

2.3.2 Particle-based methods.

Particle-based methods have become more common recently due to the increased availability of computer power for research and industry applications. In lieu of discretizing the domain of interest to solve the NS and continuity equations, particle-based methods assume the fluid to act as small particles colliding with each other. By means of the theory of kinetics, physical properties, fluid phases and complex geometries can be modelled without special treatments or complex boundary conditions. However, tracking the location and velocity of the particles is required, together with interparticle forces calculation to solve Newton's momentum conservation at every time step. Depending on the method and application, a particle may represent atoms, molecules, or systems of molecules, providing a microscopic (mesoscopic) view of the fluid domain.

Particle-based methods have been studied extensively, including molecular dynamics, dissipative particle dynamics, multi-particle collisions and smoothed particle hydrodynamics. A detailed overview of the theory and fundamentals of the particle-based methods for the interested reader can be found in (Oñate & Owen, 2011).

Several examples of the simulation of inkjet process operations have been reported using various particle-based methods. For example, Fernandez-Toledano et al. (2017) employed large molecular dynamics simulations to study mechanical force equilibrium at the three-phase contact line of a fluid bridge between two flat plates. This study was the first of its kind to validate Young's equation at a nanoscale level, proving that the tangential force at the liquid and solid interface is significantly larger than the work of adhesion equations when strong layering of liquid molecules is present at the liquid-solid interface. Later, Aphinyan et al. (2018) used particle dynamics simulations to understand polymer ink agglomeration in nozzles in 3D nano-inkjet printing processes and the role of surfactants in controlling it. Then, Zhang et al. (2019) modelled the evaporation phenomena occurring simultaneously with wetting drop dynamics using a molecular dynamics approach. They explained the pinning-depinning mechanism of the contact line in nanodroplets when the substrate is heated heterogeneously. Results showed that at certain conditions, the contact line speed is no longer relevant to the evaporation rate in some contact line stick-slip stages. Also, Fernández-Toledano et al. (2019) expanded the atomistic approach of Young's equation from 2017 to simulate via molecular dynamics a capillary bridge between two flat plates, including the friction coefficient per unit length at the contact lines. This value was compared with the dynamic contact angle as a function of contact line speed using wetting kinetics theory and an excellent agreement was found. As a result, a method to measure dynamic contact angle from the fluctuations of the contact line of a capillary system at equilibrium was proposed. Further studies from Fernández-Toledano et al. (2020) demonstrated the significant influence of the receding contact angle in the pinning time dependent on the wetting conditions of the ink-substrate system. They showed that separation distance between plates has a significant effect on the pinning time along with the effect of the receding contact angle.

Although microscopic simulations using particle-based methods have observed a growing trend over the last 10 years, to model a macroscopic domain size demands a large amount of computer storage capacity as well as powerful chips to handle the

input-output operations. Fortunately, the development of particle-based methods has continued and, in an effort, to bridge the gap between the macroscale and microscale, an approach that does not track individual particle position and velocities, but particle collection distribution function emerged: the lattice Boltzmann method. In the next section we introduced this mesoscopic method that has revolutionized the computational fluid dynamics world in the last decade.

2.3.3 The lattice Boltzmann method.

The theory behind the lattice Boltzmann method has been widely documented by several authors. A detailed explanation of the Boltzmann equation, lattice arrangements, equilibrium distribution functions and sourcing terms has been presented by Mohamad (2019). Multiphase flow lattice Boltzmann principles, methods, equations of state for phase separation, and forcing schemes are thoroughly explored by Huang et al. (2015). Figure 2-5 illustrates a summary of the LBM applications found in the literature. A guide for parallel computing implementation of the LBM on a variety of platforms is provided by Kruger et al. (2017). A comprehensive list of source codes can be found in Github (2020) for various different types of simulation, programming language and physics problem. The recent implementations of open source frameworks to develop LBM simulations such as OpenLB (Krause et al., 2020), Palabos (FlowKit, 2020), waLBerla (FAU, 2020), and commercial software including SIMULIA PowerFlow (3DS, 2020) , OMNIS/LB (NUMECA, 2020), are a clear indication of the high academic and industrial potential of the method. A performance and accuracy comparison between the classical Volume-of-Fluid (VOF) method and the LBM Pseudopotential scheme was carried out by Mukherjee et al. (2018). They found that LBM produces 1 to 3 orders of magnitude less spurious velocities than VOF and is roughly 10 times faster.

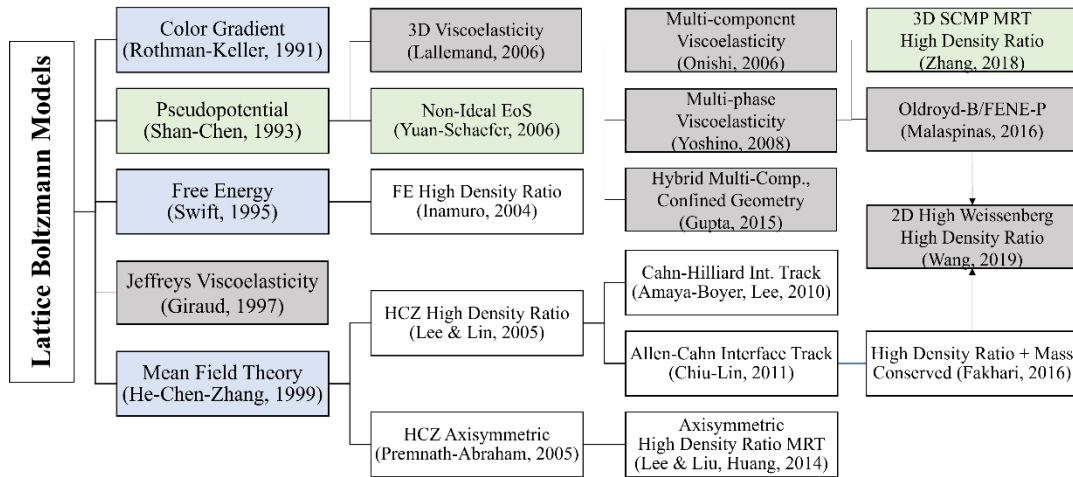


Figure 2-5 Lattice Boltzmann methods map.

Previous research has demonstrated the successful application of Lattice Boltzmann methods in modelling the different stages of the inkjet printing process. For example, Zhang et al. (2018) investigated the impact of nozzle wetting in the formation of stable drops in a piezoelectric printhead using a 3D MRT pseudopotential scheme with large density ratios. Using the dimensions of an actual printhead geometry, the drop ejection process was simulated and validated by experiments from literature. He concluded that controlling the non-ideal nozzle advancing contact angle at 90 degrees, the printability range could be extended from $Z=10$ to $Z=14$ in high Reynolds applications. Later, Liang et al. (2019) showed excellent agreement with analytical solutions and available experimental data of the breakup of a liquid thread using an axisymmetric phase-field scheme for large density ratios. Also, Berghout & Van den Akker (2019) modelled the drop formation process for a multicomponent ink using a 2D pseudopotential scheme. They increased the density ratio of the system by applying gravity to only one component, such that it behaves as a liquid, whereas the other behaves as a gas. As a result, the dynamics of the necking and the shape and motion of the apex after pinch-off agreed qualitatively with literature results. Wei et al. (2018) showed the ability of a pseudopotential scheme to handle three phase separation at meniscus induced motion of bubbles or droplets. Wu et al. (2015) studied drop impact behaviour using a 2D phase field incompressible lattice Boltzmann simulation with the Cahn-Hilliard equation to capture the interface between air and fluid media. Good correlation was found with numerical data available in literature. Then, Raman et al. (2016) investigated the interaction effects of drop impact on a solid substrate with different

wettabilities using the phase field LBM scheme. They found that the receding contact angle has a significant effect on the final shape of the drop impact process. Furthermore, Ammar et al. (2017) proposed a 3D pseudopotential lattice Boltzmann model with a multi-relaxation scheme to study drop impact dynamics on a dry and wet substrate. The model results show good qualitative correlation to numerical data available in the literature. In addition, Jansen et al. (2013) researched the influence of substrate wettability gradients in the drop spreading process using a 3D pseudopotential multi-component approach. The model was validated qualitatively using experimental data, providing good correlation results. Further studies incorporated a chemically striped substrate showing the potential of the method to simulate a controlled spreading based on the stripes aspect ratio (Jansen et al., 2016). Also, the study from Frank & Perré (2012) provides a detailed understanding of the drop spreading competition with capillarity absorption on a porous substrate by using a lattice Boltzmann phase field type based on the He et al. (1999) model. Fakhari & Bolster (2017) proposed a curved boundary treatment model to simulate drop spreading on substrates with different wettabilities using a 2D phase field lattice Boltzmann scheme. Their model proved to be more accurate than curved surfaces modelled with typical staircase approach (Stahl et al., 2010). Pravinraj & Patrikar (2017) studied partial wetting and its influence on droplet movement at micro and nanoscales using a multiphase lattice Boltzmann pseudopotential method. Results showed that droplet spreading on chemically heterogeneous surfaces can be controlled not only by the parameters of the Weber number but also by tuning the strip width ratio. Kang et al. (2018) proposed a model to predict the behaviour of droplet interaction with granular surfaces with variable advancing contact angles (from wettable to superhydrophobic). The model proved to be suitable for soils and other granular materials utilized in industrial applications.

Figure 2-6 provides a summary of the various different types of forcing schemes, boundary conditions and collision operators employed in LBM applications found in the literature.

Dimension	Fluid Type	Fluid Characteristics	Non-ideal EOS Phase Separation	Interparticle Force	Forcing Scheme	Collision Operators	Boundary Conditions	Wettability Scheme
D1Q3	Newtonian	Single Component Single Phase	Shan-Chen (SC)	Neighbours only (NB)	Shan & Chen (1993)	Single Relaxation Time (BGK)	No Slip (bbn)	Artificial "Wall density"
D2Q5			Van der Waals (VdW)		Luo (1998)		No Slip (bbl) ★	
D2Q9	Viscoelastic	Single Component Multi Phase	Redlich-Kwong (RK)		He (1998)	Two Relaxation Time (TRT)	Periodic	Apparent Contact Angle
D3Q15			Redlick-Kwong-Soave (RKS)	Guo (2002)	Symmetry			
D3Q19 ★	Non-Newtonian	Multi Component Single Phase	Peng-Robinson (PR)	NB + nearest NB (NNB)	Kupershtokh (2009) Exact Difference Method ★	Multi Relaxation Time (MRT)	Dirichlet	Contact Angle Hysteresis ★
D3Q27*			Carnahan-Starling (CS) ★				Von Neumann	

* May be needed to model viscoelasticity

★ Best for numerical stability and accuracy

⚡ Harder to implement in LBM than VOF or LS

Figure 2-6 LBM pseudopotential process map

Several recent works have attempted to improve simulation accuracy and stability of the complex dynamics observed when droplets spread and coalesce, including the implementation of Robin boundary conditions (Linder et al., 2015), the reduction of spurious currents (Shan, 2006) and a thermal lattice Boltzmann approach (Kupershtokh et al., 2018). Furthermore, the influence of substrate geometry and characteristics on droplet's spreading was assessed by Tsai et al. (2009) on superhydrophobic surfaces, Li & Thoroddsen (2015) on air bubble formation, and Tang et al. (2017) on surface roughness impact. Finally, state-of-the-art multiscale methods (Fish et al., 2021) have been explored trying to reduce simulation time without sacrificing accuracy. A good example of the simulation of inkjet-printed electronics using finite element analysis was introduced by Tilford et al. (2021) where he proposed a layer by layer approach to better capture printed object deformation. This last study uncovered a new research topic that would greatly affect the dimensional accuracy of the printed features which is the solidification mechanism, specifically for this research: UV curing of polymeric inks.

2.4 Optimisation methods.

Optimisation is the act of obtaining the best result within the available means (Ashcroft, 2020). The optimization process involves the selection of a set of design variables which we wish to study; the selection of an objective or criterion which we seek to maximize or minimize; the determination of a set of constraints based on design

requirements and the identification of a set of values for the design variables which satisfy all constraints while minimizing (or maximizing) the objective. Selection of the most appropriate optimization method depends on the characteristics of the design variables, objective function, and constraints. For example, design variables could take discrete or continuous values and have a deterministic or stochastic nature; design problem may involve only one or multiple objectives and be constrained or unconstrained; the objective function could behave in a linear or non-linear way and have a parametric or non-parametric structure, etc. Careful consideration of these characteristics coupled with a good understanding of the physics behind the design problem are required in every optimization endeavour.

From an algorithmic perspective, an optimization process needs an efficient strategy to vary design variables, evaluate the objective function and determine when a minimum value has been reached, commonly called the convergence criteria. Several approaches have been extensively studied to automate the design optimization process such as gradient based methods (Papalambros & Wilde, 2017), design of experiments (Antoy, 2014), genetic algorithms (Goldberg, 1989), calculus of variations (Rindler, 2018) and machine/deep learning techniques (James et al., 2013). Figure 2-7 shows a summary of some of the optimization approaches potentially relevant to this work, with some advantages and limitations.

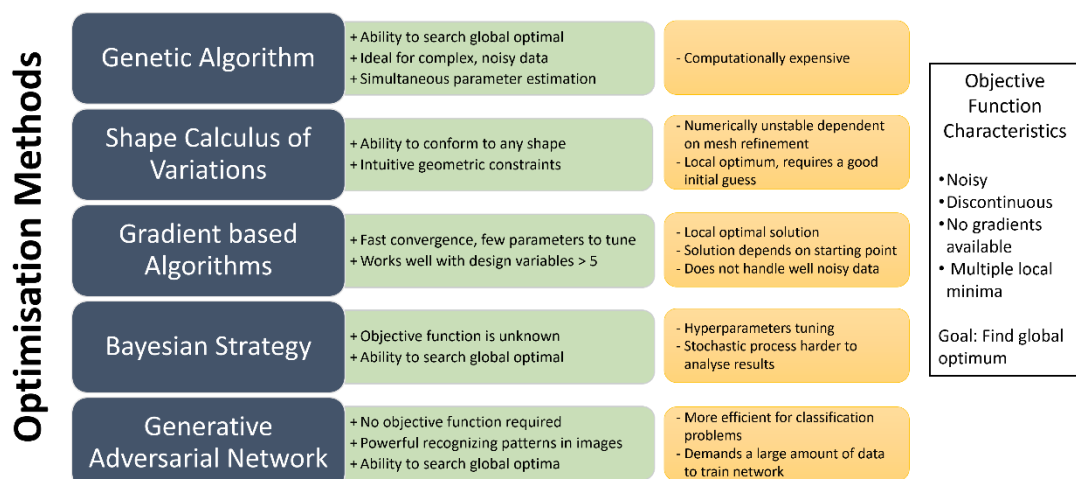


Figure 2-7 Advantages and limitations of optimisation methods.

With the increasing availability of data, the state-of-the-art in optimization methods has been driven by developments in the Artificial Intelligence (AI) arena in recent years. Machine learning, deep learning, and reinforcement learning techniques to develop predictive models have risen exponentially over the last decade. These techniques are focused on the study of computer algorithms that allow computer programs to automatically improve through experience. The ability to learn “on the go” and adapt to new process data, gives these methods a clear advantage over the classical algorithms. Although a comprehensive overview of the theory and principles behind machine learning (Murphy, 2012) and deep learning (Goodfellow et al., 2016) has been released, it still remains an active area of research with several industrial applications. For example, Hernandez et al. (2013) utilized a genetic algorithm method to find the optimal Cowper–Symonds material model parameters for steel characterization from a single Taylor test experiment. Hernandez derived the normalized central geometric moments from the deformed shape obtained via finite element simulations and demonstrated efficient solution of first-class inverse problem. Later, Chen et al. (2015) proposed an inverse finite-element analysis method coupled with a gradient-based non-linear least squares optimization approach to find the optimal viscoelastic-viscoplastic constitutive model parameters for a polymeric material based on nanoindentation experiments. Results from the method showed an accurate prediction of the material viscoelastic-viscoplastic material properties. Also, Viquerat & Hachem (2020) developed a computational fluid dynamics method using a finite volume approach coupled with a convolutional neural network to predict the drag coefficients of low Reynolds flows over 2D irregular shapes. The CFD simulation was first validated against NACA airfoils drag coefficients and neural network trained and optimized by the simulation results. Results showed accurate predictions and the model could potentially be extended to 3D shapes. Gongora et al. (2020) demonstrated the potential of Bayesian networks to optimize the number of experiments required to determine the toughest complex structures built from an additive manufacturing process. Gongora et al observed an almost 60-fold reduction in the number of experiments needed to identify high-performing structures relative to a grid-based search such as Latin Hypercube or Direct Montecarlo simulation. Kim et al. (2020) implemented a generative adversarial neural network (ANN) coupled with a molecular dynamics simulation to develop new crystalline porous materials. Training of the neural network was performed using as inputs the energy and molecular topologies of

approximately 30000 zeolites. Inverse design of materials can be achieved with the ANN by biasing the energy dimension, which correlates with material properties. Finally, Grieves & Vickers (2017) defined the concept of the Digital Twin as “a set of virtual information constructs that fully describes a potential or actual physical manufactured product from the micro atomic level to the macro geometrical level”. This represents the current pinnacle of physics-based/data-driven models predictive and prognostic capabilities for optimized product/process performance. Using this concept, the optimal printing strategy for fine features could be targeted for a given ink-substrate system.

The selection of optimised process parameters and material properties to improve the quality of AM parts has been the subject of several research studies by industry and academia. To accomplish an efficient exploration of the parameter design space, optimisation techniques ranging from traditional gradient based methods to more sophisticated probabilistic, evolutionary and machine learning techniques have been employed. For example, Lanzotti et al. (2015) determined the impact of layer thickness, deposition speed and flow rate on the dimensional accuracy of a RepRap 3D printer by means of a full factorial Design of Experiments (DOE) approach. Useful guidelines were formulated for the best accuracy of 3D printed parts. Mohamed et al. (2015) provided a review of research work on optimisation techniques used in AM material extrusion technology to find the optimal parameters influencing surface roughness, dimensional accuracy, build up time and material properties of 3D printed parts. Successful industrial applications of the Taguchi method, response surface methodology (RSM), genetic algorithms (GA) and artificial neural networks (ANN) were identified. More recent studies utilized Taguchi optimization and ANOVA techniques on inkjet printing process to determine optimal parameters for the fabrication of thick ceramic coatings (Rahul et al., 2017) and silver nanoparticle electrodes to create high-resolution patterns with low resistance (Nguyen et al., 2017). With the evolution of computational capabilities, more sophisticated optimisation techniques coupled with high-fidelity simulations to explore large design spaces have been exploited. Using a multi-objective optimization (MOO) design method for drop-on-demand printing parameters coupled with fully connected neural networks (FCNNs), Shi et al. (2019) found the optimal parameters for bioprinting precision and stability of cell arrays. Zhao et al. (2020) determined the optimal laser sintering process

parameters for a printed microstrip antenna using a high-fidelity simulation and experimental work. However, the application of optimisation techniques has not been limited to finding optimal process parameters. Several studies have been reported in the literature where material properties were determined by means of minimizing shape or morphology deviations from a target experiment. Chen et al. (2015) proposed an inverse finite-element analysis method coupled with a gradient-based non-linear least squares optimization approach to find the optimal viscoelastic-viscoplastic constitutive model parameters for a polymeric material based on nanoindentation experiments. Hernandez et al. (2013) utilized a genetic algorithm method to find the optimal Cowper–Symonds material model parameters from a single Taylor test experiment. Hernandez derived the normalized central geometric moments from the deformed shape obtained via finite element simulations and demonstrated the efficient solution of a first-class inverse problem.

2.5 Data-driven compensation methods.

Despite the inkjet printing process advances observed in the last decade, several challenges remain in the generation of dimensionally accurate 3D objects. The differences between the digital object and the final printed product can lead to part tolerances not being satisfied and therefore a potential waste of time and material. Several strategies have been reported in the literature to improve geometric quality in AM. For example, by controlling inkjet printing process variables based on the observed variation of those variables or by controlling inkjet printing process variables based on the observed product deviation, or by controlling input digital product geometry based on the observed product deviation (Huang et al., 2014). Another classification to address the approaches used to eliminate or reduce the errors between intended and actual geometry includes physics-based modelling, parameter process calibration and prescriptive product design adjustment (Decker & Huang, 2019). Each strategy has proven to work adequately under certain conditions but there is no one model that fits all applications. Studies on this subject are dominated by the team of Huang from the University of Southern California, with some industry leading reports as follows:

Tong et al. (2008) proposed a compensation method to slice file format approach for 3D object accuracy improvement based on compensation of slice files used in SLA and material extrusion processes by minimizing the sum of square of all the residual non-repeatable errors using conventional gradient-based methods. Later, Navangul et al. (2013) developed a new approach to locally reduce the CAD to STL translation error which reduces the form and profile error of critical features to satisfy part tolerances. Then, Huang et al. (2014) proposed a novel statistical method based on Bayesian networks to predict and compensate digital objects to improve the quality of both cylindrical and prismatic parts made using stereolithography technology. Next, Huang et al. (2016) developed a methodology to quantify pattern transfer completeness for multiple inkjet-printed shapes. Huang's methodology was seen to be suitable for sub-micrometre manufacturing inspection systems based on pattern images acquisition. Also, Jin et al. (2016) proposed a predictive model to control the accuracy of out-of-plane deformations in a printed part using stereolithography technology. Wu et al. (2018) generated a data driven predictive approach to estimate surface roughness from material extrusion technology using random forests approach. They also demonstrated a real-time monitoring system to monitor the health condition of a 3D printer and material extrusion processes using multiple sensors, which represents the first attempt to build a digital twin for AM applications. Furthermore, Chowdhury et al. (2018) created a compensation algorithm for a STL file for 3D applications in which instead of using gradient based optimization, uses an artificial neural network to learn and predict dimensional error due to thermal gradients, then used the results to compensate for errors in the STL file. In addition, Decker & Huang (2019) designed a prescriptive product design adjustment model for 3D objects in which instead of using gradient based optimization, uses an ensemble of random forests to learn and predict dimensional error. Future work using this approach is to generate a compensation policy for inputs required by the FDM process. Finally, Huang et al. (2020) devised a strategy using machine learning for additive manufacturing (ML4AM) for enhancing 3D printing performance. This work established a shape deviation generator as a novel data analytical framework through a convolution formulation to model the 3-D shape formation in stereolithography processes.

In additive manufacturing technologies, one topic that is still under deep investigation is how to actively control the dimensional accuracy of printed objects in a timely

manner. The references cited in the next lines lie under two categories: efficient image processing techniques and data-driven inverse problems approaches. In the first category, Veltkamp (2001) introduced the concept of similarity measures for shape recognition and proposed a methodology to develop shape matching algorithms for shape quality evaluation; Flusser et al. (2016) proposed several algorithms to compute image moments for 2D and 3D image analysis and pattern recognition; Wang et al. (2020) developed a unified Shape-From-Shading approach for 3D surface reconstruction using fast eikonal solvers (Jeong & Whitaker, 2008), successfully quantifying 3D volume from a single image and Durou et al. (2020) used diffusive and specular reflection models to find shape dimensions from single and multiple images using photometric 3D reconstruction techniques. In the second category, Cui et al. (2015) proposed a data-driven projection-based model reduction technique to reduce the computational cost of repeatedly evaluating numerical PDE models which could help achieve faster compensation of 3D digital objects and Li et al. (2020) developed a Fourier neural operator that is up to three orders of magnitude faster than traditional PDE solvers and achieves superior accuracy compared to previous learning-based solvers under fixed resolution. Finally, Kapteyn & Willcox (2020) developed a methodology for creating a data-driven digital twin from a library of physics-based models representing various asset states using machine learning approach.

Although significant progress has been made to model and predict the shape of planar objects either driven by controlling printing parameters or compensating digital objects to cancel shape deviations from target, most of the effort to date is in VAT photo-polymerisation and material extrusion technologies. In the next section we discuss the gaps in the knowledge found from the literature reviewed.

2.6 Summary of literature and identified gaps in the knowledge.

After performing a thorough review of the current literature regarding the physics behind the inkjet printing process, electronic materials compatible with the additive manufacturing technology, current equipment capability used in industry, physics-based numerical methods suitable for inkjet printing, optimisation techniques and data driven compensation methods utilized to mitigate the distortion of 3D printed parts, the author has reached to the following conclusions:

Inkjet printing has successfully been used to fabricate microelectronic devices such as capacitors, transistors, and solar cells as discussed in Section 2.1. Several authors recognize that features such as digital design integration, contactless deposition, and minimal material waste are notable advantages offered by inkjet printing, but its low production throughput and time-consuming process to achieve accurate parts limit technology adoption in the printed electronics industry. The literature survey reveals that there is still a vast amount of research needed to develop dielectric inks with compatible substrates suitable for inkjet in a reliable and timely manner. The significant trial-and-error testing to achieve adequate, accurate and consistent printed electronics is currently impeding realization of the potential of inkjet printing. Therefore, it is critical to acknowledge the reliability of functional and printable inks with compatible substrates; to seek a better understanding of the physics behind the jetting process and to develop fast and accurate modelling and optimisation methods to enable the full potential of inkjet technology.

Since the scope of this investigation is limited to UV-curable dielectric inks deposited in non-porous flat substrates, several dielectric materials and substrates have been identified as potentially suitable for inkjet printing as discussed in Section 2.2. Regarding the dielectric materials, Poly (4-vinyl phenol) (PVP) is the most widely used dielectric from the literature, demonstrating the ability to produce acceptable tracks using inkjet printing, but unfortunately it is not stable at ambient conditions adding complexity to its formulation. Another dielectric material widely used in inkjet printing is Tri (propylene glycol) diacrylate (TPGDA) offering a good balance of dielectric and structural properties, reliable jetting performance, minimal volume loss and good thermal stability. Therefore, TPGDA is selected as the test dielectric material for this work. Regarding substrate selection, a clear consensus exists that the quality of printed parts greatly depends on the observed ink-substrate system compatibility, considering both wetting and adhesion behaviour. Although there is increasing application of flexible substrates in printed electronics such as paper, polyethylene naphthalate (PEN), polyethylene terephthalate (PET) and polyimide (PI), the scope of this investigation is limited to flat, rigid, and non-porous substrates. For this work, glass and nitride coated silicon wafer are the selected substrates because both have a non-porous, non-reactive and relatively smooth adhesive surface.

AM material jetting processes such as inkjet printing inherently manifest a variety of complex physicochemical hydrodynamic phenomena taking place in different time and length scales, as discussed in Section 2.1.2. Starting in the printhead side, the stability of the drop formation process greatly depends on the build-up energy driven by pressure and frequency inside the chamber, the viscosity and surface tension of the ink and the geometry and wetting properties of the nozzle. Then, after droplets impact the substrate, the complex interaction between merging drops, the surface free energy of the substrate and the irradiation of UV energy, which triggers the ink solidification, play a crucial role in defining the dimensional accuracy of the print. Within this context, a quantitative understanding of the competition process occurring between the drop coalescence timescale and the curing timescale of the photo-polymerisation is still to be developed. Furthermore, the highly nonlinear and transient behaviour governing the drop coalescence and solidification and its interaction with inhomogeneous substrates facilitate the generation of instabilities in the prints such as bulges, scallops, pores, and break-ups. Therefore, understanding and modelling the complex dynamics phenomena behind the jetting, deposition and solidification of droplets remains very challenging both experimentally and numerically.

In addition to the inherent multiphysics and multiscale nature of inkjet printing, a plethora of printing process parameters must be tuned to achieve an accurate print. Several research studies conclude that the main parameter influencing the stability of single tracks and films is the drop spacing. However, the effect of printing frequency, standoff distance, ejection speed, surface tension, viscosity, advancing and receding contact angle and its combined interaction on the generation of stable printed features is still largely unknown. Furthermore, from the author's point of view, there might be an underestimation of the role of the uncertainty in drop landing location and footprint size have on the surface morphology stability of printed features. Finally, there is no clear consensus on the limits that define whether an ink is printable or not from a droplet formation perspective. Therefore, a more rigorous methodology is required to standardize these limits and fully exploit the inkjet process potential.

With respect to current research on theoretical models, Stringer and Derby's theory (Stringer & Derby, 2010) is the most used for the validation of numerical methods simulating the inkjet process. Based on hydrostatic and volume conservation assumptions, the analytical model provides an accurate estimate of the footprint

diameter of single drops and the average width of single tracks as a function of droplet volume, static contact angle and drop spacing. However, a theoretical model useful for the numerical validation of films and multi-layered parts is still to be developed. In addition, a stability diagram for single tracks sheds some light on the limits of bulging, scalloping and separation, but unfortunately does not always agree with experiments as other factors may come into play, impacting the accuracy of the model. Thus, a more accurate approach to identify the stability regime for single tracks and films remains an area under current research.

It is clear that in order to advance the science behind inkjet, very high resolution and dynamic measurements would be necessary. Despite the progress observed in ultra-high speed digital imaging in recent years, it is still extremely challenging to visualize the jetting, impact, merging and spreading of inkjet-printed droplets as they are in the order of tens of microns interacting at frequencies over a megahertz. For this reason, numerical simulations have been utilized to model the jetting process, make predictions for control parameters, and guide experimental work. From the literature review, the lattice Boltzmann (LB) method is the most widely used to model droplet impact, spreading and coalescing phenomena in the last decade. Due to its ability to model free surface flows without an interface tracking scheme and its ability to run efficiently on massively parallel architectures, the LBM is selected to perform high fidelity simulations of the inkjet deposition process for this investigation. Although several studies report good agreement to experimental data, information about the solution time and computational resources employed is not provided. It is expected that a LB model would capture accurately the print morphology, but not in a timely manner. After further investigation of the application of reduced order modelling techniques, it is concluded that surrogate models capable to execute quickly without losing accuracy from the high-fidelity predictions have not been thoroughly investigated.

The survey of the literature reveals a great interest in studying how to improve the dimensional accuracy of additive manufactured parts. Several optimisation studies have been reported for VAT photopolymerisation and material extrusion technologies, but there is little scientific evidence for the case of inkjet printing. Furthermore, most of the research focuses on reducing the error between the target and printed shapes by process parameter optimisation or geometry compensation, but there have not been

investigations of methods to avoid and compensate this error simultaneously. In addition, inverse design methods such as “Shape from Shading” have not been explored in the context of inkjet printing and its potential to reconstruct the morphology of a printed feature in real time is largely unknown. Finally, the development of optimization frameworks which consider not only the printing parameters, but the shape of the pattern to print, material properties, wetting characteristics and printing scan strategies to mitigate the distortion of 3D inkjet-printed parts as a whole process requires attention to unlock the adoption of the technology by industry.

Although inkjet printing has proven to be a reliable and cost-effective method to fabricate electronics components, the effort to find the optimal parameters to obtain a uniform and stable film is still remarkably high. Computational fluid dynamics simulations have been extensively employed to build high-fidelity models of the inkjet printing processes using both classical and particle-based methods with good correlation to experimental data; however, the simulation time to determine drop impact and spreading dynamics is significantly high to be used within an optimisation algorithm, rendering this method impractical. Surrogate models capable of fast execution without losing accuracy in the flow field prediction have not been thoroughly investigated to the best of the author’s knowledge. Furthermore, evidence from the literature review shows that little analytic attention has been paid to the influence of printing parameters and surface morphology on the final deposition pattern for 3D inkjet printing applications. Finally, studies about error compensation techniques used in additive manufacturing technologies are still scarce. There are a few articles providing insights of error compensation methods for VAT photo-polymerisation and material extrusion technologies, but little scientific evidence was found for inkjet printing technologies.

In summary, through the review of literature, two main gaps in the knowledge were identified that form the foundation of the work presented in this thesis:

A fast and accurate methodology to predict the surface morphology of inkjet-printed features based on hybrid physics-based and data-driven models has not been developed.

A multi-objective optimisation approach to minimise the distortion of 3D inkjet-printed parts with fine features considering the uncertainty of droplet size and landing position has not been devised.

3 Materials and Experimental Methods.

This chapter provides detailed information about the selected materials, experimental methods including testing artifacts design and measurement methodologies to characterise the surface morphology of printed features used in this research. Section 3.1 describes materials details such as the ink formulation, physical properties and type of substrates and cleaning processes. The benchmark artifacts designed for validation purposes with overall dimensions for 2D and 3D applications; the printing setup and operational parameters to obtain a stable drop ejection process; the procedures to characterise the surface morphology of printed features using coherence scanning interferometry (CSI) and micro-CT scanning; and the design of experiments to assess the influence of printing parameters are explained in Section 3.2.

3.1 Materials.

3.1.1 Ink formulation.

In this study, the ink formulation comprised of tripropylene glycol diacrylate (TPGDA) which is one of the most common acrylate monomers used for photopolymerisation. This UV curable low viscosity ink is utilized as structural base material in printed electronics applications due to its demonstrated printability, transparency and good mechanical and dielectric properties (He et al., 2017).

TPGDA (a mixture of isomers containing Monomethyl Ether of Hydroquinone (MEHQ) and Hydroquinone (HQ) as inhibitors, technical grade) was purchased from Sigma Aldrich and used as received. 2,4-diethylthioxanthone (DETX) and Ethyl 4-dimethylamino benzoate (EDB) were used as photoinitiator and accelerator, respectively. TPGDA was mixed with 3 wt% of DETX and 3 wt% of EDB at room temperature in an amber vial and then stirred at 800 rpm for 30 minutes to fully dissolved the initiators. The prepared ink was then sparged using nitrogen for 15 minutes to help minimize inhibitions brought by pre-dissolved oxygen. The material was prepared in house by Yinfeng He.

3.1.2 Ink physical properties.

TPGDA physical properties reported in literature are shown in Table 3-1. Physical properties were measured at a temperature of 25°C (He et al., 2017). Reference values from literature were employed for initial modelling assumptions, but measured values for density, surface tension and viscosity were derived for the analytical model.

Table 3-1 TPGDA physical properties

Physical Property	Value
Density (g/mL)	1.03
Surface Tension (mN/m)	30.78
Viscosity (mPa s)	10.03

3.1.3 Substrates.

In this research, two substrates were selected to carry out the experiments: glass microscope slides and silicon nitride coated wafers.

Glass microscope slides with ground edges were procured from Biosigma (Venice, Italy). The slides have an area of 26 x 76 mm, a thickness of 1-1.2 mm and a 45 ° angle at corners. Before printing, glass slides were washed with detergent and wiped with normal paper to remove residues. Then, rinsed with ultra-purified water and watermarks removed with cloth. Finally, glass was rinsed with acetone, dried for 2 minutes, and wiped with soft cloth.

Silicon nitride coated wafers were purchased from Inseto (Andover, UK). The wafers have a diameter of 100 mm, a thickness of 525±25 µm, P type, <100> orientation, Boron(B) doped, CZ grown, PRIME grade with resistivity of 1-20 ohm.cm and are single side polished with SEMI standard flat. Silicon nitride coating applied by low pressure chemical vapor deposition of thickness 200 nm on both sides. Before printing, wafers were rinsed with acetone, then dried using a nitrogen gun and residues removed by wiping with soft cloth.

The cleaning process enabled the substrates to observe a reliable droplet spreading and coalescence during preliminary printing tests.

3.2 Experimental methods.

3.2.1 Density.

The density was calculated by depositing 0.5 mL of the ink with a syringe in an analytical balance (ABT 100-5M, KERN & SOHN GmbH, Germany) at room temperature, which at the time was 22°C. Five replicates of the measurement were performed. The ratio between the average mass and volume determined the density of the ink.

3.2.2 Surface tension.

The surface tension was measured by slowly generating a 1 mL pendant drop at the tip of a needle loaded in a Drop Shape Analyser (DSA100, KRÜSS GmbH, Germany) at a temperature of 22 °C. Five replicates of the measurement were performed. DSA software calculates the surface tension by fitting the theoretical curvature of the drop profile to the actual recorded pendant drop shape. The needle outer diameter used as reference size was 0.51 mm. The values used for air density and gravitational acceleration were 0.0012 g/mL and 9.8 m/s², respectively.

The static contact angle was measured by depositing a 1 mL droplet on substrates loaded in a Drop Shape Analyser (DSA100, KRÜSS GmbH, Germany) at a temperature of 22 °C. To mitigate the effect of impact, substrates were lifted to reach the drop from the syringe. The static contact angle was measured as soon as the droplet detached from the needle tip. Contact angle measurements were taken using the sessile drop method from DSA native software. Substrates were previously cleaned following the procedure described in Section 3.1.3. Ten replicates of the measurement were performed for each substrate.

The advancing and receding contact angles were calculated by slowly tilting a 1 mL sessile drop sample until it begins to move in the downhill direction. A Drop Shape Analyser (DSA100, KRÜSS GmbH, Germany) with a tilting table accessory (PA3220) was used to perform the measurements at a temperature of 22 °C. Contact angles were measured immediately before actual motion of the drop takes place using DSA native software. A tilting rate of approximately 1 °/s was employed. Substrates were previously cleaned following the procedure described in Section 3.1.3. Ten replicates of the measurement were performed for each substrate.

3.2.3 Viscosity.

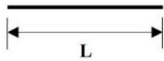

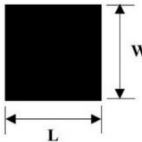
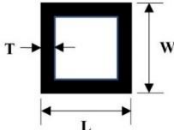
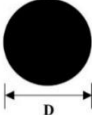
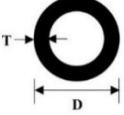
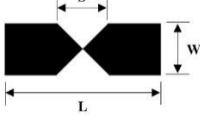
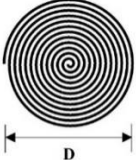
The viscosity of the ink was measured with a rotational rheometer (Kinexus Pro, Malvern Instruments Ltd., UK) equipped with a 40 mm parallel plate geometry and programmed with a shear rate table between 10 s^{-1} and 1000 s^{-1} at a room temperature of 25°C . The plate gap was set to $150 \mu\text{m}$ and each measurement was repeated three times. Although the shear rates during the jetting process are 2 to 4 orders of magnitude larger than the maximum shear rate from the rotational rheometer, the viscosity measurement at 100 s^{-1} was used in this investigation which is an accepted assumption considering the ink behaves as a Newtonian fluid.

3.2.4 Artifacts design.

3.2.4.1 2D

Digital images of 2D artifacts were generated using a MATLAB script which takes as input the required pattern type, dimensions, printing origin, resolution, and image size in pixels. The output of the script was a bitmap (BMP) file ready to be used for the printer. The geometry of the artifacts was chosen to assess the capability of the printer to generate fine features such as corners and thin lines in a stable and consistent manner. Table 3-2 shows a list of the 2D artifacts used in this research, including schematic description and dimensions. A single pixel track artifact was selected to assess the effect of printing parameters on the width and thickness of the feature and compare results with Derby's theoretical values. The 3-pixel track artifact was chosen to investigate the influence of multiple nozzles printing simultaneously on the dimensions of printed tracks. The solid square and circle patterns' purpose is to investigate the effect of printing parameters on film dimensions and determine differences between in-scan and cross-scan printing directions in straight and curved edges. The hollowed square and circle patterns' purpose is to evaluate the capability of inkjet printing to generate fine features such as internal and external corners and assess the minimum stable thickness of hollowed patterns. Finally, the bowtie and Archimedean spiral patterns, which are common structures in the printed electronics field, were included to determine if a large change of section will impact the material distribution of the film pattern and assess the minimum achievable separation between spirals to prevent potential short circuits, respectively. All patterns were identified to validate the optimal printing parameters to be derived in the investigation.

Table 3-2 2D testing artifacts dimensions.

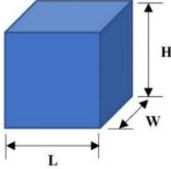
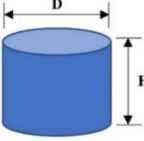
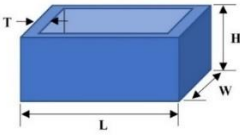
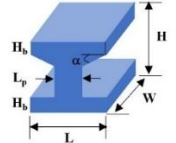
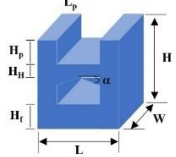
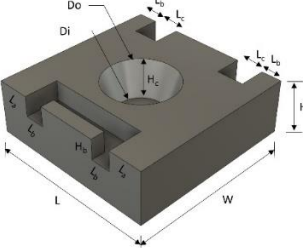
2D Artifact	Schematic	Dimensions
1-pixel track (1 nozzle used to print)		L = 1.5 mm Note: Artifact used for DOE
3-pixel track (3 nozzles used to print)		L = 1.5 mm
Solid square film		L = W = 1 mm Note: Artifact used for DOE
Hollowed squared film		L = W = 1.5 mm T = 0.2 mm
Solid circular film		D = 1.5 mm
Ring film		D = 1.5 mm T = 0.2 mm
Bowtie film		L = 3 mm W = S = 1 mm
Spiral film		D = 5 mm N = 12 (Number of spiral loops)

3.2.4.2 3D

3D models were created using Autodesk Fusion 360 computer aided design (CAD) software. The geometry was saved in STL format and sliced using a MATLAB script which automatically generates a bitmap file per layer. 3D artifacts were chosen to evaluate the deformed geometry of layer-by-layer build-ups and understand the limits of DIJP to construct accurate fine features in 3D structures. Table 3-3 shows a list of the 3D artifacts used in this research, including schematic description and dimensions. A cuboid artifact was chosen to investigate the effect of multilayer printing on squared corners and determine the chemical shrinkage influence on regular patterns. The cylinder artifact was selected to assess the effect of printing parameters and multilayer

printing on curved edges and investigate shrinkage behaviour in fully symmetric patterns. The cage artifact was identified to determine the capability of DIJP to print thin walls and internal corners. The I-structure was selected to investigate the material redistribution during DIJP when change of sections happen as well as the impact on the dimensions of features with small angles. The last artifact is a sensor package designed by TI which incorporates actual manufacturing dimensions and tolerances and evaluates the capability of DIJP to print fine features such as channels, vertical slots, and cone holes. All artifacts were identified to validate the optimal printing parameters and the geometry compensation approach to be derived in the investigation.

Table 3-3 3D artifacts dimensions

3D Artifacts	Schematic	Dimensions
Cuboid		$L = W = 2 \text{ mm}$ $H = 0.75 \text{ mm}$
Cylinder		$D = 1 \text{ mm}$ $H = 0.9 \text{ mm}$
Cage		$L = 2 \text{ mm}$ $H = W = 1 \text{ mm}$ $T = 0.2 \text{ mm}$
I-structure		$L = W = H = 1 \text{ mm}$ $H_b = 0.2 \text{ mm}$ $L_p = 0.4 \text{ mm}$ $\alpha = 15^\circ$
H-structure		$L = 1 \text{ mm}; W = 0.5 \text{ mm}$ $H = 1.5 \text{ mm}$ $L_p = 0.2 \text{ mm}$ $H_p = 0.4 \text{ mm}; H_f = 0.5 \text{ mm}$ $H_h = 0.2 \text{ mm}; \alpha = 15^\circ$
TI Temperature Sensor Packaging		$L = W = 2.5 \text{ mm}$ $H = 0.8 \text{ mm}; L_a = 0.5 \text{ mm}$ $L_c = 0.4 \text{ mm}; L_b = 0.3 \text{ mm}$ $Do = 1 \text{ mm}; Di = 0.7 \text{ mm}$ $H_c = 0.5 \text{ mm}$

3.2.5 Printing.

The formulation based on TPGDA was printed with a Dimatix DMP-2830 material printer at ambient pressure and temperature (1 atm, 20 °C). The ink was injected into a print cartridge (DMC-11610) which was then fixed to a printhead consisting of 16 nozzles of 21 μm in diameter. To keep nozzles clear and functioning properly, every start of printing, nozzles were jetted for 500 ms at 1.5 kHz, then purged for 1 s at 5 psi and jetted again for 500 ms at 1.5 kHz followed by nozzle plate contact with cleaning pad to remove fluid residue. Stable droplets were obtained through adjustment of the pressure-generating waveform shown in Figure 3-1a with a peak printing voltage of 25 V yielding droplets of 10 pL in volume. The droplet velocity was set at 6 m/s and aligned for selected series of working nozzles, which was measured using real time observations of the jetted drops obtained directly from the printer drop watcher software as illustrated in Figure 3-1b.

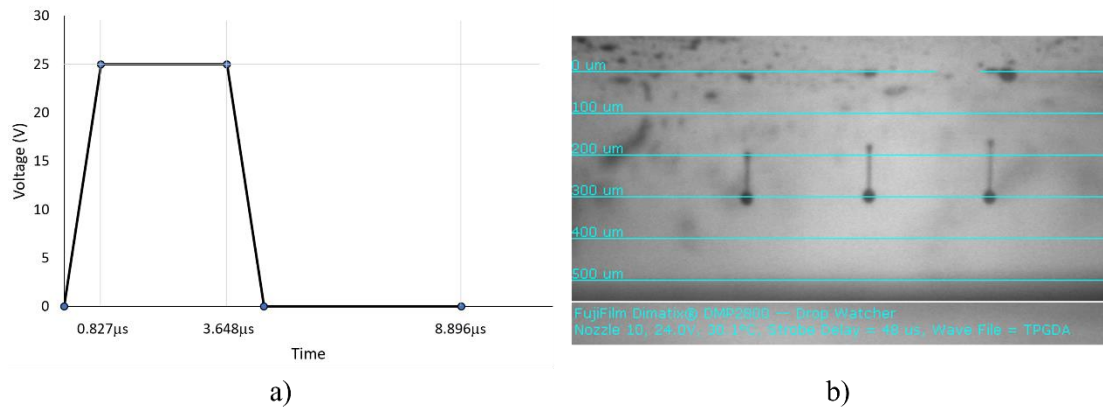


Figure 3-1 a) Jetting waveform and b) Jetted drops velocity measurement

The substrate was fixed to the printer base platform at the top left corner using masking tape. Substrate temperature was kept at room temperature (20°C) with vacuum functionality turned off and substrate thickness set at 1.20 mm and 0.55 mm for the glass microslide and silicon wafer, respectively. The pattern to print was loaded as a bitmap file created with required resolution, setting the printing reference point location at upper left corner. Before jetting the pattern, the cartridge mounting angle (sabre angle) was adjusted to the corresponding drop spacing resolution and a drop offset calibration procedure was performed following the printer manual. Finally, a

physical reference point in the substrate was defined using the fiducial camera tools so that the reference point of the bitmap pattern is aligned and printed at this location on the substrate.

When launching the job, the printing unit was located at the platform origin (top left corner) and the printing direction fixed from left to right (X direction) and then from top to bottom (Y direction) as depicted in Figure 3-2. The printing unit consists of a printhead and a UV LED unit, which moves together in the printing direction. Photocurable ink droplets were deposited onto the substrate and the UV unit scanned across the printed area following the printhead. The UV energy triggered the photopolymerisation process to transform the liquid monomer ink to a solid. The fixed distance between the UV unit and printhead was 45 mm. The UV unit had a wavelength of 365 nm with eleven UV levels that control the light intensity. All printing jobs were carried out using the maximum UV level which corresponds to a light intensity of 1245 W/m².

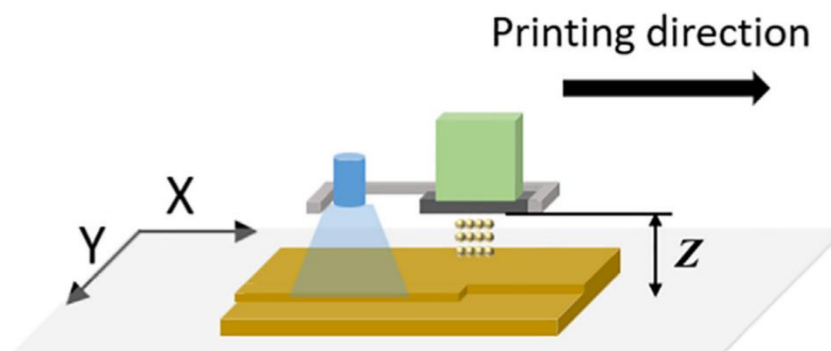


Figure 3-2 Printing mechanism of a DIMATIX DMP-2830 Inkjet printer

Once the printed job was completed, images of the feature were taken using the fiducial camera which had a resolution of 2.54 μm per pixel and a field of view width of 1.62 mm and height of 1.22 mm. The camera was set on dark field mode with the light intensity slider almost all the way to the left to optimize the contrast of the image.

For this investigation, the cartridge print height, nozzles to use, jetting frequency and drop spacing resolution were varied to understand its effect on the surface morphology of printed artifacts.

3.2.6 Optical microscopy.

A Nikon Eclipse LV100ND Optical Microscope was used to measure single drops footprint diameter and height. To estimate the droplet height multiple images at different focus points were taken and a 3D model was built up from the data utilizing Z-series option in manual mode. MATLAB script was used to visualize and measure the droplet morphology and to extract boundary edges and cross-sections for further analysis.

3.2.7 Coherence scanning interferometry.

Droplet size and surface morphology of the printed samples were obtained using a ZYGO NewView™ 8300 Coherence Scanning Interferometry (CSI) system. Measurements were taken at a controlled temperature of 20°C, isolated from noise and dust, and using an objective lens with magnification of 20x. Surface morphology of printed features was provided in text file format containing x, y, and z coordinates for further analysis.

Printed specimens were measured by Mr. Nathan Roberts (University of Nottingham)

3.2.8 Micro-CT scanning.

Micro CT scanning of the testing artifacts was carried out on a Nikon microCT scanner (Derby, UK) with typical X-ray beam settings of 51 kV and a 92 mA current, 1000 ms exposure time, two frames, and 3142 projections. Samples were mounted on a foam sample holder. No filtering was implemented, and the calculated scan resolution was 6.2 µm. The Nikon CT-Pro software was used to reconstruct the samples. MATLAB script was used to remove the support structure, visualize, and measure the printed 3D objects.

3.2.9 Droplet volume.

Using the Dimatix Drop Manager software, the volume of an individual drop was calculated by jetting a specific number of drops into a preweighed vial. The net weight of the jetted drops was found by reweighing the vial in an analytical balance (ABT 100-5M, KERN & SOHN GmbH, Germany) and subtracting the empty vial weight at room temperature, which at the time was 23 °C. The ratio between the net weight and the number of jetted drops determined the average weight of each drop. The volume

of an individual drop was calculated using the ink's density. To accurately measure the weight of jetted drops, the jetting time was set at 50 s for 11610 cartridge and at 210 s for samba cartridge. Four nozzles jetting at 5 kHz were selected to perform the calculation in both cartridges.

3.2.10 Determining droplet footprint diameter, position accuracy and precision.

To determine the jetting process capability, basic statistics regarding the droplet landing position and size were measured using an image of an array of drops taken by the Dimatix fiducial camera and MATLAB software to extract feature dimensions using image analysis.

A 10 x 10 array of drops was printed on a cleaned substrate by setting a large enough drop spacing to avoid drop coalescence, selecting the minimum printing frequency and standoff distance required for a stable drop formation and using a single nozzle. Before capturing the grid image, tuning the position, focus, and brightness of the fiducial camera was required to achieve the highest contrast image possible. The resulting image was analysed using an app programmed in MATLAB to measure footprint diameter (average, range, and standard deviation) and the distance between drop centres along in-scan and cross-scan directions (average and standard deviation). The drop position bias (accuracy) was calculated by subtracting the average drop spacing from the actual value defined in the target pattern. The drop landing position precisions along the in-scan and cross-scan direction were calculated by averaging the drop spacing standard deviation in the corresponding direction. An Anderson-Darling normality test was carried out to validate that measured data follows a normal distribution. Three replicates of the measurement were performed and values for footprint diameter and landing position accuracy and precision were averaged.

This procedure is critical for model calibration purposes.

3.2.11 Determining theoretical static contact angle and layer thickness assuming a spherical cap shape and volume conservation.

With the measured values of the droplet volume and footprint diameter, the droplet height and static contact angle were calculated assuming the deposited droplet has a spherical cap shape, and that volume is conserved. First, the droplet height was determined by solving iteratively Equation (6). Then, the radius of the sphere defining

the cap was computed using Equation (7) and the spherical cap contact angle was determined by Equation (8)

$$V_{drop} = \frac{\pi h}{6} (3r^2 + h^2) \quad (6)$$

$$R = \frac{r^2 + h^2}{2h} \quad (7)$$

$$\sin \theta_{th} = \frac{r}{R} \quad (8)$$

With the measured values of droplet volume and feature footprint area, together with the total number of drops and drop spacing defined by the target pattern, the theoretical layer thickness was calculated assuming that volume is conserved, and the final shape has a spherical cap cross section. First the total volume of ink was determined by the product between the measured droplet volume and the total number of drops in the selected pattern to print. Then, the total area was estimated by the product of the measured footprint area and the square of the drop spacing. Finally, the layer theoretical centroid along the z direction was determined using Equation (9) and the theoretical layer thickness h_t was calculated by solving iteratively Equation (10).

$$\bar{z} = \frac{N * V_{drop}}{ds^2 * A_{fp}} \quad (9)$$

$$\bar{z} = \frac{3(2R - h_t)^2}{4(3R - h_t)} \quad (10)$$

3.2.12 Determining printing parameters effect on the stability of single tracks and square films.

A Central Composite Design (CCD) was employed to investigate the effect of critical parameters of the inkjet printing process including drop spacing, printing frequency and standoff distance. The surface morphology stability of single tracks and square films characterised by the average and maximum width, length and thickness were selected as the response variables. The experimental design built a second order (quadratic) model for each response variable that enabled the effect quantification of

the parameters and its interactions among them using statistical techniques. Printing parameters bounds were chosen based on the region of inkjet printing operability of interest. The matrix of experiments performed for the study of single tracks and square films are shown in Table 3-4 and Table 3-5, respectively. Experiments were carried out in a random order. Details about the dimensions of the single track and square film used in the parametric study can be found in Section 3.2.4.1. Using Dimatix fiducial camera, an image was captured for each feature for further post processing of the surface morphology using MATLAB app.

Table 3-4 Matrix of experiments for single tracks

Run #	Drop spacing (μm)	Printing frequency (kHz)	Standoff Distance (mm)
1	40	2.5	1
2	40	2.5	1.5
3	40	4	1
4	10	1	0.5
5	40	2.5	1
6	40	2.5	1
7	40	2.5	1
8	70	2.5	1
9	10	1	1.5
10	40	2.5	1
11	70	4	1.5
12	70	1	0.5
13	40	2.5	1
14	10	4	1.5
15	40	2.5	0.5
16	10	4	0.5
17	40	1	1
18	10	2.5	1
19	70	1	1.5
20	70	4	0.5

Table 3-5 Matrix of experiments for square films

Run #	Drop spacing (μm)	Printing frequency (kHz)	Standoff Distance (mm)
1	30	2	1
2	30	2	1.5
3	30	3	1
4	10	1	0.5
5	30	2	1
6	30	2	1
7	30	2	1
8	50	2	1
9	10	1	1.5
10	30	2	1
11	50	3	1.5
12	50	1	0.5
13	30	2	1
14	10	3	1.5
15	30	2	0.5
16	10	3	0.5
17	30	1	1
18	10	2	1
19	50	1	1.5
20	50	3	0.5

After performing the experiments, all features were measured using coherence scanning interferometry as discussed in Section 3.2.7 and the results fed to the CCD matrix; then, least-squares regression analysis was performed to obtain the coefficients of the quadratic transfer function that relates each response variable to the drop spacing, printing frequency and standoff distance. Finally, the statistical validity of the transfer function was assessed using adjusted R^2 and mean square error as performance indicators, and significant effects were determined.

4 Computational Methods.

In this chapter, the computational and analytical methods implemented in this research are presented to the reader. The chapter is divided into six sections: physics-based models, data-driven models, surrogate methods, optimisation techniques, analytical models, and hybrid approach. The lattice Boltzmann multiphase flow model and the finite element chemo-thermo-mechanical model implementation are documented in the physics-based section. The 'shape from shading' inverse problem and the image analysis-based methods used to reconstruct the surface morphology of a printed feature are described in the data-driven section. The surrogate model, based on a response surface methodology, is described next. There follows, a description of a series of analytical models that were used to incorporate the effects of droplet location and size uncertainty, flow dynamics behaviour and UV exposure time into the overall modelling framework. Finally, a hybrid methodology to perform the prediction of single and multilayer parts in a holistic manner is proposed.

4.1 Physics-based prediction models.

Modelling the deposition and solidification of droplets involves the solution of complex equations describing multiphase flow and photo-polymerisation phenomena, as discussed in Section 2.1. In this work, the deposition process which includes the impact, spreading, and merging of droplets was simulated using the lattice Boltzmann method. The solidification process which includes the cross-linking of monomers triggered by UV light was simulated using a semi-coupled chemo-thermo-mechanical finite element approach. Details about the implementation of both models are described below. For details about LB and FE theory, the reader is referred to the work of Huang et al. (2015) and Zienkiewicz et al. (2013), respectively.

4.1.1 Modelling droplet impact, spreading and coalescing in inkjet printing.

4.1.1.1 Governing equation.

The deposition of droplets in inkjet printing was simulated using the discretized lattice Boltzmann transport equation, given by,

$$f_i(\vec{x} + \vec{e}_i\delta_t, t + \delta_t) - f_i(\vec{x}, t) = \Omega_i(\vec{x}, t)\delta_t + S_i(\vec{x}, t)\delta_t \quad (11)$$

where f_i is the particle distribution function representing the fluid density, \vec{x} is the particle position vector, \vec{e}_i is the particle microscopic velocity vector in the i th direction, δ_t is the time step, Ω_i is the collision operator and S_i is the forcing term in velocity space. Equation (11) describes the motion of particle distributions under the influence of external forces and particle collisions. In this study, the Boltzmann transport equation was employed to simulate the impact, spreading and coalescing of droplets on flat, non-porous substrates.

4.1.1.2 Model implementation.

The algorithm used to implement the lattice Boltzmann model in this investigation is depicted in Figure 4-1. Material properties, LB configuration parameters, simulation parameters and boundary conditions are required to set-up the model. The propagation of initial particle distributions to neighbouring nodes is first performed, followed by the macroscopic density and velocity fields calculation and the boundary bounce-back execution. Then, the maxwell equilibrium distribution function is obtained assuming 2nd order Taylor expansion and the interaction forces are determined. Finally, the collision of particle distributions is carried out and the results are recorded in an output file. The cycle is repeated until the last time step or convergence has been reached. The LB method was programmed in MATLAB to benefit from efficient matrix manipulation and results post-processing.

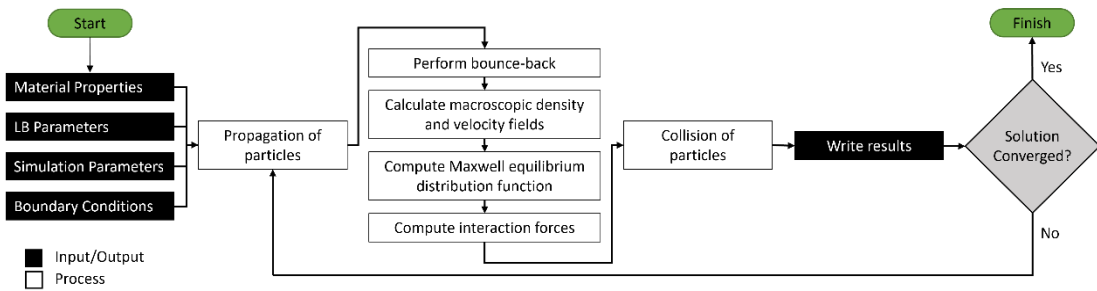


Figure 4-1 Lattice Boltzmann implementation flowchart.

A single component, multiphase pseudopotential scheme was selected following a discrete velocity stencil D3Q19. The pseudopotential scheme assumes a microscopic interparticle force calculated only from nearest neighbours' interaction which leads to the macroscopic separation of phases. To enable the simulation of fluid systems with large density ratios, the Carnahan-Starling equation of state (Kupershtokh et al., 2009) was selected. Furthermore, a multiple relaxation time (MRT) collision operator was implemented to improve the accuracy and numerical stability of the simulation at large density ratio, together with an improved forcing scheme (Li et al., 2013) extended to moment space (Zhang et al., 2014) to control model thermodynamic consistency. Also, an additional source term to adjust surface tension independently of density ratio was included in the model (Ammar et al., 2017). All equations used to develop the code are included in Appendix 11.1.1.

4.1.1.3 Numerical validation.

Since the lattice Boltzmann method approximates the solution of the Navier Stokes equations using kinetic theory, several benchmark tests were performed to validate the numerical model with analytical results such as thermodynamic consistency and mechanical stability at large density ratios, surface tension agreement with Laplace's law, 2nd order spatial accuracy model response and static contact angle and contact angle hysteresis evaluation. Benchmark tests used Carnahan-Starling equation of state with parameters fixed at $a=0.25$, $b=4$, $R=1$ and strength parameter $G=-0.333$ to ensure positivity of the square root of the pseudopotential function. For the MRT model, the relaxation parameters s_1 , s_4 , s_6 and s_8 and the free parameters s_{11} , s_{13} , s_{17} , s_{18} and

s19 were set to 1.0. The relaxation parameters s2, s3, s5, s7, s9 were set to 1.1. These parameters influence the diffuse interface width and careful selection is critical for numerical stability and accuracy. As shown in Figure 4-2, results from benchmark tests agree with analytical solutions which confirm the validity of the numerical solution. Benchmark tests details are included in Appendix 11.1.2 for reference.

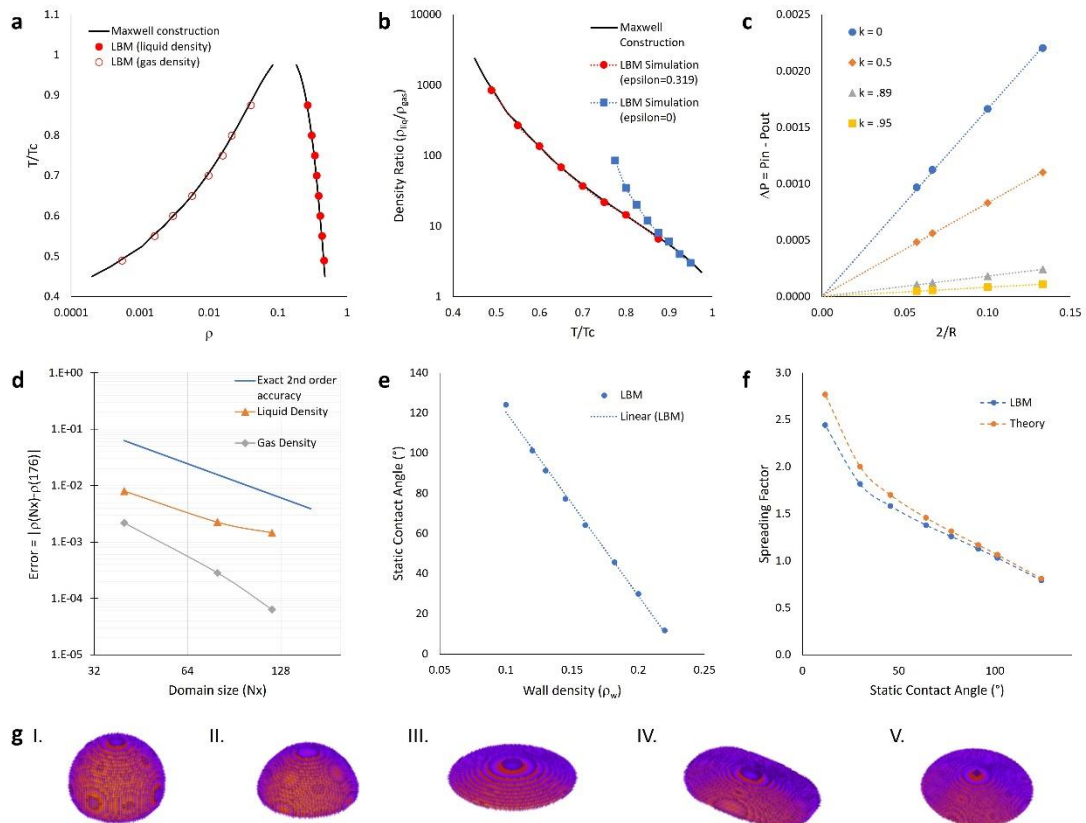


Figure 4-2 Lattice Boltzmann benchmark tests. a. Analytical vs numerical coexisting densities. b. Validation of the capability to model density ratio up to 870 when parameter $\epsilon = 0.319$. c. Laplace's law validation, model is capable to modify surface tension independently of density ratio by tuning parameter κ . d. Validation that model is second order accurate in space. e. Static contact angle varies linearly to the artificial wall density enabling the model to handle different wetting conditions. f. Analytical vs numerical static contact angle shows excellent agreement. g. Drop simulations for different wetting conditions. I. Lyophobic surface. II. Neutral surface. III. Lyophilic surface. IV. Two sequential drops with contact angle hysteresis included. V. Two sequential drops without contact angle hysteresis.

4.1.1.4 Simulation of printing single tracks.

Single tracks were simulated using four sequential and equally spaced impacting droplets on a solid, dry, flat, and non-porous substrate, as illustrated in Figure 4-3. All droplets were initialised with the same impact speed and volume. The height of the first drop (H_0) was set at 20 μm . Drop spacing (ds) along the printing direction, drop

spacing (dh) along the vertical direction, advancing (θ_a) and receding (θ_r) contact angles were selected as simulation variables to study their effects on the stability of single tracks.

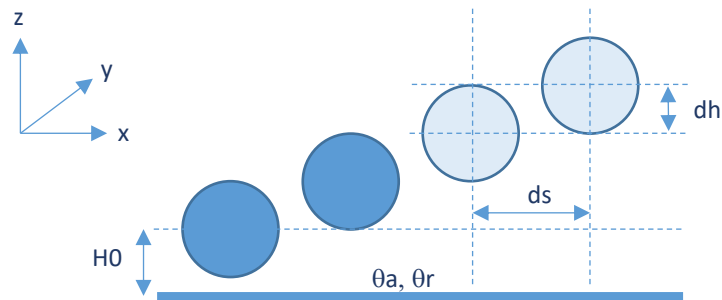


Figure 4-3 Single tracks modelling assumptions.

A summary of the fluid properties, droplet characteristics and relevant dimensionless numbers employed in the simulation is shown in Table 4-1.

Table 4-1 Fluid properties, simulation parameters and relevant dimensionless numbers

Description	Value
Density (ρ)	1030 kg/m ³
Viscosity (μ)	10.0 mPa s
Surface Tension (γ)	30.8 mN/m
Density ratio	870
Dynamic viscosity ratio	542
Droplet impact velocity (U_0)	6 m/s
Droplet in-flight volume (V_{drop})	10 pL
Droplet in-flight diameter (d_0)	26.7 μm
Reynolds (Re)	16.5
Weber (We)	32.2
Printability Parameter (Z)	2.91
Bond (Bo)	5.86e-05

Material properties and simulation parameters were input in SI units. Time and space discretization were determined using the droplet in-flight diameter, Re and We numbers. Lattice Boltzmann parameters were fixed at $R=1$, $a=0.25$, $b=4$ and $T/T_c=0.4898$ to achieve a density ratio of 870. To ensure mechanical stability and achieve the required surface tension, the parameters $\varepsilon = 0.319$ and $\kappa = 0.89$ were chosen. The relaxation parameters s_1 , s_4 , s_6 and s_8 and the free parameters s_{11} , s_{13} , s_{17} , s_{18} and s_{19} were set to 1.0. The relaxation parameters s_2 , s_3 , s_5 , s_7 , s_9 were set

to 1.1 to match the kinematic viscosity and drop speed accordingly. The maximum physical size simulated was 235 μm x 100 μm x 120 μm considering four equally spaced spherical droplets with high phase density in a surrounding domain with low phase density. In addition, equilibrium particle distributions and velocity fields were set to zero, except the droplet domains which are falling with an impact velocity of 6 m/s. A half-way bounce-back rule was applied at bottom boundary to simulate no-slip condition and periodic boundary conditions were implemented in the rest of the boundaries. To control the surface wettability, the desired contact angle was imposed at different surface lattice sites of the solid boundary as depicted in Figure 4-4. Contact angle hysteresis was modelled using two wall boundary conditions triggered by a threshold parameter on density while the contact line expands or contracts during the simulation.

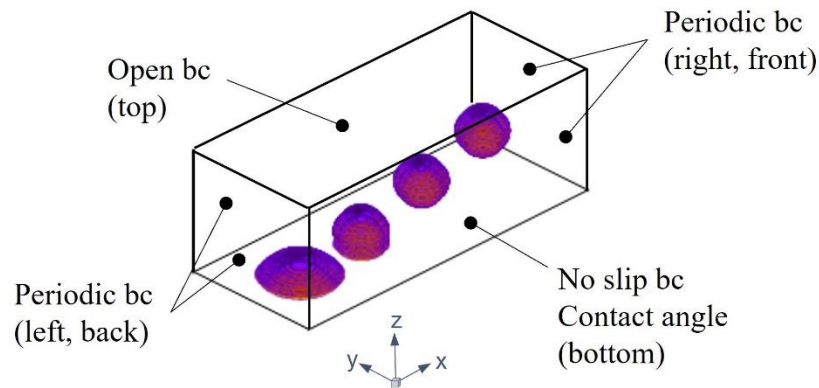


Figure 4-4 Boundary conditions schematic for single track simulation.

The convergence criterion used in this study was determined by Equation (12) where the summation was taken over the whole computational domain.

$$\frac{\sum |u_x(t) - u_x(t - 500\Delta t)| + |u_y(t) - u_y(t - 500\Delta t)| + |u_z(t) - u_z(t - 500\Delta t)|}{\sum |u_x(t)| + |u_y(t)| + |u_z(t)|} \leq 10^{-6} \quad (12)$$

A text file was generated containing the simulation results which includes x, y and z coordinates, density, velocity field, pressure, and interaction forces for every 1000 timesteps and when convergence criteria was reached. From the last results file (i.e.,

at convergence), the surface morphology of the single track was segmented and measured using a MATLAB in-house script.

4.1.1.5 Simulation of printing square films.

Square films were simulated using a 4x4 array of sequential and equally spaced impacting droplets on a solid, dry, flat, and non-porous substrate, as illustrated in Figure 4-5a. All droplets were initialised with the same impact speed and volume. The height of the first column of drops (H_0) was set at 20 μm . This droplet configuration mimics the inkjet process using multiple nozzles simultaneously. Drop spacing (ds) along the printing direction, line spacing (ls) perpendicular to printing direction, drop spacing (dh) along the vertical direction, advancing (θ_a) and receding (θ_r) contact angles were selected as simulation variables to study their effects on the stability of square films. The maximum physical size simulated was 300 μm x 300 μm x 150 μm with boundary conditions illustrated in Figure 4-5b. The rest of the modelling assumptions followed the same process described to simulate single tracks.

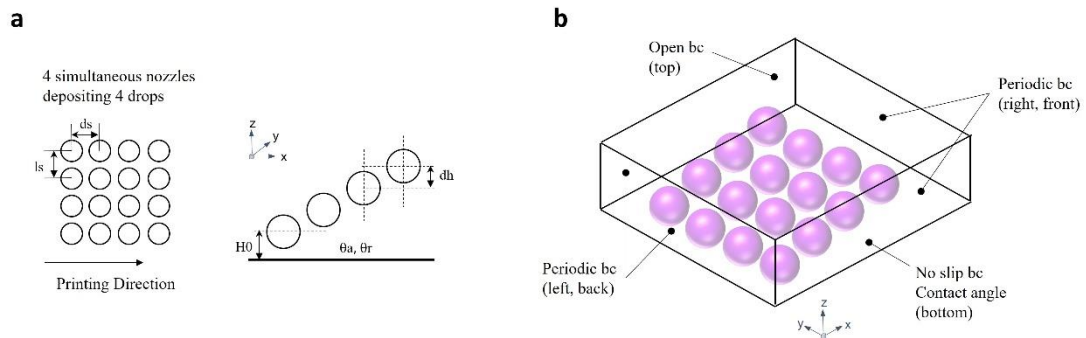


Figure 4-5 Square film. a. Modelling assumptions, b. Boundary conditions

4.1.2 Modelling the deformation of UV curable materials in inkjet printing.

4.1.2.1 Governing equations.

The deformation of inkjet-printed parts made from photocurable polymers is a complex multiphysics and multiscale process involving irradiation, photopolymerisation, and thermo-mechanical behaviour of materials. Conservation of mass,

momentum and energy coupled with photo-polymerisation reaction kinetics relations and material constitutive laws must be solved simultaneously to fully simulate the process. In addition, other computational challenges arise due to different length and time scales observed in the physical process. Therefore, in this investigation an alternative modelling strategy is proposed to facilitate the prediction of the deformation observed in 3D inkjet-printed parts using a semi-coupled photo-polymerisation and structural finite element approach.

The photo-polymerisation process was modelled using a semi-empirical approach developed by Zhao et al. (2021) based on experimental work performed on TPGDA films. The model predicts the degree of monomer consumption as a function of UV dosage, which is expressed as follows,

$$\chi = \chi_{max,p}(1 - e^{k_{r,p}\lambda}) + \frac{\chi_{max,a}}{(1 + e^{k_{r,a}(\lambda-\lambda_c)})} \quad (13)$$

where χ is the degree of monomer consumption, λ is the UV dosage and $\chi_{max,p}$, $\chi_{max,a}$, $k_{r,p}$, $k_{r,a}$ and λ_c are fitting parameters obtained using experimental results. The first term of Equation (13) considers the classical theory of free radical polymerization and the second term, the auto-acceleration (Trommsdorff-Norrish) effect. Furthermore, to consider the light attenuation effect influencing the UV dosage in multilayer printing, the total UV radiation dose λ_n of any printed point at layer n can be estimated as,

$$\lambda_n = \lambda_U + \sum_{n-1}^1 \lambda_{A,n-1} \quad (14)$$

where λ_U is the unattenuated UV radiation dose of the full X-Y pattern and λ_A is the attenuated UV radiation dose. In this investigation, the kinetic model described by Equation (13) was used to determine the degree of curing of printed layers employing the cumulative UV radiation dose with light attenuation described by Equation (14). The reader is referred to the work of Zhao et al. (2021) for full details on the photo-polymerisation mechanism, assumptions and full set of relevant equations. For a comprehensive review of the free radical photo-polymerisation process incorporating

heat and mass transfer effects, the reader is referred to the work of Leistner et al. (2020).

The structural model considers two aspects of the evolution of the mechanical properties: shrinkage due to the photo-polymerisation and the evolution of material properties during solidification. The model is assumed isothermal under an elastic constitutive behaviour. The governing equations that describe the mechanical behaviour of materials solved in this investigation are the quasi-static linear momentum balance (Equation (15)) and Hooke's law (Equation (16)).

$$\nabla \cdot \vec{\sigma} + \vec{f} = 0 \quad (15)$$

$$\vec{\sigma} = \vec{C} : \vec{\varepsilon}_e \quad (16)$$

where $\vec{\sigma}$ is the stress tensor, \vec{f} is the body force, \vec{C} is the elastic stiffness tensor and $\vec{\varepsilon}_e$ is the elastic strain tensor. The chemically induced cure shrinkage strain tensor $\vec{\varepsilon}_{ch}$, the total strain tensor $\vec{\varepsilon}_{tot}$ and Young's modulus $E(\vec{\chi})$ were modelled respectively as:

$$\vec{\varepsilon}_{ch} = \frac{1}{\chi_{max}} \vec{\chi} \varepsilon_{ch,max} \vec{I} \quad (17)$$

$$\vec{\varepsilon}_{tot} = \vec{\varepsilon}_e + \vec{\varepsilon}_{ch} \quad (18)$$

$$E(\vec{\chi}) = \begin{cases} e_0 E_{pol}, & \vec{\chi} < \chi_{gel} \\ \left(\left(\frac{1 - e_0}{\chi_{max} - \chi_{gel}} \right) (\vec{\chi} - \chi_{gel}) + e_0 \right) E_{pol}, & \vec{\chi} \geq \chi_{gel} \end{cases} \quad (19)$$

where $\varepsilon_{ch,max}$ is the strain at maximum degree of curing χ_{max} , \vec{I} is the unity tensor to account for the volumetric shrinkage, $e_0 \ll 1$ is a factor used to reduce the polymerized Young's modulus E_{pol} for the case when the degree of curing is less than the gel point χ_{gel} . The resulting stiffness matrix was isotropic, and the Poisson's ratio was assumed constant. The structural mechanics model described above was employed by Westbeek et al. (2021) to model the evolution of the mechanical properties in a vat photo-polymerisation application.

4.1.2.2 Model implementation.

To simulate the deformation of 3D inkjet-printed components made from photocurable materials, a semi-coupled chemo-mechanical finite element model was implemented in ABAQUS (Simulia, Providence, RI) following the process shown in Figure 4-6.

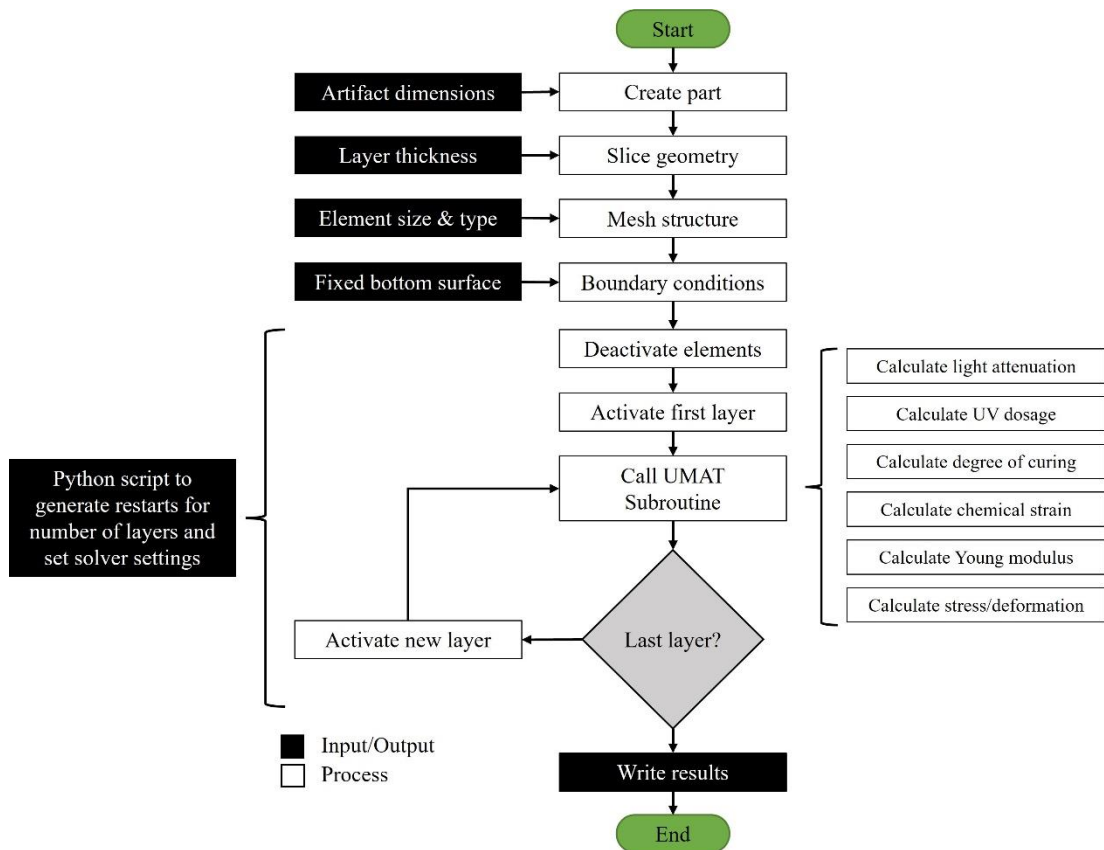


Figure 4-6 Finite element implementation flowchart.

The modelling starts with the definition of the geometry which could be created using ABAQUS part module or importing a CAD model. Then, the geometry is sliced considering an estimated layer thickness representative of the actual value obtained from the inkjet printing process. Next, a structured mesh of 8-noded hexahedral shaped elements is created with a uniform size of 0.002 mm. In the bottom surface a fixed displacement boundary condition is applied. To simulate the sequential layer deposition observed in the inkjet printing process, multiple simulation restarts corresponding to the number of layers in the part were created. At each restart, the mesh elements from the deposited layer are activated and combined with the mesh

elements of layers beneath using the inactive element method (Denlinger & Irwin, 2014). Before launching the simulation, all elements are deactivated except for the elements in the domain of the first layer. Then, a user material subroutine (UMAT) is called to calculate the degree of curing, chemical strains and Young's modulus required to determine the deformation and stress of the structure. After the first layer is cured, the elements in the second layer are activated and material properties updated accordingly. This process is repeated until the last layer is processed. Finally, nodal and element displacements and stresses are saved for further post-processing.

An alternative implementation to the semi-coupled finite element approach described above was devised to accelerate the numerical process. The approach is based on the solution of the thermal expansion phenomenon. First, instead of solving the degree of curing and the evolution of mechanical properties in a transient manner within the elemental domain, the degree of curing is calculated analytically using MATLAB and input as a body load distribution to the FE domain. To account for the photopolymerisation shrinkage, an effective coefficient of expansion (in this case contraction) is calculated as the ratio of the total chemical strains (Equation (17)) and the difference between an artificial temperature load and reference temperature. To account for the material property evolution, the Young's modulus is updated at every simulation restart employing the analytically determined distribution of degree of curing as input for Equation (19). The simulation of the layer-by-layer inkjet printing process using the inactive element method remains unchanged.

4.1.2.3 Mesh size determination.

Due to the computationally intensive process observed in finite element analysis, a balance between accuracy and solution time is required through the adequate selection of the mesh size. To determine an element size that would not compromise the accuracy of the results, a mesh convergence study was performed assuming static and linear elasticity conditions. A TPGDA plate (0.5 x 0.5 x 0.01 mm) discretized with 8-noded hexahedral elements and fixed displacements on bottom surface was subjected to a uniform pressure load of 1 MPa on top surface as shown in Figure 4-7a. The following mesh sizes were evaluated in the study: 0.020, 0.015, 0.010, 0.005. To assess the convergence of the mesh, displacements and stresses were extracted from the linear

region defined in Figure 4-7a. Results showed that displacements and stresses at region of interest converged as the mesh density increased while reaction forces at bottom surface are balanced as illustrated in Figure 4-7c-d. For this investigation, the domain was discretized using an element size of 0.005 mm for further FE simulations.

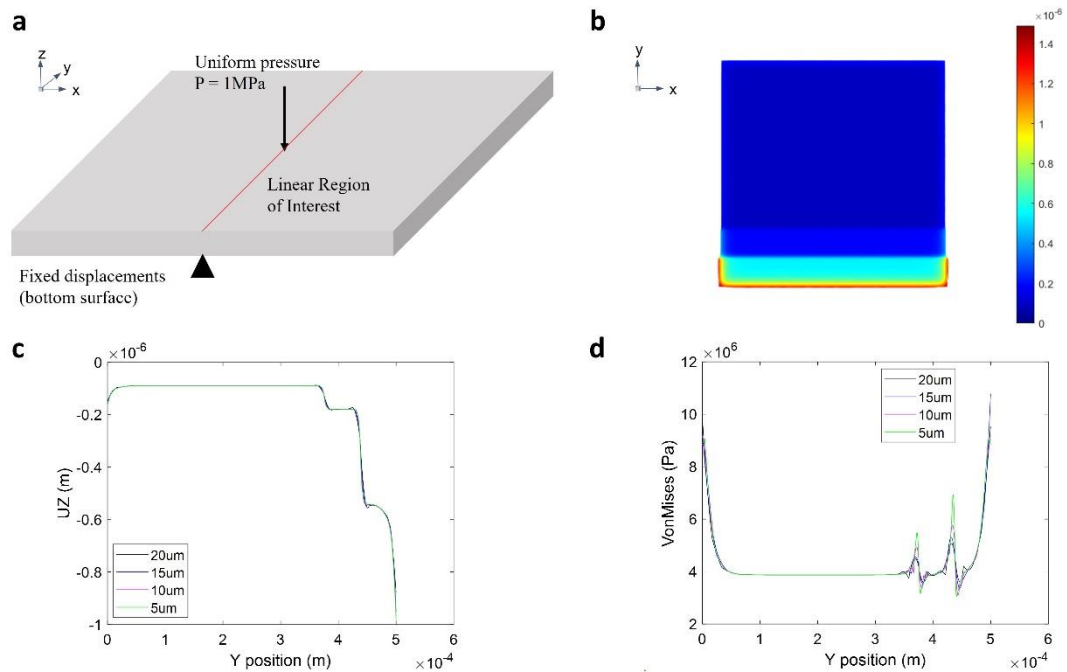


Figure 4-7 Mesh convergence study: a. Boundary conditions; b. Displacements magnitude distribution; c. Displacements at region of interest for multiple element sizes; d. Von Mises stress at region of interest varying mesh size.

4.1.2.4 Simulation of printing rectangular cage.

The cage artifact described in Section 3.2.4.2 was chosen to benchmark the accuracy of the finite element simulation. The geometry was sliced in 50 layers along the width direction, assuming a layer thickness of 0.01 mm. The domain was discretized with a static mesh of uniform 0.005 mm 8-noded hexahedral elements. Fixed displacements on the bottom surface were applied. Relative displacement and residual force convergence tolerances were both set at 1e-4, large displacement, non-linear geometry effects and line search were included. For the UV dosage calculation, a unidirectional printing direction starting at the top left corner and moving from left to right and then from top to bottom was assumed, as shown in Figure 4-8.

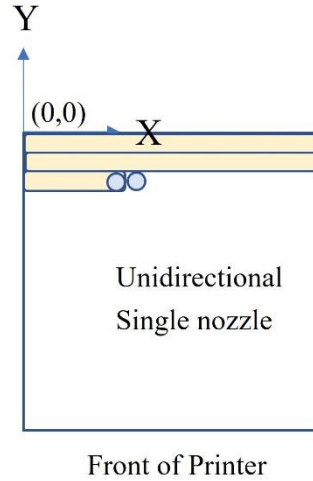


Figure 4-8 Printing strategy.

Fitted parameters for Equation (13) to calculate the degree of curing are shown in Table 4-2.

Table 4-2 Fitted parameters for degree of curing estimation.

Parameters	Value
$\chi_{max,p}$	0.2079
$\chi_{max,a}$	0.5729
$k_{r,p}$	-0.0083
$k_{r,a}$	-0.1258
λ_c	14.0719

For the material property evolution, the volumetric shrinkage of TPGDA was assumed to be 9.5% based on the average values found in the literature (Schmidt & Scherzer, 2015)(Chen et al., 2018). Young's modulus of the fully polymerized material was set to 575 MPa from experimental compression tests performed by He et al. (2017) and the reduced Young's modulus was estimated setting $e_0 = 0.05$, the Poisson's ratio was assumed constant with a value of 0.38, the gel point was assumed to occur at a degree of curing of 0.4 and the maximum degree of curing achievable based on experimental results from Zhao et al. (2021) was set to 0.8. Mesh and boundary conditions are illustrated in Figure 4-9.

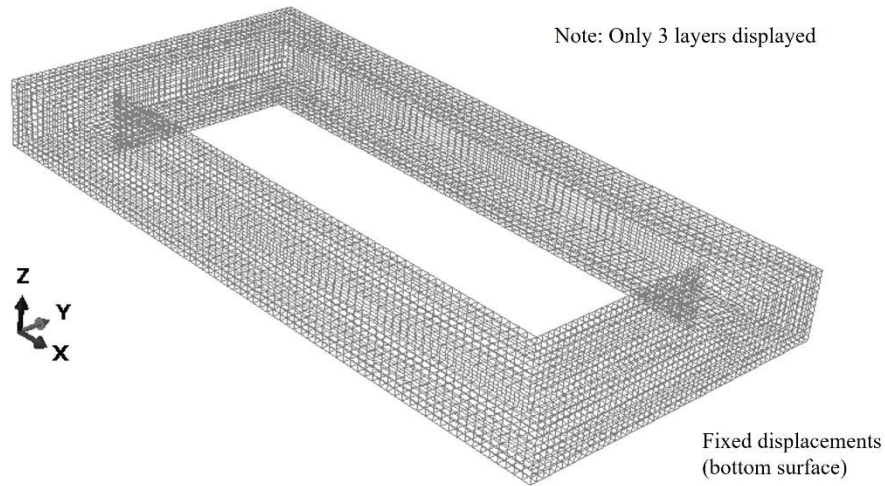


Figure 4-9 Mesh and boundary conditions of rectangular cage.

4.2 Data-driven prediction models.

In section 4.1, theoretical models resulting from deriving partial differential equations based on conservation laws and physical principles were developed to simulate the inkjet printing deposition and solidification processes. These models attempt to mimic reality using a feedforward approach, ergo, without relying on physical measurements of the process. In this section, data driven models to predict the deformed geometry of inkjet-printed films are described that use two photometric 3D reconstruction techniques: shape-from-shading and shape-from-minimum-energy. Shape-from-shading infers the geometry of a scene from a single image by inverting a reflection model describing the image formation. Shape-from-minimum-energy builds the geometry of a scene by image analysis assuming a spherical cap cross section. For a comprehensive review of photometric reconstruction techniques, the reader is referred to the work of Durou et al. (2020).

4.2.1 Shape from Shading surface reconstruction.

4.2.1.1 Governing equations.

The shape-from-shading problem was modelled assuming an orthographic camera projection and frontal lighting, motivated by the work of Wang et al. (2020). The system of equations to infer the 3D surface ($z(x, y)$) of a given image implemented in this investigation is,

$$I(x, y) = \omega_d(A \cos \theta_i + B \sin^2 \theta_i) + \omega_s \cos^n \theta_i \quad (20)$$

$$\cos \theta_i = \frac{1}{\sqrt{1 + \|\nabla z(x, y)\|^2}} \quad \sin^2 \theta_i = \frac{\|\nabla z(x, y)\|^2}{1 + \|\nabla z(x, y)\|^2} \quad (21)$$

$$A = 1 - \frac{0.5s^2}{s^2 + 0.33} \quad B = \frac{0.45s^2}{s^2 + 0.09} \quad (22)$$

$$\|\nabla z(x, y)\| = \sqrt{\frac{1}{I(x, y)^2 - 1}} \quad (23)$$

$$z(x, y) = \Gamma(x, y) \quad (24)$$

The image irradiance model represented by Equation (20) was derived as the linear combination of the Oren-Nayar and Blinn-Phong reflectance models, where ω_d and ω_s are weighting factors for the diffuse and specular reflections, respectively; A and B are coefficients to account for the effect of surface roughness; and n is a factor controlling the surface shininess. These parameters were employed to characterise the reflectance map of the image. The 3D reconstruction of the surface was achieved by the solution of the eikonal PDE type described by Equation (23) subjected to a Dirichlet boundary condition based on a shape prior ($\Gamma(x, y)$) expressed in Equation (24) to avoid convex/concave ambiguity. Two efficient numerical approaches were employed to solve the eikonal PDE: Lax-Friedrichs finite difference scheme (Durou et al., 2020) and first-order Godunov scheme (Wang et al., 2020) both accelerated by the fast sweeping method.

4.2.1.2 Model implementation.

The shape-from-shading problem flow chart used in this investigation is illustrated in Figure 4-10. The algorithm was implemented in MATLAB.

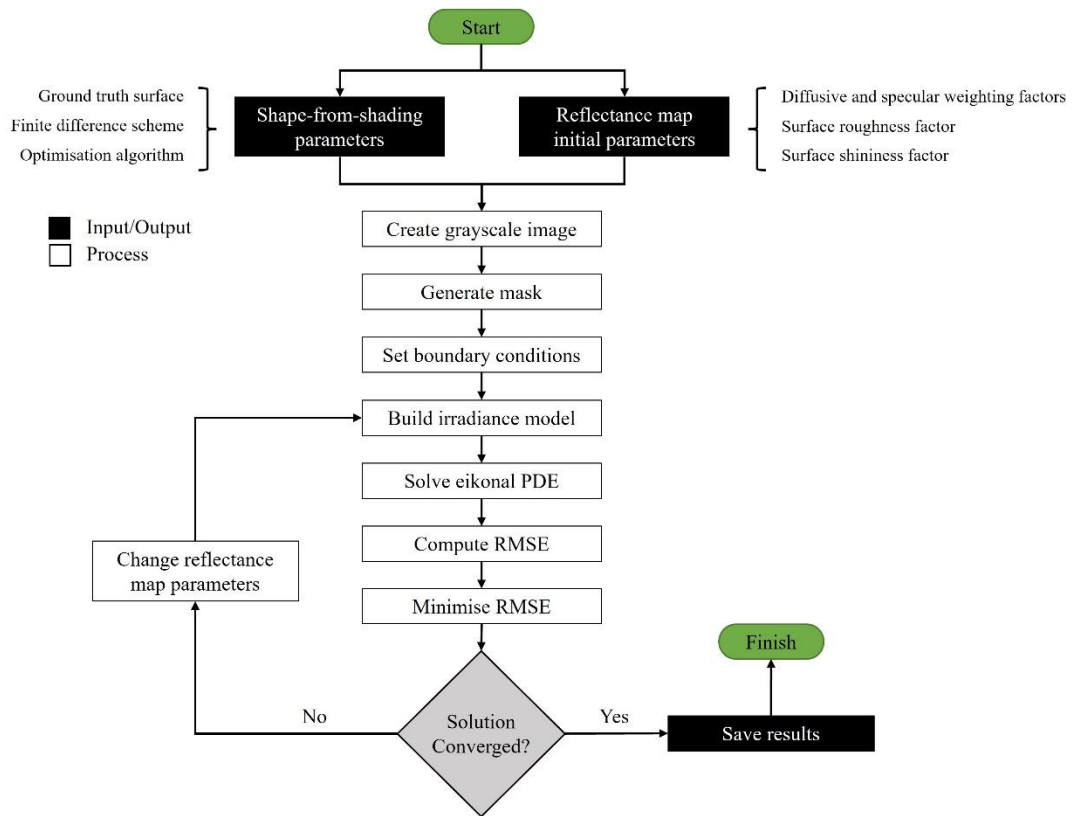


Figure 4-10 Shape-from-shading implementation flow chart.

The process starts with the definition of the ground truth surface, the selection of the finite difference scheme and the optimisation method. The ground truth surface is only required once for calibration purposes. Then, initial values for the reflectance map parameters are set to create a synthetic grayscale image representative of the ground truth. To limit the domain to where the surface reconstruction is required, a mask for the grayscale image is generated by turning pixels outside of the region of interest to black. The mask is employed as a boundary condition for the eikonal PDE and the numerical approximation of the surface is launched by solving the irradiance model and eikonal equation. The reconstructed surface is then compared to the ground truth using two performance metrics: root mean square error (RMSE) and maximum absolute deviation (MAD). If RMSE is greater than 0.1, then an optimisation method to search the reflectance map parameters space that would minimise RMSE is triggered. The optimisation routine stops when the value of RMSE is less than 0.1. Finally, results are saved for further processing. The optimised reflectance map

parameters are then employed to reconstruct the surface of printed films from different images.

4.2.1.3 Surface reconstruction of half sphere using synthetic image.

The model was validated using a half sphere ground truth surface with a radius of 75 μm under four different reflection scenarios, as shown in Figure 4-11a-b. Synthetic grayscale images of 512x512 pixels were generated by varying the reflectance map parameters listed on Table 4-3. The Lax Friedrichs scheme was chosen to infer the geometry of the images which resulted in the reconstructed surface shown in Figure 4-11c. Results showed excellent agreement between ground truth and reconstructed shape, with MAD, RMSE < 3.5 μm and are consistent with experiments reported by Wang et al. (2020).

Table 4-3 Reflectance map parameters for synthetic images.

Parameter	Scenario 1	Scenario 2	Scenario 3	Scenario 4
ω_d	0.8	1	0.5	0.5
ω_s	0.2	0	0.5	0.5
σ_{sr}	0	0.3	0	0.3
n	5	0	10	10

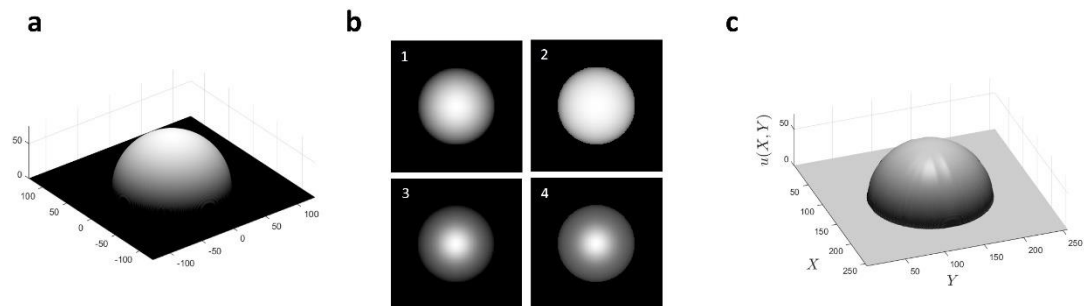


Figure 4-11 Model validation using synthetic half sphere images. a. Ground truth surface: b. Synthetic images generated using the reflectance map parameters from Table 4-3; c. Reconstructed surface using Lax-Friedrichs scheme: MAD = 3.18 μm , RMSE = 3.24 μm , CPU time = 122 s

4.2.2 Minimum-energy-shape method for surface reconstruction.

The minimum-energy-shape method reconstructs the surface morphology of inkjet-printed features using image analysis to extract the footprint edge and assuming the

feature's cross-section tends towards a spherical cap shape. The core of the method lies in the fitting of a second-degree polynomial using two opposite points from the footprint and the maximum estimated height to build the spherical cap shape as illustrated in Figure 4-12. The method was implemented in MATLAB following the process steps depicted in Figure 4-13.

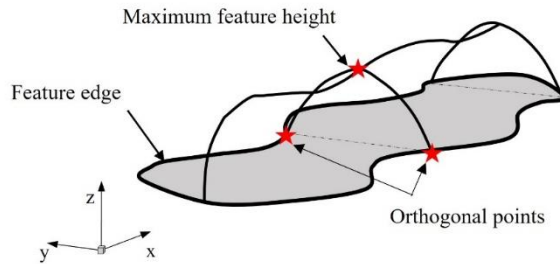


Figure 4-12 Spherical cap volume reconstruction schematic.

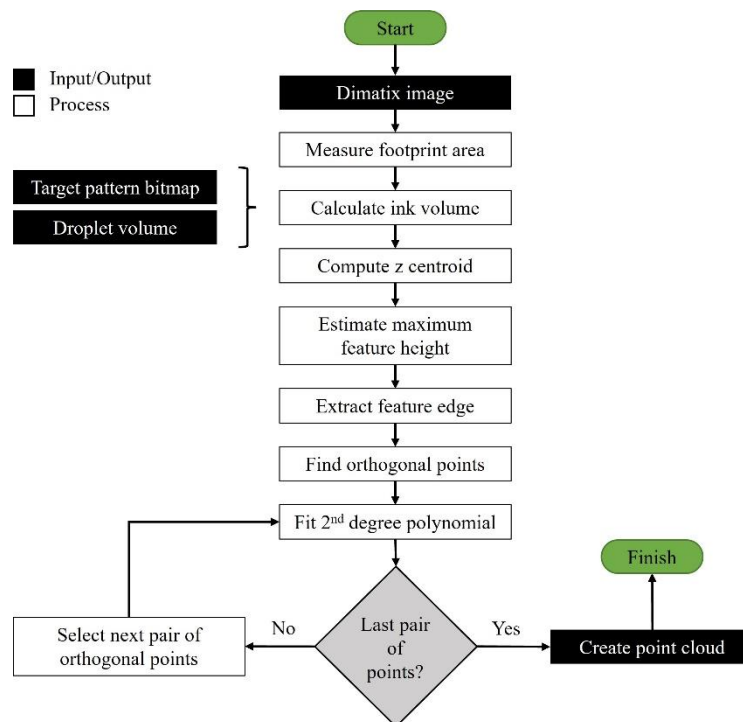


Figure 4-13 Minimum-energy-shape implementation flow chart.

The process starts with image analysis of the printed feature. In this investigation, all images were taken using the Dimatix fiducial camera which generates images with a resolution of 2.54 $\mu\text{m}/\text{pixel}$. The image is converted to grayscale to segment the feature's footprint and compute region properties such as centroid, area and edge

boundary. Then, the volume of ink required to print the feature is calculated by multiplying the number of drops defined in the target pattern bitmap times the droplet volume corrected by shrinkage factor. The ratio between the volume of ink and the footprint area determines the average centroid in z direction and the maximum height of the spherical cap was computed following the procedure discussed in Section 3.2.11. Finally, a pair of opposite points from the edge boundary was identified every five micrometres along the feature's length and a second-degree polynomial was fitted for every pair. The method is limited to single tracks and symmetric solid and hollowed patterns for single and multi-layered artifacts. The approach is not able to reconstruct the surface with the roughness from the real image.

4.3 Stochastic prediction model.

The high-fidelity models used in this investigation to simulate the deposition and solidification of droplets provide an accurate representation of the physics behind inkjet printing for small and simple shapes. However, large, freeform shapes, as required in real-life printing applications, increase the simulation time from hours to days, or weeks. Although, a significant reduction in the solution time, without losing much accuracy, was achieved by implementing a surrogate model from a sample of high-fidelity simulations, the prediction of freeform shapes is still computationally not feasible. Furthermore, previous models do not consider the effect of droplet position and size uncertainty or the simultaneous use of nozzles, which may play a key role in the quality of inkjet-printed parts. Therefore, in this section an analytical model is introduced to predict fast and accurately the surface morphology of inkjet-printed parts for any size and shape considering droplet size and position uncertainty, multi-nozzle printing, UV exposure time and chemical shrinkage. From the author's point of view this analytical model represents the most significant contribution of the present work and the novelty of the research.

4.3.1 Model derivation.

In this section, details of the predictive model derivation are described. The analytical model is a semi-empirical, semi-coupled multi-physics approach, which incorporates the following physical situations in the prediction of the surface morphology of inkjet-

printed parts: droplet position and footprint size uncertainty models to estimate realistic shapes and statistical thresholds for feature stability; fluid quasi-static models to account for material flow redistribution in the final deposited shape; a semi-empirical photo-polymerisation model to determine the spatial distribution of the curing level and estimate the localised shape shrinkage; a theoretical model to find the optimal printing parameters and a film stability diagram based on the equations of motion. The multi-physics analytical model derived, enables the fast prediction of inkjet-printed parts geometry as a function of printing parameters, wetting characteristics and physical properties for any printing pattern; thus, delivering a novel methodology for real-time part quality control.

4.3.1.1 *Determination of droplet position and footprint size uncertainty and overlap map metric for film defect prediction.*

This study commenced by deriving a relationship for the droplet position uncertainty as a function of printing parameters including printing frequency, drop spacing, standoff distance, drop ejection velocity and jet straightness (Rosario, 2017).

$$DPE_a = sd * \tan \theta_{js} \quad (25)$$

$$DPE_b = \frac{sd * pf * ds}{U_e} \quad (26)$$

$$DPE_{tot} = \sqrt{DPE_a^2 + DPE_b^2} \quad (27)$$

where sd is standoff distance, θ_{js} is the jet straightness, pf is the printing frequency, ds is the drop spacing and U_e is the droplet ejection velocity. The total drop position error DPE_{tot} is given by Equation (27). Assuming a normal distribution of the error, the droplet position uncertainty DPU can be calculated as follows,

$$DPU_{the} = \frac{DPE_{tot}}{6} \quad (28)$$

Alternatively, an experimental methodology to measure the droplet position precision and accuracy was proposed in Section 3.2.10. Using the measured standard deviation

of the drop centre position along in-scan and cross-scan directions, the total droplet position uncertainty was calculated as follows,

$$DPU_{exp} = \sqrt{\sigma_x^2 + \sigma_y^2} \quad (29)$$

Using the measured footprint diameter range and assuming footprint diameters follow a normal distribution, the droplet footprint size uncertainty was given by,

$$DSU_{exp} = \frac{d_{fp,max} - d_{fp,min}}{6} \quad (30)$$

A graphical representation of the inkjet-printed drops without and with droplet position and footprint size uncertainty is illustrated in Figure 4-14.

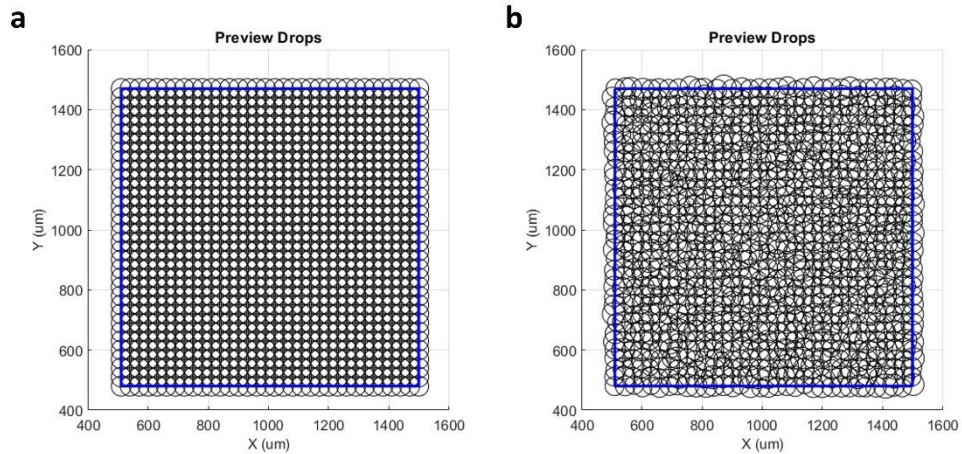


Figure 4-14 Droplet deposition representation: a. Without droplet position and size uncertainty; b. With droplet and position uncertainty

Introducing the uncertainty due to droplet position and footprint size creates a more realistic map of the overlap between droplets which has been found a critical factor in determining the stability of printed tracks and films. Depending on the overlap level, unstable line regimes such as bulges, scallops and break-ups are observed, affecting the quality of the print. To statistically detect if bulges and break-ups would be present in the feature, an overlap map of the droplets was generated. The map identifies locations where droplets do not overlap at all and where droplets fully overlap which indicate potential film break-ups and bulge initiation, respectively. Due to the random

nature of the methodology, the overlap map does not predict the exact location of the defects, but the number of defects due to the introduced uncertainty in the position and size of the droplets. A Monte Carlo simulation with a sample size of 1000 was run to determine the average number of defects expected in the film given the measured uncertainty. Two types of defect were observed in this study, namely bulges and break-ups, which are related to material overflow and discontinuity, respectively. An overlap map showing high probability areas of film separation is presented in Figure 4-15 for illustration.

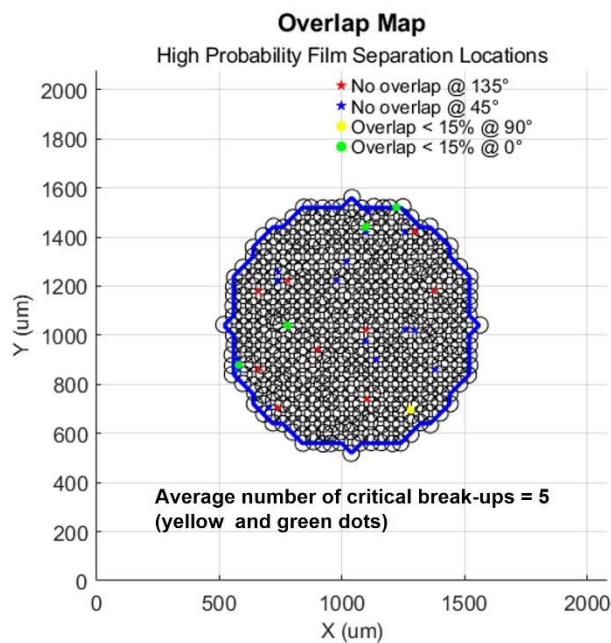


Figure 4-15 Example of overlap map metric to detect film defects.

The skeleton of the printed features was defined by the droplet deposition considering the bitmap resolution, and the droplet position and footprint size uncertainty. However, the model did not account at this point for material redistribution due to fluid dynamics effects when droplets spread and merge on a solid substrate. Therefore, a quasi-static fluid model was introduced next to incorporate transient flow effects in the predictive model, as described in the next section.

4.3.1.2 Determination of material overflow in single tracks and films.

An analytical model to predict the surface morphology of printed features was derived assuming the shape of deposited droplets tends to a spherical cap and volume is conserved. The surface morphology of single tracks was characterised using the four parameters: ABW, MBW, ABH and MBH shown in Figure 4-16, alongside the footprint edge.

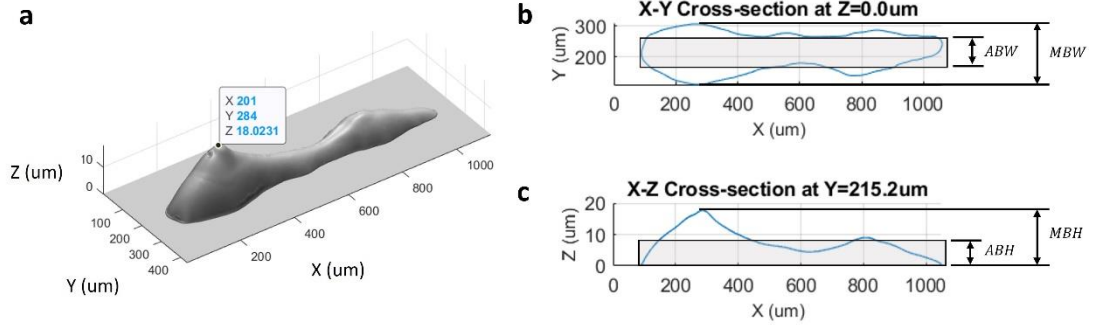


Figure 4-16 Surface morphology characterisation of single track: a. 3D view showing maximum height of printed feature; b. Top view defining average (ABW) and maximum (MBW) width; c. Front view defining average and maximum height.

The model developed here builds upon the work of Stringer & Derby (2010) in which the average width (ABW) of a single track can be estimated as,

$$ABW = \kappa * \varphi * \frac{1}{\sqrt{ds}} \quad (31)$$

$$\kappa = \sqrt{\frac{8 \sin^2 \theta_a}{2\theta_a - \sin 2\theta_a}} \quad (32)$$

$$\varphi = \sqrt{V_{drop}} \quad (33)$$

where ds is drop spacing, κ is a shape function depending on the advancing contact angle and φ is a factor accounting for the volume effect.

To calculate the maximum width of an edge, the average width was employed as baseline and a correction factor was proposed. The core idea behind the definition of the correction factor is that the local material flow is dominated by the competing viscous and surface tension forces which influence the spreading and coalescing of

droplets and consequently the final shape of inkjet-printed features. Therefore, the maximum bead width was estimated by multiplying Equation (31) by a factor ψ that results from the ratio between the momentum diffusivity and capillary diffusivity, expressed as,

$$MBW = \psi * \kappa * \varphi * \frac{1}{\sqrt{ds}} \quad (34)$$

$$\psi = \left(1 + 2\pi * \frac{\mu^2}{\rho\gamma d_{fp} \cos \theta_a} \right) \quad (35)$$

where ρ, σ, μ are physical properties of the ink corresponding to density, surface tension and dynamic viscosity, respectively; d_{fp} is the footprint diameter and θ_a is the advancing contact angle.

The average bead height which corresponds to the centroid of the printed feature along the z direction was calculated by dividing the droplet in-flight volume by the area defined by the shape function and drop spacing given by,

$$ABH = \frac{V_{drop}}{\kappa * \varphi} * \frac{1}{\sqrt{ds}} \quad (36)$$

The maximum bead height was found by solving Equation (37) iteratively for MBH which determines the location of the centroid in the z-direction for a spherical cap shape,

$$ABH = \frac{3(2R - MBH)^2}{4(3R - MBH)} \quad (37)$$

$$R = \frac{(MBW^2 + MBH^2)}{2MBH} \quad (38)$$

Further considerations to the above were required to accurately represent the observed droplet dynamic effects in printed features. Bulges, scallops, and isolated drops (islands) are common defects observed in inkjet-printed films that can be attributed to the complex transient behaviour between droplets and substrate. To model single track bulging, an equation to calculate the minimum number of drops required to avoid the

presence of bulges is proposed. The appearance and size of primary bulges was determined by the number of drops at which the capillary timescale regulated by the surface tension becomes dominant over the drop frequency, together with the influence of drop spacing considerations, which is expressed as,

$$pbnd = \frac{t_f}{t_c} = \frac{1/pf}{\sqrt{\rho d_{max}/\gamma}} \quad (39)$$

Using the viscous timescale and the frequency at which each drop is deposited, the number of drops at which the viscous timescale becomes dominant dictates the appearance of secondary bulges in line patterns, given by,

$$sbnd = \frac{t_f}{t_c} - \frac{t_f}{t_v} = \frac{1/pf}{\sqrt{\rho d_{max}/\gamma}} - \frac{1/pf}{\mu d_a / \gamma \theta_a^3} \quad (40)$$

And the frequency of secondary bulges was estimated as follows,

$$sbfq = \sqrt[3]{\frac{t_f d_a^2}{t_v ds^2}} \quad (41)$$

The lengths of the primary (L_p) and secondary (L_s) bulges were calculated by multiplying the average drop spacing by the number of drops determined in Equations (39) and (40), respectively. The widths of the primary (W_p) and secondary (W_s) bulges were calculated by finding the total volume of the number of drops determined in Equations (39) and (40), respectively and solving iteratively for the spherical cap diameter that would match the required advancing contact angle. This diameter was then compared to Equation (34) and the minimum value was chosen. The length reduction (L_r) was estimated by compensating the extra material required to satisfy the bulge height with material from the length, assuming mass was preserved.

Figure 4-17 shows the prediction of a single track incorporating the material redistribution due to transient flow effects using the derived quasi-static flow model.

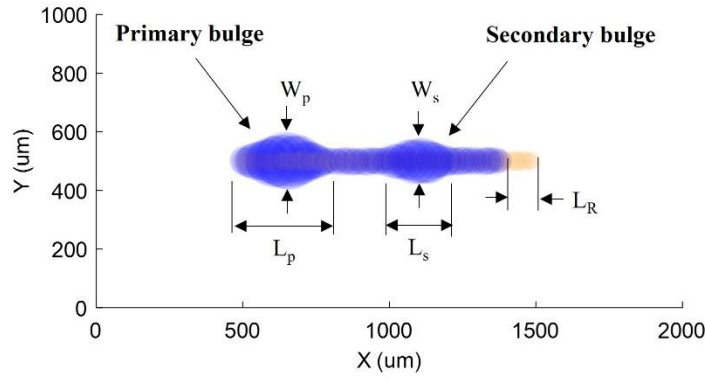


Figure 4-17 Single track prediction with transient flow effects.

The proposed model is capable of predicting material overflow in single tracks and films. However, the effect of the photo-polymerisation process on the final printed shape has not been considered so far. Therefore, a semi-empirical model to account for shrinkage due to solidification was the next feature to be added to the overall modelling strategy, as presented in the next section.

4.3.1.3 Determination of curing strain using photo-polymerisation model.

Shrinkage strain due to curing was determined using a semi-empirical photo-polymerisation model derived by Zhao et al. (2021) using the equations described in Section 4.1.2.1. First, UV dosage for each droplet was calculated based on the speed, and trajectory of the printer's UV light unit and the intensity of the UV light. Then, the polymerisation level for each element of the printing pattern was determined using Equation (13) with fitted parameters from Table 4-2. The distribution of the degree of polymerisation was calculated assuming unidirectional swaths, starting at the top left corner with printing direction from left to right, top to bottom, as illustrated in Figure 4-8. Finally, the curing strain distribution across the pattern was calculated using Equation (17) with parameters $\varepsilon_{ch,max}$ and χ_{max} set to 0.967 and 0.8, respectively. The model assumed that shrinkage predominantly affects the thickness of the printed structure, which is consistent to the work of Tilford et al. (2021).

4.3.1.4 Determination of optimal resolution, printing frequency and standoff distance for stable thin and thick film printing.

An analytical model based on wetting dynamics theory was proposed to determine the optimal spacing, printing frequency and standoff distance required to print thin or thick

films in a stable manner. The core of the model assumes that a sufficient condition to achieve film stability is when the ratio of the traverse speed and the contact line speed is equal to the ratio of the ejection speed and the capillary speed, which is expressed as,

$$\frac{U_T}{U_{CL}} = \frac{U_e}{U_c} \quad (42)$$

where U_T is the printer traverse speed, U_e is the droplet ejection speed, U_c is the capillary speed and U_{CL} is the contact line speed. This relationship provides a connection between macroscopic quantities such as traverse speed and ejection speed which are functions of printing parameters and microscopic quantities, such as the contact line speed and capillary speed, which in turn are functions of the surface tension and dynamic viscosity.

The contact line speed was estimated using the lattice Boltzmann simulation described in Section 4.1.1. The value of U_{CL} used throughout this investigation was 0.047 m/s. Contact line speed values estimated using Cox-Voinov spreading law from literature are within 0.1-0.3 m/s for pure substances spreading on flat, rigid surfaces (Snoeijer & Andreotti, 2013) and contact line speed measured values of an ink with similar properties to TPGDA were reported by Thompson et al. (2014) to be 0.01 m/s. Therefore, a good agreement between reported values from the literature and our simulation results was observed.

The capillary speed was calculated by the ratio between the surface tension and dynamic viscosity of the ink,

$$U_c = \frac{\sigma}{\mu} \quad (43)$$

The traverse speed is a function of the printing frequency and drop spacing and printing frequency is related to stand off distance and droplet speed at impact, as follows,

$$U_T = pf * ds \quad (44)$$

$$pf = \frac{U_e}{sd} \quad (45)$$

The optimal printing parameters to achieve stable lines were calculated by solving Equations (42), (43), (44) and (45). To print stable thin lines, the optimal drop spacing was set to the maximum drop spacing which occurs when the average bead width (Equation (31)) is equal to advancing footprint diameter. To print thick lines, the optimal drop spacing was set to the minimum achievable drop spacing of the printer. Optimal values were checked against printing parameter bounds defined in Table 4-4. In a case that the optimised printing parameters were out of bounds, the procedure was repeated until bound constraints were satisfied.

Table 4-4 Critical printing parameters bounds.

Parameter	Min	Max
Drop spacing (μm)	5	254
Printing frequency (Hz)	700	15000
Standoff distance (mm)	0.25	1.5

The analytical model provided a fast way to estimate the critical printing parameters required to achieve stable thin and thick single tracks and films. However, the stability region defined by the onset of instability thresholds was not considered. Therefore, a stability diagram for single tracks and films considering the drop location and size uncertainty is introduced in the next section.

4.3.1.5 Determination of stability diagram for films using stochastic thresholds.

A graphical tool to show the stability region for freeform films was constructed using the predicted material overflow at edges as a function of the drop overlap. The diagram reports the minimum achievable width based on the volume and wettability characteristics defined as inputs as well as the overlap limits required to print a stable single track or film. Instability thresholds for the onset of bulges and break-ups were determined using the multiphase flow physics-based prediction model for single tracks and films described in Section 4.1.1. Each threshold was defined as an overlap value at which instabilities start to appear during the inkjet printing simulation. Since the simulation was run with constant parameters, thresholds were corrected to incorporate the effects of droplet position and footprint size uncertainties to obtain a more conservative definition of the region of stability for single tracks and films. Finally,

the stability diagram was complemented with the optimal printing parameters derived using the procedure from Section 4.3.1.4.

To find the most conservative thresholds defining the onset of instabilities, droplet position and footprint size uncertainties were incorporated as depicted in Figure 4-18.

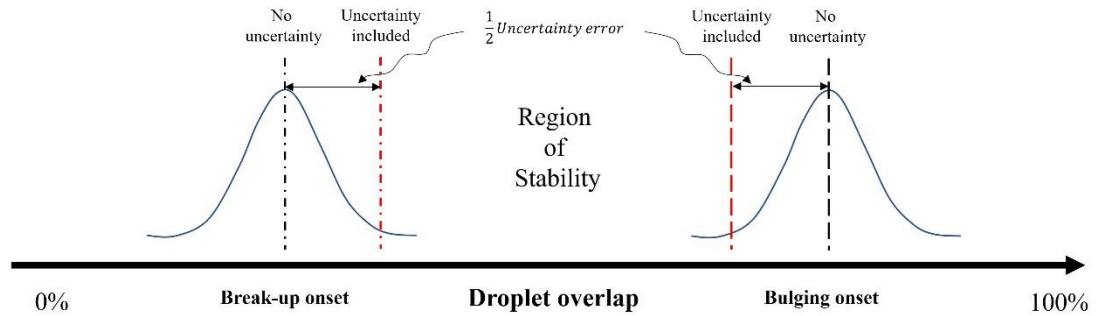


Figure 4-18 Methodology to introduce uncertainty to instabilities thresholds.

Assuming the error distributes normally, the corrected threshold was determined by adding half of the uncertainty error to the break-up threshold and subtracting half of the uncertainty error to the bulging threshold determined from simulation. The recommended threshold provides a more conservative estimate of the stability region, reducing the size of the stability region due to the introduced uncertainty. An example of a stability diagram derived using proposed methodology is shown in Figure 4-19.

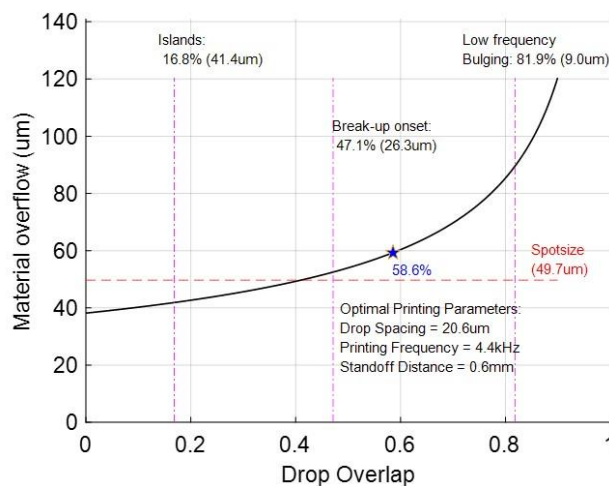


Figure 4-19 Example of film stability diagram.

4.3.2 Model implementation.

The analytical model was implemented in MATLAB following the process steps illustrated in Figure 4-20.

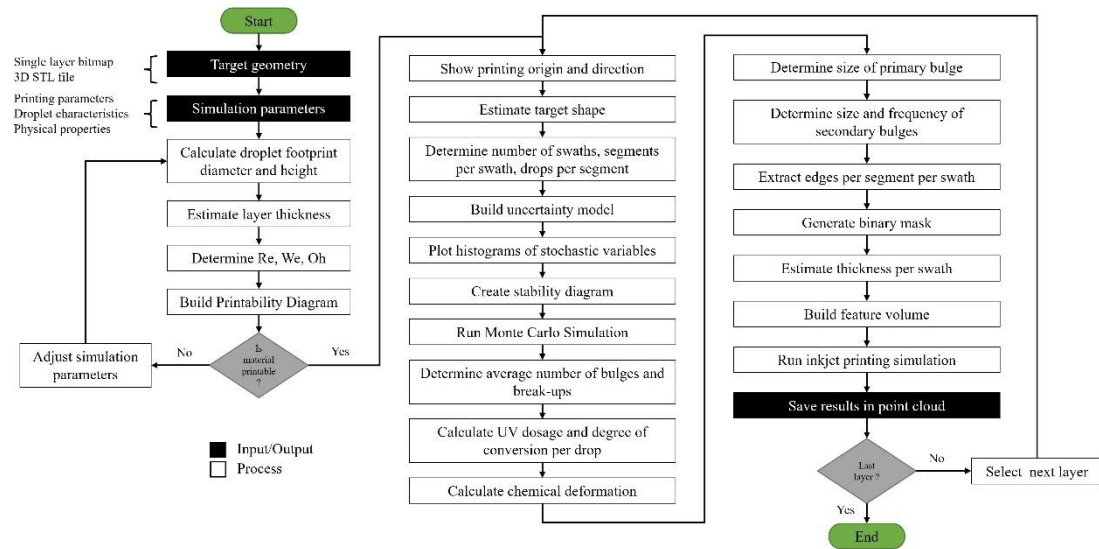


Figure 4-20 Analytical model flow chart.

The model is capable of handling single and multiple nozzles to simulate the printing of desired patterns. It is assumed that the printing start location is at the top left corner of the defined build area and the printing direction is from top to bottom and left to right, as illustrated in Figure 4-8. No temperature effects are considered and droplet volume is conserved throughout the prediction. The model allows the variation of X and Y resolution by manipulating the drop spacing and the wetting characteristics by adjusting the advancing and receding contact angles. The prediction model requires a bitmap image with the desired pattern, the physical properties of the ink, the selection of printing parameters such as printing frequency and standoff distance, and the drop characteristics such as in-flight volume and impact velocity.

If the printability range is satisfied then the model continues execution, otherwise it prompts the user that there exists a high probability of drop ejection failure or drop splashing on the substrate. Using Reynolds and Weber numbers, a printability diagram depicts the feasibility area for given inputs.

If the image type has RGB data, it is converted to an 8-bit grayscale and then to a binary image to identify boundary edges accurately. Domain size is then calculated by extracting extreme boundary locations in X and Y directions. At this step, the model identifies if single edges are present and classifies internal and external edges from shapes within image.

Once domain size is defined an integer number of swaths is computed and the cross-scan resolution is corrected by constraining the line spacing value. Centre locations along the cross-scan direction can be derived by setting the printing start location at the top left corner. This feature enables the user to use any image regardless of its resolution as long as it provides a pixel to microns conversion factor. Nevertheless, the intention of the predictive model is to mimic the inkjet printer system which requires an image format in the desired printing resolution.

By intersecting a horizontal line which simulates each swath trajectory with the print shape boundary edges, the model computes the length and number of drops required to create each printed segment per swath. The number of drops per segment is a function of drop spacing and footprint diameter, which are known values, but since the system requires a discrete number of drops, the resulting value is rounded up. To ensure accuracy of the model, the length is recalculated using the corrected value of number of drops. Then drop centre locations in the in-scan direction are determined. This information is saved to a file which can be used to generate a pattern since it contains all drop locations needed by the printer.

If the image presents edges that are not part of a closed shape, the model places a single drop on each pixel. In the case of shape boundary edges, the model takes as inputs the number of swaths, number of segments and number of drops and generates the segment footprint by interpolating the results obtained from the high-fidelity model at drop overlap locations. The model takes advantage of the periodic nature of the instabilities observed in line patterns and replicates the behaviour regardless of the number of drops used in the segment. This procedure captures the transient behaviour from physics-based model and footprint edge waviness can be estimated in a fast and reliable manner. For the cases of line bulging and break up, an equation to determine the minimum number of drops required to avoid the presence of bulges is proposed. Using the viscous timescale and the frequency at which each drop is deposited, the number

of drops at which the viscous timescale becomes dominant dictates the appearance of secondary bulges in line patterns. The appearance and size of primary bulges is determined by the number of drops at which the capillary timescale regulated by the surface tension becomes dominant over the drop frequency together with the influence of drop spacing considerations. Line pattern break-up has been associated with the effect of a receding contact angle presence. As the receding contact angle increases, the probability of break-up increases in a non-linear way. The model uses the contact line speed predicted by the high-fidelity model together with drop spacing and receding contact angle to calculate when break-up occurs.

With the footprint defined the next step is to determine the thickness across the pattern. The model allows the direct interpolation of the thickness from the lattice Boltzmann results or to incorporate a mathematical model of the expected cross-section for a particular ink-substrate system. For example, a UV curable ink would tend to show a spherical cap cross-section while a solvent-based ink would show accumulation of material at the extremes with very shallow thickness at the centre of the pattern due to the “coffee ring effect”. In this study, a UV curable dielectric ink is simulated thus a second-degree polynomial fits the expected spherical cap cross-section. Two points are available from the footprint prediction and the remaining one is obtained via LBM thickness interpolation at the centre of the path for multiple locations across the length of the pattern. The number of locations where the cross-section is calculated drives the final 3D pattern point cloud density. In this way, free-form shapes can be simulated as a function of the desired resolution and ink to substrate contact angle hysteresis.

The model can create 3D objects by the superposition of layers with different shapes and materials. It assumes a constant layer thickness which is added layer after layer, mimicking the way a traditional inkjet printer works. The predicted final shape of the product has the typical surface finish observed in actual printed components, following the waviness of the edges layer by layer. Furthermore, the top surface shows a non-uniform pattern that is product of the cumulative deformations from previous layers. The output of the process is a dense point cloud defining the surface morphology of the 3D printed object. An example of the outputs generated by the proposed analytical model are illustrated in Figure 4-21.

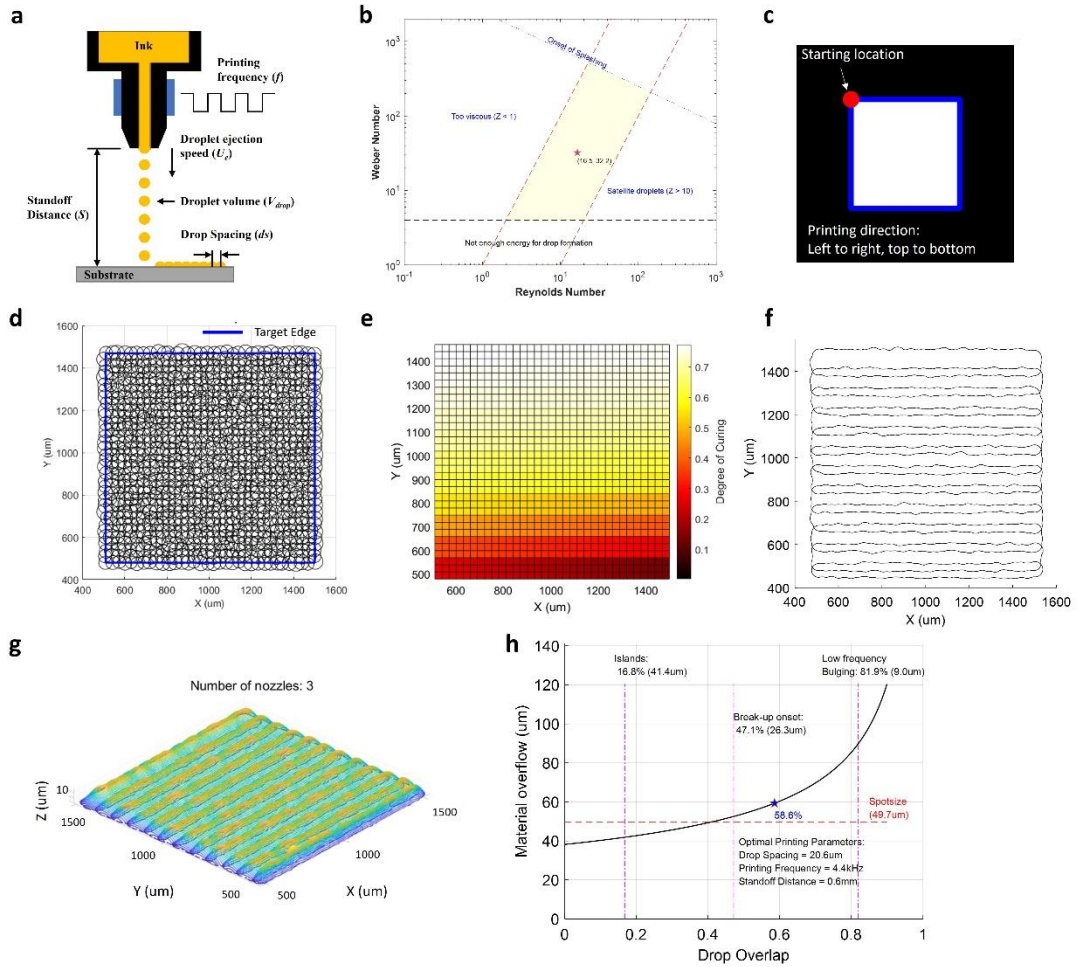


Figure 4-21 Analytical model outputs for the prediction of a square film: a. Printing parameters inputs. b. Printability diagram showing material is printable. c. Pattern bitmap illustrating start location and direction of printing. d. Overlap map of droplets including position and size uncertainty. Map shows no indication of film break-ups. e. Curing degree map based on UV accumulated dosage used to estimate film shrinkage. f. Film footprint edges capturing non-uniform surface morphology due to the use of multiple swaths, the width of the swath determined by the number of nozzles used while printing. g. Point cloud of the predicted film surface morphology. h. Stability diagram showing optimal printing parameters and thresholds for the onset of bulges and break-ups.

4.4 Surrogate modelling approach.

4.4.1 Model implementation.

A surrogate modelling strategy was introduced as a cornerstone of this investigation to develop faster prediction models employing the results of high-fidelity physics-based simulations. The central idea is to generate a set of response surface equations for multiple locations (x, y, z coordinates) along the surface of simulated artifacts from physics-based in silico experiments. Each response surface requires a goodness of fit evaluation to ensure the statistical validity of the method which is achieved using conventional measures of fit such as R^2 statistic and residuals plots. Statistically valid

equations define the feature's surface morphology such as the bead width and thickness as a function of the design variables subject of study for each location. Then, spline interpolation is employed to build the surface ensuring feature continuity. Transient effects from the high-fidelity model are captured by a simpler transfer function, enabling fast exploration of the design space with minimal loss of accuracy. The surrogate modelling strategy was implemented in MATLAB following the process steps illustrated in Figure 4-22.

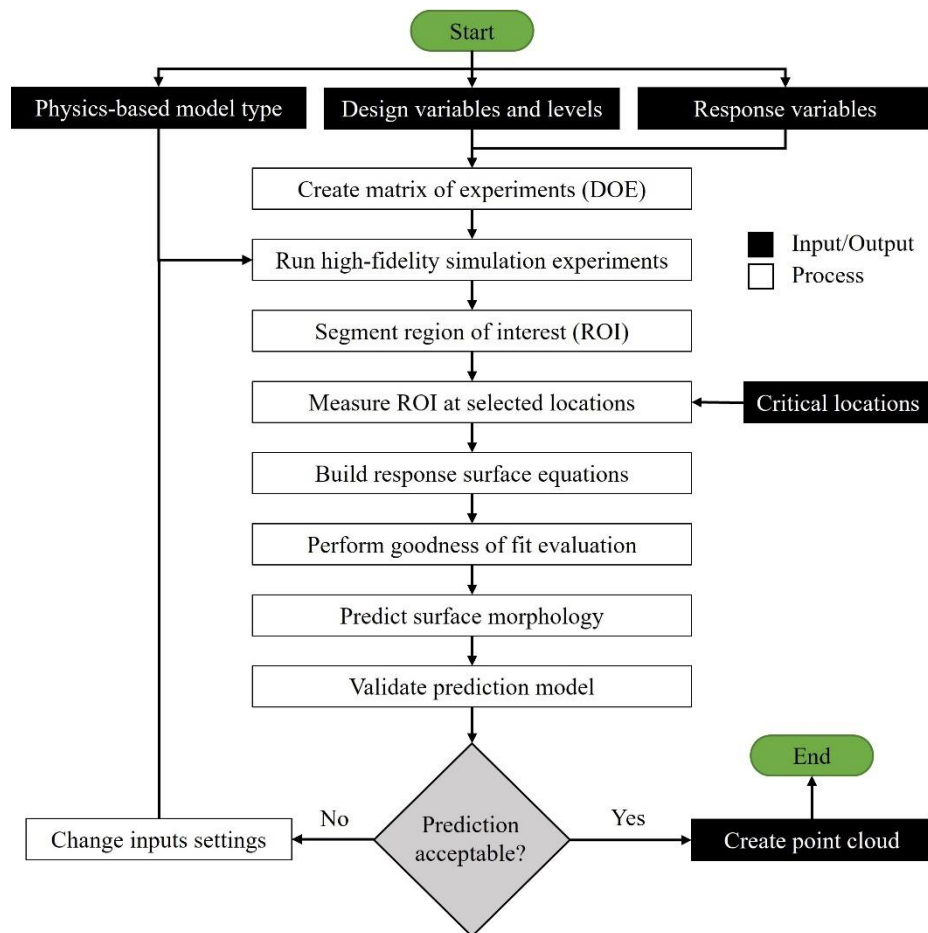


Figure 4-22 Surrogate modelling strategy implementation flow chart.

The strategy to create a surrogate model from high fidelity physics-based simulation requires the definition of the physics-based model type, the design variables (i.e., parameters of study) together with their levels (i.e., parameter bounds) and the response variable(s) (i.e., characteristics desired to predict). With this information, a matrix of experiments is generated assuming a central composite design of

experiments to account for non-linear behaviour of the design variables. Then, the experiments are conducted using the selected high-fidelity physics-based model following the simulation setup details described in Sections 4.1.1.4 and 4.1.2.4. Simulation results require further processing before the response surface equations are constructed. First, the region of interest (ROI) is segmented to avoid the potential selection of undesired artifacts in the analysis. Then, the overall dimensions of the segmented ROI such as length, width and thickness are measured at selected critical locations. The number of critical locations defines the number of response surfaces to be generated, which is an important factor determining the surrogate model efficiency. Response surface equations are built at each critical location and a visual tool utilising “traffic-light” colours, illustrates the level of each measure of goodness of fit. If the fit is not acceptable, the model is improved using variable transformation, adding more points to the regression, or reducing the design space being explored before the physics-based model is changed. The discrete surface morphology predicted by the surrogate model is enhanced using a spline interpolation scheme to ensure continuity and connectivity within the surface. Finally, the root mean square error (RMSE) between the high-fidelity and surrogate model surface morphology is calculated to assess the accuracy of the surrogate model prediction. If the prediction is acceptably accurate, then the coordinates of the surface are saved as a point cloud object for further processing.

4.4.2 Definition of surrogate model for multiphase flow simulation.

A Central Composite Design (CCD) approach was employed to investigate the effect of critical parameters of the inkjet printing process, including drop spacing along horizontal and vertical directions and advancing contact angle. CCD builds upon the full factorial design and contains additional points for capturing curvature effects in the design space. The application of the response surface methodology allows us to identify not only the impact and sensitivity of factors, but also to determine if any interactions exist between them or if nonlinear effects are present. In addition, it helps us to understand how both the mean and variation of a response change with different factor settings, facilitating probabilistic analysis when a factor’s uncertainty comes into play.

Before constructing the matrix of experiments associated with a 3-factor central composite design, realistic factor bounds were selected to cover the region of inkjet printing operability of interest. Since inkjet printing resolution varies inversely to drop spacing along the printing direction; bounds were calculated based on typical resolution values used for printed electronics applications by the following equation,

$$Resolution = \frac{25400}{ds} \quad (46)$$

where resolution is given in dots per inch (dpi) and drop spacing (ds) in microns. The maximum and minimum resolutions used were 1200 dpi and 400 dpi, respectively. For the drop spacing in the vertical direction, the limits are bounded to domain size constraints in high fidelity simulations. The maximum and minimum limits used were 26.7 μm and zero, respectively. The wetting behaviour is characterised by the advancing and receding contact angles which are bounded by lyophilic substrate assumptions. The receding contact angle was fixed at 5 $^{\circ}$. Table 4-5 summarises the design variable bounds used in the study.

Table 4-5 Design variables bounds.

Design variables	min	centre	max
Horizontal drop spacing (ds)	20 μm	40 μm	60 μm
Vertical drop spacing (dh)	0 μm	13.4 μm	26.7 μm
Advancing contact angle (θ_a)	45 $^{\circ}$	67.5 $^{\circ}$	90 $^{\circ}$
Receding contact angle (θ_r)	5 $^{\circ}$	5 $^{\circ}$	5 $^{\circ}$

The number of runs required by a three factor face centred CCD is 15, considering the DOE does not require replicates and only needs a single centre point since experiments are performed in silico. Table 4-6 shows the matrix of combination of factors following the standard order,

Table 4-6 Central composite design of experiments.

Run	ds (μm)	dh (μm)	θa (°)	θr (°)
1	20	0	30	5
2	20	0	90	5
3	20	26.7	30	5
4	20	26.7	90	5
5	60	0	30	5
6	60	0	90	5
7	60	26.7	30	5
8	60	26.7	90	5
9	20	13.4	60	5
10	60	13.4	60	5
11	40	0	60	5
12	40	26.7	60	5
13	40	13.4	30	5
14	40	13.4	90	5
15	40	13.4	60	5

After completing the design of experiments runs using the high-fidelity multiphase flow simulation, the results files were processed to take width and thickness measurements at identified locations along the printed track length. These measurements were fed as responses to the CCD matrix and a least-squares regression analysis was performed to obtain the coefficients of the following general full quadratic transfer function form,

$$Y = C_0 + C_1X_1 + C_2X_2 + C_3X_3 + C_4X_1X_2 + C_5X_1X_3 + C_6X_2X_3 + C_7X_1^2 + C_8X_2^2 + C_9X_3^2 \quad (47)$$

Before proceeding with validation runs using the high-fidelity model, a statistical assessment to evaluate the goodness of fit of each response surface equation is required. Using traditional measures of fit such as the R^2 statistic, adjusted and predicted R^2 values, a plot of residuals and mean square error, the statistical validity of the equations was assessed, and significant effects were found. Calculating multiple measures of fit for several response surface equations is a high time-consuming task. Therefore, a visual tool illustrating with “traffic-light” colours the level of each measure of fit was implemented. Finally, the response surface equations goodness of fit was evaluated using random space points within factor design bounds and acceptable error limits were determined. The final validation run was performed with random parameter settings within bounds to ensure the high-fidelity model and

surrogate model were acceptably consistent. Figure 4-23 illustrates the methodology used to derive the surrogate model required for an efficient process optimisation.

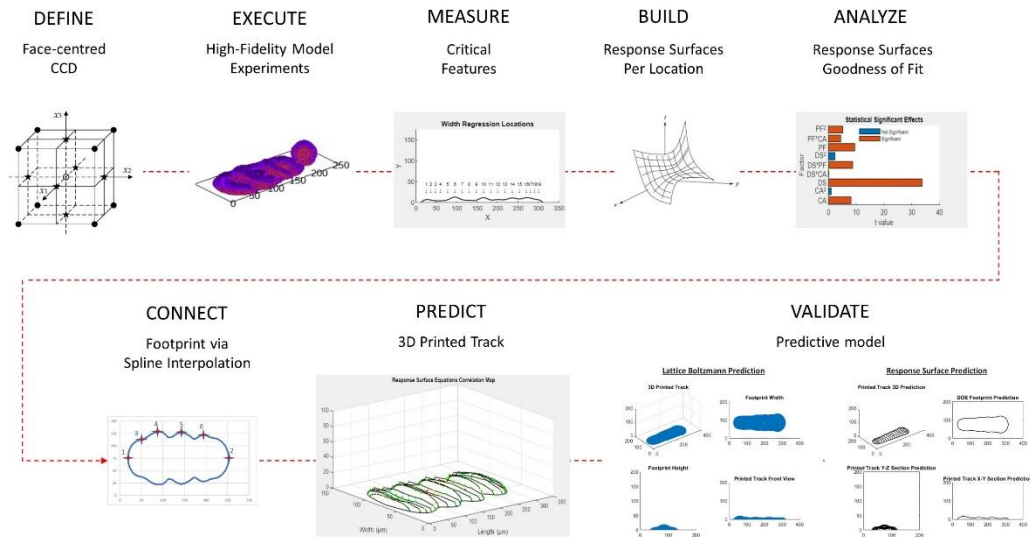


Figure 4-23 Surrogate model development for high fidelity multiphase flow simulation.

4.5 Optimisation models.

4.5.1 Parameter optimisation using multi-objective genetic algorithm approach.

4.5.1.1 Model implementation.

A genetic algorithm (GA) technique was selected to perform the optimisation of critical parameters of the inkjet printing process. GAs are stochastic, population-based algorithms that search randomly by mutation and crossover operators among population members. Several studies have proven that GAs work efficiently when objective functions are noisy, discontinuous and have multiple local minima. In addition, GAs do not depend on the initial search point to find the global optimum, as is the case with traditional gradient based optimisation techniques.

Essentially, the optimisation process is performed as follows: the GA's initial population of candidate solutions is generated by a random combination of genes. Then, each member of the population is measured using a fitness function which quantifies the aptitude of the individual against the defined objective function. The

individuals with the highest fitness value have the highest probability of being selected as parents for the next generation population. Finally, a new population is generated by either combining two of the selected candidates (crossover) or by random modification of a member's genes (mutation). This process is repeated until a convergence criterion is satisfied. The technique was implemented in MATLAB which minimizes the fitness function given as input. Default values for number of generations, crossover, and mutation probabilities were utilized.

To determine the fitness function, the geometric moments concept proposed by Hernandez et al. (2013) was employed. The main idea is to represent an image of the footprint shape obtained by the surrogate model using its two-dimensional geometric moments invariant to translation and scale. The concept is suitable for our problem since the shape of the footprint is a piecewise continuous bounded function which ensures geometric moments are unique and exist. The central geometric moments (CGM) are defined mathematically by the following equation,

$$\mu_{pq} = \int_{-\infty}^{\infty} \int_{-\infty}^{\infty} (x - \bar{x})^p (y - \bar{y})^q f(x, y) dx dy \quad (48)$$

where the sum of p and q define the central geometric moments order, \bar{x} and \bar{y} represent the image centroid and $f(x, y)$ represents the image as a density function. Then, to make CGM invariant under translation and scale, the normalized central geometric moments (NCGM) are given by,

$$\eta_{pq} = \frac{\mu_{pq}}{\mu_{00}^{(p+q+2)/2}} \quad (49)$$

Utilizing the geometric moments methodology proposed by Hernandez et al. (2013), the fitness function is defined as the Euclidean norm of the normalized central geometric moments vector difference between predicted footprint by surrogate model and target shape.

$$\phi = \|NCGM_{predicted} - NCGM_{target}\| \quad (50)$$

The optimal values of the parameters under investigation are found when the fitness function, stated as a least-squares minimization problem, proposed in Equation (50), is minimum. The problem could be solved unconstrained only with design variables bounds defined; however, a set of non-linear equations are optionally implemented to provide constraints to the maximum standard deviation allowed for footprint width and thickness features.

4.5.1.2 Optimisation approach used in multiphase flow simulation of single tracks.

A multi-objective genetic algorithm was employed to find the optimal values of the horizontal drop spacing, vertical drop spacing, and advancing contact angle to produce the most stable and uniform single track as described in Section 4.1.1.4. Nonlinear constraints to the maximum standard deviation allowed for footprint width and thickness features, were set at 5 μm and 2 μm , respectively.

Figure 4-24 illustrates the optimisation process map consisting of 4 main steps: 1) an image of the target line footprint formed by the deposition of four sequential microdroplets is created. Target line dimensions such as length and width are determined using volume conservation assumptions. 2) a printed line footprint image is predicted using the validated surrogate model with random set of printing parameters and wetting characteristics. 3) normalized central geometric moments up to fourth order, are calculated for both target and predicted footprints. 4) a genetic algorithm minimizes the difference between the normalized moments to determine the optimal set of process parameters.

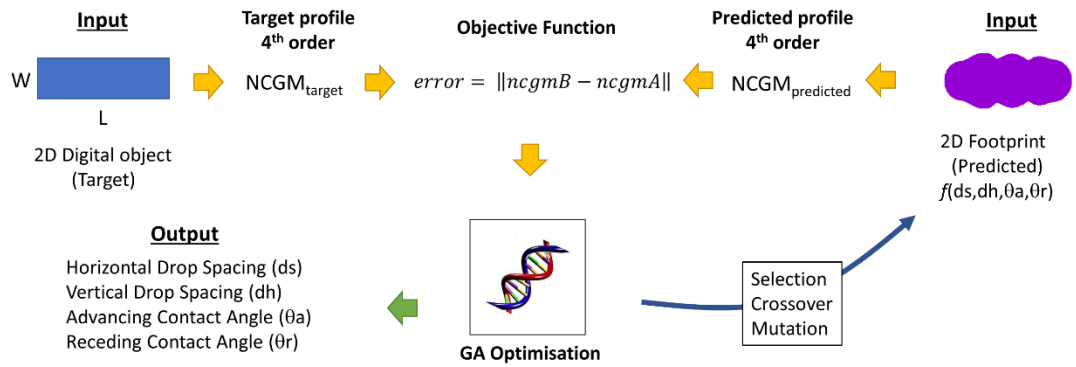


Figure 4-24 Optimisation methodology

4.5.2 Geometry compensation using convolutional neural network approach.

Geometry compensation of inkjet-printed parts using a convolutional neural network was implemented in this investigation motivated by the work of Chowdhury et al. (2018). The methodology was originally developed to make appropriate geometric modifications to counteract the thermal effects resulting from a finite element simulation of an AM process. The core of the approach lies in a convolutional neural network that approximates the geometric deformation data for a part as a function of the coordinates of its surface points. In this investigation, the methodology was extended to account for dissimilar target and deformed point clouds which enable the use of prediction models with unstructured discretisation or scanned data defining part geometry. An overview of the geometry compensation methodology proposed is given in Figure 4-25.

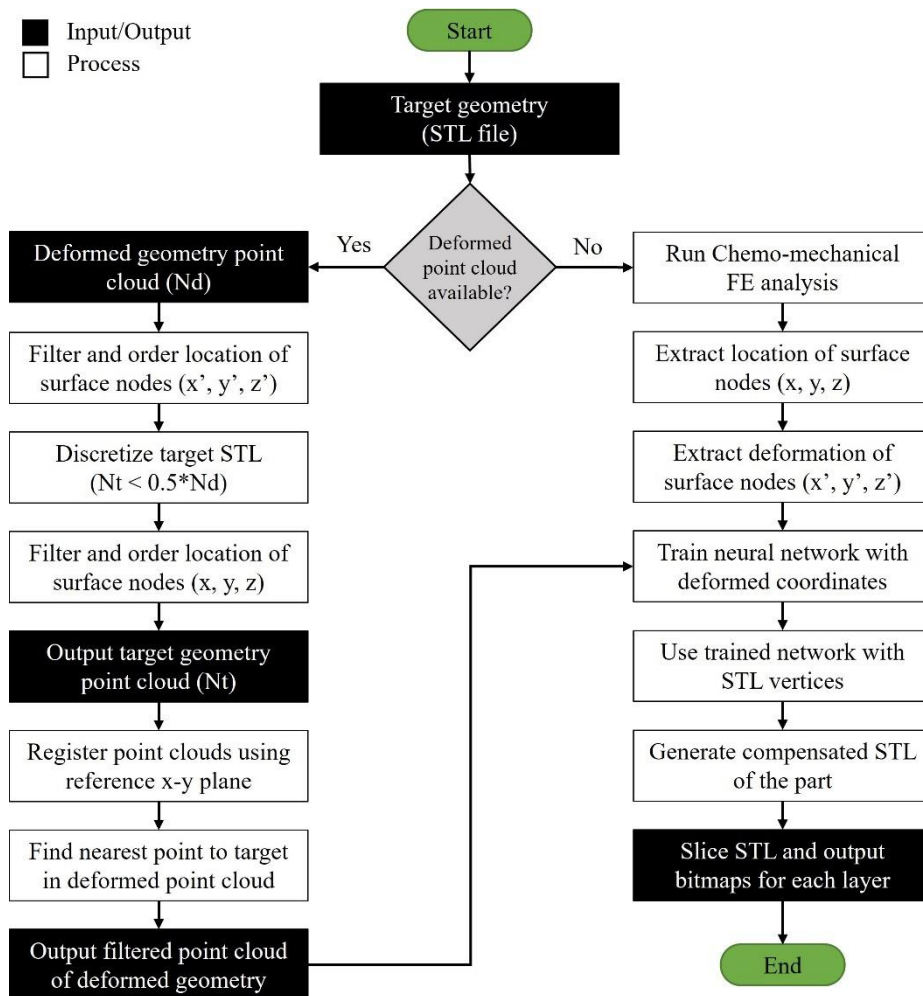


Figure 4-25 Overview of geometry compensation methodology.

The geometry compensation methodology was implemented in MATLAB using the neural network toolbox. The architecture of the convolutional neural network consisted of 3 input nodes, 15 nodes in a hidden layer and 3 output nodes. The error backpropagation was calculated using the Bayesian regularization method and the error minimization was performed using the steepest descent method. The selected network architecture and solution algorithms kept the mean square error within an acceptable range (i.e., $MSE < 1e-3$) at a relatively low computational time (i.e., solution time in the order of seconds).

The methodology starts with the definition of the target geometry using a CAD model in STL format. If no data exists regarding the deformed shape of the printed artifact, a chemo-mechanical simulation is run following the procedure described in Section 4.1.2. The simulation outputs the deformation data of the part geometry and the surface node's locations are filtered for the deformed and undeformed states. If data exists

regarding the deformed shape of the printed artifact either coming from simulation or experiments, a common discretization of the part geometry must be employed to apply the compensation correctly. First, the deformed data is filtered to generate only external faces of the part geometry, followed by discretization of the target geometry. The target geometry must have a coarser discretization than the deformed geometry. Then, target and deformed point clouds are aligned (registered) using the iterative closest point algorithm assuming both parts rest on a reference x-y plane. Once the point clouds are properly aligned, the nearest neighbour algorithm is applied to find the closest point in the vertical direction. This procedure ensures a one-to-one mapping for deformed and undeformed states enabling correct training of the neural network. The network is trained using the x, y, and z coordinates of the deformed geometry as inputs and the undeformed coordinates are set as target, as shown in Figure 4-26a. Then, the error is defined by the difference of the actual output of the neural network and the desired geometry coordinates. This error is back-propagated to determine weights on hidden layers, which represent the learning behaviour of the network. After the network is trained, the original STL vertices are used as input to the network such that the output are the compensated vertices required to build a printed 3D structure that is optimised to the target geometry, as illustrated in Figure 4-26b. Finally, a compensated STL file of the part is generated and sliced to define the layers required for 3D inkjet printing systems.

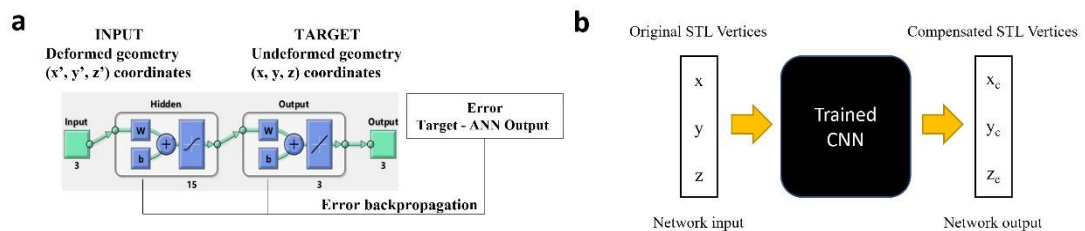


Figure 4-26 Convolutional neural network for geometry compensation: a. CNN training schematic; b. CNN compensation schematic.

4.6 Prediction and optimisation framework for inkjet-printed parts.

The prediction and optimisation of inkjet-printed parts was performed following a two-step approach as illustrated in Figure 4-27. The first step determines the optimal

printing parameters for every layer to achieve the most accurate, uniform, and continuous film by running a prediction model as described in Sections 4.1, 4.2 or 4.3 followed by the generation of a surrogate model as discussed in Section 4.4 and the parameter optimisation with a multi-objective genetic algorithm introduced in Section 4.5.1. The second step compensates the geometry of each layer to account for the deviations found between target geometry and measured data from either computer or lab experiments by employing the CNN compensation methodology explained in Section 4.5.2. A MATLAB GUI was programmed to guide the process in a structured manner. All functions are included in Appendix 11.3.

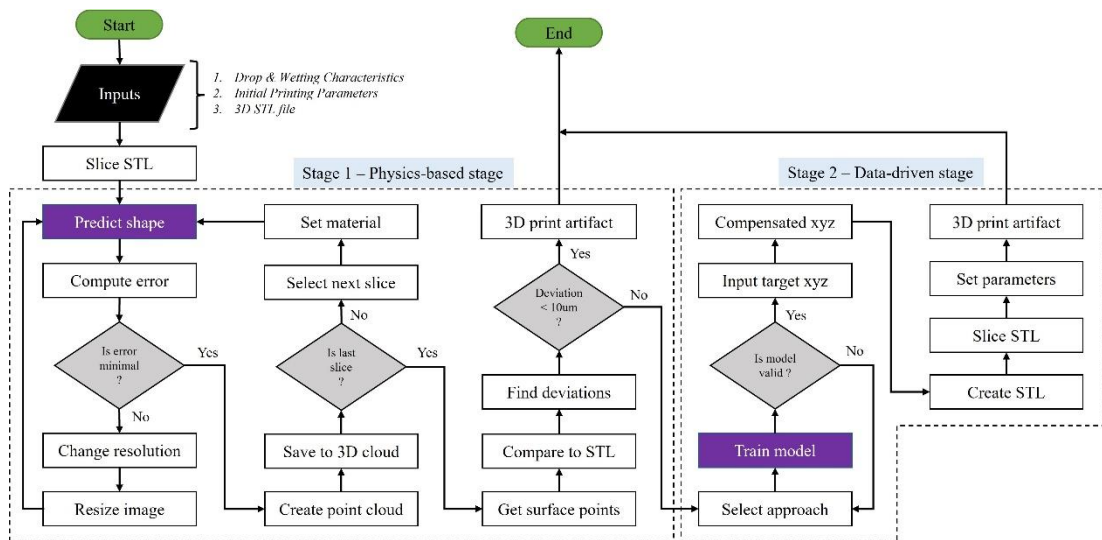


Figure 4-27 Hybrid physics-based and data-driven framework.

The hybrid framework was implemented as follows. First, the target geometry was input in STL format and bitmap layers were generated based on the expected layer thickness of the chosen material. Printing parameters, droplet and wetting characteristics alongside material physical properties were defined to initialize the prediction model. Each layer was run through the selected prediction model and the error defined by the difference between target and predicted shapes was computed. Design variables (i.e., printing parameters) were changed until the minimum error was achieved which involved updating the target bitmap layer every iteration. When the minimal error was found, the optimal values of the design variables are saved, and a 3D point cloud is created. The process was repeated for every bitmap layer sliced from the STL file and each consecutive layer point cloud was superimposed on top of each

other, building a 3D object with optimised layers. The quality of the part was assessed by calculating the geometry deviations from target explained in Section 4.7.3. The root mean square was computed and if it was less than the accuracy threshold (default value was 10 μm), then the program terminates, and the bitmap layers were created for actual printing of 3D object. In the case that the root mean square error was greater than the accuracy threshold, then the surface point cloud predicted by the physics-based model was used to train a neural network which employs the x, y, z coordinates of the STL file vertices as target. Before training the neural network, both point clouds should be aligned and a one-to-one mapping between vertices is required for efficient training purposes. Once the ANN is trained, the target geometry coordinates are input to the network and the compensated geometry is created as output. Then a STL file can be written and sliced for 3D printing purposes.

4.7 Post-processing methods.

4.7.1 Automatic extraction of surface morphology from CSI measurements.

Single tracks and films printed for the validation of the prediction models were measured using coherence scanning interferometry, as discussed in Section 3.2.7. Although some images and cross sections of the features were obtained using the native software of the equipment, an additional text file containing the raw measurement data and scanning settings was requested to enable comparison of experiments against predictions. A clean point cloud, measurements of length, width, thickness, footprint area and volume as well as plots of cross sections at critical locations were obtained from the CSI raw data file using an in-house MATLAB script. The script required the ZIGO raw data file, the type and number of features to measure (i.e., grids, single tracks, solid and hollowed films), the target layer bitmap and the control parameters for the segmentation accuracy (i.e., default settings used). Details on the script implementation are discussed in Section 4.7.1.1. An example of the script output is given in Figure 4-28

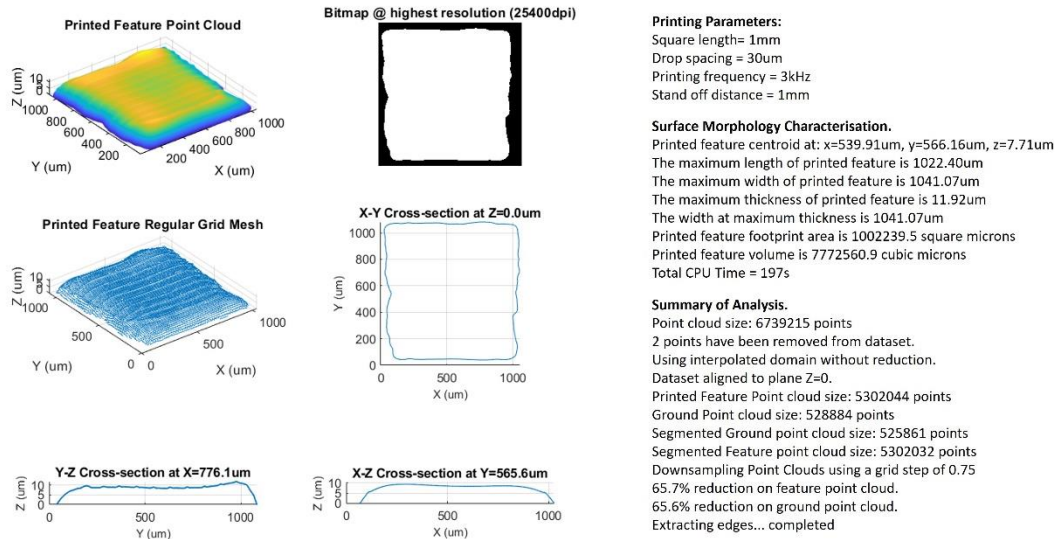


Figure 4-28 Square film measurements report

4.7.1.1 MATLAB script implementation.

Post-processing the CSI raw data was a very time-consuming and error prone task. First, datasets must be cleaned and aligned before feature identification, segmentation and measurement takes place. Furthermore, a reasonable density of points must be chosen to facilitate data manipulation and graph generation. Finally, measurements of overall dimensions and the generation of feature's mask, mesh and cross-sections for every printed feature required a long processing time. Therefore, a semi-automatic workflow was programmed in MATLAB as illustrated in Figure 4-29. All functions are included in Appendix 11.3 for reference.

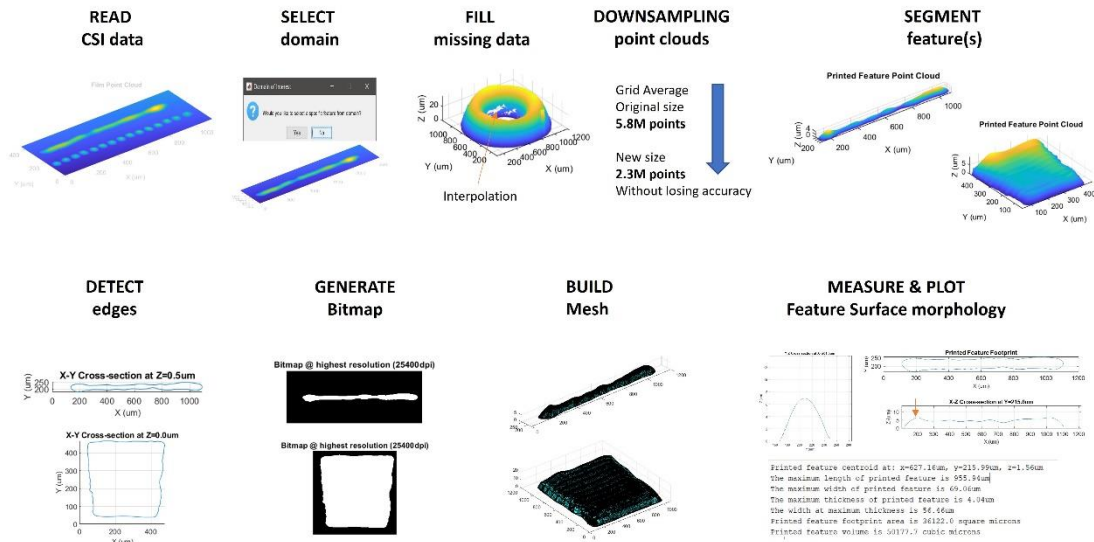


Figure 4-29 Semi-automatic workflow for post-processing CSI measurements.

A dataset is first converted from pixels to micrometres and the bottom left corner defined as the origin of a cartesian coordinate system. Missing data is identified and depending on the location, size and criticality is either eliminated or generated using an interpolation scheme. Outliers are removed if a statistical threshold defined in the control parameters is exceeded. The dataset size is then reduced by down-sampling using a box grid filter technique with a grid step size defined in the control parameters. Correct alignment of the bottom plane to reference x-y plane at $z=0$ is checked, and dataset translation and rotation is performed if needed. Selection of the region of interest is done interactively to narrow down the domain and facilitate further processing. The domain is split into ground and feature datasets through a segmentation algorithm based on surface normals. The feature dataset is further segmented to identify printed features using a k-tree clustering algorithm with an accuracy defined in the control parameters. A point cloud containing the feature's morphology is generated to facilitate comparison against target geometry. Further operations to obtain footprint boundary, area, volume, mask, finite element mesh, and plot of cross-sections of measured artifacts are then performed. Finally, a summary of the results is generated containing the plots and overall feature's dimensions. Optionally, an overlay between target bitmap layer and actual footprint is provided.

4.7.2 Automatic extraction of footprint dimensions from Dimatix images.

Images of single tracks and films printed for the validation of the prediction models were obtained using the fiducial camera of the Dimatix printer, as described in Section 3.2.5. Footprint boundary, region properties and overall dimensions were extracted from the images using an in-house MATLAB GUI based on image analysis techniques. The methodology was developed for the cases when CSI measurements were not available. The GUI interactively required the path location of the image file, image resolution, binarization threshold and feature type (i.e., grids, single tracks, solid or hollowed films). Overlay plots of the extracted footprint and original image were provided for validation purposes. Details on the script implementation are discussed in Section 4.7.2.1. An example of the GUI output is given in Figure 4-30.

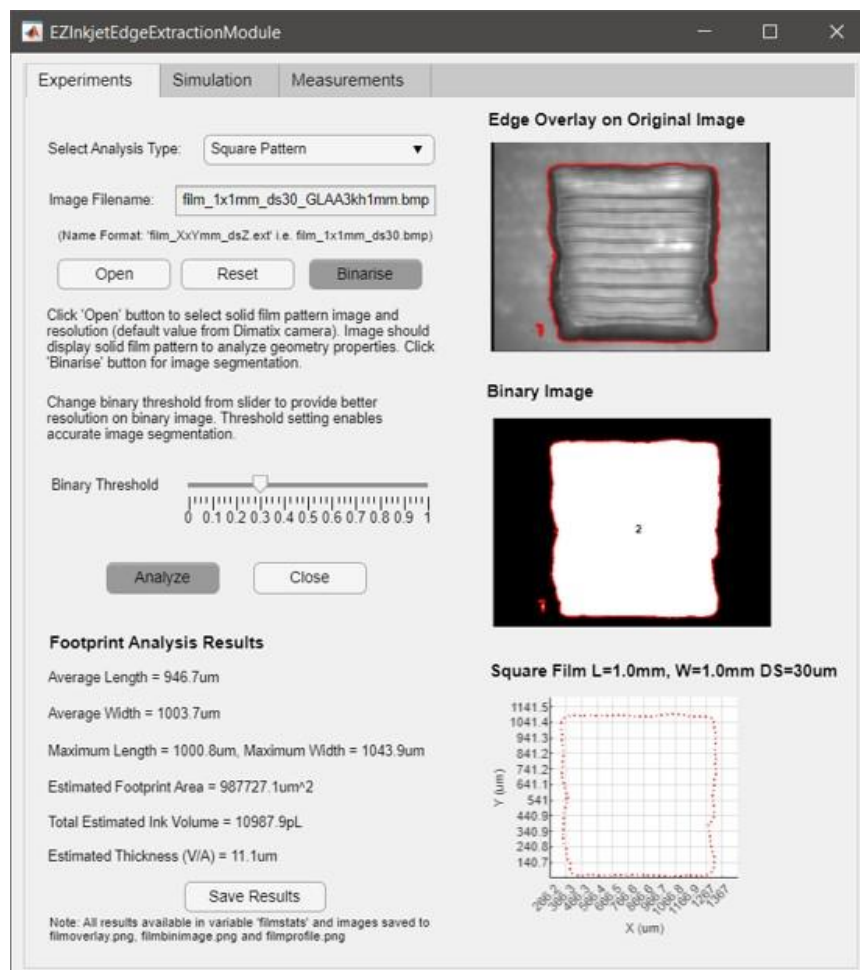


Figure 4-30 Square film image analysis report

4.7.2.1 MATLAB script implementation.

A GUI to accelerate the measurement process of printed features using digital images was built in MATLAB using App Designer. The selected image is first converted from RGB to grayscale to enable image segmentation techniques. The original image is displayed in GUI and its resolution is requested interactively. A binary image is then created employing a default threshold value, but to obtain the most accurate representation of the object of interest, the threshold must be adjusted using a slider control located below the binary image. Boundary edges and region properties are calculated from the binary image and the feature footprint is plotted to show overall dimensions. Depending on the selected feature type, a summary of measurements is displayed including average length and width, footprint area and theoretical volume and layer thickness, which are calculated as discussed in Section 3.2.11. In the special case of a grid of droplets image, measurements displayed include average footprint diameter, theoretical drop height, average distance between drops and standard deviation of the centroid location per line of drops in the vertical and horizontal directions. Finally, all results are stored in a structure array and saved in a MATLAB workspace file (*.mat) for further post-processing. Overlay plots of extracted edge and original image are saved in separate files (*.png) for validation purposes. All functions are included in Appendix 11.3 for reference.

4.7.3 Determining geometrical deviation of inkjet-printed parts.

The geometrical deviation measurement of inkjet-printed parts was implemented in MATLAB following the procedure shown in Figure 4-31. The target geometry, defined by an STL file, and the point cloud of the deformed geometry were inputs to the program. First, the Euclidean distance between each point of the deformed geometry and all triangles from the STL file was determined. Then, the nearest triangle for each deformed point data was identified by finding the minimum distance from the list of distances determined in the first step for every point. Finally, the sign of the deviation was calculated by comparing triangle normal and vector projection of the deformed point along the triangle normal directions. Positive deviation was obtained if both vectors point to the same direction, negative deviation if opposite. A graphical

representation of the part deviations and root mean square error performance indicator were provided. All functions are included in Appendix 11.3 for reference.

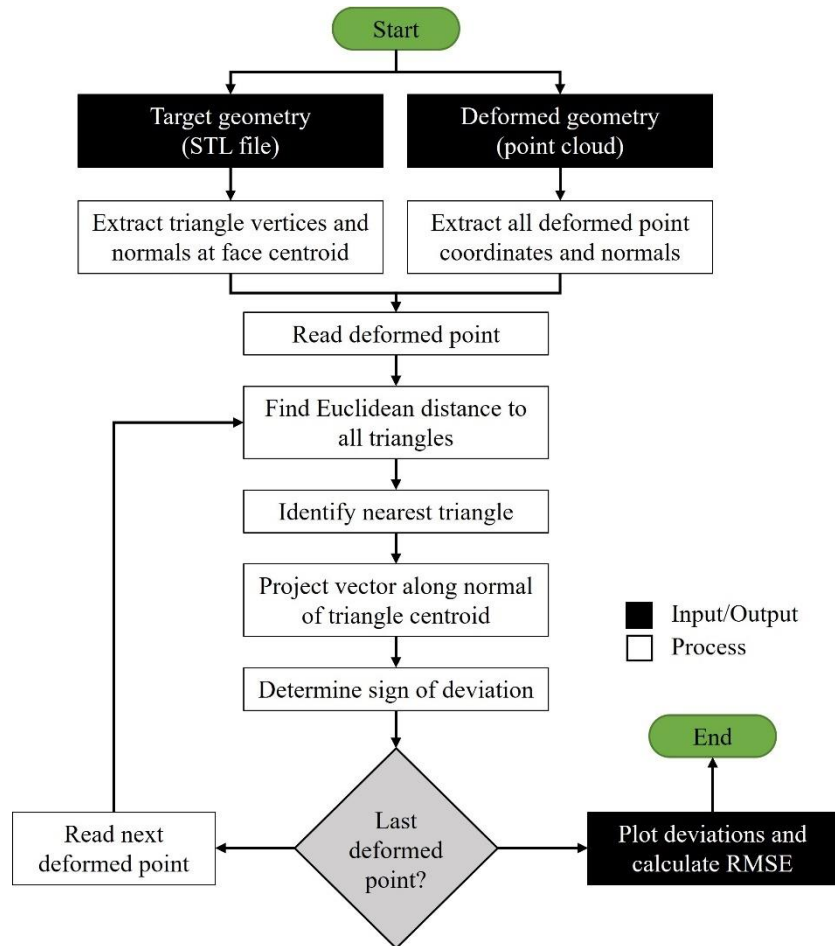


Figure 4-31 Geometry deviation measurement methodology.

5 Surrogate model-based optimisation of printing parameters for the stability of single tracks.

5.1 Introduction.

The primary building blocks of the inkjet printing process are the single tracks. Their formation is influenced by the printing parameters, the physical properties of the ink and the substrate wettability. Drop spacing, printing frequency and stand-off distance are considered key control parameters in the formation of uniform tracks. Also, the advancing and receding contact angles as a dynamic measurement of the substrate wettability play a critical role in the generation of defect free tracks. To understand the relationship between such factors and the surface morphology of single tracks and find the optimum combination of printing parameters, a surrogate modelling framework to improve the quality of inkjet-printed tracks in a fast and accurate manner was proposed. This chapter presents the results of the surrogate model-based optimisation (Reyes-Luna et al., 2023a) of critical inkjet printing parameters to achieve stable single tracks using high-fidelity simulations and lab experiments for framework validation.

5.2 Methodology.

The formation of single tracks was simulated by the sequential deposition of four microdroplets on a flat, rigid, and non-porous substrate using the lattice Boltzmann method discussed in Section 4.1.1.2. LB model parameters, material properties, droplet characteristics and boundary conditions used in the simulations were described in Section 4.1.1.4. The matrix of experiments defined to investigate the effect of critical printing parameters and wettability together with details about the surrogate model strategy including how to calculate the response surface equations, analyse the statistical validity of the model and build the surface morphology were explained in Section 4.4.2. Optimal printing parameters were found employing a multi-objective genetic algorithm approach with a non-traditional fitness function as discussed in Section 4.5.1.2. Finally, the surrogate model approach was validated running single

track experiments defined in Section 3.2.12 and testing that optimal printing parameters produce a stable single track.

5.3 Results and discussion.

The results obtained from the surrogate model-based optimisation of inkjet-printed single tracks are presented in this section. First, the analysis of the results from building the surrogate model using high-fidelity multiphase flow simulations are discussed in Section 5.3.1. Followed by the analysis of the results obtained when the surrogate model was built using actual measurements of single tracks created in the Dimatix printer, included in Section 5.3.2. Finally, optimal printing parameters were compared to validate the surrogate model-based optimisation approach in Section 5.3.3.

5.3.1 Surrogate model-based optimisation using lattice Boltzmann multiphase flow simulations.

5.3.1.1 Lattice Boltzmann multiphase flow simulation results.

All results are presented using dimensionless time, bead width and bead thickness calculated by the following expressions,

$$t^* = \frac{u_0}{D_0} t, \quad BW^* = \frac{BW}{D_0}, \quad BT^* = \frac{BT}{D_0} \quad (51)$$

Furthermore, the extent of overlap ratio (O) is calculated using (Stringer & Derby, 2010) droplet equilibrium diameter D_{eqm} as follows,

$$D_{eqm} = \sqrt[3]{\frac{8D_0^3}{\tan \frac{\theta_{eqm}}{2} \left[3 + \left(\tan \frac{\theta_{eqm}}{2} \right)^2 \right]}} \quad (52)$$

$$O = 1 - \frac{ds}{D_{eqm}} \quad (53)$$

The overlap ratio is included in all results along with drop spacing and resolution for the completeness of the study and future reference.

High fidelity model results of the evolution of four droplets deposited on a flat substrate are presented in Figure 5-1. Three model simulations were run with horizontal droplet spacing at $ds=30,50,70$ corresponding to $20\ \mu\text{m}$, $33\ \mu\text{m}$ and $47\ \mu\text{m}$, respectively with fixed vertical droplet spacing and advancing contact angle at 20 and 60° , respectively. At $ds=30$ and 50 , there was clearly an overlap between successive drops, which creates an immediate bridge between droplets. Then, a rapid increase in bead width and thickness at the connecting neck occurs due to the Laplace pressure of newly deposited droplet driving flow into the bead main body of fluid. The overflow effect results in a contact line expansion at neck, the drop surface above the initial contact point changes from concave to convex. A single bulge is formed when $ds=30$ and multiple bulges are formed when $ds=50$ due to the exceedance of the prescribed advancing contact angle. For the larger horizontal drop spacing of $ds=70$, the droplets impact separately on the substrate and the edges then spread until contacting the surface of the previously deposited drops. As droplets do not collide immediately after impact, a smaller width and thickness at the neck location is observed due to the lower inertial forces. Surface tension forces cannot overcome the surface energy imposed by contact angle hysteresis and consequently a scalloped shape emerged. Equilibrium is reached after $t^*=5.51$ with a convergence towards a spherical cap with pinning of the contact line far away from neck locations defining the final footprint of the printed line.

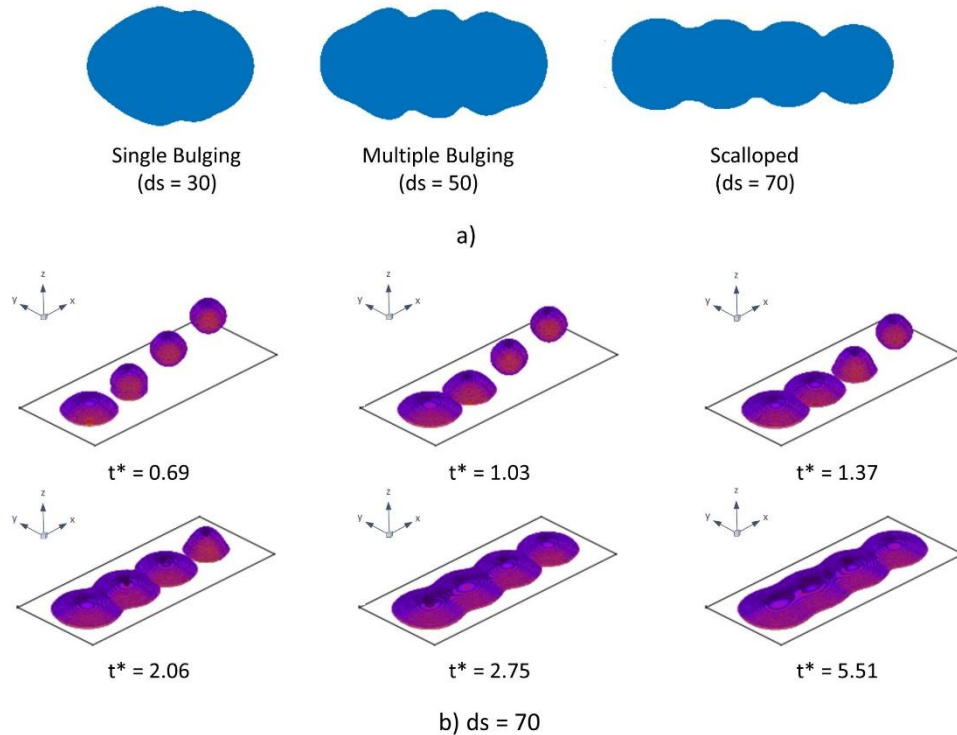


Figure 5-1 Four sequential drops deposited at different drop spacings ($Re=16.52$, $We= 32.2$, $dh=20$ and $\theta_a=60^\circ$): a) 2D Footprints, b) 3D Time evolution at $ds=70$

The dynamics of the impact, spreading and coalescence process of four successive droplets deposited for line formation at different horizontal drop spacings are quantified in Figure 5-2. Dimensionless bead width (BW^*) and thickness (BT^*) are plotted against dimensionless time (t^*). For comparison purposes, results from a single drop impingement are included. It is observed in the kinematic phase that the dimensionless bead width increases following Tanner's power law and in agreement with previous experimental and numerical studies (Jung et al., 2013). When horizontal drop spacing is set to $ds=30$ corresponding to $20 \mu\text{m}$, the contact line spreads beyond the equilibrium value, which confirms bulge formation due to the overflow effect discussed earlier. Temporal evolution of bead width and thickness behave in a similar manner to that seen with a single droplet of larger volume, showing one maximum spreading point without connecting ridges. When horizontal drop spacing is set to $ds=70$, corresponding to $47 \mu\text{m}$, the bead width at neck locations is smaller than the equilibrium value, due to slower neck expansion, which yields a scalloped morphology. At both drop spacings, the behaviour of BT^* shows almost no oscillation,

which can be attributed to a damping effect created by the interaction with neighbouring droplets.

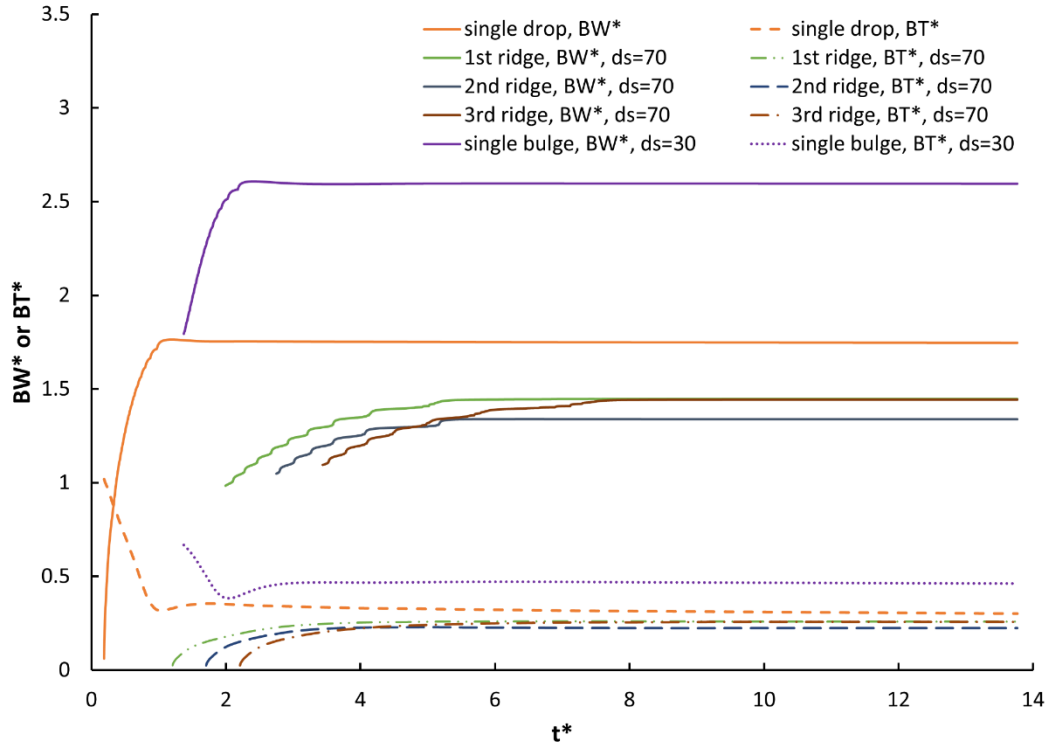


Figure 5-2 Evolution of printed line dimensionless bead width and dimensionless thickness.

Finally, the results of the high-fidelity simulation were compared against the analytical model described by Equation (31). The analytical model based on volume conservation and a spherical cap shape of the single track, predicted the average width as function of the drop spacing, droplet volume and advancing contact angle. As shown in Figure 5-3, good agreement between the predicted average width of the multiphase flow simulation and the analytical model was observed, demonstrating the strong influence of drop spacing and advancing contact angle in the morphology of single tracks. The simulation overpredicted the average width from theoretical model due to transient effects caused by the different drop spacing in the vertical direction (equivalent to the printing frequency) used in the study. The effect of droplet volume size was not considered in high-fidelity simulations and additional experiments are required to quantitatively assess its impact.

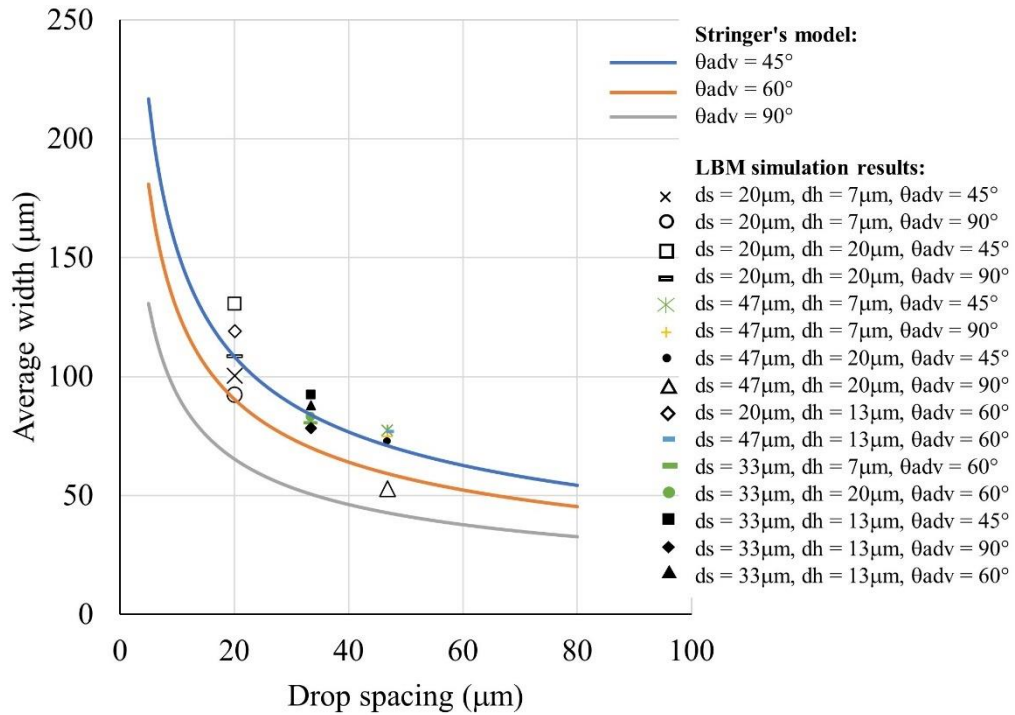


Figure 5-3 Average width prediction: lattice Boltzmann model vs theoretical model (Stringer & Derby, 2010)

5.3.1.2 Surrogate modelling results.

One of the key advantages of using the response surface methodology is the ability to quantify a factor's main effects, combined effects, and non-linear behaviour. Figure 5-4 shows the effect of individual factors on the bead width measured at droplet centres. Pareto charts shows statistically significant effects (p-value less than 0.05) in orange bars and non-significant effects in blue. Contour plots based on the response surface illustrate the combined effect of the drop spacing and advancing contact angle on bead width and consistent results are obtained at measured locations with the vertical drop spacing fixed. It was found that horizontal drop spacing is the most significant factor driving bead width stability and size. The overall trend indicates that as drop spacing increases, bead width size decreases, but not in a linear relationship since curvature effects are statistically significant. Interestingly, the second most significant effect results from the interaction between horizontal drop spacing and vertical drop spacing, which confirms that transversal speed as derived from droplet frequency of impact and the distance between droplets has a direct impact on bead width size and stability. The third most significant effect comes from the advancing contact angle, which has an inversely proportional relationship with respect to bead

width in a quasi-linear fashion since the quadratic term is not significant. As advancing contact angle increases, printed line width decreases. Furthermore, the effect of vertical drop spacing on bead width is not constant for all drop measurement locations. For the first two droplets, as vertical drop spacing increases, bead width decreases and for the last droplets the relationship inverts suggesting different coalescing modes are present due to transient effects between droplets. From the response surface plots, it is found that as drop spacing decreases and advancing contact angle decreases, the observed bead width reaches its maximum value at all locations. Since the maximum and minimum measured bead width is different at all locations, we confirm that the printed line shows a non-uniform pattern.

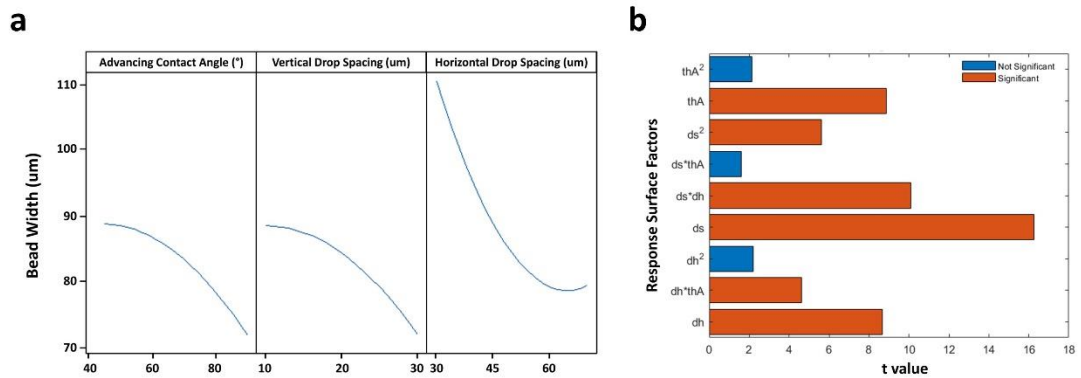


Figure 5-4 Bead width measured at first droplet centre: a. Main effects; b. Statistically significant effects.

After eliminating the statistically non-significant effects from the bead width transfer function, a more detailed study of the predictive capability of the model was performed. An Anderson-Darling test was run at each measured location to verify the residuals are normally distributed. Results show residuals are normally distributed with p-values of 0.146, 0.833, 0.6, 0.453, respectively, hence the selected function terms are adequate for error prediction. The percentage error of the predictive model versus the predicted bead width is illustrated in Figure 5-5. It is observed that % error is randomly distributed and therefore the prediction error values are not a function of the fitted bead width. To complement the model goodness of fit evaluation, Table 5-1 lists the correlation coefficients (predicted and adjusted), mean square error, maximum error percentage, and bead width transfer functions. Prediction models have a correlation coefficient greater than 99% with adjusted values within 5% providing

good confidence that functions are modelled with the right terms. Consequently, the root mean square error is at least one order of magnitude less than the bead width mean, proving the variation unexplained by factor inputs is negligible. Most importantly, the maximum % error of the prediction is less than 5%, proving model has a good predictive accuracy.

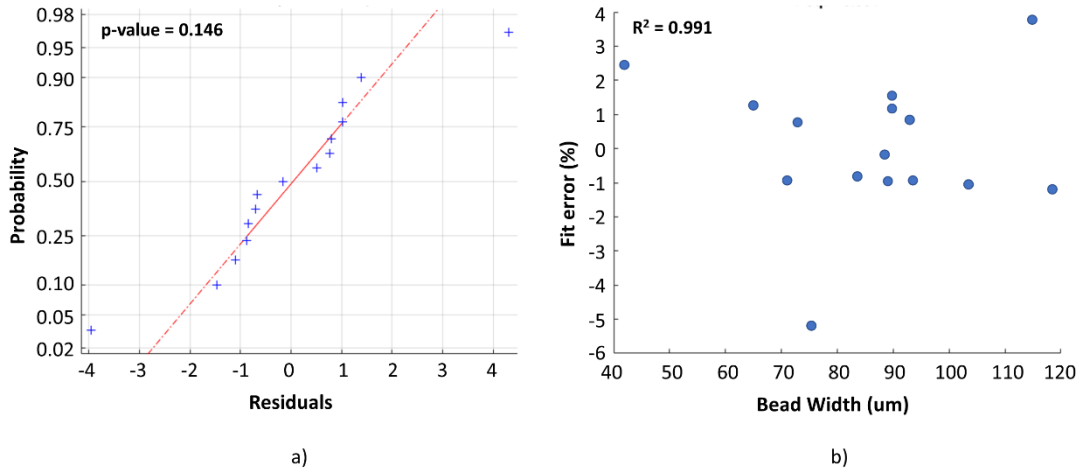


Figure 5-5 Bead width measured at first droplet centre: a) Residuals Normality, b) Percentage of error vs fit.

Table 5-1 Bead width transfer functions and measures of fit

Location	W1	W2	W3	W4
R ²	99.1%	99.5%	99.7%	99.2%
Adj-R ²	97.6%	98.5%	99.2%	97.7%
RMSE	1.7	1.8	1.5	1.6
Max Error %	5%	4%	3%	3%
Transfer Functions				
W1 = 107.7+0.946*0a+4.982*dh-2.589*ds-0.0411*dh*dh+0.02636*ds*ds-0.02185*0a*dh-0.05379*dh*ds				
W2 = 159.9+1.241*0a+5.872*dh-4.917*ds-0.0345*dh*dh+0.04781*ds*ds-0.01896*0a*dh-0.06810*dh*ds				
W3 = 164.0+1.037*0a+7.393*dh-5.828*ds-0.0646*dh*dh+0.05647*ds*ds-0.01551*0a*dh-0.06254*dh*ds				
W4 = 115.6+0.976*0a+6.137*dh-4.001*ds-0.0640*dh*dh+0.03650*ds*ds-0.01329*0a*dh-0.03388*dh*ds				

The same statistical approach used to derive the predictive model for the bead width was also applied to estimate the bead thickness. Measurements of the bead thickness were taken at droplet centre locations. For the bead thickness prediction, curvature does not play a statistically significant role for any factor. The main effect impacting bead thickness is the vertical drop spacing which is related to the physical printing frequency. As the vertical drop spacing is increased, the bead thickness decreases in agreement with experimental work observed within non-solvent inks. As more time

for spreading of the droplets is allowed with lower printing frequencies, droplet thickness is reduced accordingly. It is also found that interactions of horizontal drop spacing and advancing contact angle with vertical drop spacing are statistically more significant than main effects. This is an important contribution of the analysis that could build upon the volume conservation assumptions from theoretical models used to compute bead thickness. Transfer functions predicting bead thickness are built using statistically significant terms and main effects. Prediction residuals are normally distributed for all measured locations indicating the absence of special cause variation induced by the prediction model. Furthermore, a plot of the predicted error against the fitted bead thickness, shows a random pattern which indicates the residual values do not depend on whether the regression model is predicting low, medium, or high values. Additional fitness measures are included in Table 5-2 along with the bead thickness transfer functions. Correlation coefficients for droplet locations 2 and 3 show poorer correlation than locations 1 and 4 due to the presence of one outlier. If outliers are excluded from the transfer function calculation, correlation coefficients increase to 89% and 94%, respectively. It was decided to leave all points for transfer function calculation to capture all potential transient effects coming from the physics based high fidelity simulation. Since adjusted correlation coefficients are within 5% of predicted, enough degrees of freedom are available to compute with confidence transfer function coefficients. Root mean square errors are approximately 10% the value of the resulting average bead thickness (12.8 μm) and the maximum residual is 1.5 μm , proving sufficient accuracy to compute bead thickness for this specific application.

Table 5-2 Bead thickness transfer functions and measures of fit.

Location	W1	W2	W3	W4
R ²	94.9%	85.0%	90.3%	99.8%
Adj-R ²	90.1%	81.8%	85.6%	99.4%
RMSE	1.6	1.5	1.4	0.5
Max Residual	1.1 μm	1.5 μm	1.5 μm	0.4 μm
Transfer Functions				
H1 = 49.90-1.321* θ a-1.73*dh+0.429*ds+0.00805* θ a*dh+0.01174*dh*ds				
H2 = 56.30-0.497* θ a-1.427*dh-0.874*ds+0.00922* θ a*dh+0.01153*dh*ds				
H3 = 39.50+0.0770* θ a-1.9170*dh-0.5180*ds+0.03020*dh*dh				
H4 = 26.72+0.0621* θ a-1.7568*dh-0.0276*ds+0.03347*dh*dh				

Measures of fit evaluated for the prediction of bead width and thickness only describe transfer function quality at the regressed data points. To determine the accuracy of the

prediction model, additional validation runs were performed using five random points within the design space. The maximum percent error fit stayed within 5% for bead width prediction and the maximum residual observed within 1.5 μm for the bead thickness estimation. These results confirmed that the statistical predictive model provides adequate, reliable, and consistent estimations of line morphology features within the proposed design space bounds.

Using statistical analysis to derive transfer functions for bead width and thickness at drop centre locations, the proposed method is to replicate this approach to a set of points along and across the printed track. A cloud of points defining the line morphology was generated along with its corresponding transfer function to predict bead width and thickness based on design factors. After completing simulation tests, the results were cleaned and filtered to measure widths and heights at 19 different locations along the printed line length and 7 locations across the width. Then, a set of regression equations were created at each location to predict the printed track surface. To evaluate the goodness of fit of the overall surrogate model, the process was automated using MATLAB to show descriptive statistics, correlation factors, residuals patterns and main effects at each location. The graphical interface shown in Figure 5-6 allows the user to see all locations together using a “traffic-light” grade (green, yellow, red nomenclature) based on the regression statistical results. Based on the goodness of fit results, the user can identify locations on the printed shape that may indicate a high risk of error compared to the high-fidelity LBM simulation prediction. For the pilot run, corresponding to a printed line shape, 90% of the equations used to predict the 3D shape had correlation coefficients larger than 95%, with prediction errors less than 7%; equations graded as yellow were 8% which means correlation coefficients were between 85%-95% with prediction errors less than 15% and only 2% of the equations showed a poor correlation coefficient (less than 80%) with predicted errors greater than 20% (only 3 equations out of 152).

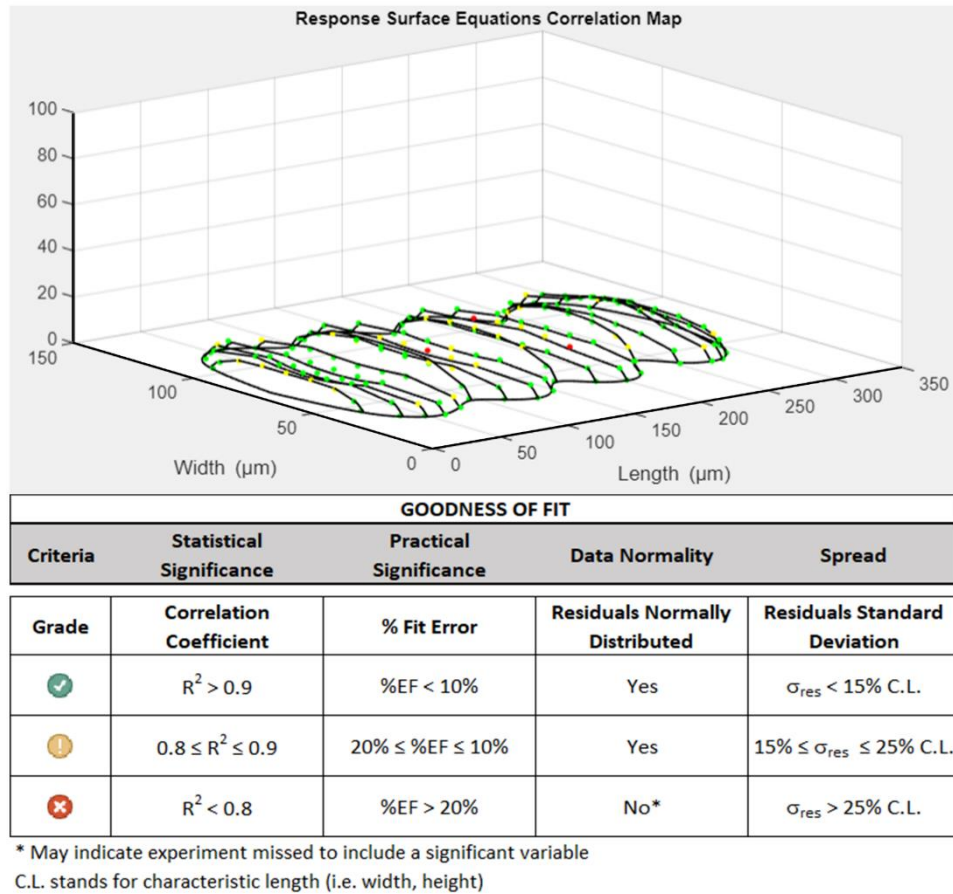


Figure 5-6 Printed track prediction model goodness of fit results.

Statistical measures of fit for the overall model satisfied quality requirements defined in Figure 5-6 and the model is thus deemed acceptable. Finally, a validation test was simulated with our high-fidelity lattice Boltzmann model using a set of parameters within the predefined design variable bounds. The purpose of the test was to ensure the predictive model captures accurately the transient behaviour observed when depositing four drops sequentially to form a printed track on a flat substrate. Figure 5-7 shows a comparison of the results obtained from the response surface model and the LBM simulation, confirming good prediction accuracy and reliability.

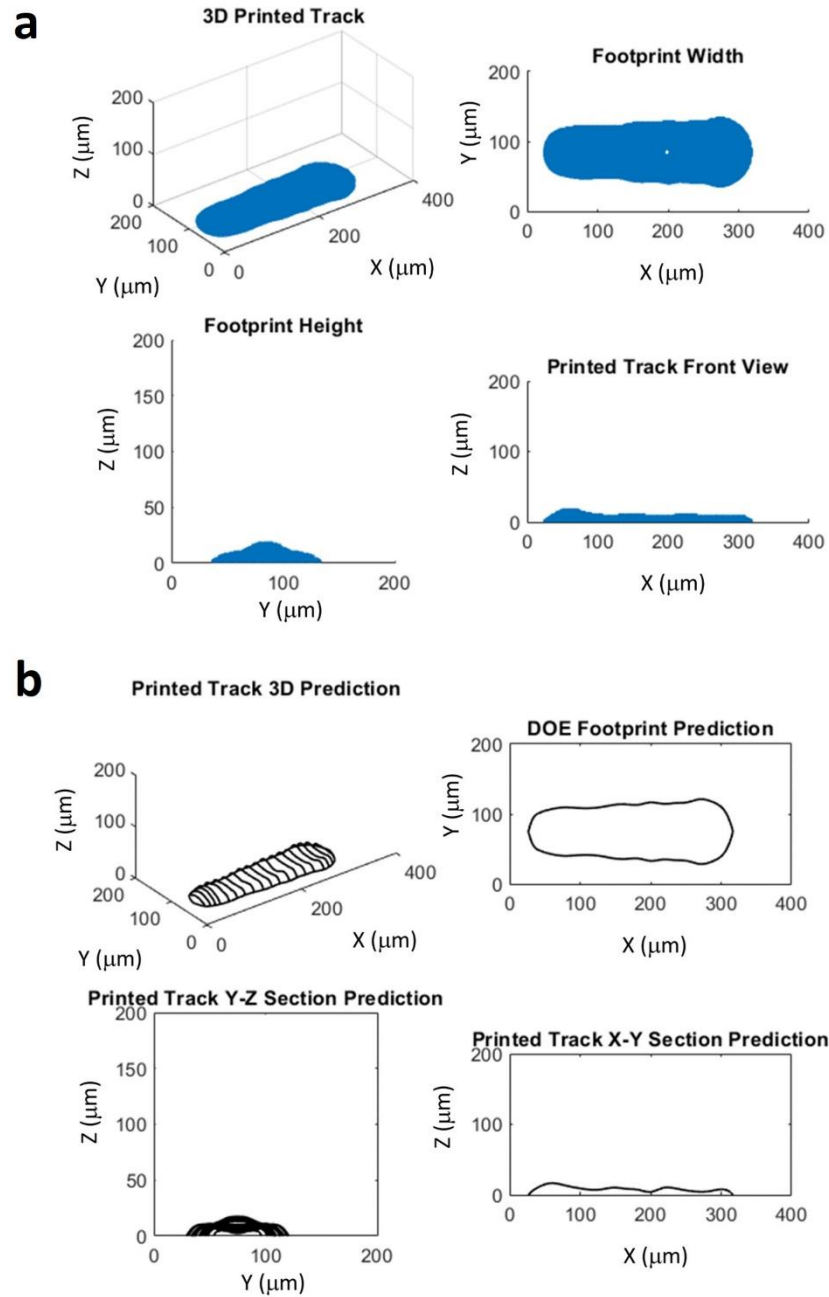


Figure 5-7 Results comparison between a. High-fidelity lattice Boltzmann; b. Surrogate model.

5.3.1.3 Optimisation results.

A multi-objective genetic algorithm was employed in MATLAB to search for optimal settings of horizontal and vertical drop spacing and advancing contact angle. The objective function was calculated from the normalized central geometric moments of the predicted and target footprints. Figure 5-8 shows the objective function value for 15 simulation runs defined by the central composite design of experiments as a

function of overlap ratio. The figure also incorporates the line morphology observed in each case. It was found that using the error norm of the normalized central geometric moments as a fitness measure for optimisation yields adequate and consistent results. Furthermore, clusters of points clearly identified the line morphology regimes as a function of overlap ratio and a trend towards a uniform and stable line is observed as the objective function is minimized. Careful analysis of the objective function based on geometric moments is needed, since the accuracy of the method is predicated on the order of moments used in the calculation. In this case, up to 4th order moments were included. Additional objective functions were implemented for Pareto front construction based on the least squares error of predicted bead thickness against target, least squares error of predicted width against target and a weighted objective function combining any of the three objectives previously defined. Nonlinear constraints were defined based on the mean and standard deviation of the line width and thickness to be less than 5 and 2 microns, respectively. Design variable bounds were also incorporated in the optimisation setup to explore space within the region of interest and physical parameters feasibility was ensured.

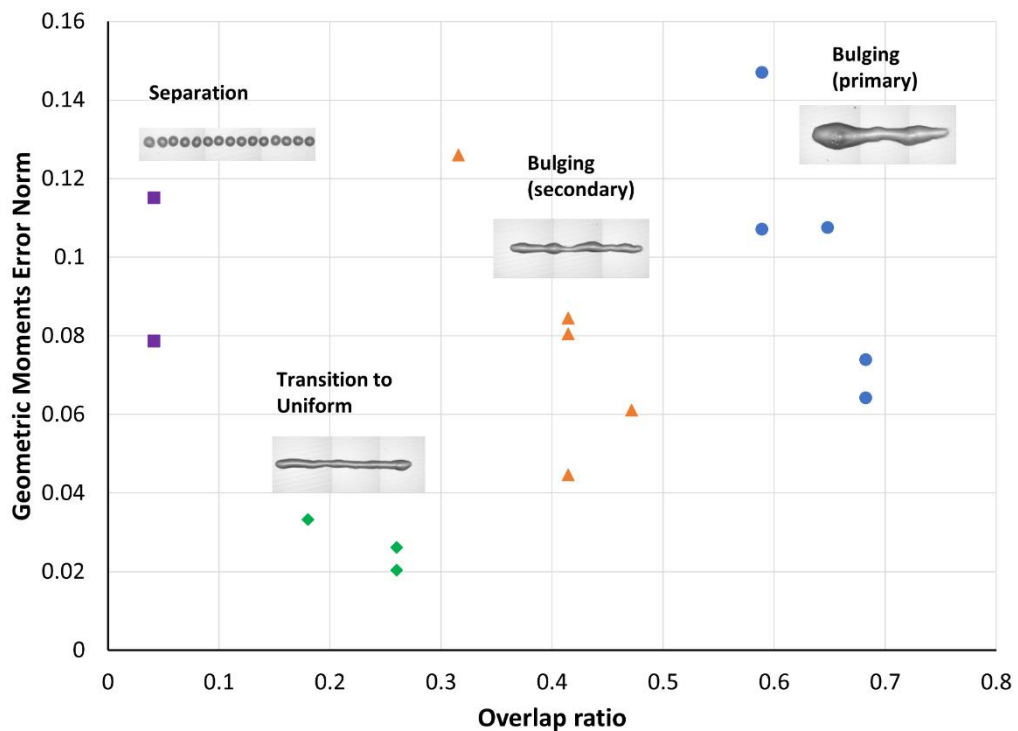


Figure 5-8 Simulation results mapped onto line formation regimes and the normalized central geometric moments error function.

The multi-objective genetic algorithm was setup using a population size of 100 individuals, with a maximum number of generations fixed at 600, and convergence criteria for objective function and constraints set as $1e-6$ and $1e-4$, respectively. No scaling was required on genes since values were of the same order of magnitude. The crossover fraction was fixed at 80% and the mutation rate set to adapt with respect to the last successful or unsuccessful generation. The Pareto front was constructed keeping 35% of individuals from the first front and then selecting fittest individuals from higher fronts.

Results from the optimisation are presented on Figure 5-9a. The Pareto front was constructed using in the x-axis the objective values based on normalized central geometric moments which corresponds to width dimensional accuracy and in the y-axis the objective values based on least squares error of bead thickness which corresponds to thickness dimensional accuracy. Each pink dot represents a set of parameters evaluated by the search algorithm. The Pareto front is built in less than 3 minutes evaluating more than 5000 combinations seeking the global minimum.

Based on Pareto front results, the set of parameters that provide the best trade-off between line thickness and width stability for our dielectric line are horizontal drop spacing = 56, vertical drop spacing = 12 and advancing contact angle = 46° , corresponding to $37.4 \mu\text{m}$ (equivalent to an overlap ratio of 25.2%), $8.0 \mu\text{m}$ (equivalent to an application with high printing frequency) and 46° , respectively. The set of design parameters which provide the minimum edge waviness for our dielectric line are horizontal drop spacing = 67, vertical drop spacing = 12.2 and advancing contact angle = 45.8° , corresponding to $44.8 \mu\text{m}$ (equivalent to an overlap ratio of 30.2%), $8.1 \mu\text{m}$ (equivalent to an application with high printing frequency) and 45.8° , respectively. Although, the observed waviness along the edge matches the target pattern better than the best trade-off parameters, the printed track shows larger differences in the thickness at several locations which could impact electrical performance and accuracy of next printed layers. The set of design parameters which provide the most uniform thickness for the dielectric track are horizontal drop spacing = 36.1, vertical drop spacing = 10.2 and advancing contact angle = 45° , corresponding to $24.2 \mu\text{m}$ (equivalent to an overlap ratio of 51.6%), $7 \mu\text{m}$ (equivalent to an application with high printing frequency) and 45° , respectively. Unfortunately, this set of parameters yield a printed track converging to a bulging instability regime due to the large overlap

between droplets. A validation run was performed using the lattice Boltzmann high fidelity model to assess both thickness and width dimensional accuracy of the printed track, confirming that the optimal set of parameters yields a stable line morphology, illustrated in Figure 5-9b.

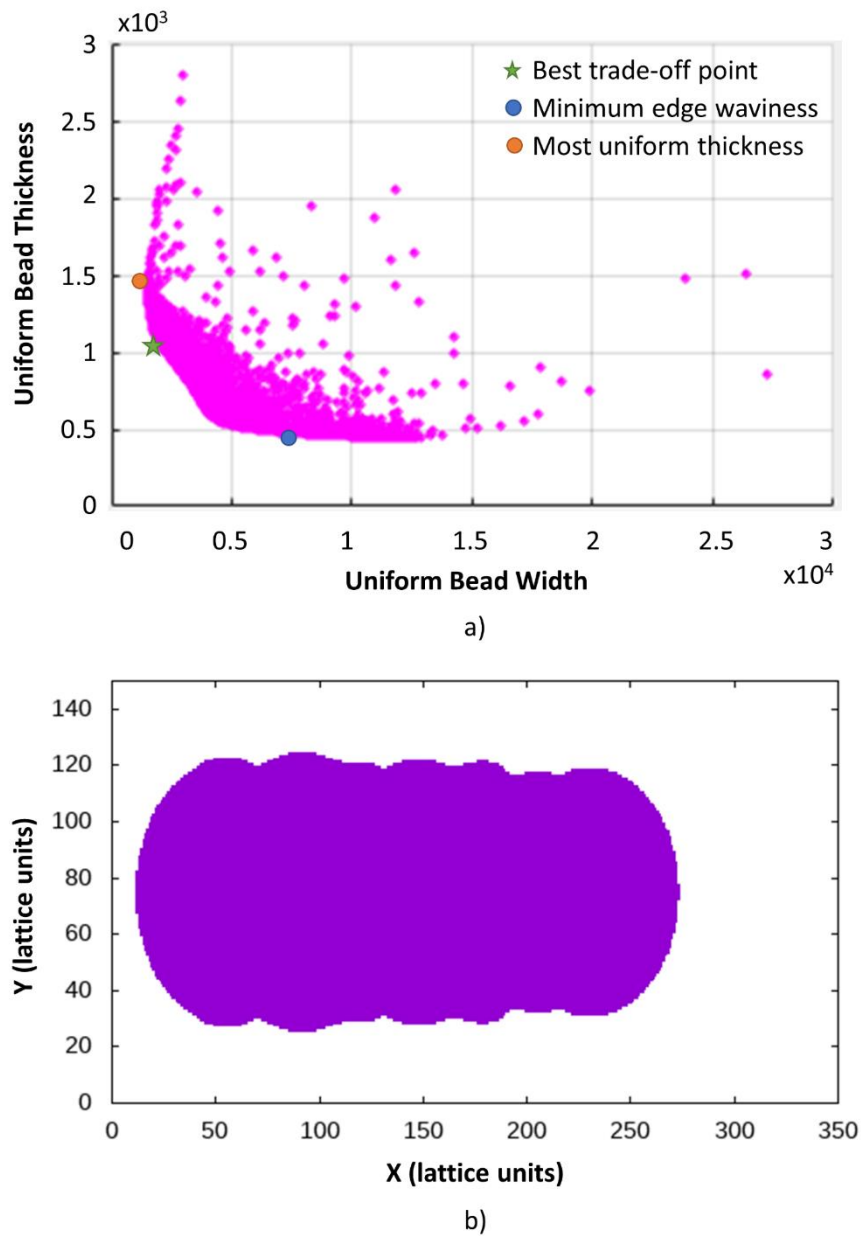


Figure 5-9 a) Pareto front and b) Validation run with optimal factor settings.

5.3.2 Surrogate model-based optimisation using experiments performed in Dimatix printer.

5.3.2.1 Experiments results.

A single pixel line of 1 mm in length was printed on glass following the procedure described in Section 3.2.5. A total of 20 experiments were performed using the matrix of parameters defined in Table 3-4. Printed lines images following the experimental run order from left to right, top to bottom are shown in Figure 5-10.

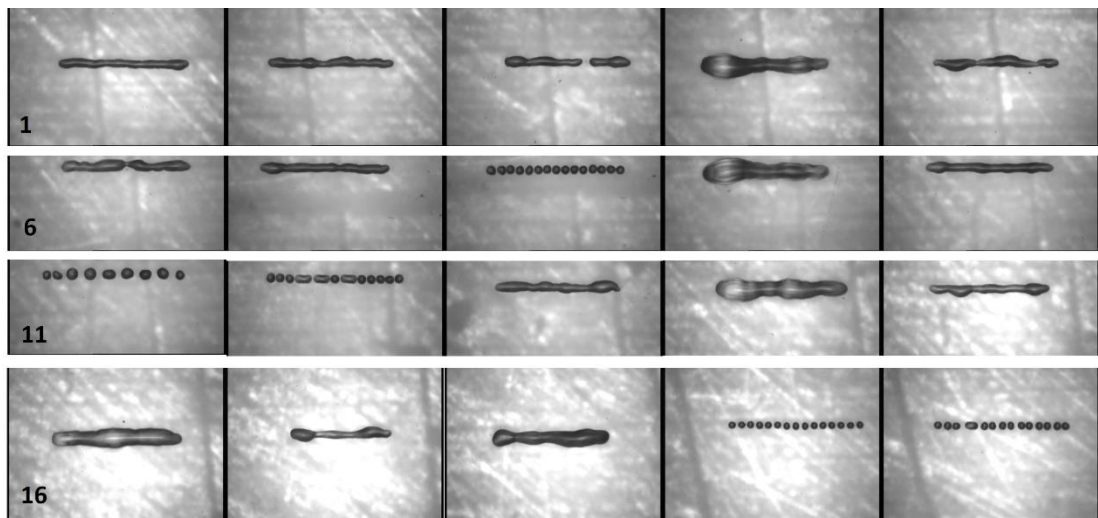


Figure 5-10 Images of printed lines $L = 1$ mm following response surface methodology.

Lines were measured using coherence scanning interferometry (CSI) to accurately define its surface morphology as discussed in Section 3.2.7. CSI data was employed to build a transfer function between critical printing parameters and the morphology of single tracks following the same surrogate modelling strategy used for the high-fidelity simulation results. Measurements were delivered as a point cloud file for each feature as illustrated in Figure 5-11 and were post-processed using the method described in Section 4.7.1. Mean, standard deviation and maximum values of width and thickness were then calculated as shown in Figure 5-12 using a discretization scheme with grid size $N = N_x = 50$ and $N_y = 9$. Table 5-3 lists the normalised central geometric moments (NCGM), waviness, and roughness factors calculated from the single-track dimensions to be used as fitness functions for optimisation purposes.

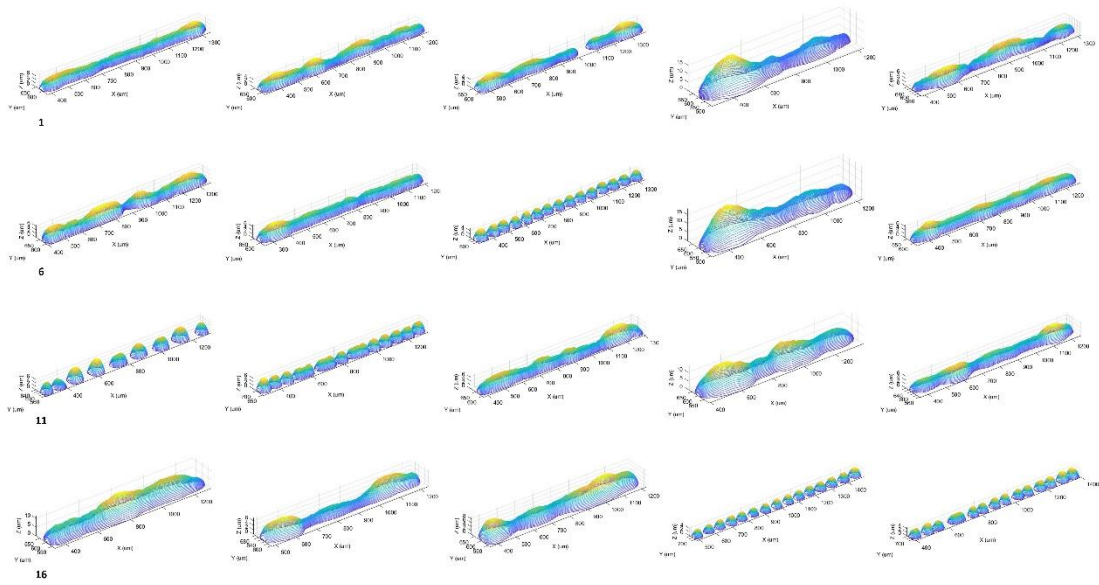


Figure 5-11 CSI measurements used to generate surrogate model

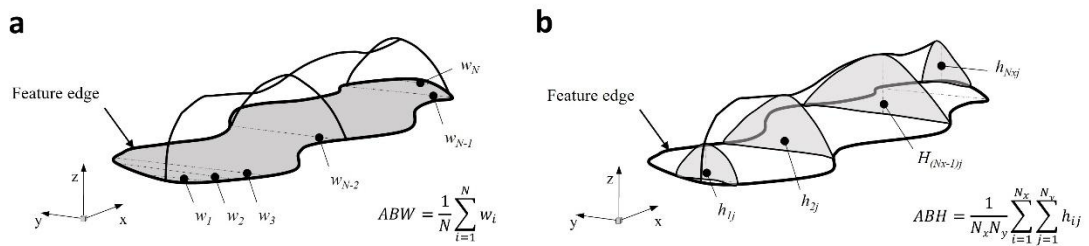


Figure 5-12 Average width and thickness calculation.

Table 5-3 Calculated fitness functions based on experimental results.

Run #	Drop spacing (μm)	Printing frequency (kHz)	Standoff Distance (mm)	Overlap (%)	NCGM fitness function	Waviness fitness function	Roughness fitness function
1	40	2.5	1	37.3	0.4184	0.1438	0.5512
2	40	2.5	1.5	37.3	0.1290	0.1760	0.5681
3	40	4	1	37.3	1.2913	0.3333	0.5955
4	10	1	0.5	84.3	2.1014	0.3095	0.7640
5	40	2.5	1	37.3	0.5214	0.2506	0.6169
6	40	2.5	1	37.3	0.5123	0.2060	0.5811
7	40	2.5	1	37.3	0.1216	0.1667	0.5633
8	70	2.5	1	-9.7	4.3665	0.4156	0.6712
9	10	1	1.5	84.3	2.2138	0.2614	0.7085
10	40	2.5	1	37.3	0.4614	0.1529	0.5514
11	70	4	1.5	-9.7	5.4151	0.7431	0.6685
12	70	1	0.5	-9.7	2.2088	0.2841	0.6268
13	40	2.5	1	37.3	0.4090	0.1967	0.5799
14	10	4	1.5	84.3	2.1193	0.2032	0.6181
15	40	2.5	0.5	37.3	0.3542	0.2070	0.5877
16	10	4	0.5	84.3	2.1002	0.1768	0.5882
17	40	1	1	37.3	0.9454	0.2707	0.6302
18	10	2.5	1	84.3	1.8330	0.1915	0.6029
19	70	1	1.5	-9.7	9.2372	0.5827	0.6771
20	70	4	0.5	-9.7	6.7176	0.5339	0.6593

5.3.2.2 *Surrogate modelling results.*

This section details the surrogate model adequacy and the analysis of the effect of printing parameters and its interactions in the surface morphology of single tracks. Figure 5-13a shows measured data of a single track generated with a drop spacing of 10 μm , printing frequency of 1 kHz and standoff distance of 0.5 mm. Figure 5-13b illustrates the morphology predicted by the surrogate model using the same printing parameters with a coarse discretisation scheme. It was found that the predicted morphology matches the real footprint to within 2 μm and both the location and magnitude of the maximum width and thickness were accurate to 1 μm . Real and predicted morphologies were unstable showing the formation of large bulges along the feature's surface and a shorter track length compared to target by 30 μm was found in both cases. Overall, excellent agreement between the measured and predicted features was achieved over the whole surface morphology with maximum absolute deviation less than 2 μm . To validate the surrogate model prediction throughout the design space, a comparison of all the measured data was plotted against its corresponding prediction values. Figure 5-13c-f illustrate the models for average width, maximum width, average thickness, and maximum thickness predictions versus measured values, respectively. For the average and maximum width models, there is an excellent agreement between the predictions and the experiments, with about 95% of data points within 5% error, with a single point out of the 10% error threshold (around 12% error at 100 μm). For the average and maximum thickness models, there is a good agreement between predictions and experiments, with about 90% of data points within the 10% error, observing the lowest for one point at the lower value of thickness (25% error at a thickness of 4 μm). Particularly, the model to predict the maximum thickness shows 30% of data points out of the 10% error threshold, which is likely to be caused by the material redistribution influenced by the interaction of viscous and capillary forces and non-uniform UV light exposure, which were not considered in the prediction model. Nevertheless, using the prediction models to build the surface morphology of single tracks as function of printing parameters provided an accurate method to determine instabilities such as material overflow (bulges) or disjointed (break-ups) tracks as well

as precise predictions to within 2 μm and therefore, were considered adequate for this investigation.

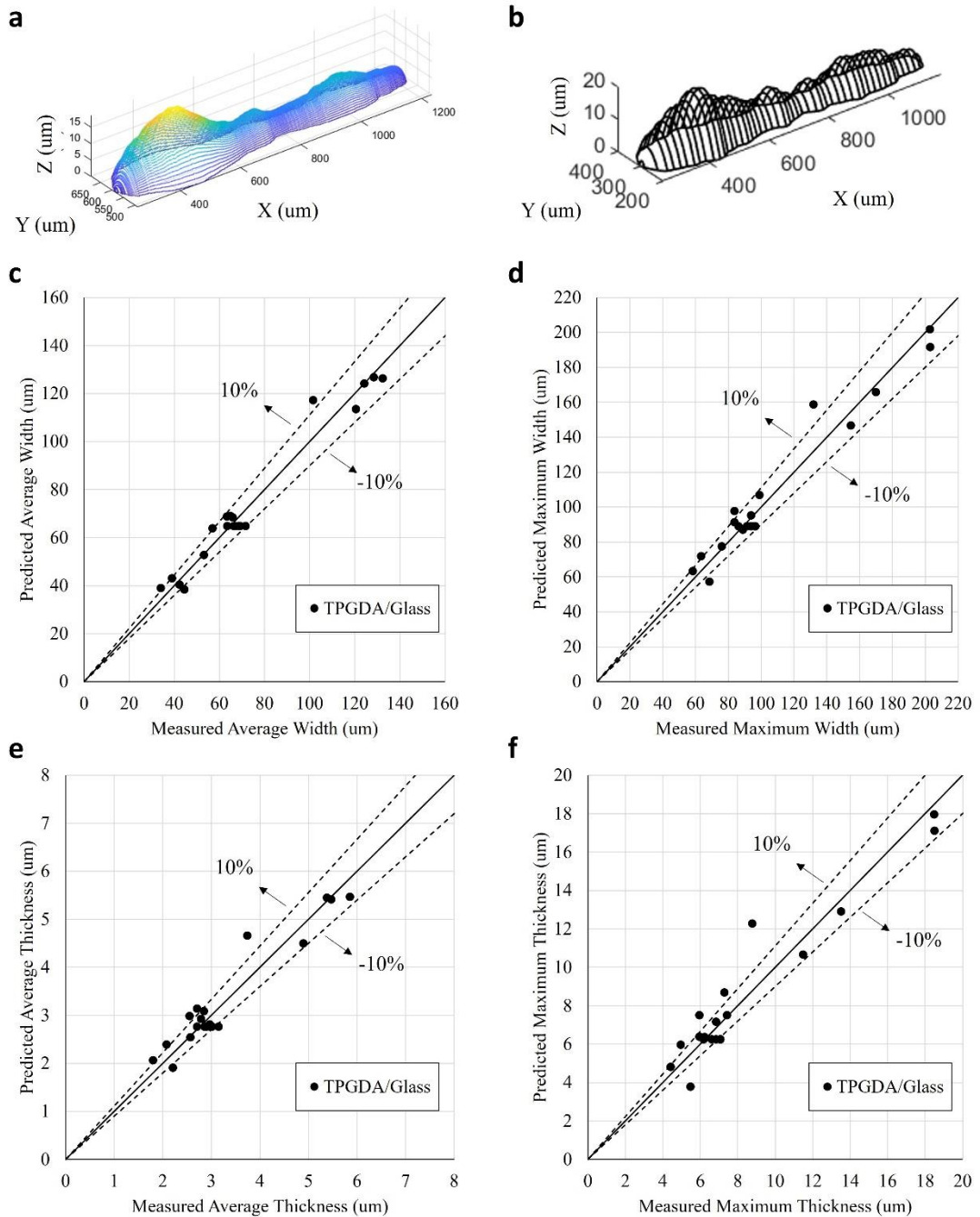


Figure 5-13 Validation of the surface morphology prediction model for single tracks by comparing samples printed with printing parameters defined in matrix of experiments. a) Measured surface morphology of single track; b) predicted surface morphology built using surrogate model. c)-f) deviation assessment of the predictive models for the average width, maximum width, average thickness, and maximum thickness, respectively.

The relationships among the width and thickness as function of the printing parameters studied are depicted in Figure 5-14a-b and Figure 5-15a-b, respectively. The coefficient of determination for the average and maximum width, average and maximum thickness are 0.97, 0.95, 0.92 and 0.92, respectively. The analysis of variance confirmed that prediction models are statistically significant using a significance level of 5%. A residual analysis was done to test for defects such as non-normality, non-independent and non-constant variance. The models were found to be free of all these defects. For the average width prediction, the drop spacing and the square of the drop spacing were found to be the only factors statistically significant, which is consistent to the models derived by other researchers (Stringer & Derby, 2010)(Kang et al., 2010). Eliminating non-significant factors from the model improves the correlation coefficient of determination but increased the error between predicted and measured values. Therefore, no term was eliminated from regression model. For the maximum width prediction, it was found that drop spacing, drop spacing squared and the interaction between drop spacing and printing frequency is statistically significant which indicates the critical role of the printing traverse velocity in the control of the material overflow on single tracks.

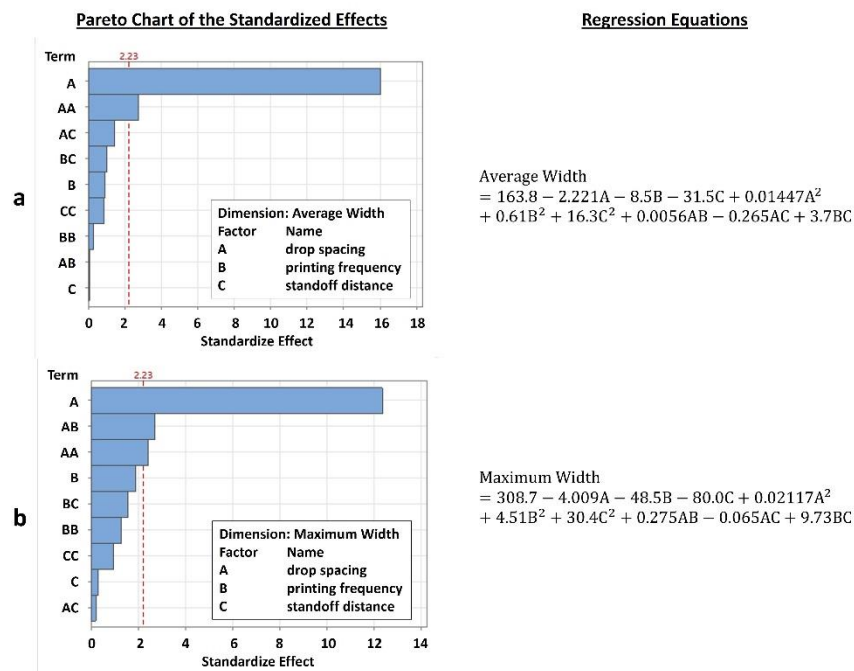


Figure 5-14 Statistical analysis of predictive model. a) Average width; b) Maximum width.

For the average and maximum thickness prediction models, it was found that drop spacing is the most important factor driving the regression behaviour. Interestingly, for the case of the maximum thickness, the interaction effect between drop spacing and printing frequency and the printing frequency main effect turned out to be statistically significant which indicates that printing frequency plays a critical role defining uniform tracks. Although, regression models could be simplified to only consider significant factors, eliminating factors showed a detrimental effect on the prediction model accuracy. Therefore, no term was eliminated from the thickness regression models. Finally, the assumption to develop the experiment using a central composite design to capture parameter curvature effects was key to find accurate relationships between printing parameters and surface morphology characteristics.

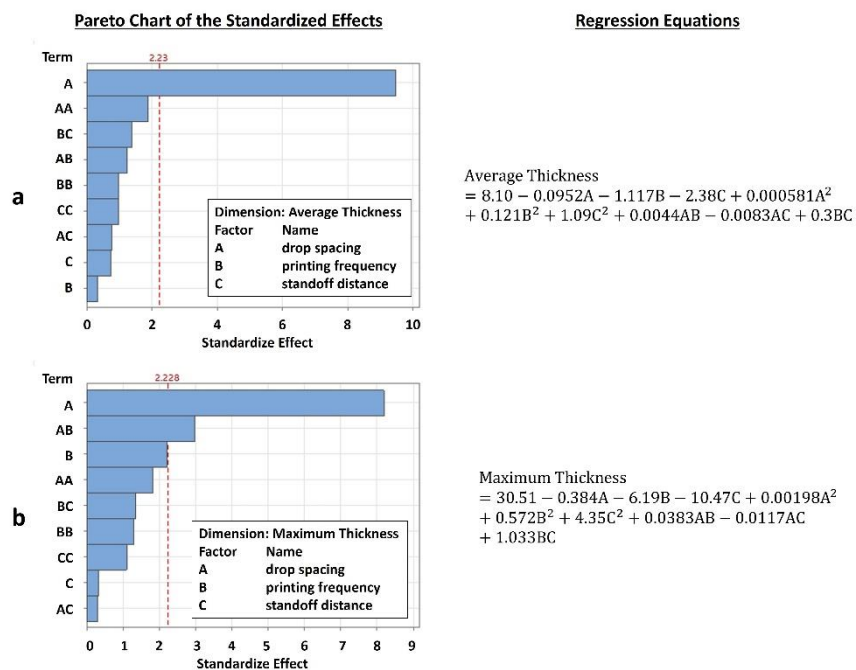


Figure 5-15 Statistical analysis of predictive model. a) Average thickness; b) Maximum thickness.

Summarizing, the prediction models provide a fast and accurate way to characterise the surface morphology of single tracks. The most important factor driving printed feature's stability is the drop spacing. As drop spacing increases, the width and thickness decrease in a non-linear manner. Although, printed frequency and standoff distance and its interactions have a minor non-linear effect on average track

dimensions, they play a key role characterising accurately the tracks' material overflow. Setting the lowest frequency with the lowest drop spacing and the highest standoff distance forms unstable tracks due to the presence of bulges. Given the complex non-linear behaviour of the morphology prediction models, a parameter optimisation was performed to find the combination of printing parameters that produce the most stable track and results are presented in next section.

5.3.2.3 *Optimisation results.*

In this section the results of the parameter optimisation using the surrogate model constructed from experiments are presented. Figure 5-16 illustrates the fitness functions used to find the most stable track as function of the printing parameters and a comparison between measured and predicted values. Three fitness functions were calculated in this investigation: the error norm of the normalized central geometric moments between the predicted and target footprints, the waviness factor defined as the ratio of the standard deviation of the footprint width and the average width, and the roughness factor defined as the ratio of the standard deviation of the feature's thickness and the average thickness. The first two are used to minimise edge waviness and the third to minimise thickness roughness. There is an excellent agreement between the means of predicted values and experiments, showing a quadratic relationship between fitness functions and printing parameters. An independent evaluation of the effect of each printing parameter on the NCGM fitness function indicates that a drop spacing of approximately 34 μm (approximate droplet overlap of 48%) with a printing frequency of 2.5 kHz and a standoff distance of 1 mm would minimise the error between the predicted and target footprints. Furthermore, the morphology edge waviness is minimised when the drop spacing, printing frequency and standoff distance are set to 31 μm (equivalent to 52% droplet overlap), 2.4 kHz and 0.85 mm, respectively. The morphology surface roughness is minimised when the drop spacing, printing frequency and standoff distance are set to 40 μm , 2.8 kHz and 1 mm, respectively.

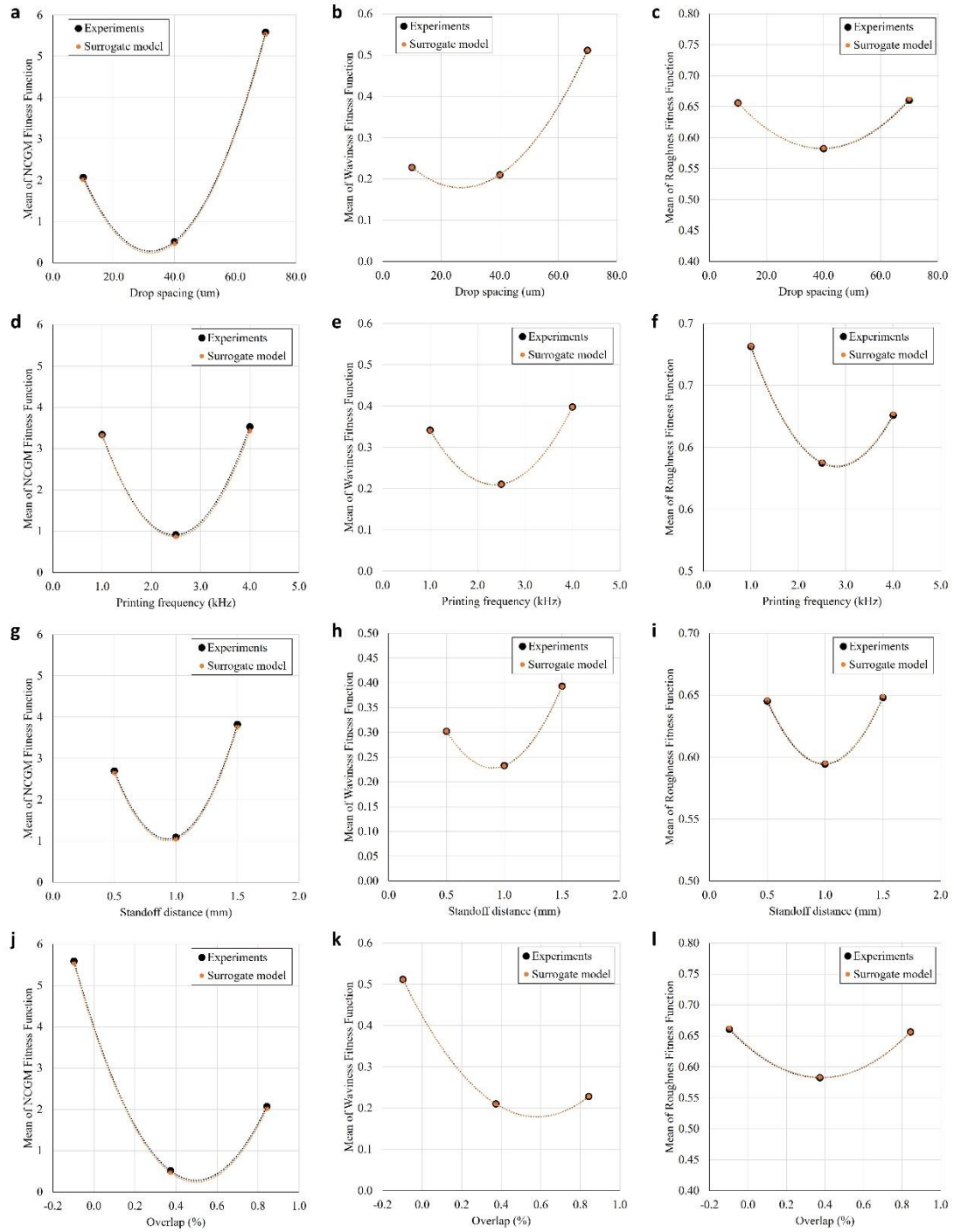


Figure 5-16 Measured vs predicted values of the fitness functions used to produce the most stable single track as function of the printing parameters. a)-c) effect of drop spacing; d)-f) effect of printing frequency; g)-i) effect of standoff distance and j)-l) effect of drop overlap on NCGM, waviness and roughness functions, respectively.

Measured data was analysed using MINITAB to build the prediction models for each fitness function. A gradient-based optimisation was performed to minimise predicted fitness functions and find optimal printing parameters. Starting point for the local optimiser was set to 40 μm, 2.5 kHz and 1 mm with a confidence level for all intervals

of 95% in all analyses. Table 5-4 lists the results obtained from the single objective optimisation. It was found that the optimal values for the printing parameters depend on the fitness function focus. NCGM error and waviness are equivalent since both are based on the feature's footprint shape whereas roughness is focused on the thickness uniformity. Drop spacing, printing frequency and its interaction are the most significant factors driving the minimum fitness functions values.

Table 5-4 Single objective optimisation using gradient based (local) approach.

Printing Parameters	NCGM error	Waviness	Roughness
Drop spacing (μm)	34.8	29.4	36.6
Printing frequency (kHz)	1.5	2.5	3.3
Standoff distance (mm)	0.5	0.5	0.5
Overlap (%)	45%	53%	42%

Results indicate that there is a trade-off between the morphology characteristics which define a stable track: width waviness and thickness roughness. Therefore, a multi-objective optimisation using a genetic algorithm (global optimisation approach) was performed to find the set of printing parameters that simultaneously minimise the waviness and roughness. Details about the optimisation procedure were described in Section 4.5.1. Figure 5-17a shows the pareto front obtained when simultaneous waviness and roughness objectives are minimised. The printing parameters that produce the most stable track representing the best trade-off point of the pareto front are drop spacing, printing frequency and standoff distance equal to 31.4 μm , 2.8 kHz and 0.5 mm, respectively. The predicted single-track morphology using the optimal printing parameters is illustrated in Figure 5-17b. The model predicts a footprint with minimal variation against width target and a very uniform thickness across the feature's length. The proposed surrogate model-based optimisation using experiments achieved fast and accurate results enabling the search of optimal printing parameters.

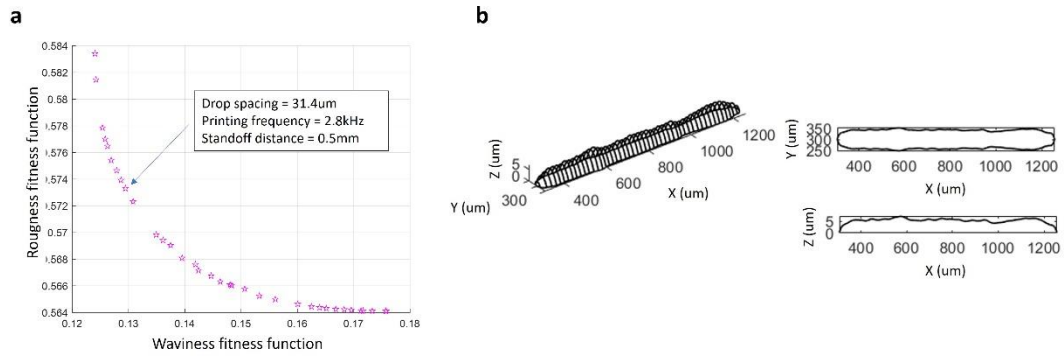


Figure 5-17 Surrogate model-based multi-objective optimisation results: a) Pareto front; b) Morphology prediction using optimal printing parameters.

A validation run was performed on the Dimatix printer to assess both thickness and width dimensional accuracy of the printed track, confirming that the optimal set of parameters yields a stable line morphology, illustrated in Figure 5-18



Figure 5-18 Validation run on Dimatix printer using optimal printing parameters.

5.3.3 Differences of the surrogate model-based optimisation results using high-fidelity simulations against experiments.

The surrogate modelling methodology proposed in section 4.4.1 has successfully constructed a transfer function relating surface morphology characteristics of single tracks with critical printing parameters using a sample of high-fidelity simulations and lab experiments. In both cases, fast and accurate predictions allowed the exploration of the printing parameters design space to find the set of optimal values that produce the most stable track. In this section, the differences in the morphology characteristics and optimal printing parameters between both assumptions are explained. Figure 5-19a-b shows the effect of droplet overlap (function of drop spacing, advancing contact angle and in-flight droplet volume) on the NCGM fitness function obtained from high-fidelity simulations and lab experiments. It was found that in both cases the droplet overlap is related to the fitness functions in a quadratic fashion. However, the

optimal value is significantly different between simulations and experiments, approximately 33% and 48%, respectively. This difference may be explained since high-fidelity simulation does not consider the variation in the droplet location and footprint size introduced by equipment tolerances and chemically inhomogeneous substrates. In addition, the simulations assume a very high printing frequency modelled by the variation in vertical drop spacing, which only provides a qualitative assessment of the influence of this factor on tracks stability.

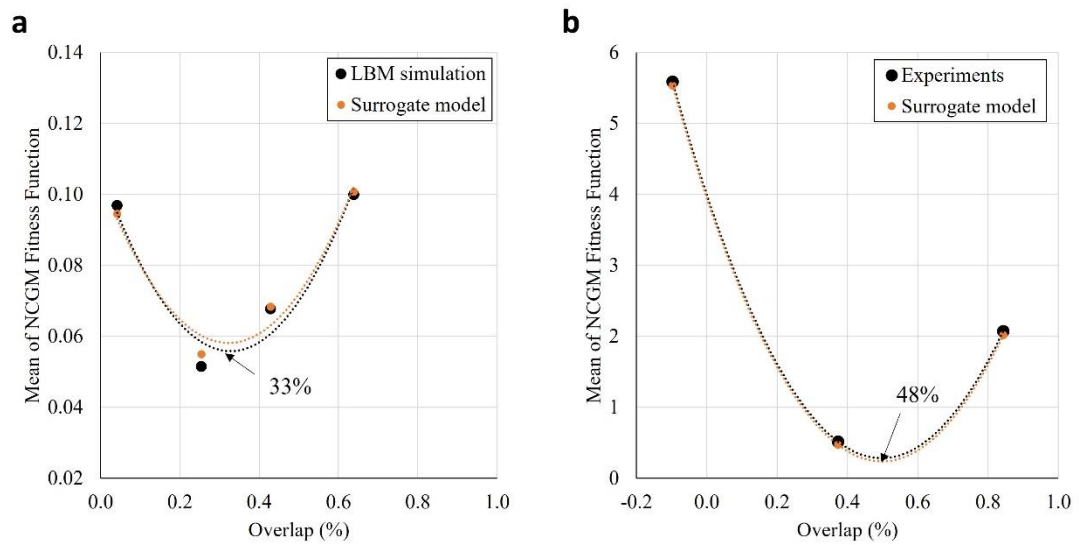


Figure 5-19 Effect of droplet overlap on NCGM error fitness function obtained from a) simulations and b) experiments.

In contrast, Figure 5-20a-d shows the effect of droplet overlap and printing frequency on the roughness fitness function from high-fidelity simulations and lab experiments. It was found that the droplet overlap value which minimises the roughness fitness function is approximately 37% and a quadratic relationship prevails for both cases. This result indicates the thickness uniformity is less sensitive to the uncertainty introduced by equipment tolerances. Furthermore, it was observed that printing frequency plays a more significant role determining track uniformity, with an optimal value of approximately 2.9 kHz from the model based on experiments and following a quadratic trend confirmed by qualitative results from model based on high-fidelity simulations.

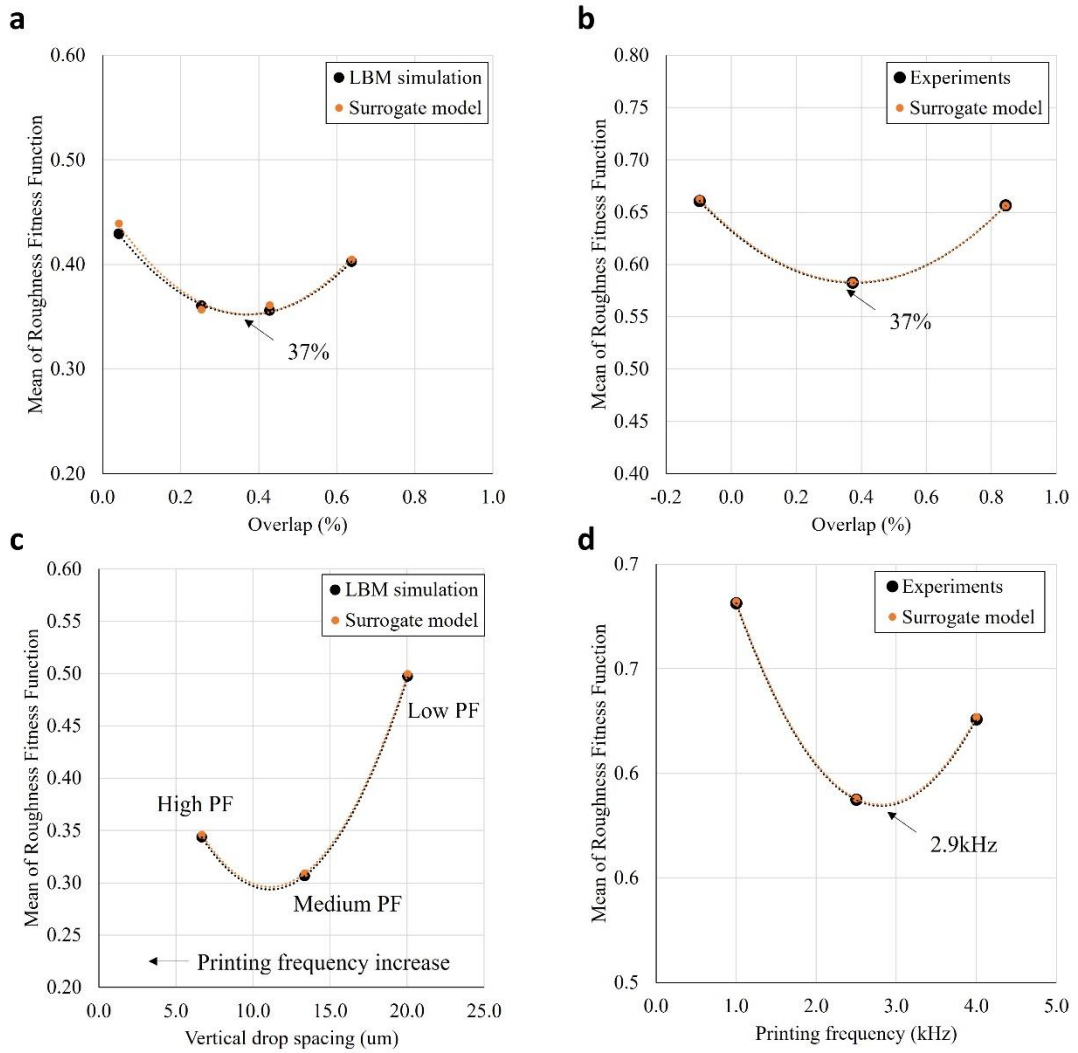


Figure 5-20 Effect of critical printing parameters on roughness fitness function. Droplet overlap effect on surrogate model based on a) simulations, b) experiments. Printing frequency effect on surrogate model based on c) simulations and d) experiments.

Overall, high fidelity simulations provided an accurate way to understand the relationships between printing parameters and surface morphology characteristics, showing similar trends as experiments. Average width of single tracks matched analytical model results derived from volume conservation assumptions, validating physics-based model predictions. However, finding the optimal printing parameters to generate the most stable single track required the use of experiments which incorporate deformation due to UV curing shrinkage, the drop position and size error due to the equipment tolerances and substrate chemical inhomogeneities. These factors have a significant effect on the final droplet overlap which was identified as the main factor influencing the final shape of the track.

5.4 Conclusions and summary.

A surrogate modelling strategy capable of predicting the surface morphology of single tracks has been established enabling the optimal selection of inkjet printing parameters in a reasonable time while capturing the transient effects from either high-fidelity simulations or lab experiments. The effects of drop spacing, printing frequency, standoff distance, and advancing contact angle on the dimensional accuracy of printed line morphology were determined. Line morphologies including isolated droplets, scalloped line, uniform line, and bulging formation were quantitatively identified as a function of printing parameters. Specific conclusions drawn from the results that have been confirmed with observations and findings in the current literature are:

- Drop spacing is the most critical parameter influencing the surface morphology stability of single tracks.
- Advancing contact angle plays a significant role determining the track width.
- Printing frequency and its interaction with drop spacing drives the track thickness uniformity.
- Standoff distance has a minor effect on the footprint waviness, but its interaction with printing frequency has a significant influence on the thickness uniformity.
- Droplet overlap which is a function of drop spacing, contact angle and droplet volume is a key predictor of the stability of printed single tracks.

This investigation constructed for the first time to the best of the author's knowledge a set of full quadratic transfer functions relating surface morphology characteristics such as average and maximum width and thickness to the critical printing parameters only requiring a limited number of experiments. Models were statistically validated through analysis of variance and verified via experimental work. Excellent agreement was found between predicted and measured values, with about 95% of data points within 10% error. Maximum absolute deviation of footprint width and feature thickness was within 10 μm and 2 μm , respectively. The fast execution of the predictive models allowed the global exploration of the design space to find the

optimum printing parameters by minimising the footprint width waviness and feature thickness roughness simultaneously. The printing parameters that produce the most stable track representing the best trade-off point of the pareto front are drop spacing, printing frequency and standoff distance equal to 31 μm , 2.8 kHz and 0.5 mm, respectively. The optimum parameters were validated in the Dimatix printer achieving a stable track.

Finally, this investigation revealed that a significant difference exists in the optimal printing parameters derived from simulations and experiments. The difference is attributed to the deformation due to UV curing shrinkage, the droplet location and footprint size variation introduced by equipment tolerances and chemically inhomogeneous substrates which are not considered in the high-fidelity simulations. Therefore, for the accurate calculation of the droplet overlap which drives the stability of single tracks, a way to quantify the uncertainty due to drop location and footprint size is required.

Current methodology was applied to the prediction and optimisation of single tracks; however, the use high fidelity simulations to model features comprised by more than 25 drops was proven to be unfeasible due to the large computational solution time. Therefore, to extend this investigation for the prediction of films, a different approach must be explored. In the next chapter, the solution of an inverse design problem to reconstruct the volume of free form printed films using a shape from shading approach is proposed.

6 Surrogate model-based optimisation of printing parameters for the stability of free form films.

6.1 Introduction.

After studying the formation of single tracks with our surrogate modelling framework in Chapter 5, the prediction and optimisation of free-form films was investigated. Similar to the single tracks, the formation of stable inkjet-printed films is influenced by the process parameters, the physical properties of the ink and the substrate wettability. Drop spacing, printing frequency and stand-off distance were considered key control parameters in the formation of uniform films. To understand the relationship between such factors and the surface morphology of films and find the optimum combination of printing parameters, our surrogate modelling framework was implemented using a hybrid physics-based and data-driven prediction model. This chapter documents the prediction model results including lattice Boltzmann simulations of square films and the 3D surface reconstruction of inkjet-printed films using a Shape-from-Shading approach (Reyes-Luna et al., 2023b) and illustrates the versatility of our surrogate modelling framework to determine the optimal printing parameters to achieve stable free-form films regardless of the simulation method employed.

6.2 Methodology.

In order to investigate the effect of critical printing parameters in the film formation, two prediction models were explored: lattice Boltzmann (LB) multiphase flow model and Shape-from-Shading reflection model. Using the LB model, the formation of square films was simulated by the sequential deposition of four lines of four microdroplets on a flat, rigid, and non-porous substrate as described in Section 4.1.1.5. Using the SFS approach, the surface morphology of inkjet-printed films was reconstructed from experimental images following the procedure explained in Section 4.2.1.2. The matrix of experiments defined to investigate the effect of critical printing parameters together with details about the surrogate model strategy including how to calculate the response surface equations, analyse the statistical validity of the model

and build the surface morphology were explained in Section 4.4.2. Then, the predicted deformed geometries obtained using the simulations were compared against film measurements and geometrical deviations were determined following the procedure from Section 4.7.3. Optimal printing parameters were found employing a multi-objective genetic algorithm approach with a non-traditional fitness function as discussed in Section 4.5.1.2. Finally, the experimental validation of the optimal printing parameters to achieve a stable free-form film was demonstrated using several shapes.

6.3 Results and discussion.

6.3.1 Surrogate model-based optimisation using LB multiphase flow method.

Before launching the parametric study to understand the role of drop spacing (horizontal and vertical) and advancing contact angle, three tests were performed varying only the horizontal drop spacing to assess the capability of the lattice Boltzmann simulation to model larger patterns and capture film bulging and break up phenomena. Assuming all droplets have a volume of 10 pL, an impact speed of 6 m/s and TPGDA ink physical properties, three simulations were run with resolutions of 1270, 762, and 540 dpi which correspond to a drop spacing of 20 μm , 33 μm and 47 μm , respectively. Vertical droplet spacing, advancing, and receding contact angles were fixed at 13.3 μm , 30 $^\circ$ and 5 $^\circ$, respectively. Each simulation was terminated after film equilibrium was reached at approximate 20000 timesteps, equivalent to 150 μs . High fidelity model results of the film evolution for the three cases are presented in Figure 6-1. It was found that film bulging occurs when the drop spacing was set at 20 μm (equivalent to an overlap of 62%) showing significant material overflow on the left, top and bottom edges of the footprint. When droplets land almost on top of each other redistribute the material towards the contact line exceeding the advancing contact angle and causing droplet to expand beyond target footprint as illustrated in Figure 6-1a. In addition, for the case when the drop spacing was set to at 47 μm (equivalent to an overlap of 8%), film separation was observed on the right edge of the square since the final line did not coalesce with the film due to material redistribution towards the first printed lines, increasing the drop spacing for the final printed line and preventing drop overlap as shown in Figure 6-1c. Finally, as illustrated in Figure 6-1b, when the drop spacing is set to 33 μm (equivalent to an overlap of 35%) a more stable

film was observed with minimal waviness at the edges and a square-shaped footprint closer to target pattern. The LB model was able to simulate small square films capturing the complex flow dynamics of multiple droplets spreading and coalescing simultaneously as well as bulging and break up phenomena.

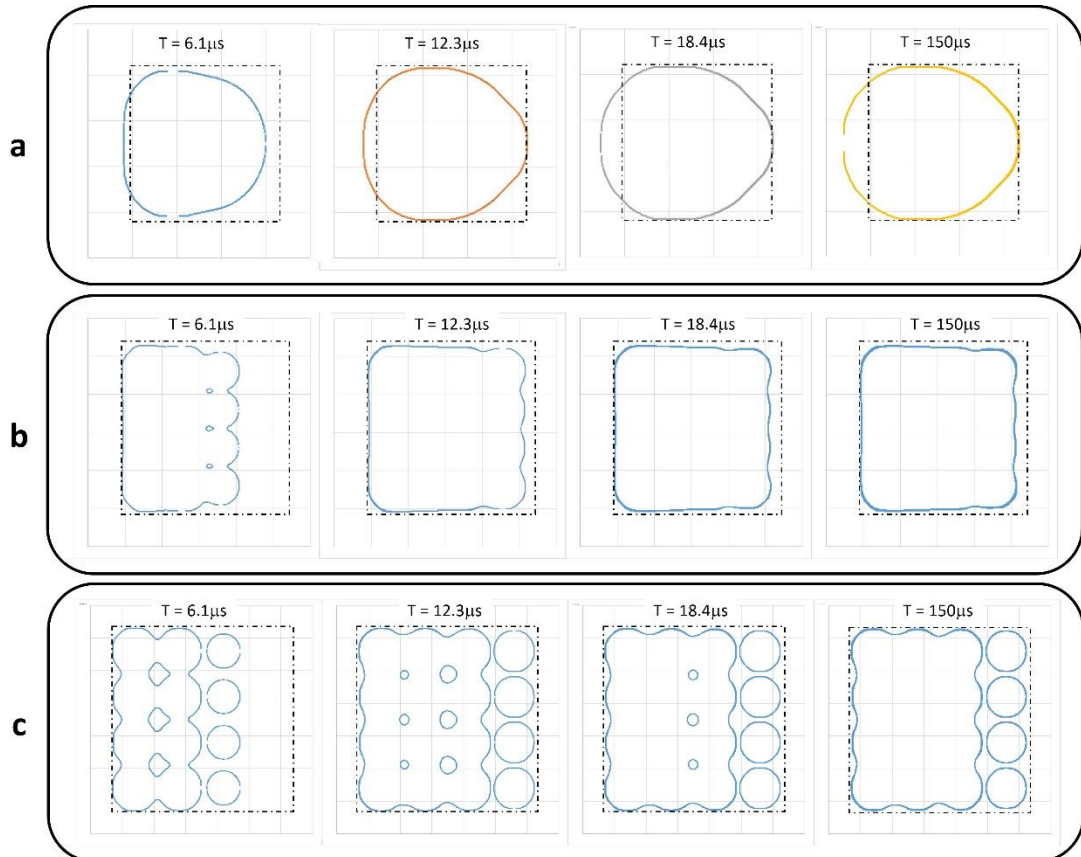


Figure 6-1 Simulation of square films using the lattice Boltzmann method varying the drop spacing only: a. Film evolution using a drop spacing of $20\ \mu\text{m}$ depicting film bulging; b. Film evolution using a drop spacing of $33\ \mu\text{m}$ yielding a stable film and c. Film evolution using a drop spacing of $47\ \mu\text{m}$ showing film break-up and significant edge waviness. All schematics show the target square footprint as a dotted line.

Numerical results are qualitatively consistent with experiments performed by Kang et al. (2010) where both bulging and break-up phenomena is present on printed films depending on drop spacing and advancing contact angle values. Furthermore, two experiments were performed in house to validate our high-fidelity model by printing a 5×5 droplet square film on silicon wafer using a drop spacing of $20\ \mu\text{m}$ and $60\ \mu\text{m}$, respectively. Material properties used for the simulation correspond to TPGDA at $20\ ^\circ\text{C}$ and assumed drop volume of $10\ \text{pL}$ with impact speed of $6\ \text{m/s}$, static contact angle of $10.3\ ^\circ$ and footprint diameter of $82.6\ \mu\text{m}$ (averaged measured data from 10×10 grid

obtained following the procedure described in Section 3.2.10) for all drops. The edge was extracted from both numerical and experimental results and overlaid to observe the differences as illustrated in Figure 6-2. Overall, good agreement was observed between high fidelity model and experimental results. Small differences in profile geometry could be explained since the LB model does not consider UV curing process which cause the printed patterns to shrink.

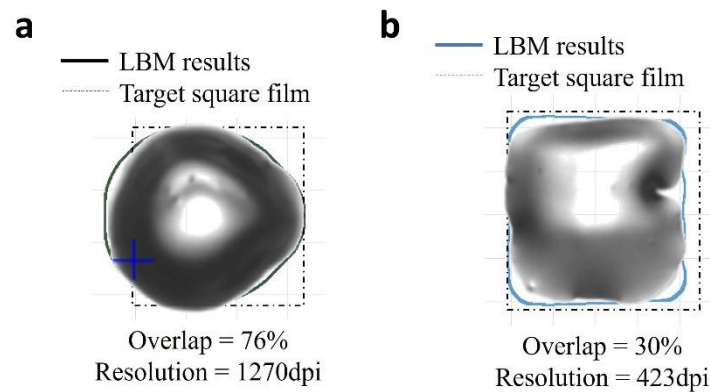


Figure 6-2 Comparison of LB model results and in-house experiments for validation purposes: a. Drop spacing = 20 μm and b. Drop spacing = 60 μm

Although our high-fidelity model based on the LB model yields accurate morphology predictions for small tracks and square films, it is not practical for the exploration of the printing parameters' space for optimisation purposes. The limitation to small square patterns with maximum 5 drops per side coupled with the large computational solution time per experiment (e.g., approximately 4.5 days) hinders the model applicability in our context. Therefore, to enable the prediction of free-form films of any size, the solution of an inverse design problem to reconstruct the volume of inkjet-printed films from experimental images using a shape from shading approach is explored.

6.3.2 Surrogate model-based optimisation using Shape-from-Shading inverse problem approach.

Using the shape from shading approach coupled with a multi-objective genetic algorithm, the optimal printing parameters to achieve a stable film were determined. First, experiments were performed to obtain the images for surface reconstruction. Next, the prediction model was built by estimating the optimal reflectance map

parameters per image. Then, the predicted surface morphology was compared against CSI measurements to validate the model and the results were used to construct the surrogate model. Finally, optimal printing parameters were determined and validated via experiment.

6.3.2.1 Experiments results.

A 1 mm square film was printed on glass following the procedure described in Section 3.2.5. A total of 20 experiments were performed using the matrix of parameters defined in Table 3-5. Printed films images following the experimental run order from left to right, top to bottom are shown in Figure 6-3. For reference, the average droplet footprint diameter measured in these experiments was $63.8 \pm 4.2 \mu\text{m}$.

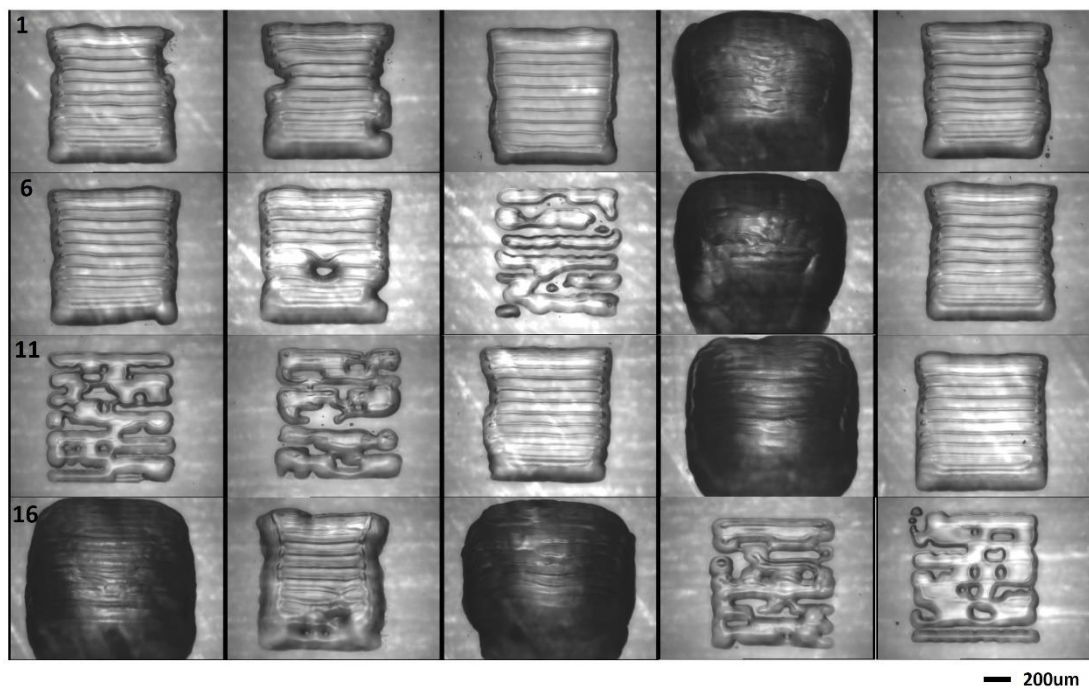


Figure 6-3 Images of printed films following the matrix of experiments described in Table 3-5.

Results showed that the selected printing parameters produce a diverse range of film morphologies, capturing film bulging and break-up phenomena as well as uniform films. Films generated with the same printing parameters (6 replicates of central point) represented by images 1, 5, 6, 7, 10 and 13 exhibit excellent agreement except for film 7 which presents a pore potentially due to substrate contamination. Films 4, 9, 14, 16

and 18 manifest excessive material overflow on the pattern edges and different reflection properties compared to the rest of experiments. These films were run with a drop spacing set at 10 μm . Films 8, 11, 12, 19 and 20 were run with a drop spacing set at 50 μm and all present islands and break ups in multiple locations due to the small overlap between droplets. The rest of the films seems to have a uniform thickness, but with larger edge waviness deviating from target pattern due to the variation of printing frequency and standoff distance. Overall, it is concluded that printed films obtained from our matrix of experiments represent an adequate sample from which to build our prediction model using the SFS approach.

6.3.2.2 Prediction results.

Images from experiments were employed to reconstruct the surface morphology of the square films using the SFS approach following the procedure described in Section 4.2.1.2. Three sets of optimal reflectance parameters were derived to address the different light reflection behaviour observed at different drop spacing levels. Films 3, 4 and 8 were measured using CSI to determine the ground truth film morphology which represent films created at drop spacings set at 30, 50 and 10 μm , respectively. The relationship between an image without reflection obtained from the CSI measurements and the real image grey levels was established and reflectance parameters optimised by minimising the root mean square error (RMSE) between images. Table 6-1 lists the optimal reflectance parameters determined for each drop spacing level.

Table 6-1 Optimal reflectance map parameters.

Reflection parameters	Ds = 10 μm	Ds = 30 μm	Ds = 50 μm
Surface roughness	0.3431	0	0.1512
Diffusive factor	0.7758	0.6011	0.8816
Specular factor	0.2242	0.3989	0.1184
Surface shininess	30.55	2.8494	23.9988

The reconstructed morphologies based on the images from our matrix of experiments are illustrated in Figure 6-4. The results are displayed following the same order of the experiments for consistency purposes. Film morphologies were reconstructed using the Lax-Friedrichs sweeping scheme implemented in MATLAB on a PC with intel core i7+ 8th Gen processor and 16Gb of DDR4 memory.

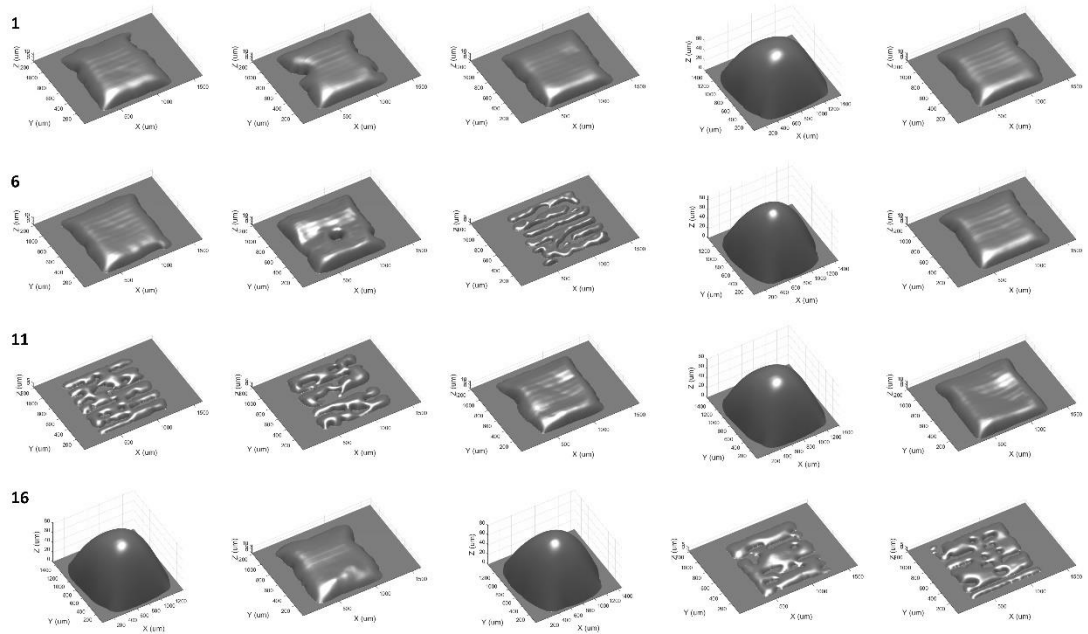


Figure 6-4 Surface morphology prediction of square films using the Shape from Shading approach.

As can be seen from Figure 6-4, the SFS approach can achieve satisfactory reconstructed morphologies from real images using the optimal sets of reflectance parameters determined from ground truth measurements. The results showed excellent agreement on the footprint boundaries prediction since the method uses a mask derived from highly accurate image segmentation procedures (e.g., maximum error less than 3 μm). In addition, it was found the SFS approach can reconstruct the surface of multiple segments with free-form shapes simultaneously in a timely manner which validates the hypothesis supporting the usage of this approach for fast prediction purposes. It is important to note that details on the surface roughness caused by printer swaths were lost in the SFS prediction and only smooth surfaces could be reconstructed. Also, it was found that the predicted film morphology is highly influenced by localized specular reflection from the image such as in films 7 and 15 which show a white band next to pore and mid centre, respectively. Overall, it is concluded that the SFS approach provides a fast way to estimate the film morphologies of printed features given three sets of CSI film measurements representing the drop spacing levels used in our experiments.

Figure 6-5 shows the predicted morphology (reconstructed film using SFS approach), the measured morphology, and the predicted shape deviations from target to assess the accuracy of the SFS approach.

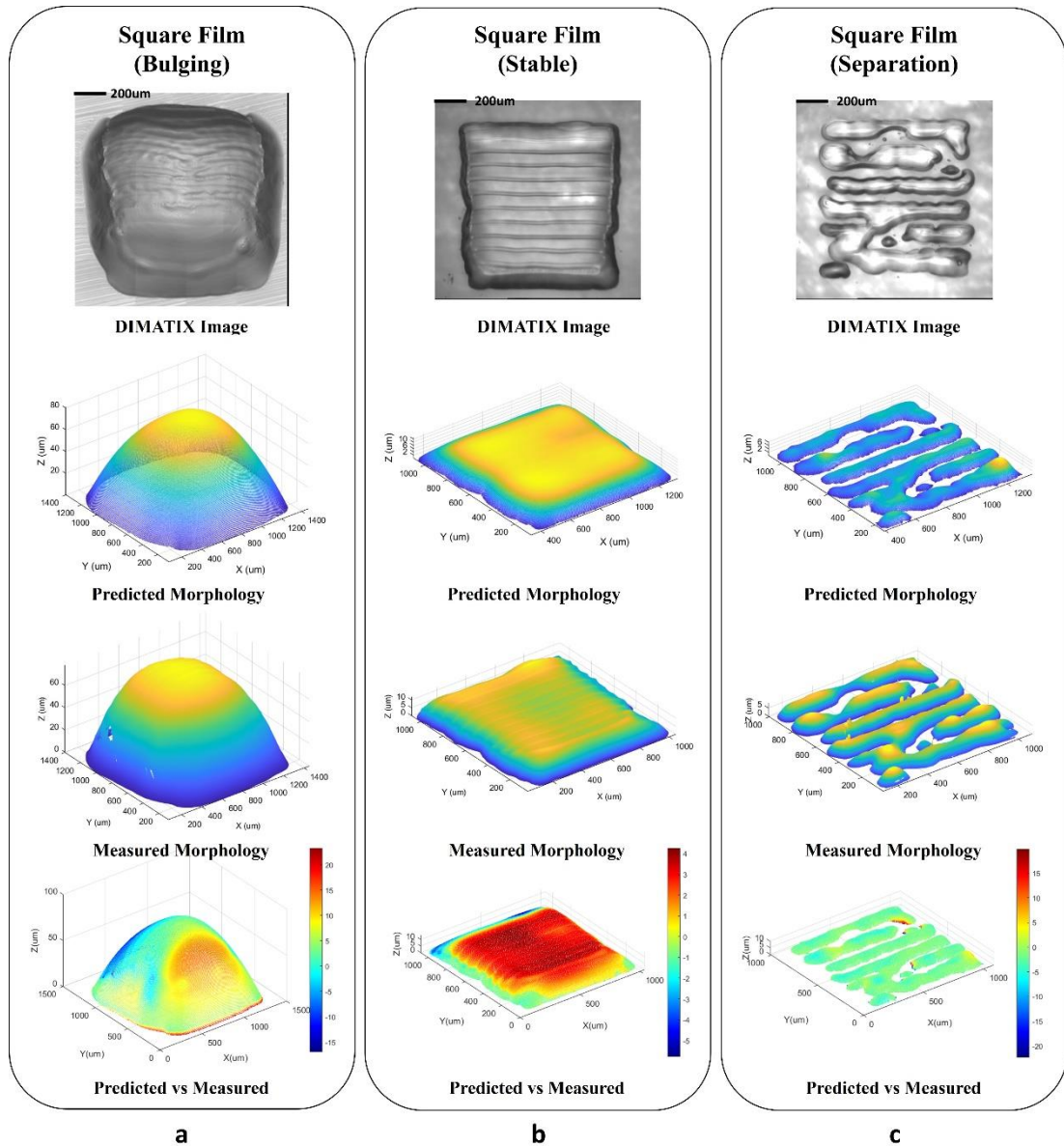


Figure 6-5 Validation of prediction model using CSI measurements: a. Bulging film ($ds=10 \mu\text{m}$, $pf=1 \text{ kHz}$ and $sd=0.5 \text{ mm}$); b. Stable film ($ds=30 \mu\text{m}$, $pf=3 \text{ kHz}$ and $sd=1 \text{ mm}$) and c. Break-up film ($ds=50 \mu\text{m}$, $pf=2 \text{ kHz}$, $sd=1 \text{ mm}$).

Overall, the reconstructed shape of the film using the SFS approach shows good agreement with film measurements. The results are presented per level of drop spacing employed in the experiments. Figure 6-5a depicts a bulging film generated using a

drop spacing, printing frequency and standoff distance of 10 μm , 1 kHz and 0.5 mm, respectively. The largest deviation from target was located on the footprint profile with a value of approximately 20 μm which may be due to an error introduced while finding the base plane for the CSI measurements data. The peak location is consistent in both geometries showing a difference of 3.2 μm at a maximum thickness of 78.3 μm , which represents an error of 4%. It was observed that the surface reconstruction is more sensitive to the specular reflection since shape was underpredicted where light was reflected the most and overpredicted in the opposite case. Figure 6-5b illustrates a uniform film generated using a drop spacing, printing frequency and standoff distance of 30 μm , 3 kHz and 1 mm, respectively. Overall, predicted film morphology overestimated the real film morphology by an average of 2.5 μm and the ridges caused by printing swaths captured in CSI measurements were lost in the SFS prediction. The peak location is consistent in both geometries at upper right corner showing a difference of 0.7 μm at a maximum thickness of 11.9 μm which represents an error of 5.8%. Finally, the shape deviations observed in the prediction of the segmented film are displayed in Figure 6-5c. Overall, the predicted film morphology underestimated the real film by an average of 2.5 μm . The largest deviation from target was located on a concentrated zone in the footprint profile with a value of approximately 20 μm due to the manual generation of the mask employed in the SFS prediction. The peak location matches the actual film measurements at a maximum value of 8.0 μm showing a difference of 0.6 μm (real vs predicted), which represents an error of 7.5%. Based on these results, it is concluded that the surface reconstruction from real images of printed features is achievable in a fast way without losing much accuracy.

Table 6-2 lists the three indicators used to assess quantitatively the accuracy and speed of the SFS prediction: mean absolute (MA) error, root mean square (RMS) error, and CPU running time. Based on the performance metrics, the less accurate prediction and slower solution time was obtained for the bulging film which may be due to the lower grey level discretisation of the film image which is related to the capability of the material to reflect (absorb) the light. The accuracy of the prediction for the films generated using a drop spacing greater than 30 μm was on average less than 3 μm and the solution time was less than 4.5 minutes. The results confirm that a good trade-off between faster and accurate solutions is achievable by implementing the SFS approach.

Table 6-2 Quantitative comparisons of predicted vs measured film morphology.

Images	Mean Absolute Error (MA)	Root Mean Square Error (RMS)	Time (s)
Figure 74a	6.4651	7.1835	689
Figure 74b	2.4745	2.7494	272
Figure 74c	2.6849	2.9833	187

Table 6-3 lists the normalised central geometric moments (NCGM) and roughness factors used as fitness functions for optimisation purposes.

Table 6-3 Calculated fitness functions based on SFS prediction results.

Run #	Drop spacing (μm)	Printing frequency (kHz)	Standoff Distance (mm)	Overlap (%)	NCGM fitness function	Roughness fitness function
1	30	2	1	53	0.0147	0.3869
2	30	2	1.5	53	0.0146	0.3872
3	30	3	1	53	0.0086	0.3076
4	10	1	0.5	84.3	0.0625	0.5680
5	30	2	1	53	0.0115	0.3860
6	30	2	1	53	0.0093	0.3335
7	30	2	1	53	0.0086	0.3847
8	50	2	1	21.6	0.0558	0.5906
9	10	1	1.5	84.3	0.0786	0.5874
10	30	2	1	53	0.0117	0.3847
11	50	3	1.5	21.6	0.0252	0.4856
12	50	1	0.5	21.6	0.0401	0.4899
13	30	2	1	53	0.0098	0.3875
14	10	3	1.5	84.3	0.0503	0.5468
15	30	2	0.5	53	0.0070	0.3810
16	10	3	0.5	84.3	0.0644	0.5492
17	30	1	1	53	0.0136	0.3855
18	10	2	1	84.3	0.0823	0.5519
19	50	1	1.5	21.6	0.0218	0.4845
20	50	3	0.5	21.6	0.0166	0.4807

6.3.2.3 Surrogate model results.

This section details the surrogate model adequacy and the analysis of the effect of printing parameters and its interactions in the surface morphology of solid square films. Figure 6-6a-c shows the measured film morphology of a square pattern printed with a drop spacing of 30 μm , printing frequency of 3 kHz and standoff distance of 1.0 mm, the reconstructed surface from the corresponding experiment image

employing the SFS approach and the predicted morphology from our surrogate model using the same printing parameters with a fine discretisation scheme (40000 equations), respectively. Comparing the main dimensions of the predicted vs real film, our surrogate model prediction underestimated the average length, width, and thickness by 22.6 μm , 13.4 μm and 0.1 μm , respectively. The locations of the maximum length, width and thickness show good agreement, but the magnitudes were overestimated by 19.9 μm , 24.4 μm and 0.2 μm , respectively. For this specific case, the error of the prediction model relative to the main dimensions is less than 2.5%. It is important to note that the 3D predicted morphology presents a non-smooth surface since every point was built using an equation as function of the printing parameters and the error level is not the same for all equations. However, the overall shape of the printed feature was successfully achieved in tenths of seconds.

To validate the surrogate model prediction throughout the design space, a comparison of the measured dimensions was plotted against its corresponding prediction values. Figure 6-6d-i illustrates the models for average length, width, and thickness, and maximum length, width, and thickness predictions versus measured values, respectively. For the average and maximum length and width models, there is an excellent agreement between the predictions and the experiments, with about 66% of data points within 2.5% error, with a single point out of the 5% error threshold which corresponds to the prediction of the average length of a disjointed film. For the average and maximum thickness models, there is a good agreement between predictions and experiments, with about 80% of data points within the 10% error, observing the lowest for one point at the lower value of thickness (35% error at a thickness of 4 μm). Particularly, the model to predict the maximum thickness shows 20% of data points out of the 10% error threshold, which is likely to be caused by the underprediction of the SFS approach in the films presenting break-ups due to the sensitivity of the model to the specular reflection that dominates the images of disjointed films. Nevertheless, using the prediction models to build the surface morphology of square films as function of printing parameters provided a fast and accurate method to determine instabilities such as material overflow (bulges) or disjointed (break-ups) films as well as precise predictions of the footprint and thickness with errors lower than 3% and therefore, were considered adequate for this investigation.

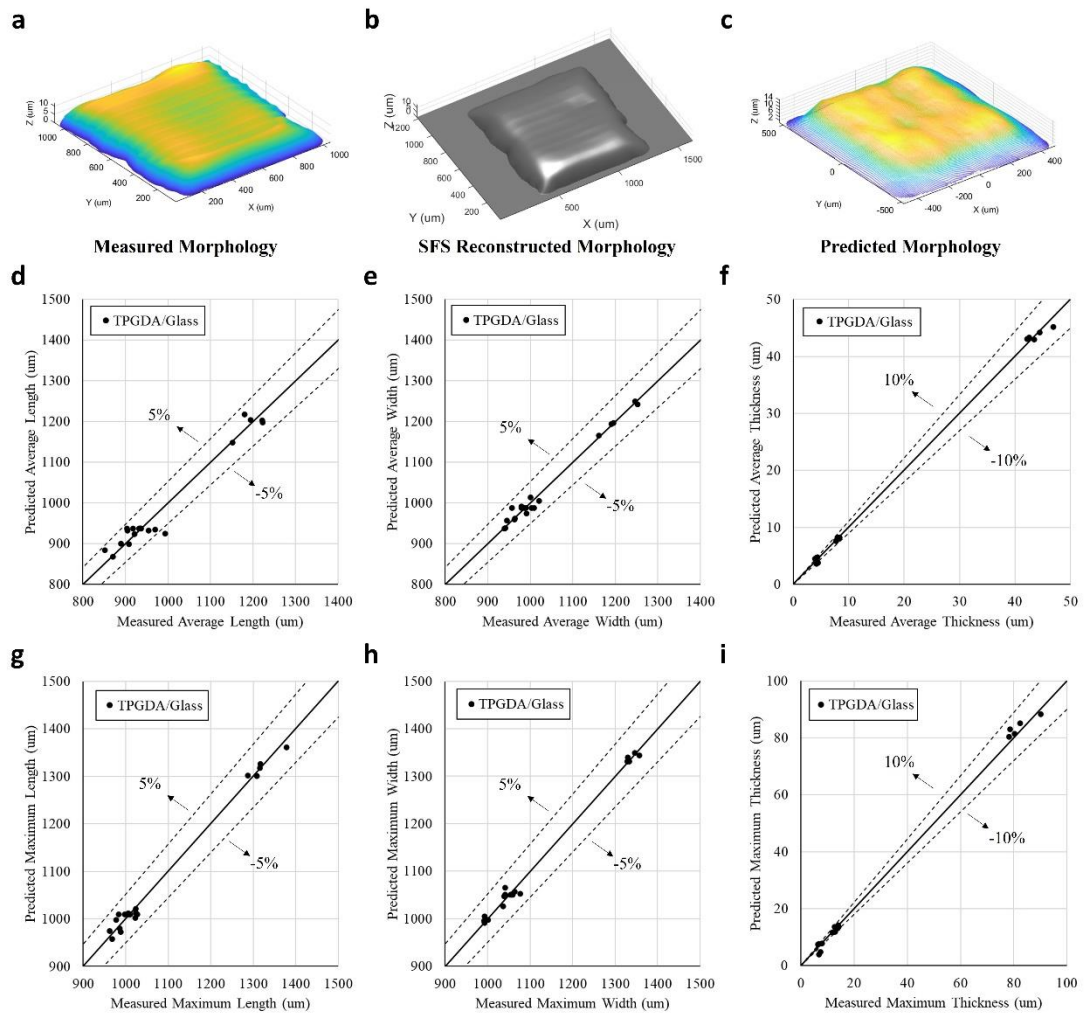


Figure 6-6 Validation of the surface morphology prediction model for square films by comparing samples printed with printing parameters defined in matrix of experiments. a) Measured surface morphology of square film; b) reconstructed surface morphology using shape from shading approach. d)-i) deviation assessment of the predictive models for the average length, average width, average thickness, maximum length, maximum width, and maximum thickness, respectively.

The response surface equations describing the average and maximum length, width, and thickness of the square films as function of drop spacing, printing frequency and standoff distance are depicted in Figure 6-7a-c and Figure 6-8a-c, respectively. The analysis of variance confirmed that prediction models are statistically significant using a significance level of 5%. A residual analysis was done to test for defects such as non-normality, non-independent and non-constant variance. The models were found to be free of all these defects. For the average length prediction, the drop spacing and the square of the drop spacing were found to be the only factors statistically significant, printing frequency, standoff distance and its interactions have minor effects. Eliminating non-significant factors from the model improves the correlation

coefficient of determination but increased the error between predicted and measured values. Therefore, no term was eliminated from regression model. For the average width prediction, it was found that drop spacing, drop spacing squared, printing frequency and the interaction between drop spacing and printing frequency are statistically significant which confirms the critical role of parameter interactions in the accuracy of the model. For the average thickness prediction, only drop spacing, drop spacing squared and the interaction between drop spacing and standoff distance are statistically significant, which is consistent to the results obtained from Zhang et al. (2017) where two thickness modes were identified depending on the standoff distance.

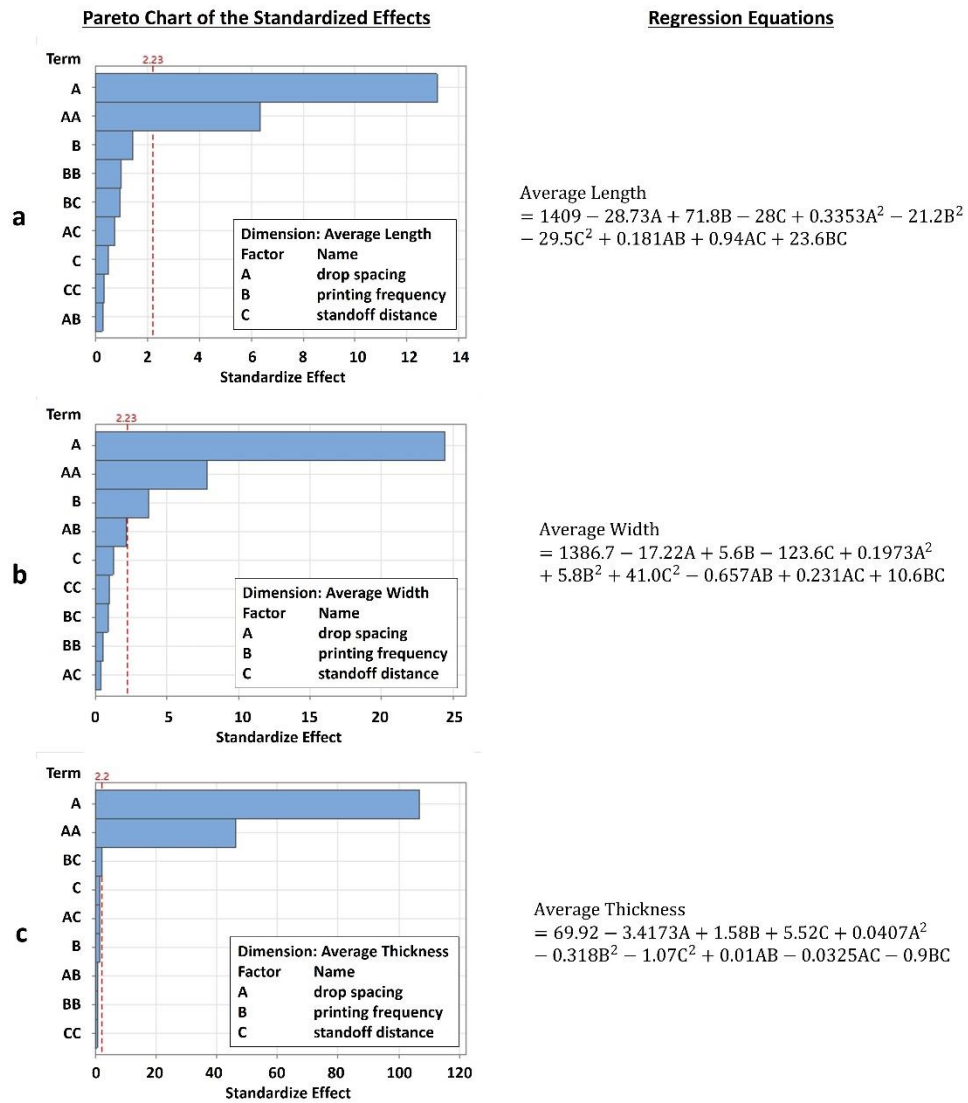


Figure 6-7 Statistical analysis of prediction models: a. Average length, b. Average width and c. Average thickness.

For the maximum length and width prediction, it was found that drop spacing, drop spacing squared and the interaction between drop spacing and printing frequency are statistically significant which indicates the critical role of the printing traverse velocity in the control of the material overflow on the edges of square films. For the maximum thickness prediction, it was observed that the interaction between printing frequency and standoff distance is statistically significant which is consistent to the results obtained for the prediction of the average thickness.

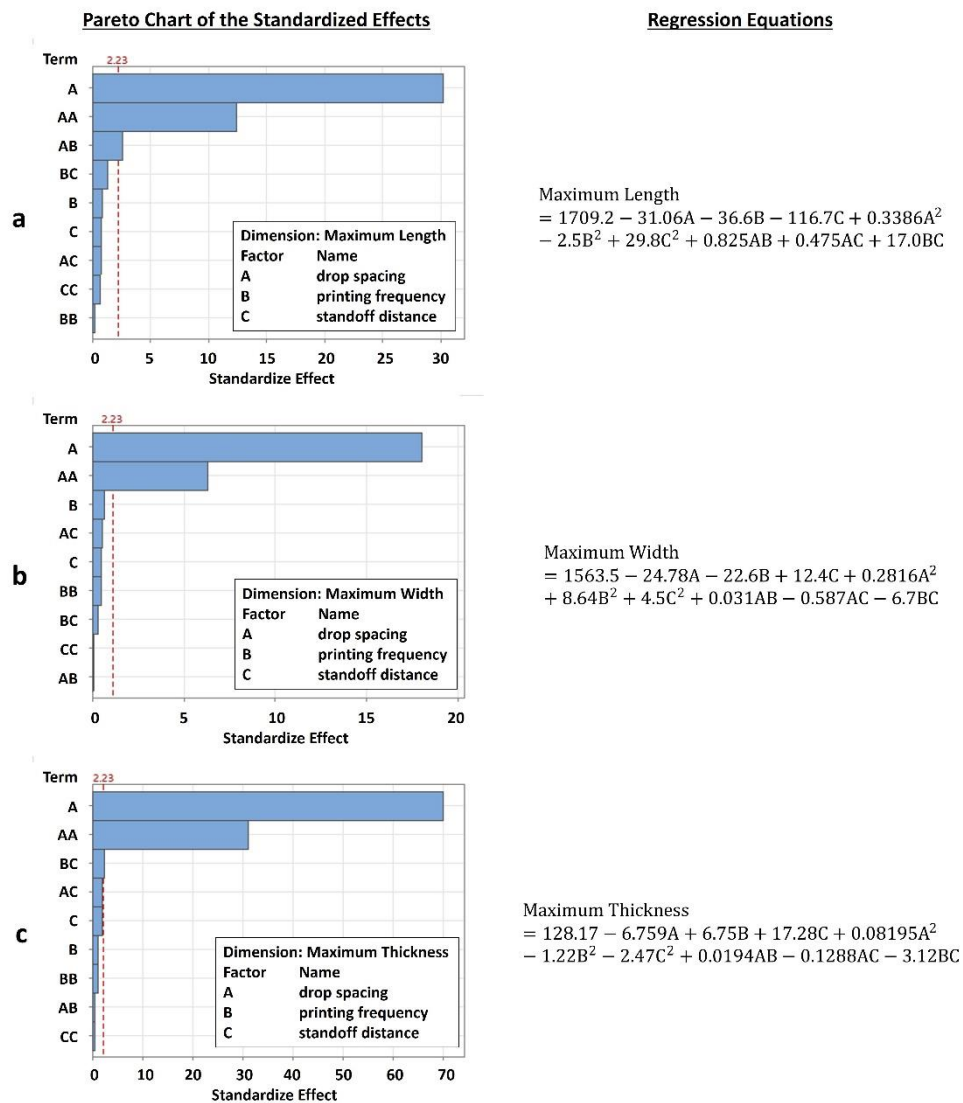


Figure 6-8 Statistical analysis of prediction models: a. Maximum length, b. Maximum width and c. Maximum thickness.

Table 6-4 lists three indicators used to assess quantitatively the accuracy of the surrogate model for each dimension: coefficient of determination (R-SQR), mean

absolute (MA) error, root mean square (RMS) error. From a statistical standpoint, the prediction models show excellent correlation with the selected printing parameters, given the coefficients of determination very close to one. From a practical significance, the less accurate model is the one derived for the average length which shows a root mean square error of 25 μm , but still good enough considering the overall dimension is 1000 μm which means an average error of 2.5%.

Table 6-4 Surrogate model accuracy indicators.

Dimension	Coefficient of determination R-SQR	Mean absolute error (MA) (μm)	Root mean square error (RMS) (μm)
Average Length	0.9591	18.3	24.8
Average Width	0.9870	9.0	11.8
Average Thickness	0.9993	0.4	0.6
Maximum Length	0.9919	10.7	12.8
Maximum Width	0.9939	8.3	10.4
Maximum Thickness	0.9985	1.2	1.7

Summarizing, the prediction models provide a fast and accurate way to characterise the surface morphology of square films. The most important factor driving printed feature's stability is the drop spacing. As drop spacing increases, the length, width, and thickness decrease in a non-linear manner. Although, printed frequency and standoff distance and its interactions have a minor non-linear effect on film dimensions, they play a key role characterising accurately the films' material overflow, similar to the results obtained for single tracks in Chapter 5. Setting the lowest frequency with the lowest drop spacing and the highest standoff distance forms unstable films due to the presence of bulges. Setting the highest frequency with the highest drop spacing and the lowest standoff distance generates segmented films. Given the complex non-linear behaviour of the morphology prediction models, a parameter optimisation was performed to find the combination of printing parameters that produce the most stable film and results are presented in next section.

6.3.2.4 *Optimisation and validation results.*

In this section the results of the parameter optimisation using the surrogate model constructed from the SFS approach results are presented. Figure 6-9 illustrates the fitness functions used to find the most stable track as function of the printing parameters and a comparison between measured and predicted values. Two fitness functions were calculated in this investigation: the error norm of the normalized central geometric moments between the predicted and target footprints and the roughness factor defined as the ratio of the standard deviation of the feature's thickness and the average thickness. The first one is used to minimise edge waviness and the second one to minimise thickness roughness. Results show good agreement between the means of predicted values and SFS predictions, showing a quadratic relationship between fitness functions and printing parameters, similar to the results obtained for single tracks. An independent evaluation of the effect of each printing parameter on the NCGM fitness function indicates that a drop spacing of 34.6 μm (approximate droplet overlap of 46%) with a printing frequency of 2.2 kHz and a standoff distance of 1 mm would minimise the error between the predicted and target footprints. Furthermore, performing an independent evaluation of the effect of each printing parameter on the roughness factor fitness function, the morphology surface roughness is minimised when the drop spacing, printing frequency and standoff distance are set to 31.9 μm (approximate droplet overlap of 50%), 2.1 kHz and 1 mm, respectively.

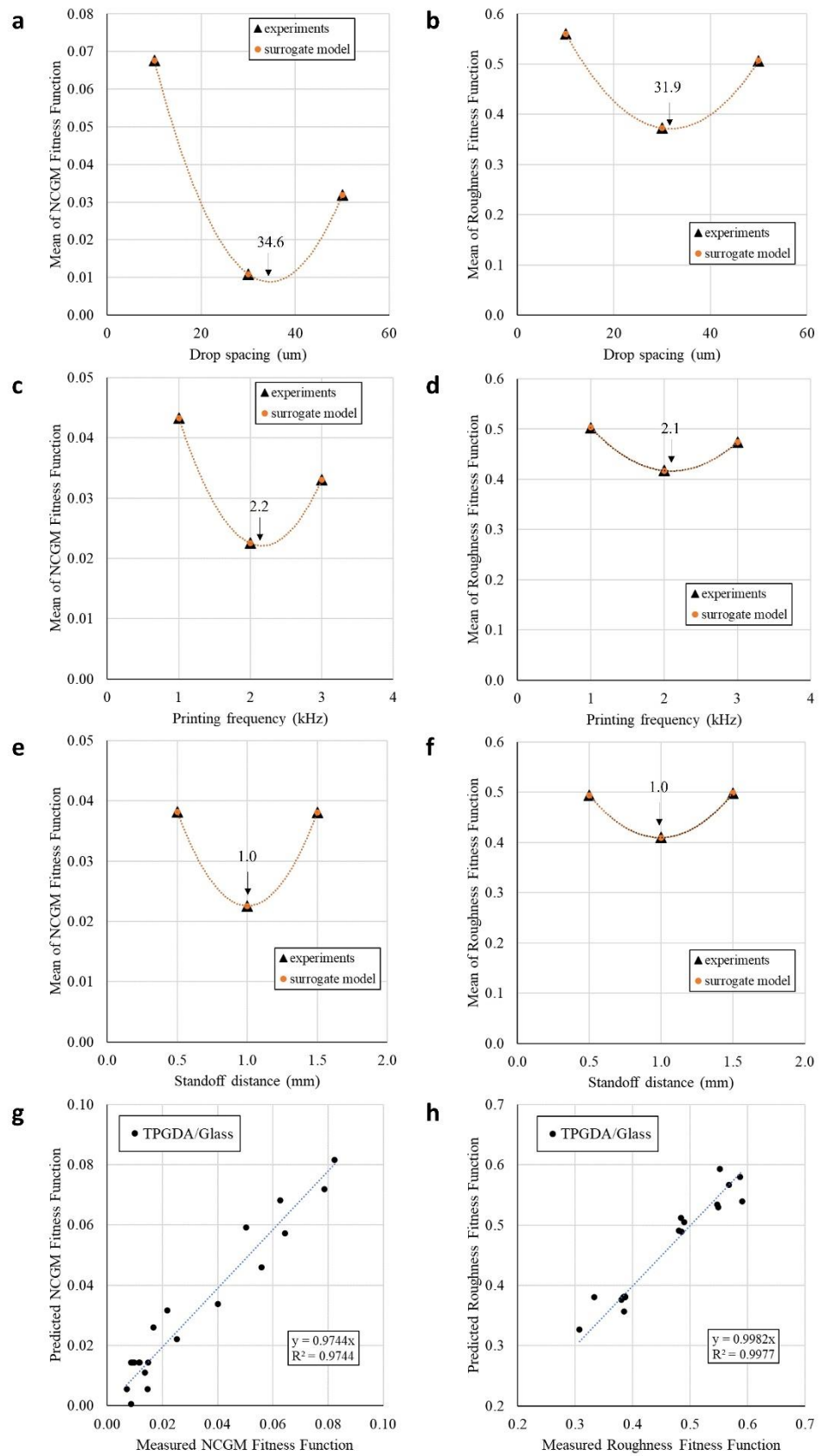


Figure 6-9 Effect of printing parameters on NCGM and roughness fitness functions. a)-b) effect of drop spacing; c)-d) effect of printing frequency; e)-f) effect of standoff distance. Predicted vs measured values of NCGM and roughness fitness functions included in g) and h), respectively.

Measured data from the predicted morphologies using the SFS approach was analysed using MINITAB to build the response surface equation for each fitness function. A gradient-based optimisation was performed to minimise predicted fitness functions and find optimal printing parameters. Starting point for the local optimiser was set to 20 μm , 1 kHz and 1 mm with a confidence level for all intervals of 95% in all analyses. Table 6-5 lists the results obtained from the single objective optimisation. It was found that the optimal values for the printing parameters depend on the fitness function focus. NCGM error measures footprint waviness whereas roughness factor is focused on the thickness uniformity. Drop spacing, printing frequency and its quadratic terms are the most significant factors driving the minimum fitness functions values.

Table 6-5 Single objective optimisation using gradient based (local) approach.

Printing Parameters	NCGM error	Roughness
Drop spacing (μm)	33.8	31.0
Printing frequency (kHz)	3	3
Standoff distance (mm)	1.5	0.5
Overlap (%)	47%	51%

Results indicate that there is a trade-off between the morphology characteristics that define a stable film depending on the fitness function used. Therefore, a multi-objective optimisation using a genetic algorithm (global optimisation approach) was performed to find the set of printing parameters that simultaneously minimise the waviness and roughness. Details about the optimisation procedure were described in Section 4.5.1. Figure 6-10a shows the composite desirability fitness results obtained when simultaneous waviness and roughness objectives are minimised. The printing parameters that produce the most stable track representing the best trade-off point of the composite desirability are drop spacing, printing frequency and standoff distance equal to 31 μm , 3.0 kHz and 0.5 mm, respectively. The predicted film morphology using the optimal printing parameters is illustrated in Figure 6-10b. The model predicts a footprint with minimal variation against target pattern and a very uniform thickness along the feature's pattern. The proposed surrogate model-based optimisation using the SFS surface reconstructions achieved fast and accurate results enabling the search of optimal printing parameters.

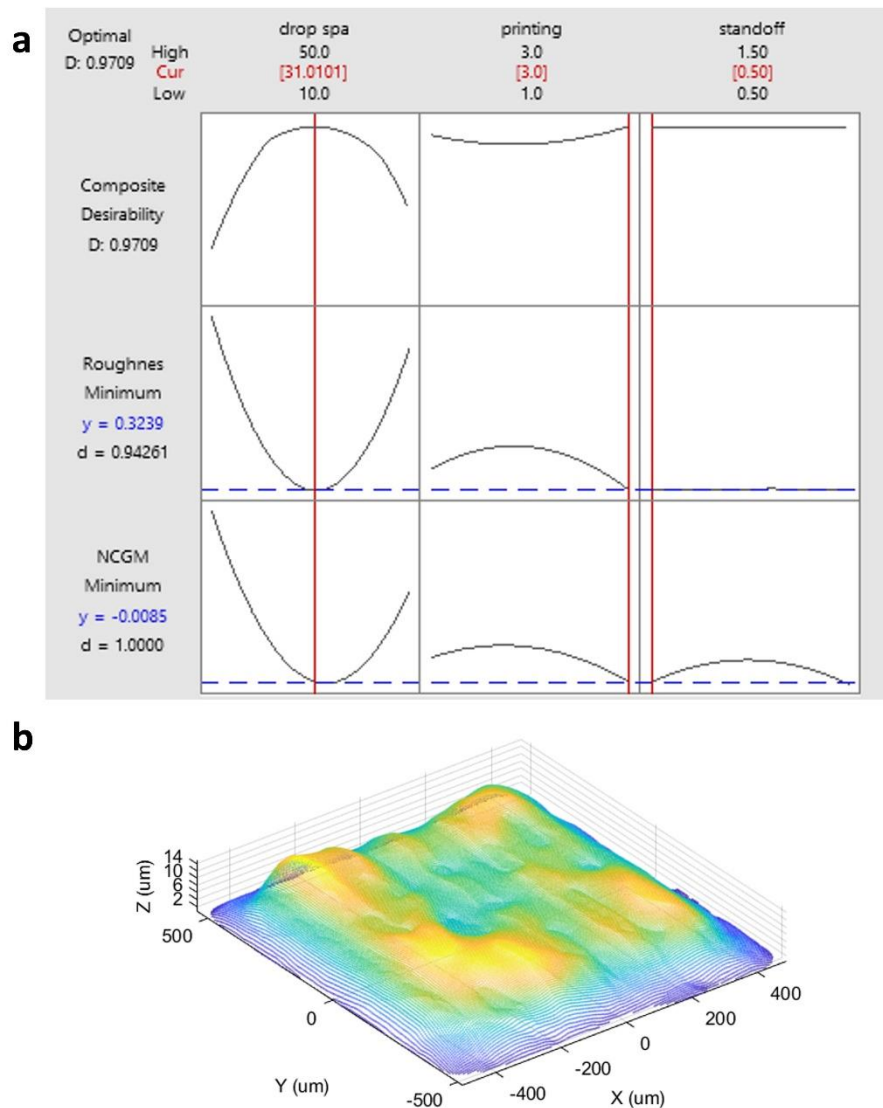


Figure 6-10 Multi-objective optimisation results. a. Optimal printing parameters and b. Film prediction using optimal printing parameters.

To validate our surrogate-based model optimisation, three patterns were printed setting the optimal printing parameters determined from the multi-objective genetic algorithm approach. Figure 6-11 a-c shows images of the printed features corresponding to a solid square, a ring, and a hollowed square, respectively. As can be seen, the optimal set of printing parameters produce a stable film morphology regardless of the target pattern. Below each image, an overlay of the target pattern and real footprint is included confirming the effectiveness of our proposed optimisation methodology. In the three cases the major difference is observed at bottom and top edges which may be explained by the lower printer accuracy in the cross-scan direction (Y axis).

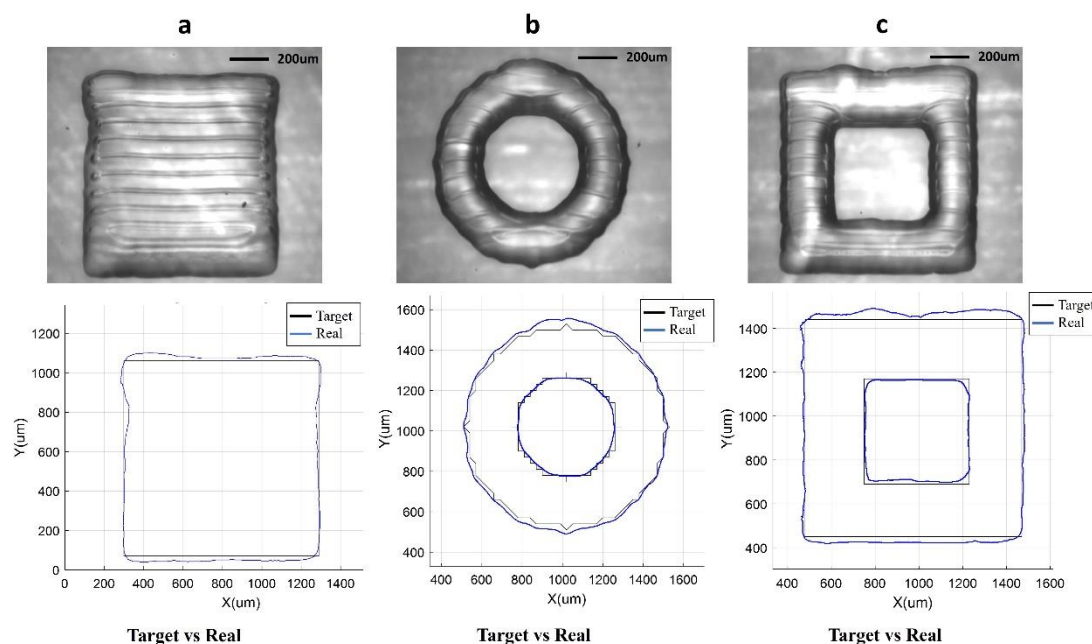


Figure 6-11 Printed free-form films using optimal parameters: a. Solid square film of side 1 mm; b. Ring film (outer diameter=1 mm, thickness=270 μm) and c. Hollowed square film of outer side=1 mm and thickness=250 μm . Target vs real Footprint overlay is included for each feature to illustrate the accuracy of the print.

6.4 Conclusions and summary.

A surrogate modelling strategy capable of predicting the surface morphology of free-form films has been established enabling the optimal selection of inkjet printing parameters in a reasonable time while capturing the transient effects from either high-fidelity simulations or lab experiments. Although our high-fidelity model based on the LB method produced accurate morphology predictions for small square films (4x4 drops), it was not practical for the exploration of the printing parameters' space for optimisation purposes. The limitation to small square patterns with maximum 5 drops per side coupled with the large computational solution time per experiment (e.g., approximately 4.5 days) hindered the model applicability for our objectives. Therefore, for fast prediction of the surface morphology of any given pattern, a photometric technique called Shape-from-Shading (SFS) was investigated. SFS approach reconstructed the volume of a printed feature using a single image by matching the surface slope created by the reflection of frontal lighting to the image grey level and solving the reflection PDE to find the feature thickness. Diffuse and specular components of reflection were considered to improve the accuracy of the

prediction. It was shown that using film images with a resolution of 2.54 μm , high contrast and single layered, the predicted thickness error is less than 20% which represents less than 3 μm . The time to reconstruct the volume was in the order of minutes, reducing 1000x the CPU solution time from our LB high-fidelity simulations.

The effects of drop spacing, printing frequency, and standoff distance on the dimensional accuracy of the film morphology were determined. Bulging and separation defects traditionally found in inkjet-printed films were quantitatively identified as a function of printing parameters. Specific conclusions drawn from the results that have been confirmed with observations and findings in the current literature are:

- Drop spacing is the most critical parameter influencing the surface morphology stability of freeform films.
- Printing frequency and its interaction with drop spacing significantly influence the film thickness uniformity and are critical to achieve adequate and accurate predictions of film dimensions.
- Standoff distance has a minor effect on the footprint waviness, but its interaction with printing frequency has a significant influence on the thickness uniformity.

This investigation constructed for the first time to the best of the author's knowledge a set of full quadratic transfer functions relating surface morphology characteristics such as average and maximum length, width and thickness to the critical printing parameters only requiring a limited number of experiments. Models were statistically validated through analysis of variance and verified via experimental work. Excellent agreement was found between predicted and measured values, with about 60% of data points within 2.5% error. Mean absolute error of the maximum film length/width and thickness was lower than 10 μm and 2 μm , respectively. The fast execution of the predictive models allowed the global exploration of the design space to find the optimum printing parameters by minimising the footprint waviness and feature thickness roughness simultaneously. The printing parameters that produce the most stable track representing the best trade-off point of the pareto front are drop spacing, printing frequency and standoff distance equal to 31 μm , 3 kHz and 0.5 mm,

respectively. It is important to note that same set of optimal printing parameters were obtained in the analysis of single tracks which represents an important discovery from this investigation. The optimum parameters were validated by printing three freeform patterns in the Dimatix printer achieving stable films.

Although the solution of the shape from shading inverse problem enabled the reconstruction of free form patterns, the approach is limited by the material reflection properties and high contrast images to accurately reconstruct the volume of printed features. Furthermore, based on the results presented in this chapter, the prediction model captured adequately the general shape of the film, but small surface artifacts generated by UV curing effects were lost. Therefore, next chapter explores a semi-coupled finite element model to predict the photo-polymerisation effect on 3D printed parts.

7 Geometry prediction and compensation for the stability of 3D printed parts using machine learning approach.

7.1 Introduction.

Chapters 5 and 6 described the results from applying the proposed surrogate modelling framework to determine the optimal inkjet printing parameters required to print stable single tracks and freeform films, respectively. These chapters focused on reducing the in-plane error between target and real footprints constrained to minimal surface roughness by optimising critical printing parameters and wettability characteristics. In this chapter, the focus is on improving the dimensional accuracy of 3D inkjet-printed parts considering the optimal printing parameters from single tracks and films and a proposed geometry compensation framework based on machine learning techniques. However, it is important to note that when a layer-by-layer approach is employed using a photocurable polymer, the partially cured material resulting from the polymerisation process plays a critical role in the final shape of the printed object. The film curing characteristics affect macroscopic material properties such as Young's Modulus, volume shrinkage, and deformation which impacts the accuracy of the printed structure. Therefore, a finite element model capable of simulating the layer-by-layer process and material properties as function of the degree of curing (e.g., degree of monomer conversion) is also explored. The results of FE simulations and experiments are used as inputs to train the machine learning method that was developed to compensate the target geometry to achieve a stable 3D printed part.

7.2 Overall Methodology.

Section 7.3.1 documents the experimental work carried out to assess the effectiveness of optimal printing parameters to produce stable 3D objects. Six 3D artifacts were inkjet-printed using the optimal parameters derived for freeform films in Section 6.3.2.4. The dimensions of the artifacts and number of layers can be found in Section 3.2.4.2. The artifacts were measured using a microCT scan following the procedure described in Section 3.2.8. A comparison of the measured geometry against target

structure was performed, along with a quantitative analysis of the results. The mean square error (MSE) metric was employed to quantify the error in the printed part.

Section 7.3.2 presents an investigation of the effect of degree of cure on the deformation of 3D inkjet-printed parts using a semi-empirical, semi-coupled photopolymerisation and structural finite element approach. Details of the modelling assumptions, formulation, boundary conditions and mesh convergence can be found in section 4.1.2. The material properties as function of degree of curing are included in the chapter for reference. Then, six artifacts were simulated layer by layer using the calculated degree of cure. Target geometry, mesh size, surface morphology point cloud, displacements and stresses were included in the FE analysis results. Finally, differences between target and deformed geometry were identified and any differences quantified using the mean square error (MSE) metric.

Finally, an error compensation approach using a neural network trained using the deformed geometry from FE simulations and experiments is reported in Sections 7.3.3 and 7.3.4, respectively. The statistical analysis of the neural network predictions was performed for each artifact which includes coefficient of determination, error convergence plot and histogram. An overlay of target and compensated geometry illustrates the overall shape differences and binary layers were generated by slicing compensated STL file at optimal resolution for inkjet printing validation purposes. For the case of the FE simulations, the compensated geometry was FE simulated to find the deformed geometry and compared versus target to validate the compensation approach. For the case of experiments, compensated binary slices were printed for the cuboid case to show the effectiveness of the proposed approach. A summary of the main findings and conclusions close the chapter.

7.3 Results and discussion.

The aim of this section is to present the results of the experimental work, finite element simulations and the geometry compensation approach developed to improve the accuracy of 3D inkjet-printed parts.

7.3.1 3D printed artifacts using optimal printing settings derived for films.

A total of six differently sized and shaped artifacts were printed and analysed to evaluate part dimensional accuracy using the optimal printing parameters determined

in section 6.3.2.4. Each artifact brings specific fine features to test the capability of the inkjet printing process such as sharp corners, curved edges, holes, and squared cavities with sizes ranging from 0.2 to 3 mm. The number of layers used to build the artifacts were 75, 90, 75, 50, 75 and 81 at 0.01 mm slice thickness. The results of the printed samples are depicted in Figure 7-1 to Figure 7-6. Each figure includes the CAD geometry, top image of printed artifact, overlay of target vs real footprint and a comparison between the measured (magenta) and CAD surface (green) point clouds. Table 7-1 presents the deviations from the main target dimensions for each artifact.

Table 7-1 Comparison of real and target dimensions of printed artifacts.

Artifact	Average deviation from target dimensions			
	Width (μm)	Depth (μm)	Height (μm)	Diameter (μm)
Cuboid	30	168	-150	--
Cylinder	--	--	-85	109
Cage	43	234	-286	--
H-structure	35	181	-101	--
I-structure	78	195	-144	--
Sensor package	35	149	-127	--

The results show that most dominant deviation in all artifacts was present in the height of the specimen, which was in all cases shorter than target. Material flow beyond target footprint boundaries was observed in all specimens exceeding required dimensions. It is important to note that for the cage artifact, the wall thickness is not uniform, showing a larger deviation in top and bottom walls compared to left and right. Furthermore, for the H-structure, the internal cavity could not be fabricated accurately, missing completely the intended polygon shape. In addition, for the I-shape structure, the difference of the target geometry with the printed sample is much more pronounced in the top section of the structure where a reduction of the section is present. Finally, for the sensor package, the maximum material overflow was observed at the vertical squared slots on the top section, failing to achieve the target internal corners at from channels and slots.

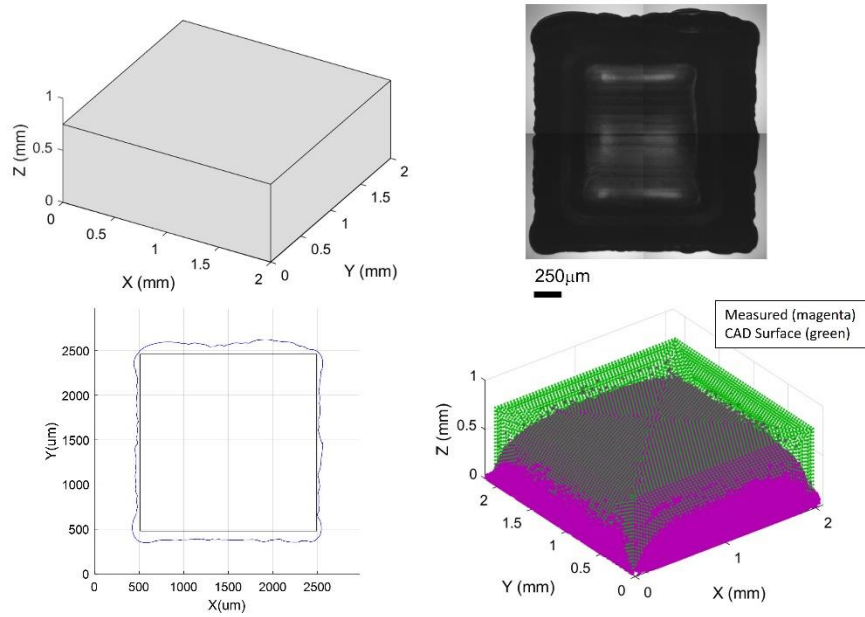


Figure 7-1 3D inkjet-printed cuboid results including CAD structure, Dimatix image, target vs real footprint and point cloud.

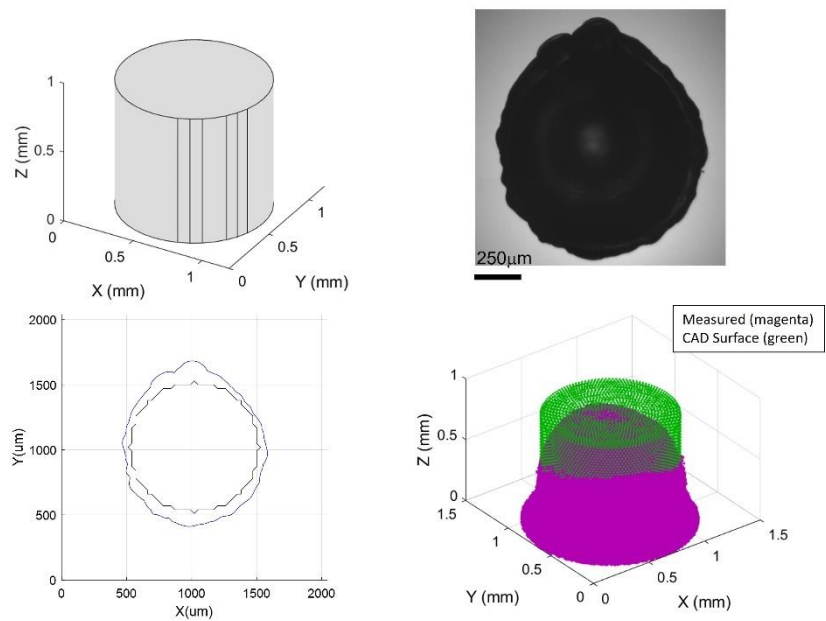


Figure 7-2 3D inkjet-printed cylinder results including CAD structure, Dimatix image, target vs real footprint and point cloud.

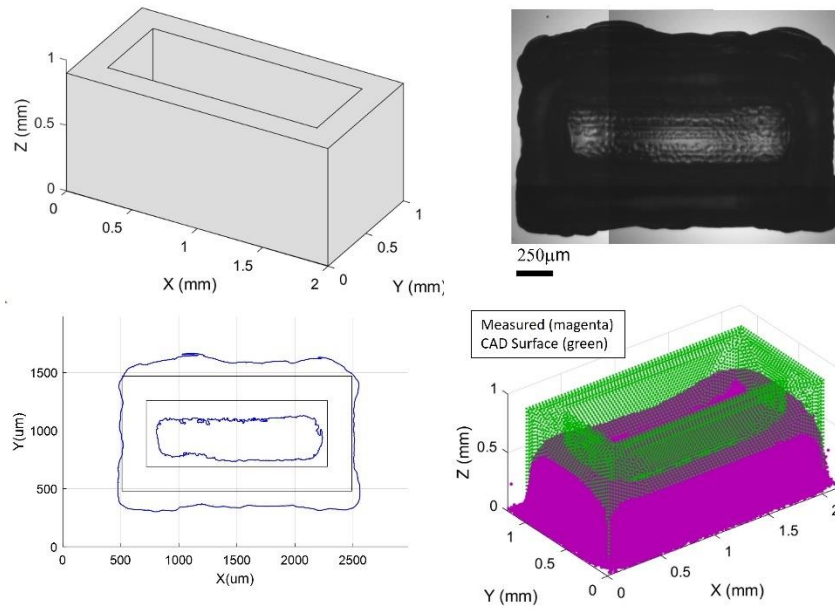


Figure 7-3 3D inkjet-printed cage results including CAD structure, Dimatix image, target vs real footprint and point cloud.

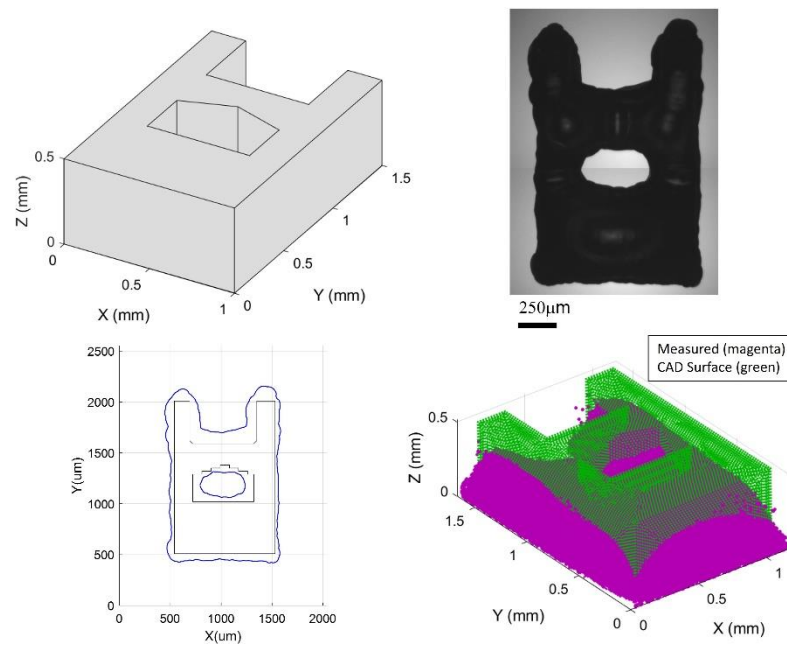


Figure 7-4 3D inkjet-printed H-structure results including CAD structure, Dimatix image, target vs real footprint and point cloud.

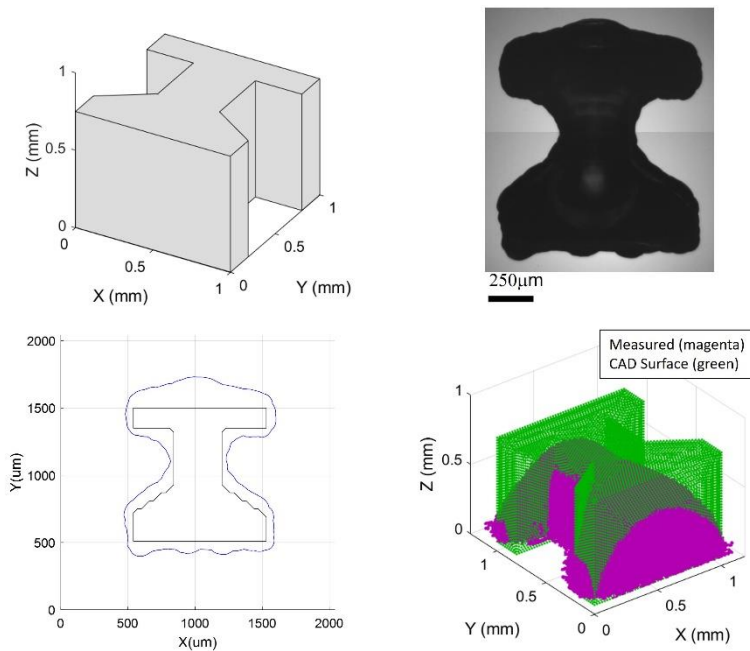


Figure 7-5 3D inkjet-printed I-structure results including CAD structure, Dimatix image, target vs real footprint and point cloud.

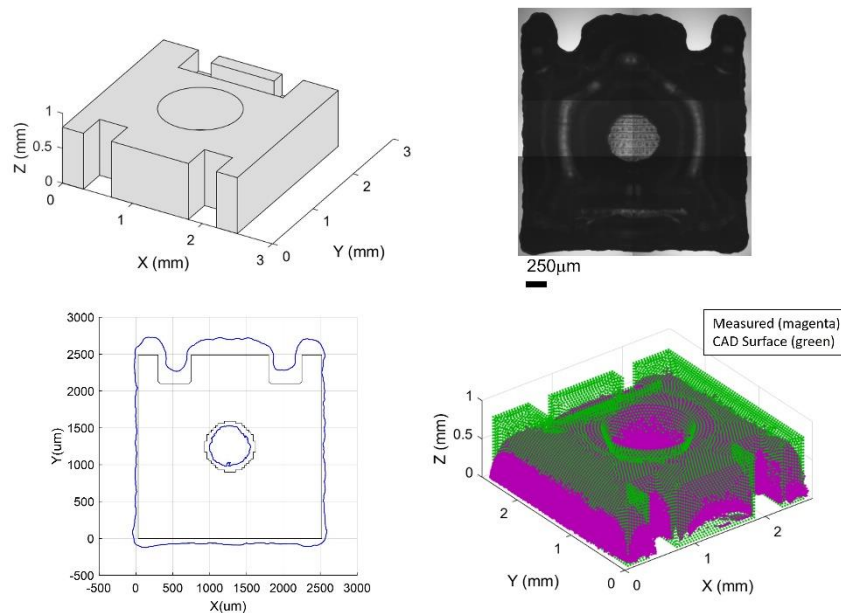


Figure 7-6 3D inkjet-printed TI sensor package results including CAD structure, Dimatix image, target vs real footprint and point cloud.

In summary, it is clearly demonstrated that using the set of optimal printing parameters derived for stable freeform films is not enough to accurately print 3D structures. All

the specimens present a height shorter than target and exceed the footprint dimensions, particularly in the cross-scan direction (Y-axis) which show deviations larger than the in-scan direction (X-axis). This behaviour is likely to be caused by the different printer tolerances in the scanning directions (i.e., tolerances are larger in the cross-scan direction). Furthermore, it was found that fine features such as corners, slots, holes, and channels do not match the intended shape owing to excessive material overflow at the pattern boundaries, particularly in the cage specimen as the hollowed pattern is deposited in the steepest section of the base layer. A potential cause of this phenomenon is the partial curing of the polymer film enabling the flow of the ink beyond the edge due to its liquid state. In addition, all specimens do not reach the target height, with the largest deviation in this dimension, which may be attributed to uneven volumetric shrinkage due to inhomogeneous curing of each layer. It is important to note that the first printed layer in all artifacts matches the target footprint quite accurately, validating the effectiveness of optimal printing parameters for single films regardless of the shape. Therefore, to fabricate accurate 3D printed parts additional process considerations need to be explored such as drop location uncertainty and partial curing of films. In the next section, an investigation into the effect of partial curing on the deformed geometry of 3D inkjet-printed artifacts is performed using a finite element approach.

7.3.2 Deformed geometry prediction model using a semi-empirical, semi-coupled photo-polymerisation and structural finite element approach.

A cuboid of size 1 mm x 1 mm x 0.5 mm is simulated using the finite element approach described in section 4.1.2. The degree of monomer conversion, Young's modulus and effective coefficient of thermal expansion are depicted in Figure 7-7a-c, respectively. The parameters employed to generate the material properties are shown at the top of each graph. The model assumes the bottom layer is fixed and the degree of monomer consumption per film is calculated using the optimal printing parameters derived in section 6.3.2. A comparison of the degree of monomer consumption distribution on a squared film with a printed sample is shown in Figure 7-8. Good agreement between film model and experiment is achieved, showing the bottom portion of the print partially cured.

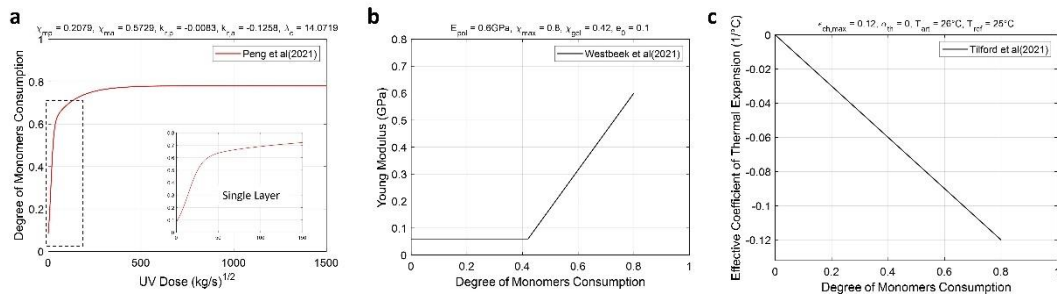


Figure 7-7 TPGDA material properties employed in FE simulation: a. Semi-empirical model of the degree of monomer consumption as function of UV dosage; b. Young's modulus as function of degree of monomer consumption assuming gel point at 0.42 and polymer Young modulus of 0.6 GPa; and c. Effective coefficient of thermal expansion (chemical contraction) assuming maximum chemical strain at 0.12.

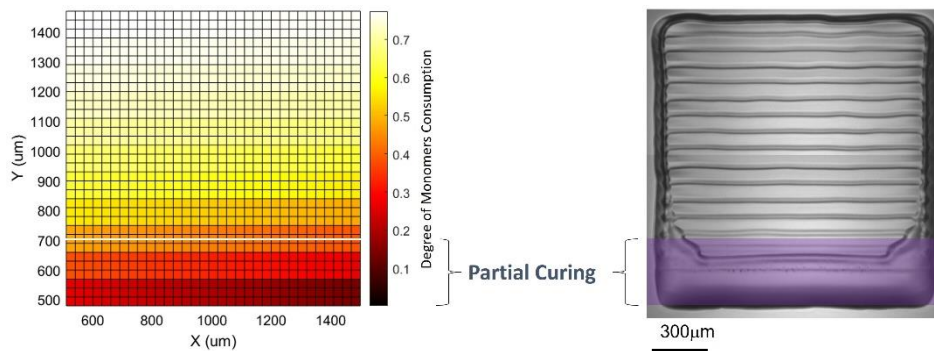


Figure 7-8 Comparison of the degree of monomer consumption distribution for a square film with the printed sample for the optimal printing parameters.

Since the interest of the current investigation lies in the geometrical prediction of the artifact, the analysis of the results is focused on displacements only. Residual stresses provided by the model are on the conservative side due to the linear elastic assumption from the constitutive model. The maximum stress is located at the bottom layer which is consistent with the fixed boundary conditions used to simulate pinning of the contact area. Stresses away from the constrained edge are 2 orders of magnitude below the Young's modulus. The results of the simulated cuboid are depicted in Figure 7-9. Printing origin is located at the upper left corner and swaths are generated from left to right in a unidirectional way, as shown in Figure 7-9a, mimicking the Dimatix printer settings. This is important since calculation of the UV dosage is location dependent. Figure 7-9b shows that the maximum shrinkage is at the top section of the printed artifact where the maximum degree of monomer consumption occurs. As the printing progresses to the bottom of the artifact, shrinkage linearly decreases due to the partial

curing of the last swaths, and higher mobility of the material is hence expected in this region. This difference in height between top and bottom sections, may explain the propensity of the material to flow towards the top section due to gravity, increasing the thickness of the film, as observed in the experiments performed in Chapter 6. Figure 7-9b illustrates the deformed shape of the cuboid with a magnification factor 2. The blue lines define the original target profile consisting of 50 layers, with each layer thickness set at 0.01 mm. As can be seen, the model requires 9 more layers to match the target height and compensate for the maximum predicted accumulated shrinkage of 83 μm . This number of layers is an upper limit, since material redistribution from bottom to top is not accounted for due to the restricted fluid behaviour of the model. Displacements in the Z-direction at the centre of the cuboid are plotted from top to bottom, presenting the overall shrinkage behaviour, as shown in Figure 7-9c. It was found that shrinkage mainly impacts the thickness of the printed structure. Furthermore, the model predicts a lateral offset towards the centre of the pattern due to cure shrinkage which although smaller than the shrinkage affecting the thickness of the printed structure does not reflect the actual material flow over the previously deposited layer boundary. This is a critical limitation of the current model to accurately predict the deformed geometry of 3D inkjet-printed parts. Figure 7-9d depicts an overlay of the predicted and target point clouds for comparison purposes. Therefore, it is concluded that under the current model assumptions, prediction of the deformed geometry does not adequately capture the material overflow observed in experiments. Note that the predicted geometry in this work is mainly used to demonstrate our proposed geometry compensation framework.

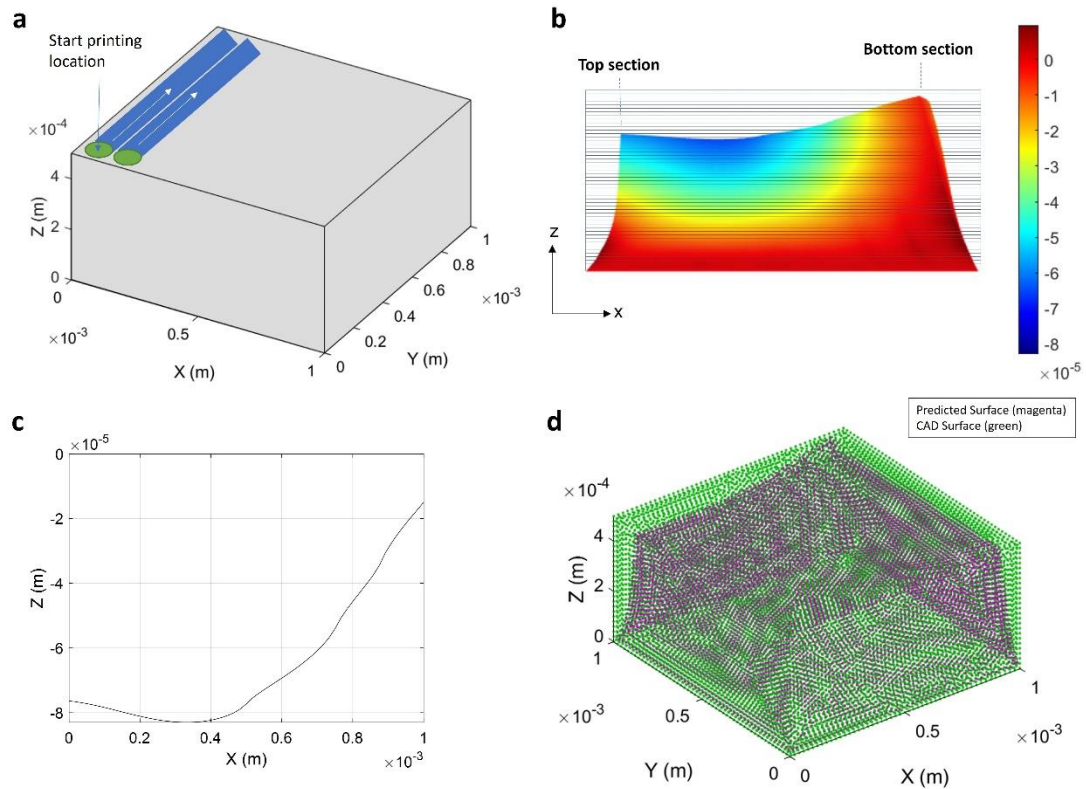


Figure 7-9 FE Results for the cuboid artifact: a. Schematic showing part orientation, printing origin and direction; b. Z-displacements contour plot with 50 layers overlaid (magnification factor = 2); c. Shrinkage behaviour of cuboid surface from top to bottom section; and d. CAD vs predicted point cloud overlay.

A total of six differently sized and shaped artifacts were simulated and analysed to obtain the deformed geometry to test the proposed geometry compensation framework. The number of layers used to build the artifacts were 75, 90, 75, 50, 75 and 81 at 0.01 mm slice thickness. The results of the simulated specimens are depicted in Figure 7-10. The figure includes the target geometry, the deformed geometry, a comparison between the predicted (magenta) and target (green) point clouds and the absolute deviation between both geometries ordered by columns. Overall, the model is capable of predicting the magnitude of the maximum thickness shrinkage fairly accurately, which validates the simplifying methodology of using static restarts instead of transient model, which reduces the FE solution time from days to minutes. However, the model does not capture the material spreading over the substrate, which is typically present in experiments, due to the perfect adhesion assumption used for the bottom layer. A potential improvement to the FE model is to incorporate the substrate geometry and model the interface assuming a friction coefficient to capture bottom layer displacements. Nevertheless, the number of layers to reach the required height

of the artifacts can be calculated just by dividing the maximum shrinkage by the assumed slice thickness, providing a simple way to compensate errors in the Z-direction. However, a more accurate compensation scheme is presented in the next section which corrects geometry in X, Y and Z directions and builds the binary slices to print the part automatically.

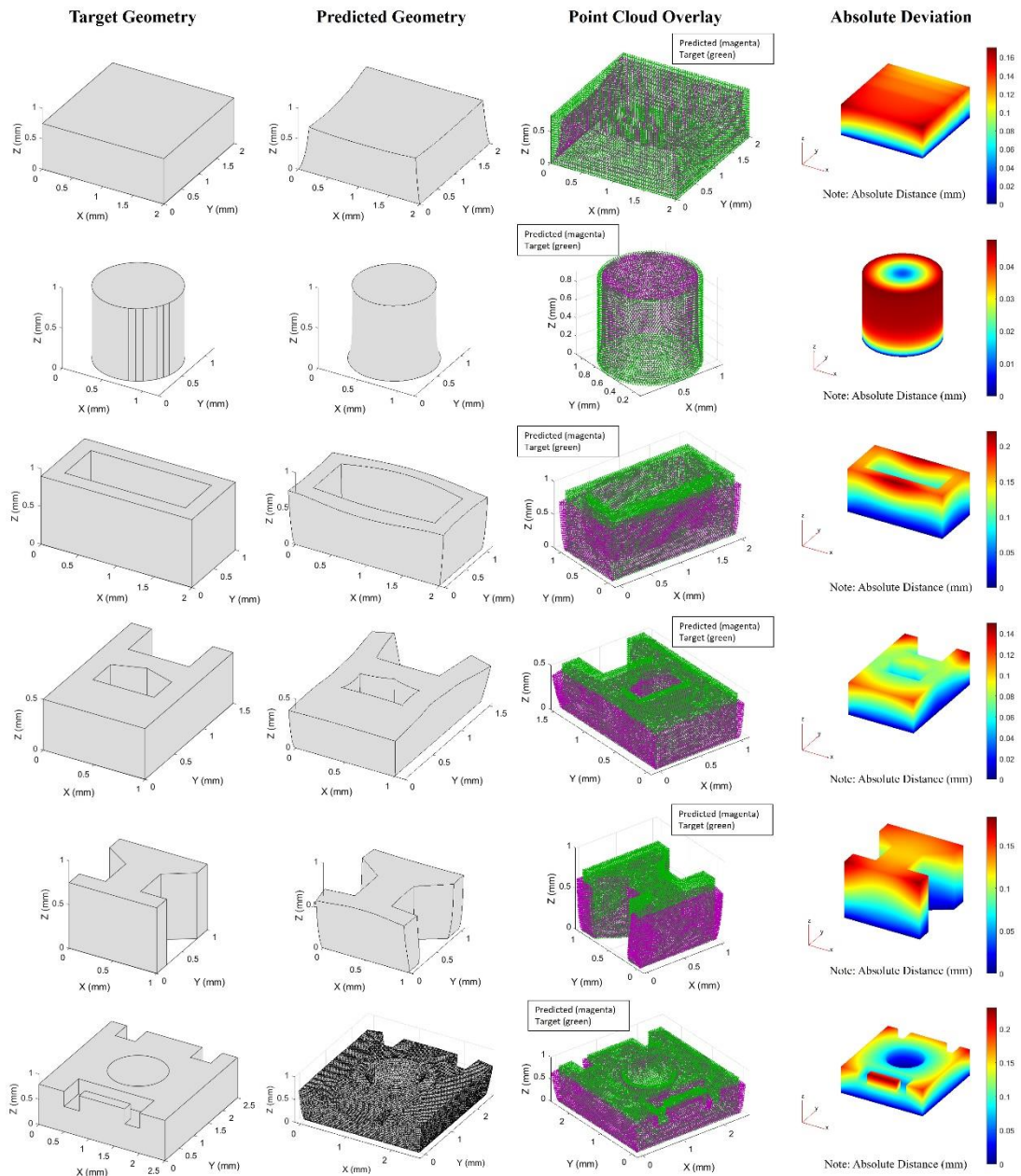


Figure 7-10 FE simulation results. Target geometry, predicted geometry, overlay of target vs predicted point clouds and absolute deviations ordered by columns, respectively.

Table 7-2 lists FE parameters such as number of elements and element size as well as the maximum deviation and mean square error between target and deformed geometries.

Table 7-2 FE parameters, simulation results and solution time.

Artifact	Mesh size (μm)	Number of elements (#)	Max absolute deviation (μm)	Maximum shrinkage (μm)	MSE (μm^2)	CPU time (s)
Cuboid	35	571939	170.5	-140.1	15.1	71
Cylinder	25	373639	48.2	-10.6	1.7	60
Cage	30	324398	221.3	-158	12.5	48
H-struct	20	538930	150	-104.7	4.6	66
I-struct	20	544560	183.6	-139.5	10	75
TI sensor	40	544510	231.1	-150.9	12.3	57

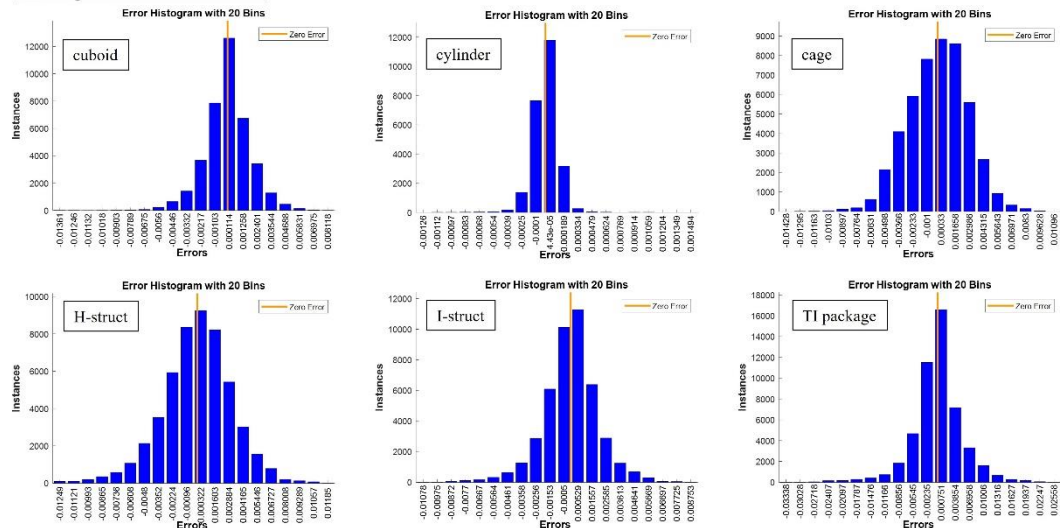
In the next section, the results of the geometry compensation framework using a machine learning approach are presented. FE predictions of the deformed geometry in the form of x, y and z coordinates are used to train a neural network and build a transfer function in order to obtain the compensated geometry required to minimise the mean square error (MSE) between target and predicted geometry.

7.3.3 Geometry compensation and validation using a neural network trained with results from FE simulations.

This section presents results from applying the geometry compensation framework explained in Section 4.5.2 using the predicted geometry from the chemo-mechanical FE simulation. Nodal coordinates from the FE simulation model before and after the deformation are employed to train the neural network iteratively until the mean squared error determined from geometry deviations is minimised. Before the network training is carried out, the deformed and target point clouds are aligned using the iterative closest point registration method. Figure 7-11 depicts the prediction error histogram and MSE minimisation plot of the neural network training process for the six artifacts tested in the investigation. The coefficient of determination for the six regression models is 0.9999. The residuals resulting from the network training are normally distributed with maximum value at ± 2.5 standard deviations within $5 \mu\text{m}$. The network training stopped when the predefined maximum number of iterations was

reached, but clearly the mean squared error has converged to minimum value. Therefore, our neural network model is statistically valid and is able to approximate the part deformed geometry as a function of the coordinates of its surface points.

Histograms of residuals



Mean squared error convergence plots

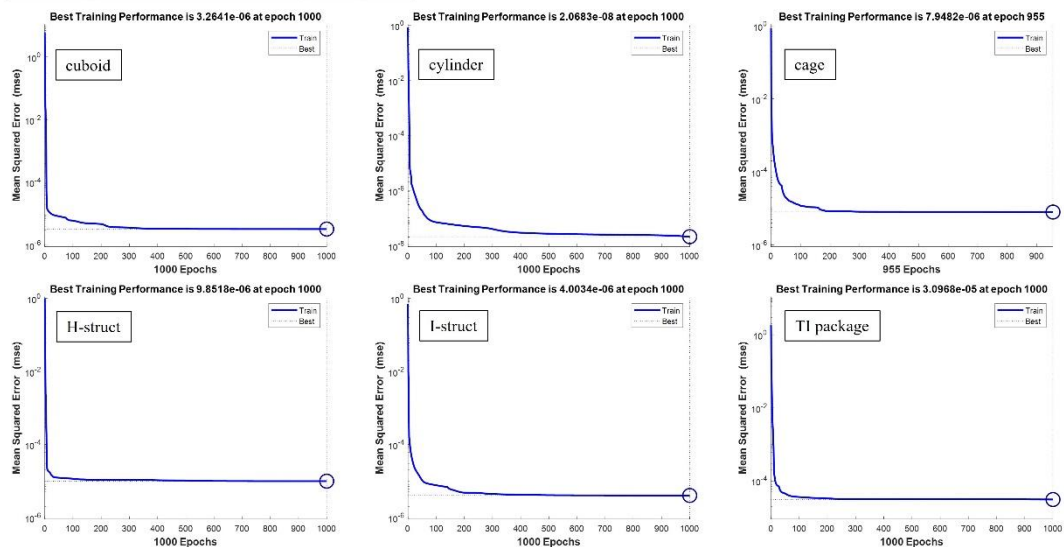


Figure 7-11 Neural network training process statistical analysis results including histogram of residuals and mean squared error convergence plots.

The compensated geometry is predicted by the trained neural network using the coordinates of the vertices from the target shape as input. The output of the network are the new 3D coordinates of the vertices from which the compensated shape is built. A total of six differently sized and shaped artifacts were compensated to evaluate the effectiveness of the machine learning framework. Figure 7-12 depicts the compensated

shape in STL format, the target vs compensated geometry overlay and the point cloud overlay before and after compensation for validation purposes.

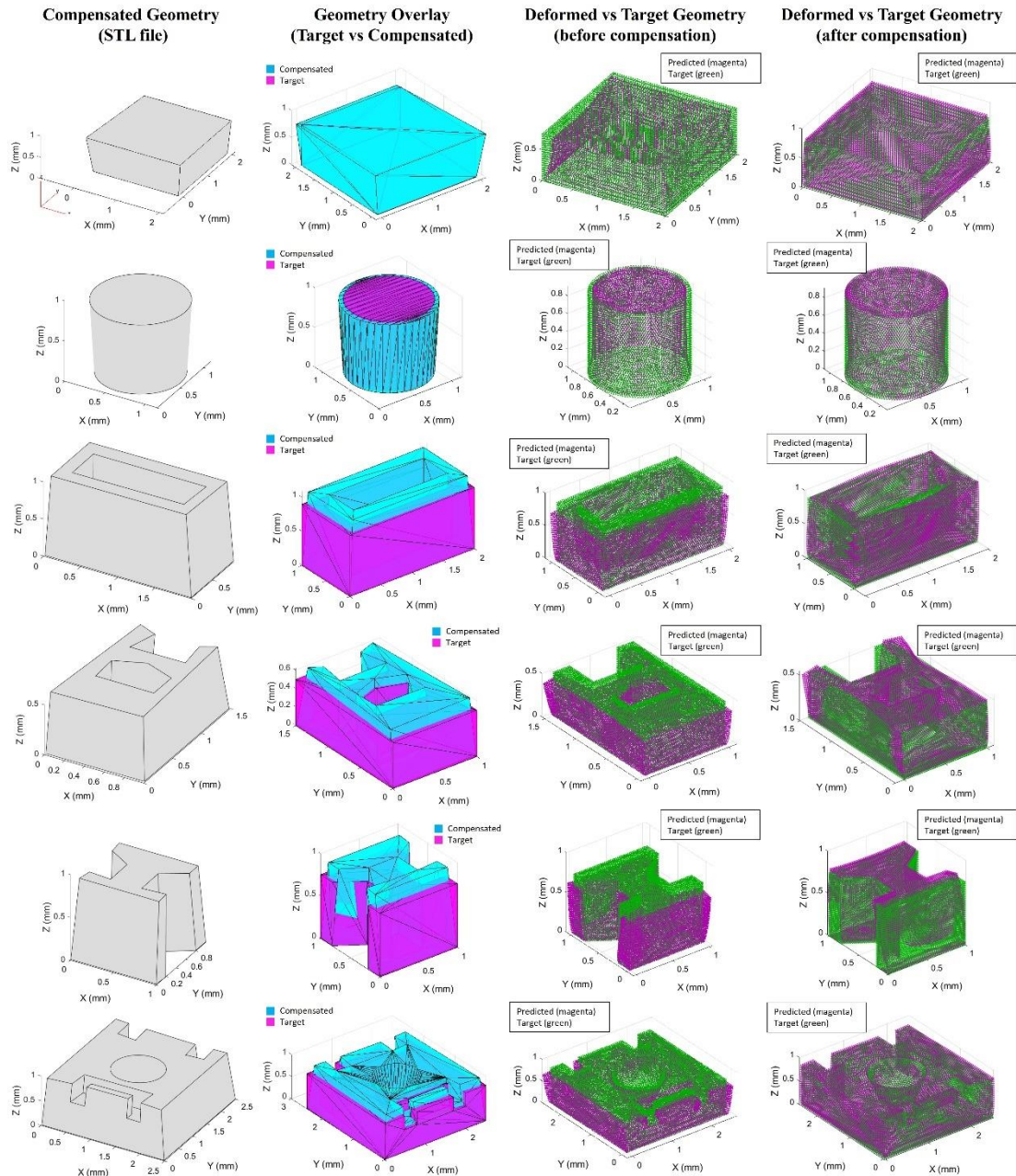


Figure 7-12 Geometry compensation framework results using FE simulation for neural network training process.

Overall, the geometry compensation framework is able to construct the shape in STL format which is vital to obtain binary layers for 3D inkjet printing application. For the cuboid and cylinder artifacts, a negative taper on the external faces of the compensated geometry is present (e.g., inverted truncated pyramid shape), since in both cases the

deformed geometry predicted by the FE simulation is fully contained in the target geometry and its cross-section area gradually reduces along the part height. For the rest of the artifacts, a positive taper on the external faces of the compensated geometry is present (e.g., truncated pyramid shape), since the deformed geometry predicted by FE simulation exceeds the lateral boundaries of the target geometry and grows almost linearly with part height. In addition, as can be seen in the geometry overlay in Figure 7-12, there is a clear increase in the height of the compensated geometry to account for the shrinkage observed in the predicted deformed geometry. It is important to note that fine internal features such as cavities, slots or channels and external patterns with pronounced changes in cross-sectional area (e.g., I-shape artifact) present a negative taper shape to account for the material excess noticeable in the FE predicted geometry. For validation purposes, the compensated geometry is FE simulated under the same assumptions as target geometry and a comparison of the shapes before and after compensation are illustrated in Figure 7-12. The results visibly show a closer match between the deformed and target shapes after the compensation process is applied for all tested artifacts. It was found that the maximum absolute deviation in micrometres after compensation was 63, 34, 182, 94, 105 and 66, respectively, which represents a net reduction in the maximum deviation from target of 44%. Deviations larger than the dot size (65 μm) are observed in the cage, h-structure and I-structure which could be attributed to inaccurate compensation when large bending of sections is present. To quantitatively evaluate the effectiveness of the compensation approach, the mean squared errors (MSE) before and after compensation are reported in Table 7-3. Considering all artifacts, the average MSE reduction between target and predicted geometries is 89%, validating our proposed machine learning geometry compensation framework.

Table 7-3 Comparison of the mean squared error before and after compensation.

Artifact	MSE before compensation (μm^2)	MSE after compensation (μm^2)	MSE Reduction (%)
Cuboid	15.1	1.50	90.1%
Cylinder	1.7	0.44	74.1%
Cage	12.5	1.54	87.7%
H-struct	4.6	0.44	90.4%
I-struct	10	0.61	93.9%
TI sensor	12.3	0.45	96.3%

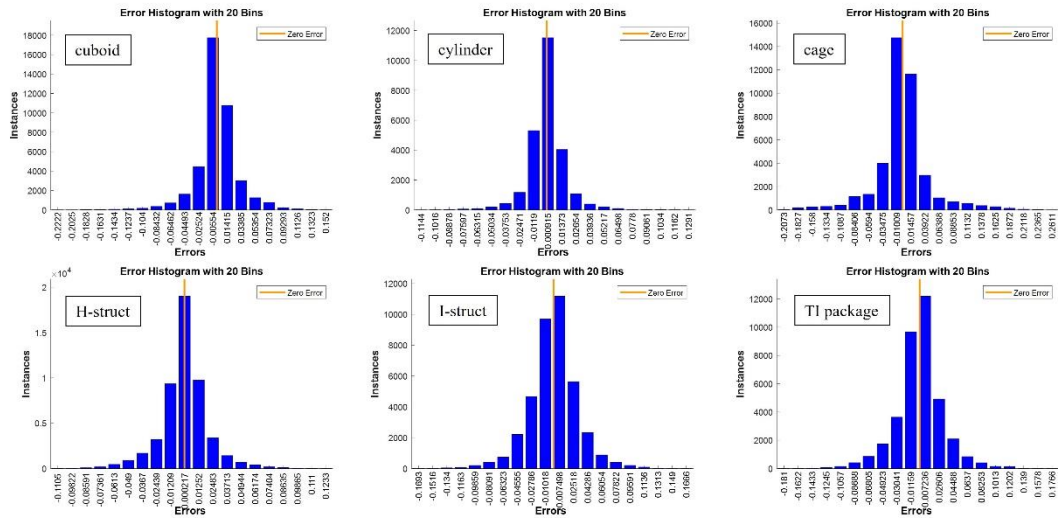
Although the compensation framework has proven to be valid for in silico experiments where the target and deformed geometries have the same number of nodes, it is critical to investigate if the same approach can be used when the deformed geometry definition comes from measurements of lab experiments (e.g., target and deformed geometries have different number of nodes). Therefore, in the next section, microCT scan measurements of the deformed geometry in the form of x, y and z coordinates are used to train a neural network, build a transfer function, and determine the compensated geometry required to minimise the mean square error (MSE) between target and measured geometry.

7.3.4 Geometry compensation and validation using a neural network trained with experimental measurements.

This section documents the results of the geometry compensation framework explained in Section 4.5.2 using measured data from the 3D printed artifacts. Nodal coordinates from microCT scan measurements together with their corresponding locations in the target geometry were employed to train the neural network iteratively until the mean squared error determined from geometry deviations was minimised. Before the network training was carried out, the measured and target point clouds were aligned using the iterative closest point registration method. Since the point cloud of measured data was extremely dense, a one-to-one correspondence between target nodes and measured data was determined employing an in-house mapping algorithm. Figure 7-13 depicts the prediction error histogram and MSE minimisation plot of the neural network training process for the six artifacts tested in the investigation. The coefficients of determination of the regression models were 0.999, 0.998, 0.995, 0.998, 0.995 and 0.999. The residuals resulting from the network training were normally distributed with the following maximum values at ± 2.5 standard deviations: 78 μm , 51 μm , 111 μm , 61 μm , 80 μm , and 84 μm , respectively. The network training process stopped for all cases when the mean squared error converged to a minimum value without reaching the maximum number of iterations limit. Although, the coefficients of determination indicate an excellent correlation between predicted and target values, the magnitude of the residuals is in the order of 100 μm which is not adequate for our purpose. Therefore, our regression models are statistically valid but not accurate

enough to approximate the part deformed geometry as a function of the coordinates of its surface points. The most likely cause of the large error in the prediction model is the presence of outliers in the measurement data point clouds. It was found that the mapping algorithm picked points inside the deformed geometry surface which introduced a large variation in the regression model. It is, therefore, recommended that in future work measurement data point clouds are filtered so that only points defining the deformed surface are kept for training the neural network. Nevertheless, from the application of the compensation framework using experimental data documented in this section, it can be seen that this is an effective method of ensuring 3D printed parts correspond to geometry specifications.

Histograms of residuals



Mean squared error convergence plots

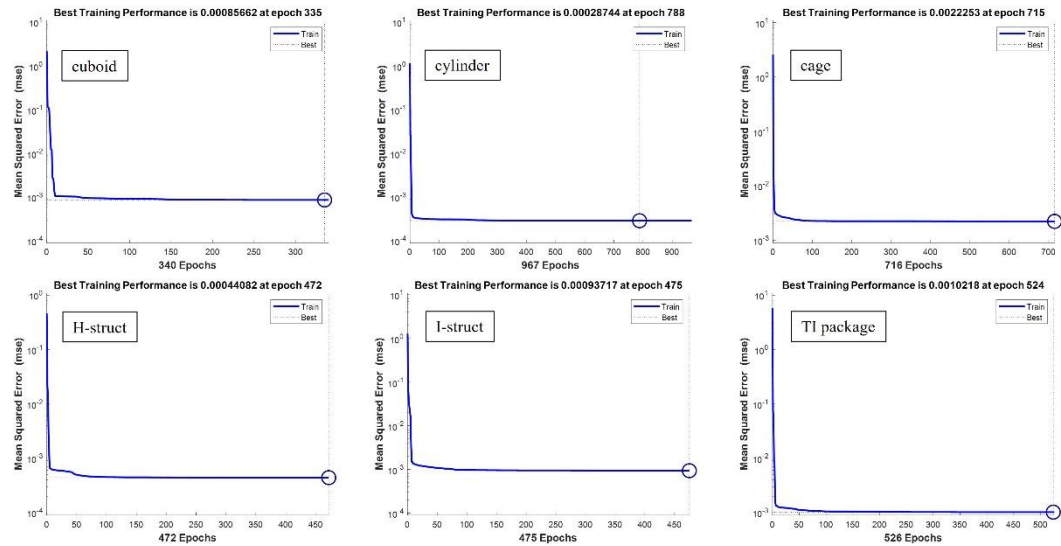
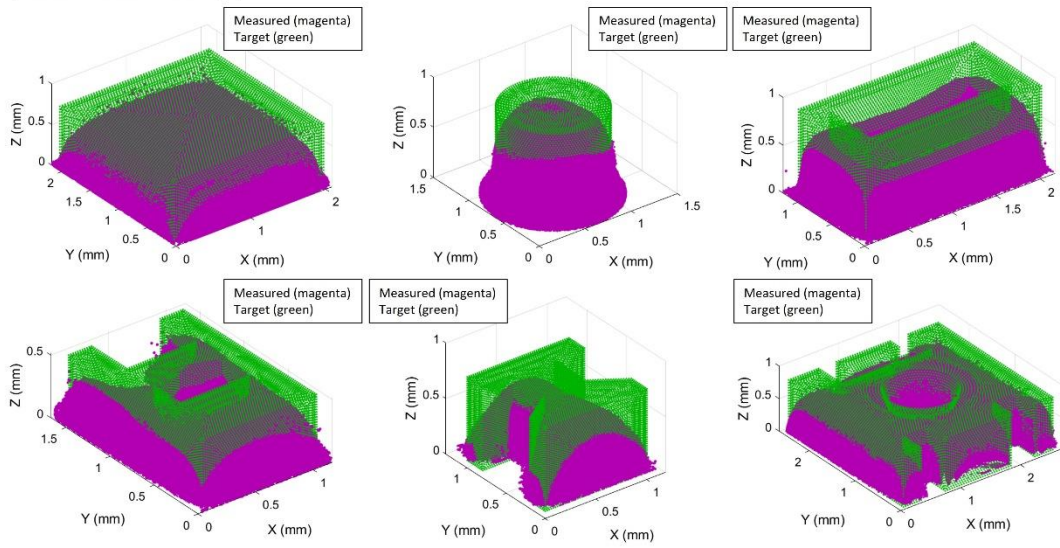


Figure 7-13 Neural network training process statistical analysis results including histogram of residuals and mean squared error convergence plots.

The target geometry of six differently sized and shaped artifacts was compensated using the neural networks trained with experimental measurements. Figure 7-14 depicts a comparison of the target shape and measured data point clouds as well as the compensated STL overlaid on target STL geometry.

Point Cloud Overlays



Geometry Overlays

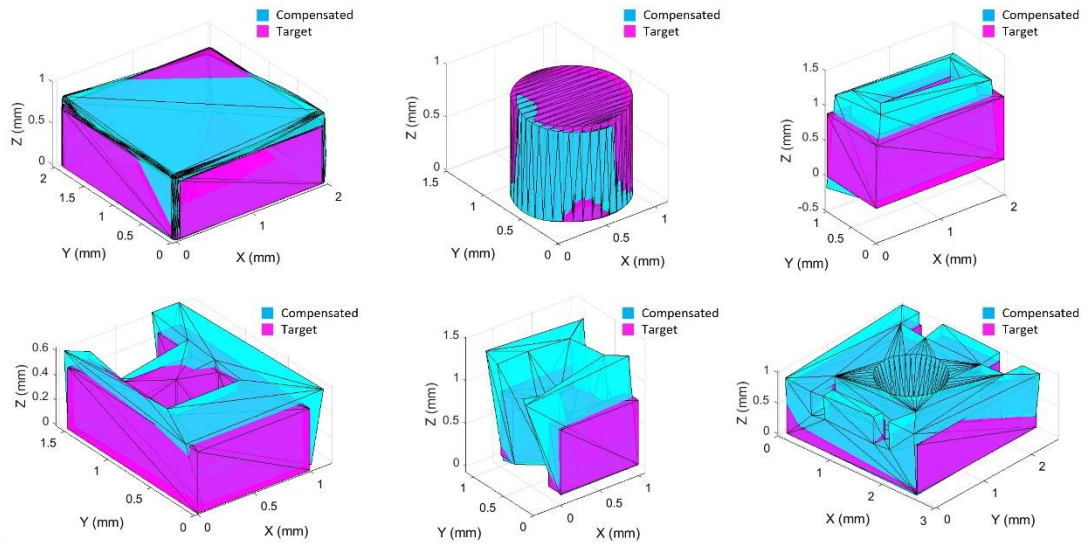


Figure 7-14 Compensated geometry using experimental data for neural network training process.

As can be seen from the point cloud overlays, the measured geometry of the artifacts does not match the intended geometry. All printed artifacts present material overflow beyond the boundary faces of the target and, consequently, the required height of the artifact is not reached. It is found that the printed artifacts with the minimum and maximum deviation to target are the cylinder and cage shapes, respectively. A detailed explanation of the experimental results can be found in Section 7.3.1. Analysing the geometry overlays illustrated in Figure 7-14, it is clearly seen that our machine learning model trained with measured data can compensate the original shape and build a STL file, which is vital to obtain binary layers for 3D inkjet printing

application. The compensated geometry of all artifacts presents a negative taper on the external faces (e.g., inverted truncated pyramid shape), since the cross-sectional area of the measured artifacts gradually reduces along the part height and away from target. The reduction of the area at bottom section of the compensated geometry is particularly pronounced to control material spreading beyond the target footprint. In addition, there is a clear increase of the height in the compensated geometry to meet the height dimension of the target shape. It is important to note that fine internal features such as cavities, slots or channels and external patterns with large changes in cross-sectional area (e.g., I-shape artifact) present a positive taper shape to account for the material excess detected in measured data. Although the compensation framework works with experimental data, the variation introduced by the measurements affects the accuracy of the prediction. Some of the vertices located at the bottom of the compensated shapes (e.g., cage artifact) are predicted below the base plane, which is not correct. Furthermore, the compensated height for the I-structure is almost twice the target height which seems inaccurate and could be explained due to the large residuals observed in the regression model.

Validation of the geometry compensation framework is conducted by a direct comparison to printed samples. Binary layers are generated from the compensated STL geometry of the cuboid artifact and printed with the optimal parameters determined in Section 6.3.2.4. Figure 7-15 illustrates DIMATIX images of the first eight layers of the cuboid using the compensated geometry. The first layer is printed employing the uncompensated pattern since film morphology matches fairly well with the target footprint. Compensated binary patterns are printed starting from second layer. As can be seen, the excess of material flow beyond the target footprint is no longer present in the printed artifact. The deformed shape still shows rounded corners, but it is qualitatively closer to target. The difference in height between the target and printed samples is greatly reduced from 140 μm to 27 μm due to the addition of 12 layers resulting from the height compensation. To quantitatively evaluate the effectiveness of the compensation approach, the mean squared error (MSE) between target and measured geometries, before and after compensation is determined. The percentage of reduction in the error due to the compensation strategy for the cuboid artifact is 72%, validating our proposed machine learning geometry compensation scheme with experimental data.

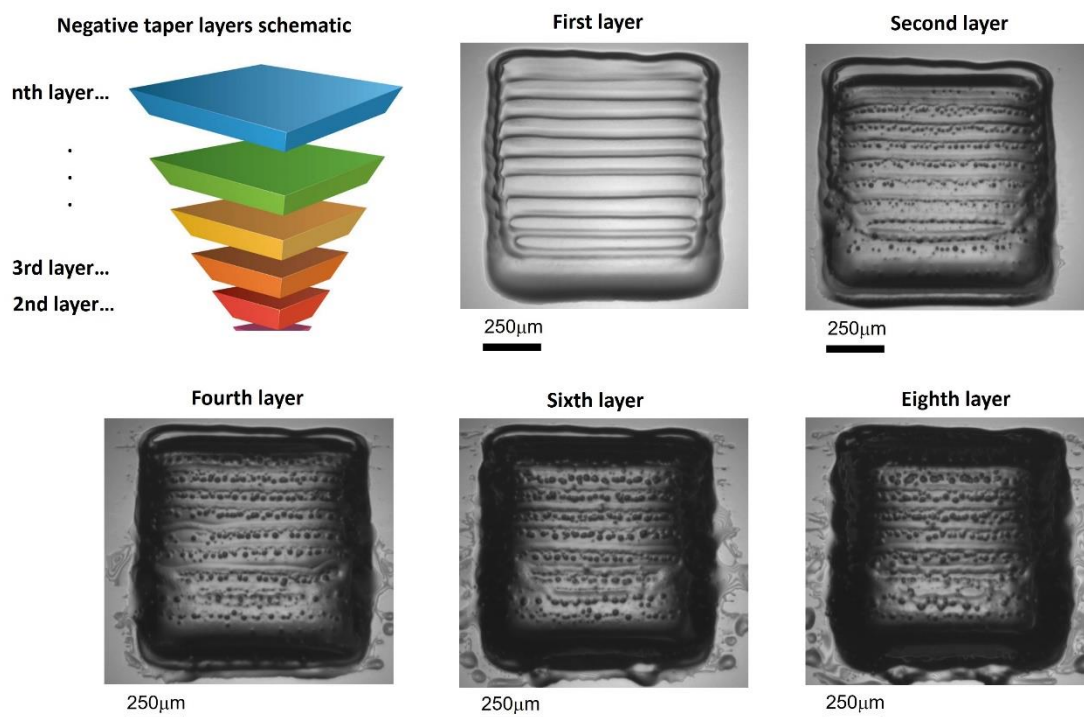


Figure 7-15 Validation of geometry compensation framework by direct comparison to printed samples. Layer Schematic and Dimatix images included.

7.4 Conclusions and summary.

In this chapter, a chemo-mechanical FE model to predict the deformed geometry of 3D inkjet-printed parts and a geometry compensation framework using a machine learning approach are implemented to improve the dimensional accuracy of 3D structures.

Printed artifacts using optimal printing parameters derived in Chapter 6 present very large deviations to the intended geometry, predominantly in the height dimension, suggesting additional physical considerations need to be investigated to achieve stable parts. Experimental observations of printed samples indicate that film partial curing plays a critical role determining final part deformation, due to its influence on the evolution of material properties. Therefore, to predict the deformed geometry considering curing characteristics in addition to printing parameters, a semi-empirical, semi-coupled photo-polymerisation and structural finite element approach is introduced. In this FE model, the degree of monomer consumption of TPGDA determined from experiments is used as an internal variable to characterize the

Young's modulus and volumetric shrinkage. A layer-by-layer FE simulation is setup using multiple restarts and predicted part deformations are determined. The comparison between the experiments and simulations indicate that the semi-empirical, semi-coupled model can capture adequately the maximum deformation of the printed structure due to chemical shrinkage in a timely manner. However, the model predicts a lateral offset towards the centre of the pattern due to cure shrinkage which although smaller than the shrinkage affecting the height of the printed structure does not reflect the actual material flow over the previously deposited layer boundary. This is a critical limitation of the current model to predict accurately the deformed geometry of 3D inkjet-printed parts. Therefore, the predicted geometry is not developed further to increase accuracy, but is instead used to demonstrate our proposed geometry compensation framework.

Since large deviations are observed between target, predicted and measured artifacts, a machine learning-based geometry compensation framework is employed to counteract the deformations resulting from the inkjet printing process. A neural network is trained using the nodal deviations resulting from the difference between target and deformed geometry. Two data sources defining deformed geometry are used to train the network: FE simulation results and experimental measurements. The compensated geometry is predicted by the trained neural network using the coordinates of the vertices from the target shape as input. For both sources, the results show significant improvements in the part's geometric accuracy after the compensation process is applied, validating the effectiveness of the proposed approach. However, when the deformed geometry is obtained from measured data, the neural network model shows larger residuals, and it is recommended that to further enhance the accuracy of the model, a thorough cleaning process of the measurements data is undertaken to reduce variability. Finally, validation of the geometry compensation framework was conducted by a direct comparison to printed samples, showing good agreement between target part design and printed artifact. Overall, it is concluded that our proposed framework successfully counteracts the deformations resulting from the inkjet printing process, improving the dimensional accuracy (quality) of 3D printing parts.

Although incorporating the effect of UV curing in the prediction model of 3D components helped understand the deformation mechanisms observed experimentally,

other material and process mechanisms occurred in practice that limited the accuracy of predictions. Therefore, the need to explore other sources of variation such as the uncertainty in droplet location and size introduced by equipment tolerances is explored in next chapter together with a multiphysics analytical framework for the fast prediction and optimisation of inkjet-printed components.

8 Analytical model-based prediction and optimisation of the morphology of inkjet-printed parts.

8.1 Introduction.

The physics-based and data-driven models described in previous chapters to simulate the deposition and solidification of droplets as well as the overall part deformation provide an effective solution of the governing physics equations behind inkjet printing for small and simple shapes. However, considering larger and freeform shapes, as required in real-life printing applications, increases the simulation time from hours to days. Although, a significant reduction in the solution time without losing much accuracy was achieved by implementing a surrogate model from a sample of high-fidelity simulations, the prediction of large, freeform shapes is still computationally intensive. Furthermore, the previous models do not consider the effects of droplet position and size uncertainty or the simultaneous use of nozzles, which play a key role in the quality of inkjet-printed parts. Therefore, in this section an analytical model is introduced for the fast and accurate prediction of the surface morphology of inkjet-printed parts for any size and shape, considering droplet size and position uncertainty, multi-nozzle printing, UV exposure time and chemical shrinkage. From the author's point of view this analytical model represents the most significant contribution of the present work, since it leverages learnings from the physics-based and data-driven models and integrates creative algorithms and heuristics rules to drive AM part quality optimisation within a computational inkjet printing environment.

8.2 Methodology.

The aim of this chapter is to present the results of the stochastic prediction model derived in Section 4.3. Details about the proposed framework to predict the surface morphology of selected features, to find the optimal printing parameters and compensate the printed geometry based on predictions are described in Section 4.6. First, a summary of the physical properties characterisation and measured droplet characteristics employed in the analytical model is presented in Section 8.3.1. Details

about the procedures employed to perform the physical properties and droplets characterisation can be found in Section 3.2. Then, the analytical model validation is presented, via experiments of printed single tracks employing different substrates and droplet sizes, in Section 8.3.4. Next, the effect of multi-layer printing with different wettabilities on footprint and thickness dimensions is investigated via experiments. Furthermore, predictions of single tracks, freeform films and 3D structures with varying printing parameters, droplet characteristics, droplet location and size uncertainty, number of nozzles and wettability are included in Sections 8.3.5, 8.3.6 and 8.3.7, respectively. Finally, a graphical user interface developed for the digital image generation, surface morphology prediction and geometry compensation is introduced.

8.3 Results and discussion.

8.3.1 Experimental results for analytical model calibration.

The results from the experiments performed to characterise TPGDA density, viscosity, and surface tension are listed in Table 8-1. Viscosity and surface tension are consistent with values obtained by He et al. (2017), but density is 10% lower than that reported value in this reference. The difference in density results could be explained by experiment variability when measuring small volumes. These physical properties are inputs to the analytical prediction model and remain fixed in this investigation.

Table 8-1 TPGDA measured physical properties.

Property	Units	Temperature	Sample size	Average	Std deviation
Density	g/ml	22°C	5	0.930	0.039
Viscosity	mPa s	22°C	3	9.780	0.231
Surface tension	mN/m	25°C	5	30.960	0.224

The printability diagram illustrated in Figure 8-1, confirms that our ink is printable considering a droplet with ejection velocity of 6 m/s and measured in-flight volume of 9.55 ± 0.19 pL, which remain fixed for the predictions.

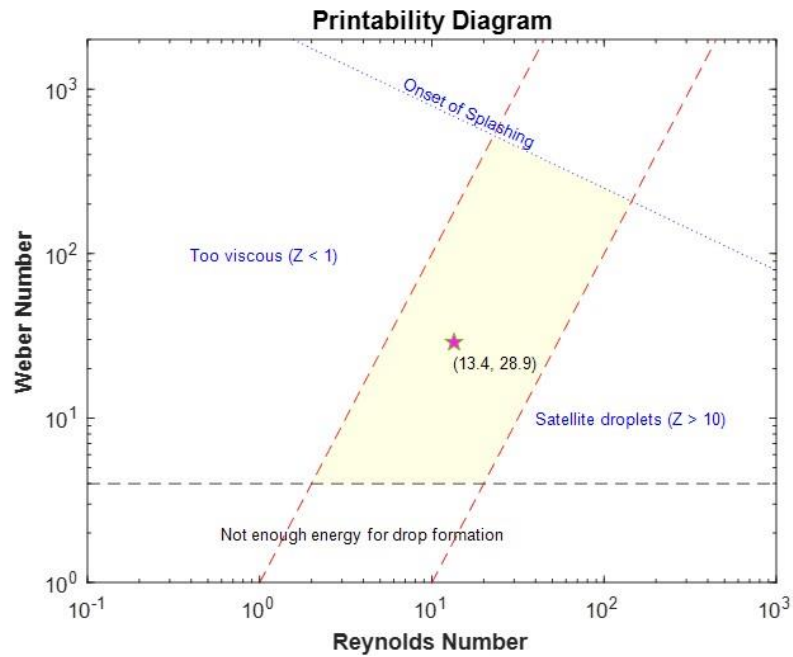


Figure 8-1 TPGDA printability diagram.

For droplet characterisation, three replicates of a 10x10 grid of TPGDA droplets deposited on a glass substrate with 10-pL native volume printhead were analysed. Drop spacing, printing frequency and standoff distance were set to 150 μm , 1 kHz and 0.5 mm, respectively. The results from the experiments performed to obtain basic statistics of footprint diameter size and droplet location and size uncertainty are listed in Table 8-2. Two sets of measurements of the printed grid were determined by image analysis and coherence scanning interferometry (CSI), respectively. CSI measurements were used to validate the results of the image analysis technique, which is a faster method to extract data from images taken with the DIMATIX fiducial camera. The results show excellent agreement between both techniques with deviations within 2.5 μm . Therefore, image analysis is employed from this point forward in this investigation to measure footprints of experiments. Details about the validation of the image analysis process with single tracks and freeform films can be found in Appendix 11.2.

Table 8-2 Droplet footprint size and location statistics.

Dimension	Units	Image Analysis	CSI
Maximum grid diameter	μm	68.1	66.4
Minimum grid diameter	μm	60.0	60.4
Average grid diameter	μm	63.7	63.8
Std. Deviation grid diameter	μm	1.4	1.0
Average drop spacing (X-direction)	μm	147.5	148.7
Average drop spacing (Y-direction)	μm	147.7	148.8
Std. deviation drop spacing (X-direction)	μm	3.5	3.8
Std. deviation drop spacing (Y-direction)	μm	3.6	3.8
Drop position variation (X-direction)	μm	0.58	0.63
Drop position variation (Y-direction)	μm	0.60	0.63
Abs. drop position error (X-direction)	μm	2.5	1.3
Abs. drop position error (Y-direction)	μm	2.3	1.2

Estimated values for droplet height and contact angle assuming droplets follow a spherical cap shape are compared to CSI grid measurements on Table 8-3. To estimate the post cured droplet volume, a volumetric shrinkage of 12% is assumed from experiments reported by Schmidt & Scherzer (2015). Results show excellent agreement with very small differences in height and volume. Therefore, the spherical cap equations and the assumed shrinkage value provide accurate estimates of the out-of-plane droplet dimensions and from this point forward are used in conjunction with image analysis for droplet morphology characterisation.

Table 8-3 Estimated values for droplet height and volume.

Dimension	Units	Spherical Cap Equations	CSI
Maximum droplet height	μm	5.3	5.4
Minimum droplet height	μm	4.1	4.2
Average droplet height	μm	4.7	4.7
Std. deviation droplet height	μm	0.2	0.2
Average contact angle (post-curing)	°	16.8	15.7
Std. deviation contact angle (post-curing)	°	0.8	0.8
Average droplet volume (post-curing)	pL	7.5	7.6
Std. deviation droplet volume (post-curing)	pL	0.2	0.2

Knowing the average and standard deviation values of the measured droplet volume (in-flight), post-curing contact angle and volumetric shrinkage factor, the footprint diameter's distribution is calculated using Equation (52) and compared to the measured distribution in Figure 8-2. Results show good agreement between the analytical model based on volume conservation assumptions and the actual measured

footprint diameter's distribution, validating the model from an accuracy and precision standpoint.

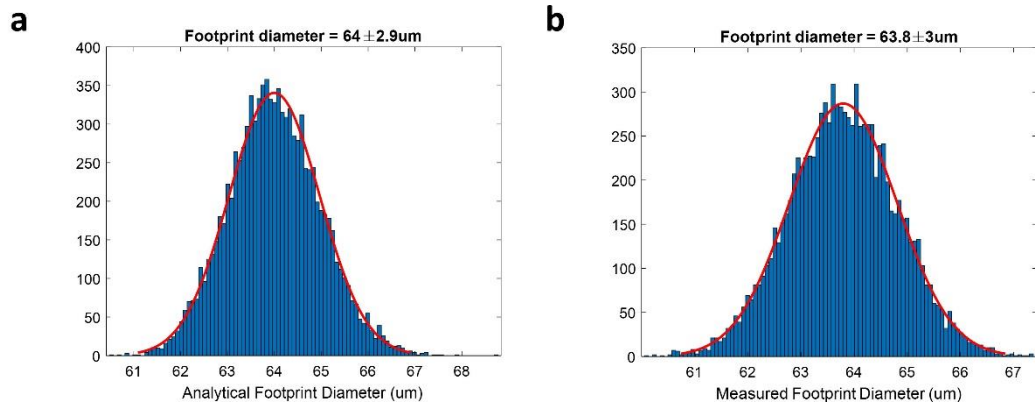


Figure 8-2 Comparison of footprint diameter normal distribution: a) analytical model and b) measured data.

In the same manner, knowing the average and standard deviation of the droplets position error in both X and Y directions, the drop position error normal distribution was calculated using image analysis measured values and illustrated in Figure 8-3. The original position of the droplets considering a constant drop spacing is corrected by this error distribution and new locations of the droplet's centre are determined. This model assumes the error distribution does not degrade with time.

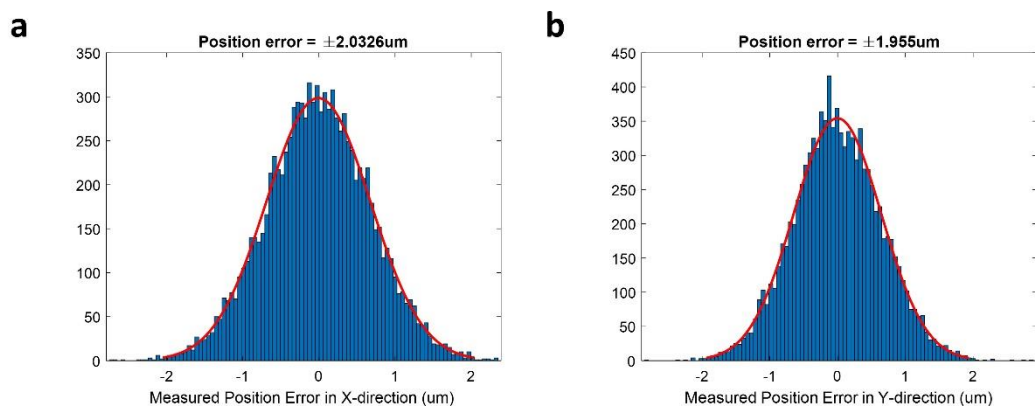


Figure 8-3 Position error distributions: a) X-direction and b) Y-direction.

Considering the footprint diameter and droplet position as random variables, enables the incorporation of a variable drop spacing in the footprint prediction through an

overlap map defined using the desired pattern to print. For example, a comparison of the overlap map for a circular pattern of 1 mm in diameter considering constant and variable drop spacing is illustrated in Figure 8-4. As can be clearly seen, the overlap map with variable drop spacing better captures the typical variation observed experimentally at the edges of printed samples.

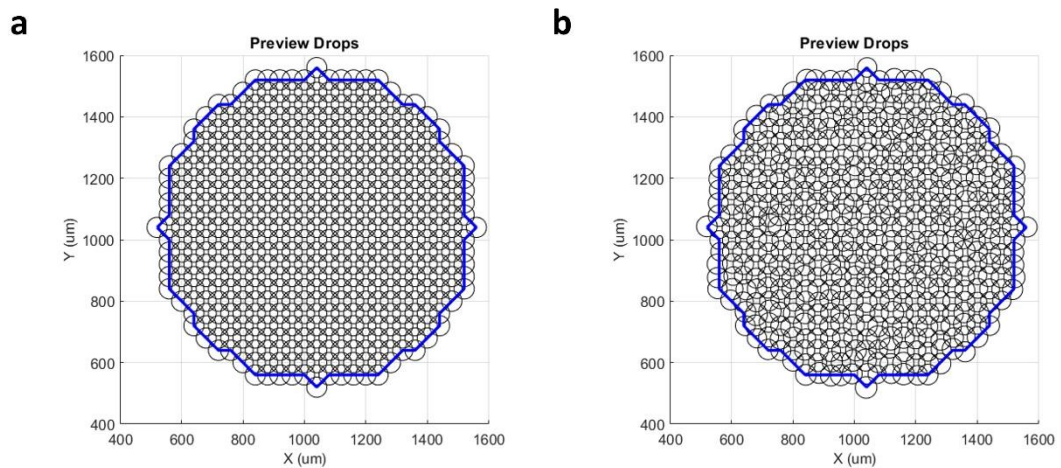


Figure 8-4 Graphical representation of inkjet-printed droplets on a circular pattern considering a) constant and b) variable drop spacing.

Since drop spacing is the most critical factor influencing the stability of printed features, capturing its variation gives this model a clear advantage identifying film defects such as break-ups and voids. In the next section, the results of the proposed film break-up prediction model and its validation are presented.

8.3.2 Break-up and bulging prediction and validation using overlap map.

Using the experimental results defined in the previous section to calibrate the analytical model and assuming a drop spacing, printing frequency and standoff distance of 50 μm , 1 kHz and 0.5 mm, respectively, a graphical representation of the inkjet-printed drops (called the overlap map) with identified high probability break-up locations is shown in Figure 8-5. The artifacts tested include a single pixel line, a square and a solid circle shape, which dimensions can be found in Section 3.2.4.1. The average number of defects is calculated via Monte Carlo simulation; hence, the actual

defect location is not accurate due to the stochastic nature of the overlap distribution. Experimental results are also included for validation purposes.

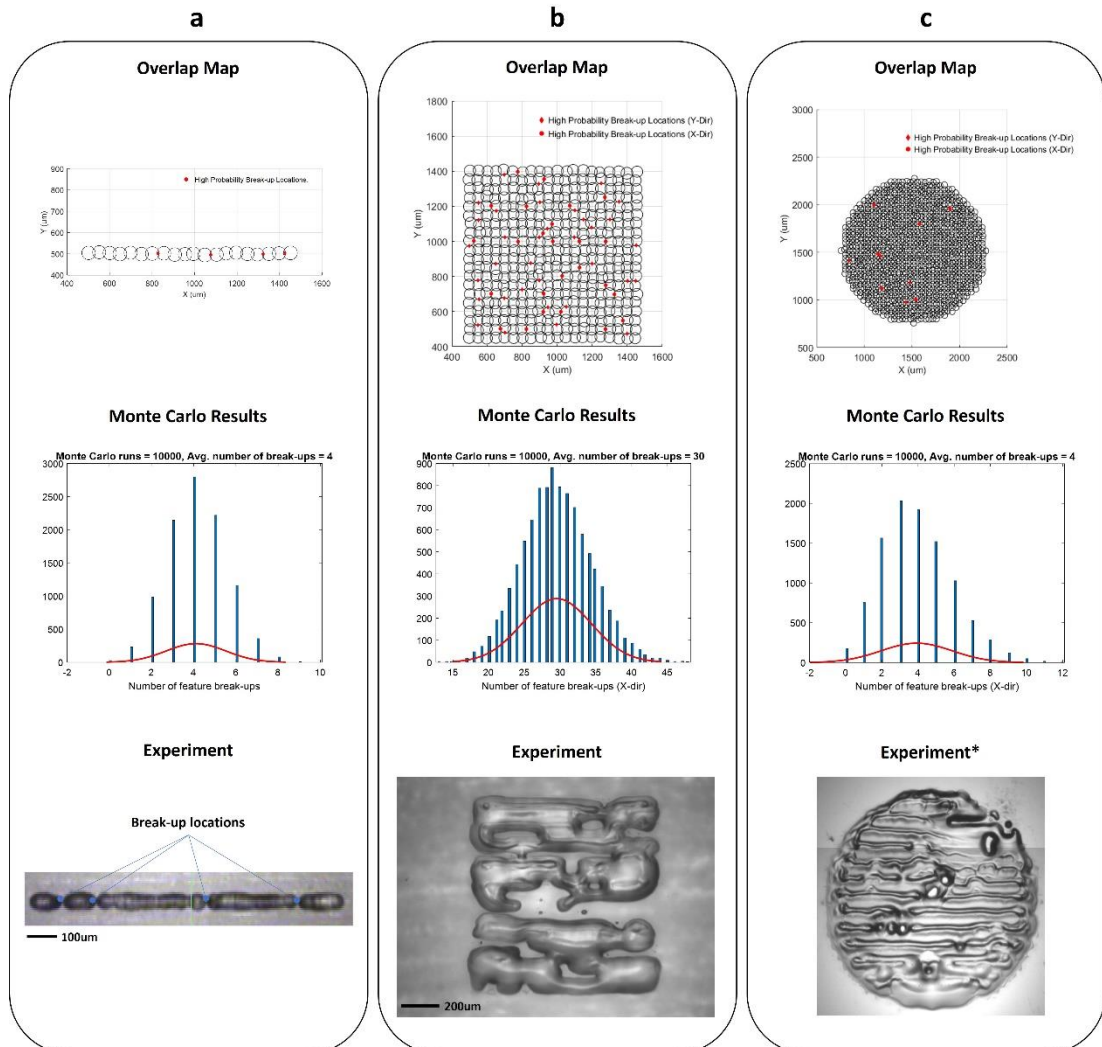


Figure 8-5 Prediction of high probability break-up locations using Overlap Map and Monte Carlo simulation. a) Single pixel line ($L=1$ mm, $ds=50$ μ m, $pf=1$ kHz, $sd=0.5$ mm), b) Solid square pattern ($side=1$ mm, $ds=50$ μ m, $pf=1$ kHz, $sd=0.5$ mm), and c) Solid circle pattern ($D=1.5$ mm, $ds=40$ μ m, $pf=1$ kHz, $sd=0.5$ mm).

Overall, the results of the overlap map analysis show excellent agreement between the statistical prediction and experiments. Figure 8-5a depicts the overlap map of a single pixel line with the locations where the overlap between droplets is close to zero indicating a high probability of break-up of the feature. The average number of break-up locations is 4 which is calculated using Monte Carlo simulation (10,000 runs). A line printed with same parameters presents multiple break-up locations, validating our prediction model for single tracks. Figure 8-5b shows a solid square pattern with an

average number of break-up locations of 30 along the x direction and another 30 along the y direction. The number of locations is the same in both directions since the model used the same position uncertainty for both directions. Experimental results of this pattern presents multiple islands due to lack of droplet overlap, validating our prediction model for regular films. Finally, a solid circular pattern is simulated with a drop spacing, printing frequency and standoff distance of 40 μm , 1 kHz and 0.5 mm, respectively, as presented in Figure 8-5c. It is found that the average number of break up locations reduces as overlap increases. For this pattern, the average number of break up locations is 4 in the x direction and 4 in the y direction, which is consistent with the results obtained when experimentally printing the pattern with the same parameters. It is important to note that without the inclusion of droplet diameter and location uncertainty, it would have been impossible to determine locations of no overlap, since a constant drop spacing of 50 μm and 40 μm produces a constant overlap of 0.22 and 0.37, respectively. Although the model does not predict the actual location of the break-ups, it does provide a statistical way to identify films with a high probability of breaking up.

In the same manner, an approximate number of film bumps, commonly known as bulges, could be predicted by identifying the locations where the droplet overlap is close to one. Figure 8-6 shows a square film overlap map estimated with a drop spacing of 10 μm and 30 μm while keeping fixed printing frequency and standoff distance at 1 kHz and 0.5 mm, respectively. The results of the Monte Carlo simulation (1000 runs) determined an average number of bulging locations of 2861, which represents 30% of the total deposited drops used to form the film. It is found that as drop spacing decreases, the number of bulges increases drastically, resulting in the formation of a large blob, which is confirmed by direct comparison to the printed sample. For the pattern simulated with a drop spacing of 30 μm , which is close to the optimal value found in Chapter 6, the overlap map does not show the presence of bulges or break-ups, confirming the capability of the statistical model to predict defect free films. Printed sample with the same parameters show a stable morphology (i.e., no bulges), validating the prediction. It is important to mention that the overlap map does not provide information about the size and location of the bulges that influence the material overflow beyond the edges of target patterns and consequently, the deformed

morphology of the features. Therefore, additional considerations need to be investigated to improve the analytical model capability to predict this behaviour.

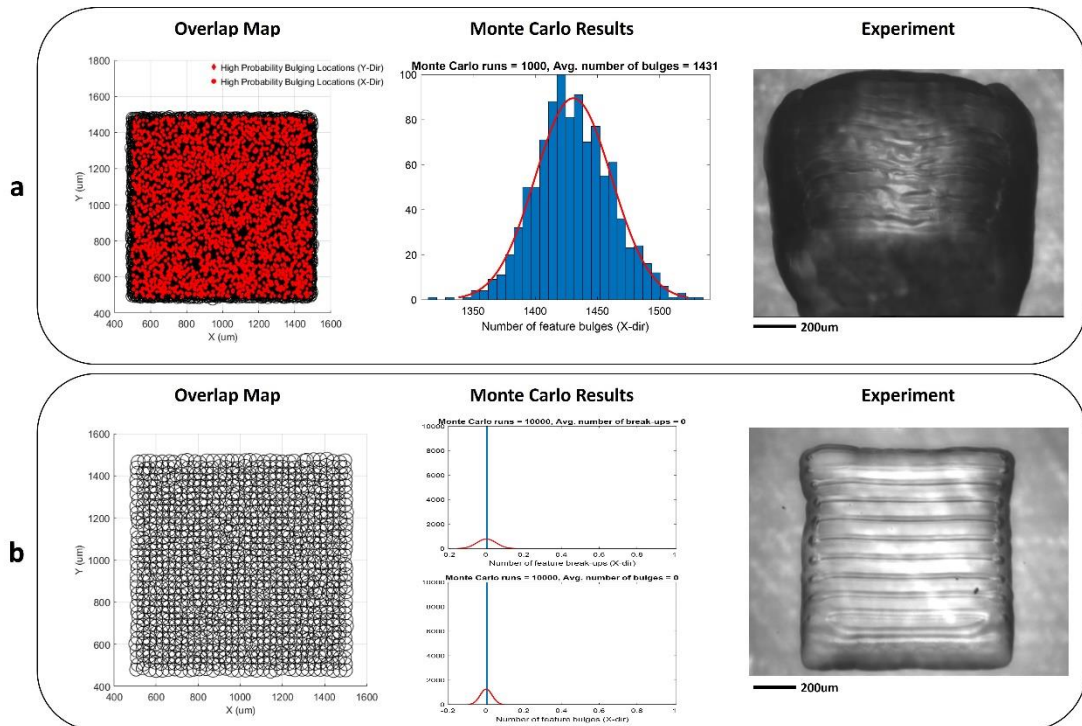


Figure 8-6 Prediction of high probability bulging locations for a solid square pattern using Overlap Map and Monte Carlo simulation. a) Drop spacing set to 10 μm and b) Drop spacing set to 30 μm .

Based on observations made from experiments, it is normal to find primary and secondary bulges on every printing swath, which location and size depend on the complex relationship between physical properties, wetting characteristics and printing parameters. In the next section, the results of our proposed model to determine the frequency and size of bulges is introduced.

8.3.3 Bulging frequency and volume prediction using viscous and capillary timescales.

A bulge in the inkjet printing context is a bump that distorts the surface of a printed feature, resulting from localised material accumulation. It is a common defect encountered in tracks and films whose formation depends on complex relationships between physical properties, substrate wettability and printing parameters. In this investigation, we propose an analytical model based on the dominant capillary, viscous

or inertial timescales to determine the size and frequency of primary and secondary bulges of single tracks. The effects of printing parameters, physical properties and wettability characteristics on the size and frequency of primary and secondary bulges are illustrated in Figure 8-7a-e. Each row shows the prediction of the number of drops forming the primary bulge, the number of drops in secondary bulges and the frequency of secondary bulges in a line of length 1 mm as a function of the droplet overlap. As can be seen in Figure 8-7a, the number of drops in the primary and secondary bulges is directly proportional to the advancing contact angle, showing a drastic change in slope at an overlap value at which bulges become more evident. For the contact angle of the ink/substrate system used in this work ($CA=18.4^\circ$), the proposed bulging threshold is approximately 67%. Furthermore, it is observed that the frequency of secondary bulges is inversely proportional to the contact angle and as droplet overlap increases the number of secondary bulges tends to one for a 1 mm single track. These results are consistent with other research studies from the literature (Kang et al., 2010)(Thompson et al., 2014). The effect of printing frequency for 1, 3 and 5 kHz is plotted in Figure 8-7b. It is found that the size and frequency of bulges is drastically reduced as printing frequency increases. This behaviour indicates that stable lines are achievable at droplet overlaps beyond 60% if the printing frequency is increased, which means that stability does not depend purely on drop spacing but also on the rate at which drops are deposited. The effect of standoff distance for 0.5 mm, 1 mm and 1.5 mm is plotted in Figure 8-7c. It is observed that varying the standoff distance has no significant effect on the size of primary and secondary bulges. However, the frequency of secondary bulges is directly proportional to the standoff distance, suggesting that setting this parameter to 0.5 mm can minimise the presence of bulges, which is also consistent with experiments. Figure 8-7d depicts the prediction results of three levels of surface tension: 15, 31 and 45 mN/m. It is observed that as surface tension increases, the size of bulges increases since larger surface tension forces dominate the flow redistribution, pulling drops towards a bulge. The frequency of secondary bulges is inversely proportional to surface tension and droplet overlap, which suggests worse stability at lower surface tension. Finally, the prediction results setting the viscosity level at 4, 11 and 20 centipoise are illustrated in Figure 8-7e and show no significant effect on the size of bulges. However, as viscosity increases the frequency of bulges decreases since flow mobility is lower, preventing bulge formation.

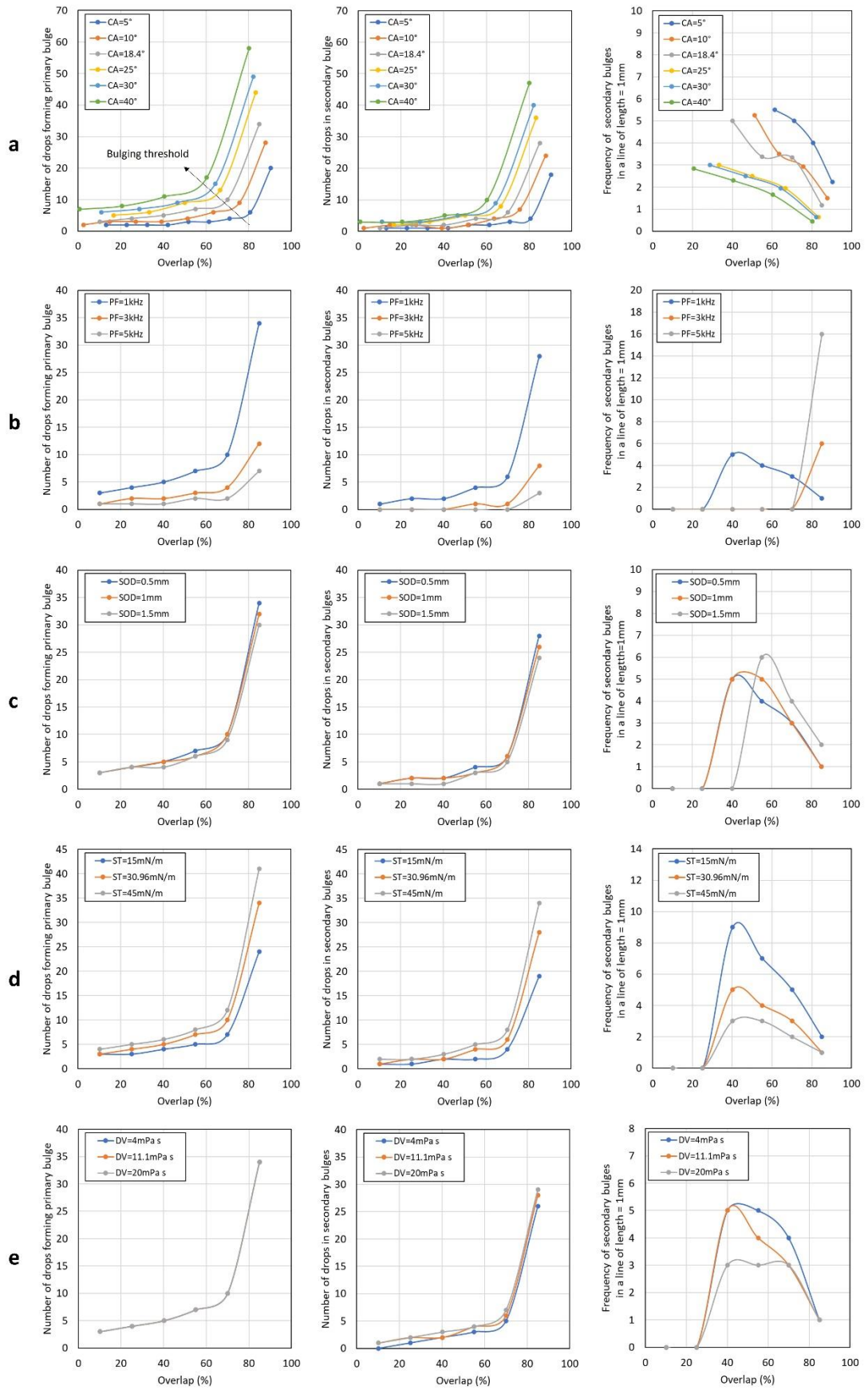


Figure 8-7 Effect of printing parameters, physical properties and wetting on the size and frequency of bulges. a) Contact angle, b) printing frequency, c) standoff distance, d) surface tension and e) dynamic viscosity.

A total of six single pixel lines of different lengths were printed and analysed using the derived relationships for the number of drops and frequency of bulges as functions of printing parameters, physical properties, and wetting characteristics. Figure 8-8 depicts a comparison of the prediction results with a drop spacing of 10 and 20 μm while printing frequency and standoff distance are fixed at 1 kHz and 0.5 mm, respectively. Physical properties and wetting characteristics are the same for both cases. It can be seen that the analytical model captures the formation of primary and secondary bulges depending on the length of printed feature. For the first 2 lines, which consist of 4 and 8 drops, respectively, the model predicts a single bulge as expected owing to the dominance of surface tension forces driving the shape towards a spherical cap. The third line shows a remanent of the deposited droplets breaking the spherical cap shape and tending to form a thinner line driven by larger inertia forces from droplets impacting the substrate. The rest of the lines which consist of 21, 35 and 50 drops, respectively, show secondary bulges whose frequency is proportional to the ratio of viscous and capillary timescales. It is evident that as drop spacing increases, the size of the primary bulge decreases, secondary bulges emerge, and the material tends to be uniformly redistributed along the printed track.

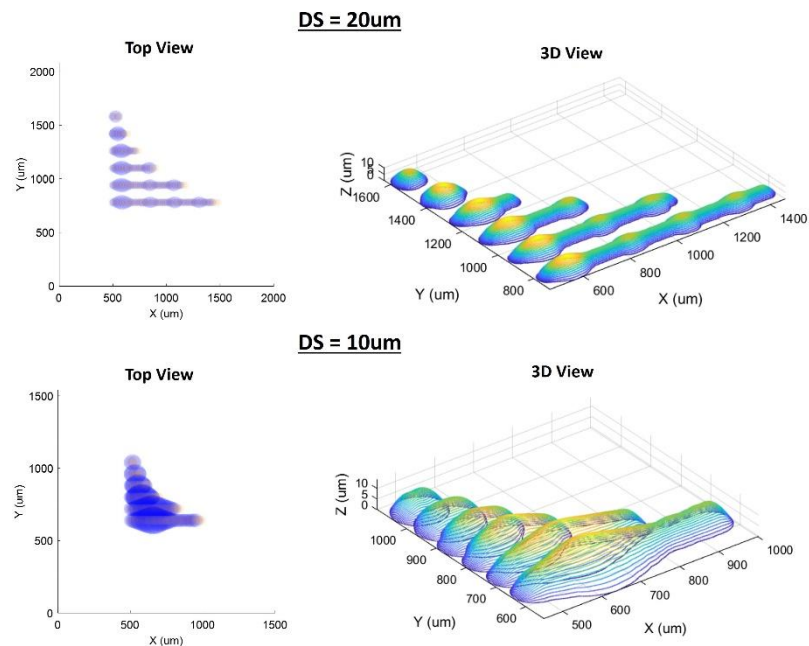


Figure 8-8 Primary and secondary bulges prediction with different drop spacing.

The analytical model derived in this section is capable of predicting the size and frequency of bulges in single tracks as well as detect the presence of defects (bulges and break-ups) using a stochastic approach. Although, the predicted effects of critical printing parameters, physical properties and wettability show consistent results with experiments from the literature, the effect on overall dimensions defining the surface morphology of single tracks must be validated. Therefore, printed samples using various different droplet volumes and substrates were generated and the surface morphology of single tracks measured to validate the analytical prediction model, as reported in the next section.

8.3.4 Experimental validation of the analytical prediction model for single tracks.

A total of six sets of single tracks were inkjet-printed to validate the prediction of the stochastic model implemented in previous sections. TPGDA was printed on silicon wafer and glass to test the model with different substrate wettabilities. Two different printheads were also used, DMC-11610 and samba®, with droplet volume sizes of 10 and 2.4 pL, respectively. Two batches of silicon wafer procured at different times from the same supplier were also used for repeatability purposes. The procedure to determine droplet footprint size and position uncertainty is described in Section 3.2.10 and was performed for each set of experiments for model calibration purposes. Figure 8-9 shows an example of the grid pattern used to calibrate the model and printed samples of single pixel lines with varying drop spacing.

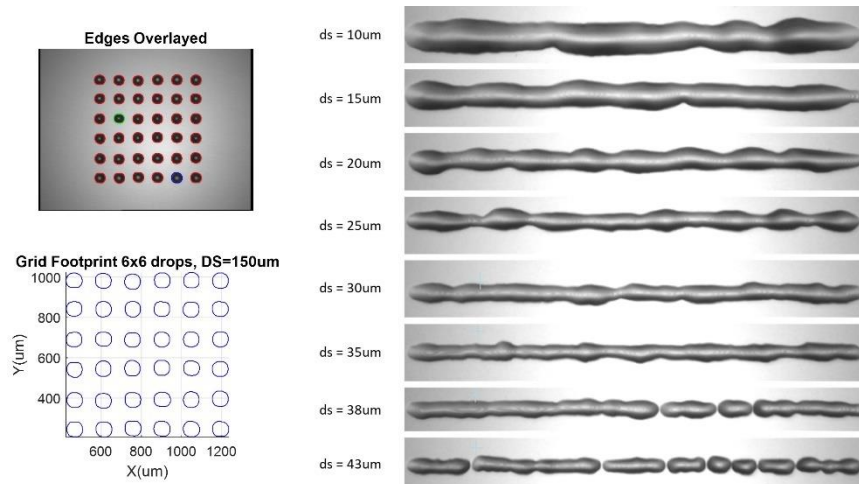


Figure 8-9 Example of model calibration grid and printed single track examples.

Table 8-4 lists the results from the grid analysis used to calibrate the analytical model.

Table 8-4 Grid analysis results for analytical model calibration.

TPGDA Droplet statistics description	Units	Nitride-coated Si-wafer				Glass microslide	
		11610		Samba®		11610	Samba®
		Batch1	Batch2	Batch1	Batch2	Batch1	Batch1
In-flight droplet volume	pL	9.55	9.55	2.3	2.3	9.55	2.3
Maximum grid diameter	μm	96.7	82.5	58.8	54.4	68.1	48.9
Minimum grid diameter	μm	89.3	78.4	49.6	49.2	60.0	44.9
Average grid diameter	μm	91.9	80.3	54.3	51.5	63.7	46.6
Grid diameter uncertainty	μm	1.2	0.7	1.5	0.9	1.4	0.7
Avg. drop spacing (X-dir.)	μm	148.5	150.2	149.7	149.6	150.7	149.5
Avg. drop spacing (Y-dir.)	μm	154.7	152.2	151.5	152.3	153.1	152.4
Position uncertainty (X-dir.)	μm	1.8	1.4	1.2	1.1	2.0	1.0
Position uncertainty (Y-dir.)	μm	2.9	2.3	3.1	2.4	2.1	1.4
Avg. drop volume (cured)	pL	8.3	8.3	2.1	2.1	8.3	2.1
Drop volume variation	pL	0.2	0.2	0.1	0.1	0.2	0.1
Maximum drop height	μm	2.7	3.4	2.1	2.2	5.8	2.7
Minimum drop height	μm	2.3	3.1	1.6	1.8	4.5	2.2
Avg. drop height	μm	2.5	3.3	1.8	2.0	5.1	2.5
Avg. contact angle (cured)	°	6.2	9.3	7.6	9.0	16.8	12.1
Contact angle variation	°	0.8	0.4	0.8	0.4	0.8	0.4
Advancing contact angle	°	8.4	12.6	10.3	12.2	20.8	16.3

Using the droplet characteristics presented in Table 8-4 and the physical properties determined in Section 8.3.1, the proposed equations derived in Section 4.3.1.2 can now be used to predict the surface morphology of single tracks. For simplification purposes, these equations are re-arranged such that all dimensions are proportional to the inverse square root of the drop spacing and a coefficient “A” which is a function of the contact

angle, droplet volume, footprint diameter and ink physical properties. Table 8-5 documents the magnitude of coefficient “A” defining the analytical prediction model for each dimension.

Table 8-5 Coefficient “A” determined using droplet characteristics from grid analysis and physical properties.

<i>Dimension</i> = $\frac{A}{\sqrt{ds}}$	Units	Nitride-coated Si-wafer				Glass microslide	
		11610		Samba®		11610	Samba®
		Batch1	Batch2	Batch1	Batch2	Batch1	Batch1
Average width	$\mu\text{m}^{1.5}$	625.4	509.7	277.0	254.3	359.0	218.8
Maximum width	$\mu\text{m}^{1.5}$	810.3	684.6	416.4	390.2	525.9	350.4
Average thickness	$\mu\text{m}^{1.5}$	15.3	18.7	8.3	9.0	26.6	10.5
Maximum thickness	$\mu\text{m}^{1.5}$	22.9	28.1	12.5	13.6	39.9	15.8

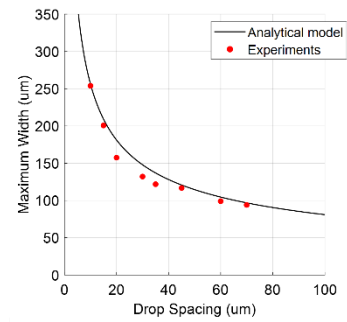
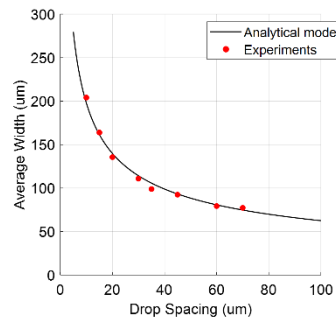
A comparison of the analytical model predictions and actual measurements for average and maximum widths of printed samples is presented in Figure 8-10. The predictions match well the experiments, with a maximum error within 20 μm , thus validating the analytical model for width dimensions.

Experiment Settings

Predictions vs Measurements

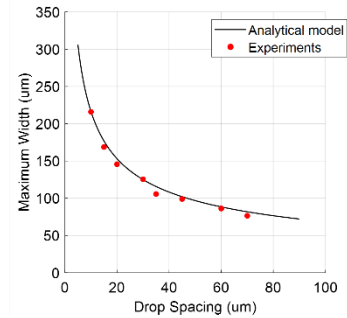
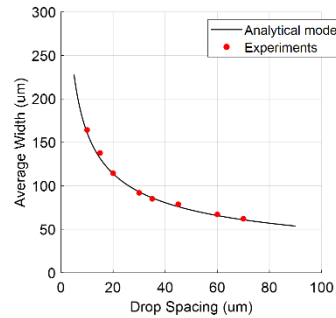
a

Ink	TPGDA
Substrate	Si-wafer
Batch	1
Printhead	11610



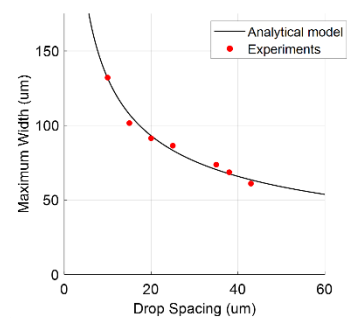
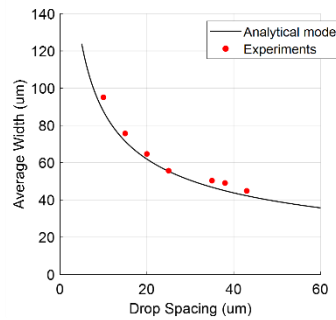
b

Ink	TPGDA
Substrate	Si-wafer
Batch	2
Printhead	11610



c

Ink	TPGDA
Substrate	Si-wafer
Batch	1
Printhead	Samba®



d

Ink	TPGDA
Substrate	Si-wafer
Batch	2
Printhead	Samba®

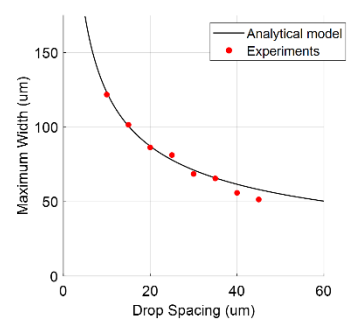
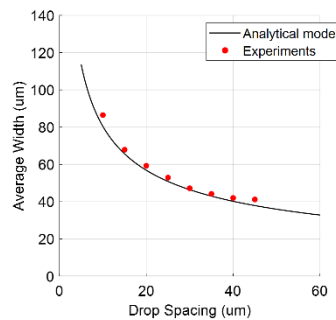


Figure 8-10 Comparison of analytical model predictions and measured data for average and maximum width dimensions of single tracks. Printed tracks on Si-wafer with native droplet volume of 10 pL displayed in a. and b. Printed tracks on Si-wafer with native droplet volume of 2.4 pL displayed in c. and d.

A comparison of the analytical model predictions and actual measurements for average and maximum heights of printed samples is presented in Figure 8-11. These predictions also match well the experiments, with maximum error within 3 μm , again, validating the analytical model for height dimensions.

Experiment Settings

a

Ink	TPGDA
Substrate	Si-wafer
Batch	1
Printhead	11610

b

Ink	TPGDA
Substrate	Si-wafer
Batch	2
Printhead	11610

c

Ink	TPGDA
Substrate	Si-wafer
Batch	1
Printhead	Samba®

d

Ink	TPGDA
Substrate	Si-wafer
Batch	2
Printhead	Samba®

Predictions vs Measurements

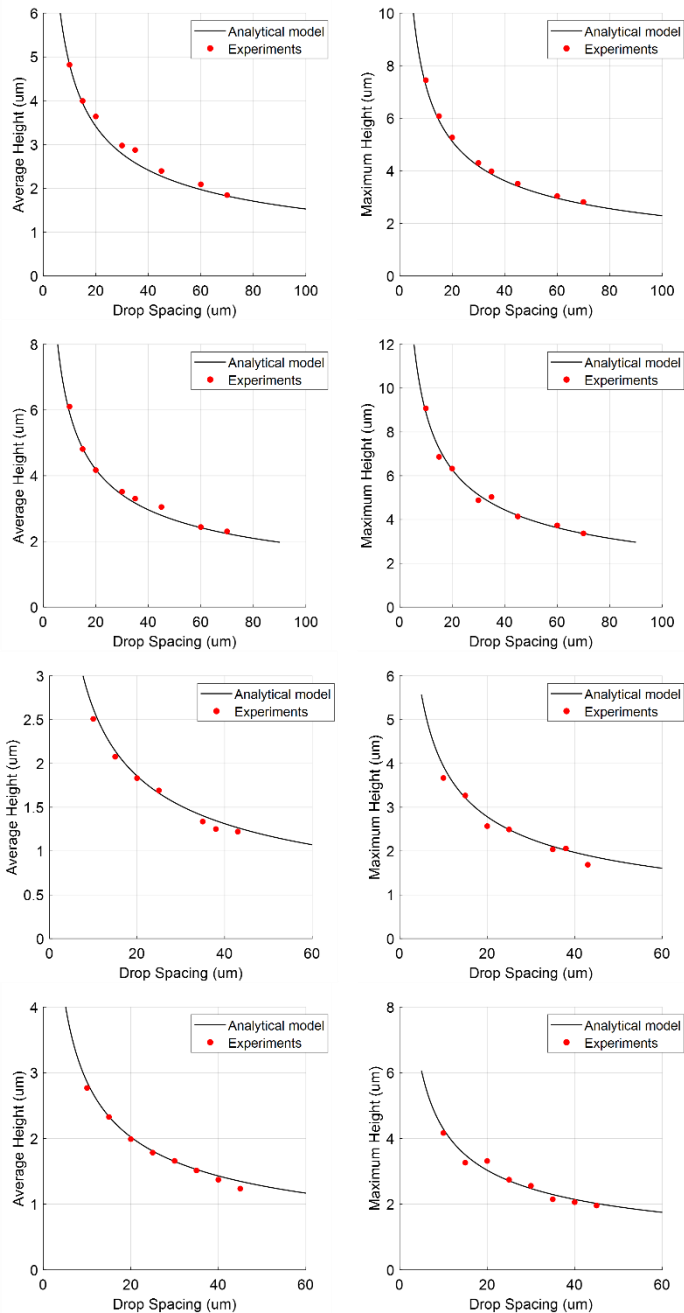


Figure 8-11 Comparison of analytical model predictions and measured data for average and maximum height dimensions of single tracks. Printed tracks on Si-wafer with native droplet volume of 10 pL displayed in a. and b. Printed tracks on Si-wafer with native droplet volume of 2.4 pL displayed in c. and d.

In order to construct the surface morphology of printed features, the validated analytical model was implemented in MATLAB following the procedure described in Section 4.3.2. The predicted surface morphology of single tracks is presented in the next section along with our proposed stability diagram and optimal printing parameters to achieve stable thin and thick lines.

8.3.5 Prediction, optimisation, and validation of the surface morphology of single tracks.

The surface morphology of eight single tracks consisting of 9 drops was simulated with the analytical model and compared to printed samples in Figure 8-12. Drop spacing was varied from 10 to 70 μm while keeping fixed printed frequency and standoff distance at 1 kHz and 0.5 mm, respectively. Samples were printed on glass with cartridge model 11610 (native droplet volume = 10 pL). The analytical model was calibrated with the grid analysis results from Section 8.3.1. It can be seen in Figure 8-12 that there is good agreement between the predicted and measure surface morphology dimensions. Importantly, it can be seen that the analytical model accurately predicts the transition from bulging to separation of single tracks. As drop spacing increases the length of the line increases, as expected, and the prediction error is less than 5%. For drop spacings below 20 μm (bulging onset equivalent to 67% overlap), the morphology of the samples has the shape of a large blob of material, consistent in both simulated and printed results. The material overflow beyond top and bottom of target boundaries matches well the prediction, with an error within 5%. The maximum thickness of the printed samples was determined using optical microscopy and the prediction error for this is less than 2.5 μm . For drop spacings above 50 μm (break-up onset equivalent to 21% overlap), the morphology of the samples is not continuous, consistent in both simulated and printed results. As drop spacing increases the number of break-ups in the line increases, matching the stochastic overlap map prediction of the average number of separations. Finally, for drop spacings between 20 and 50 μm , the morphology of the samples present primary and secondary bulges varying in frequency, consistent in both simulated and printed results. Therefore, the analytical model simulation of single tracks is validated with maximum prediction errors listed in Table 8-6.

Table 8-6 Prediction error observed in dimensions of single tracks.

Dimension	Units	Maximum Prediction Error
Length	μm	25
Width	μm	10
Thickness	μm	2.5

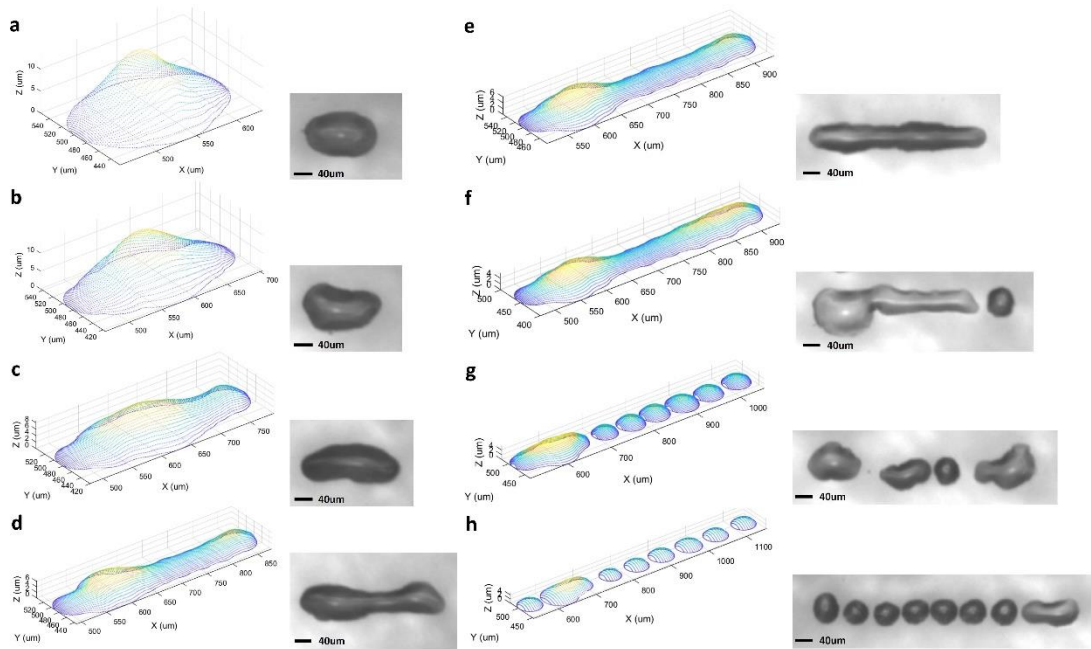


Figure 8-12 Comparison of analytical model simulation and printed samples of single tracks varying drop spacing. a. 10 μm , b. 20 μm , c. 30 μm , d. 40 μm , e. 45 μm , f. 50 μm , g. 60 μm and h. 70 μm .

In order to test the model with line patterns of different size, the surface morphology of three single tracks of 1 mm in length was simulated and compared to printed samples, with the results presented in Figure 8-13. Printing and simulation parameters all remained the same except for drop spacing, which was set to 10, 40 and 60 μm . It can be seen in the figure that the simulation results capture the transition from bulging to separation of single tracks for longer lines and show more frequent secondary bulges, as expected.

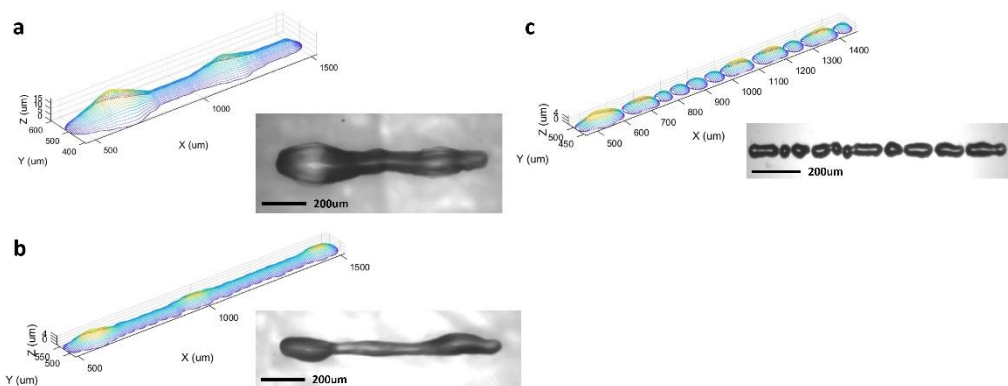


Figure 8-13 Simulated lines $L=1\text{ mm}$ vs printed samples varying drop spacing. a. 10 μm , b. 40 μm and c. 60 μm

Figure 8-14 illustrates the effect of printing frequency on the surface morphology of single tracks of 1 mm in length with fixed drop spacing and standoff distance of 10 μm and 0.5 mm, respectively. It can be seen that the simulated and printed samples show good agreement, validating the capability of the model to capture the influence of printing frequency on the feature morphology and more importantly, demonstrating that thicker lines can be achieved in a stable manner. At the lower frequency (1 kHz), primary and secondary bulges are evident in the line morphology due to the high resolution employed (equivalent to 84% overlap). However, by increasing the printing frequency, the traverse speed calculated from Equation (44) is increased, enabling better ink redistribution along the target line. At the highest frequency (4 kHz), bulges are eliminated and only a slight overflow of material is observed in the middle of the printed sample.

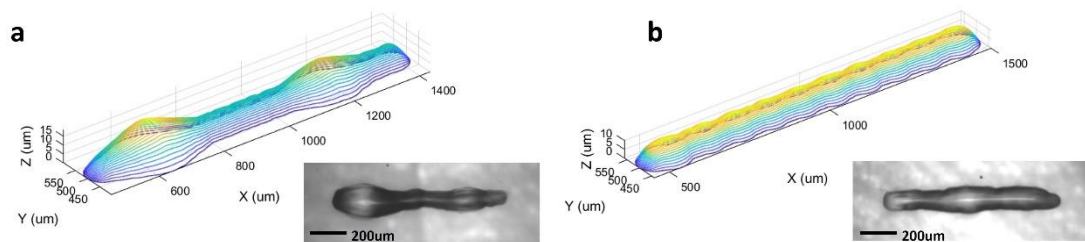


Figure 8-14 Effect of printing frequency on lines printed using high resolution (drop spacing = 10 μm). a. 1 kHz and b. 4 kHz

Finally, the optimal printing parameters were determined following the procedure explained in Section 4.3.1.4 and a stability diagram depicting the onset of bulging and separation and the optimum overlap point is shown in Figure 8-15. It was found that to achieve the thinnest stable line, drop spacing, printing frequency and standoff distance should be set to 29.6 μm , 3.1 kHz and 1 mm, respectively. In comparison, the thickest stable line was achieved setting drop spacing, printing frequency and standoff distance to 10 μm , 9.2 kHz and 0.5 mm, respectively. Given the droplet size and location uncertainty when TPGDA is printed on glass with a native droplet volume of 10 pL (cartridge 11610), the onset of bulging is predicted to be at 69% overlap (equivalent to a drop spacing of 21 μm) and the onset of breakup is predicted to be at 25% overlap (equivalent to a drop spacing of 49 μm). The threshold of isolated droplets is predicted to be at 11% overlap (equivalent to a drop spacing of 59 μm).

Bulging and separation thresholds were determined assuming the lowest printing frequency (1 kHz) and standoff distance (0.5 mm), since uncertainties were measured from the grid analysis performed with these settings.

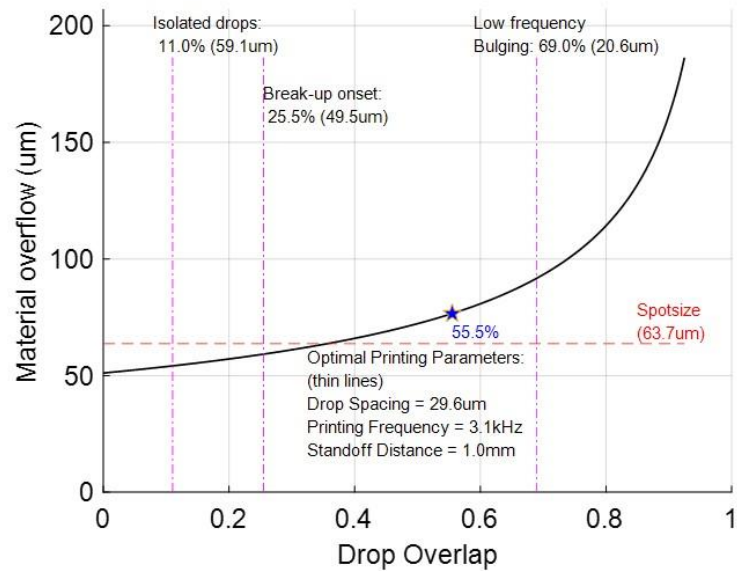


Figure 8-15 Stability Diagram for TPGDA printed on glass with cartridge model 11610. Optimal printing parameters shown are to achieve stable thinnest tracks.

Table 8-7 lists the predicted dimensions at optimal printing parameters for thin and thick lines.

Table 8-7 Predicted morphology at optimal printing settings for thin and thick lines.

Dimension	Units	Thin lines	Thick lines
Average width	µm	76.6	131.7
Maximum material overflow	µm	14.1	24.2
Predicted line thickness	µm	6.3	10.9

In the next section, the analytical model simulation of free form films and experiments performed using a variety of film patterns to demonstrate the validity of the optimal printing parameters derived for single tracks are presented.

8.3.6 Prediction and validation of the surface morphology of freeform films.

One of the advantages of the analytical model simulation is that it mimics the actual printing process, which creates films by multiple unidirectional swaths using single or multiple nozzles simultaneously. This characteristic enables the simulation to capture more accurately the morphology of real films, since it considers the interaction between swaths. Also, the width of the swaths can be varied through the selection of multiple nozzles which brings the simulation closer to reality.

Examples of both solid and hollow films were simulated and printed to demonstrate the capabilities of the analytical model to predict the surface morphology of freeform films. Figure 8-16 depicts the simulated film footprint, an image of the printed sample and the predicted morphology of the film for four different film geometries. Samples were printed on glass with cartridge model 11610 (native droplet volume = 10 pL). The analytical model was calibrated from the corresponding grid analysis results from Section 8.3.1. Drop spacing, printing frequency and standoff distance were set to 30 μm , 3 kHz and 1 mm, respectively. The results show good agreement between the morphology predictions and experiments. The analytical model captures the observed curvy distortion of the edge caused by the variation of droplet size and position, which is inherent to the printer mechanical tolerances. Furthermore, the overlap between swaths match perfectly with the horizontal bands seen in the printed samples. The main difference is observed at the bottom of the pattern, where insufficient UV exposure cause the last couple of swaths to distort irregularly due to partial curing. The degree of curing, measured by degree of monomer consumption as function of UV dosage, was considered in the analytical model to correct only the thickness of the films, following the procedure described in Section 4.3.1.3. For the solid and hollowed square patterns, simulated fine features such as corners match well with the printed samples for both interior and exterior boundaries. For the ring pattern, the simulation results capture the increase of thickness at the top of the ring, as in the printed sample, due to the use of multiple nozzles that determine the width of the swath and, consequently, its distribution along the pattern. Finally, for the spiral (antenna-type) pattern, the predicted separation between spiral swings matches the printed sample, demonstrating fine features such as channels (size equal to 200 μm) can be simulated accurately with the adequate selection of printing parameters. The non-smooth circular

boundary edge is also predicted fairly well due to the inclusion of droplet size and position variation and swaths distribution along the pattern.

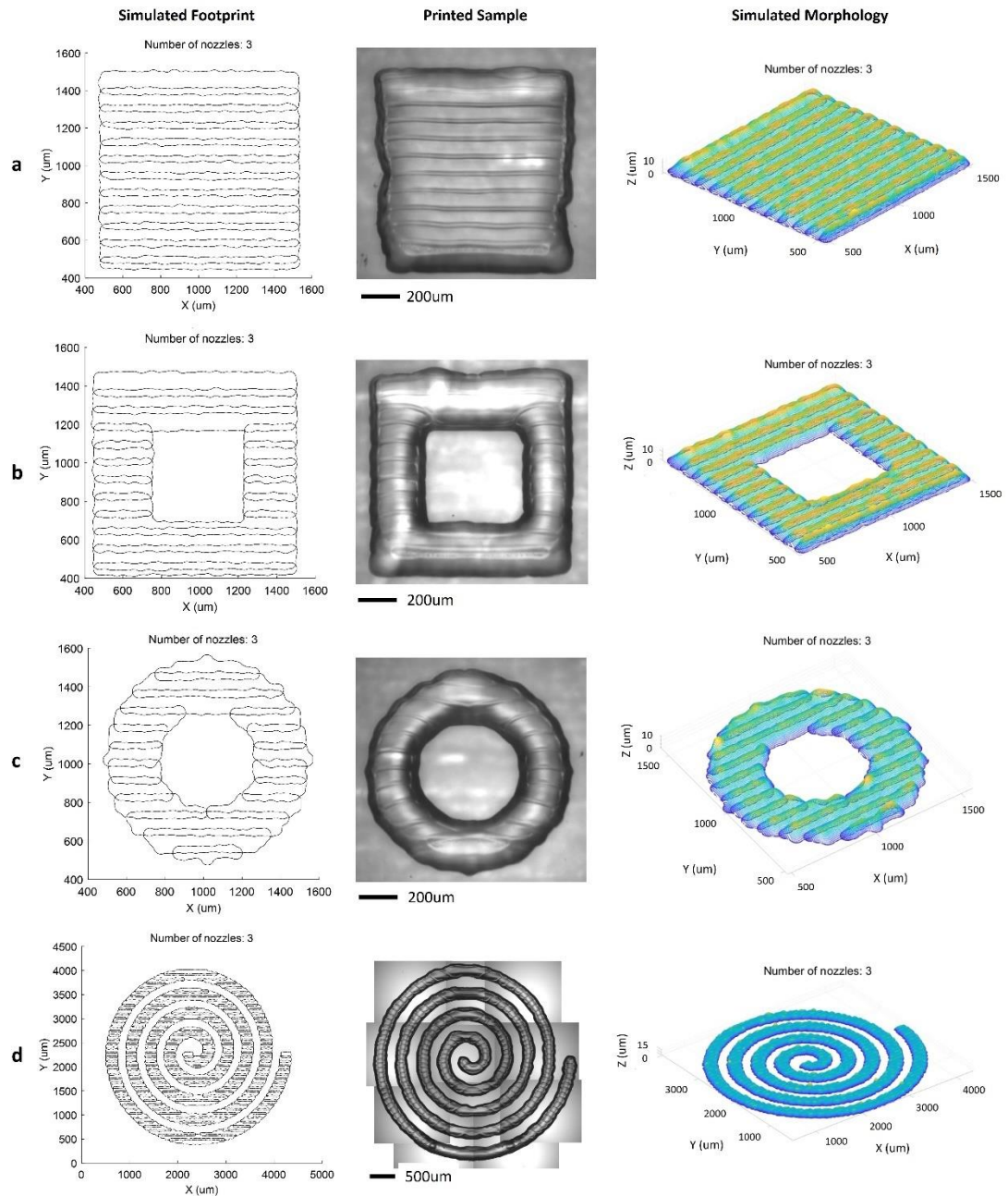


Figure 8-16 Analytical model simulation results compared to printed samples for freeform patterns. a. Solid square, b. Hollowed square, c. Ring, and d. Archimedean spiral.

Figure 8-17 illustrates two hollowed patterns simulated using single and multiple nozzles to demonstrate the capability of the analytical model to handle different swath widths and understand its effect on the film morphology. The results show a smoother

film surface and footprint edge for the prediction using multiple nozzles since larger variation is introduced with increasing number of swaths. In particular, it is found that the number of ridges increases in the film printed with a single nozzle due to the pinning and curing of single tracks. It is important to note that both cases match the overall dimensions of target pattern for internal and external features, regardless of the number of nozzles used. The main difference is noted in the surface finish and footprint boundary waviness, which is better in the simulated sample with multiple nozzles.

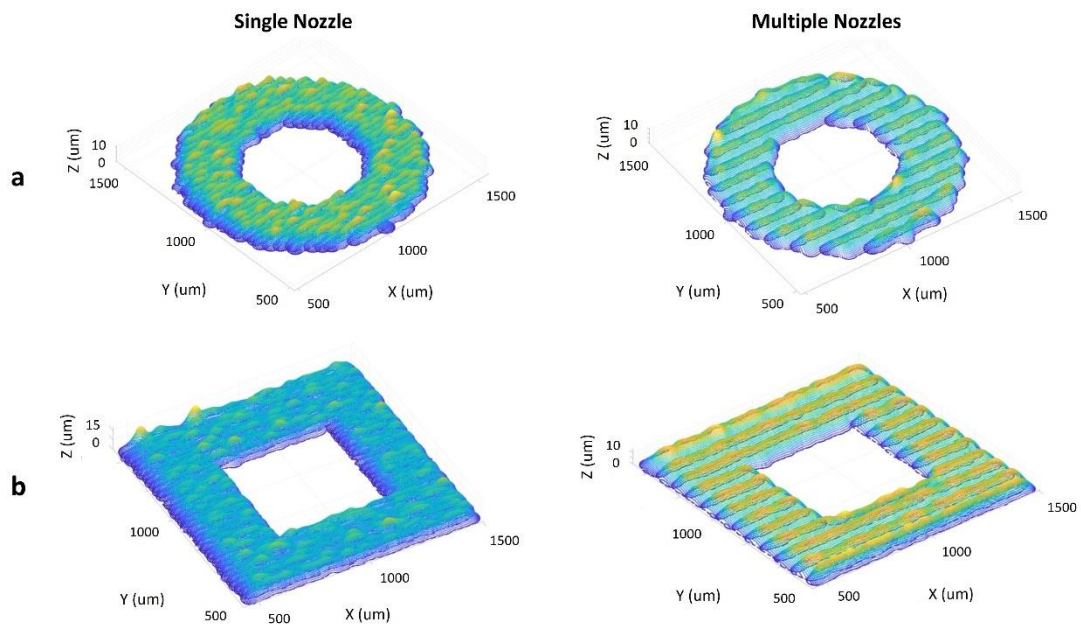


Figure 8-17 Comparison of simulated patterns using a. single and b. multiple nozzles.

The analytical model simulation can also be used to correct the edges of printed swaths to account for the material overflow caused by non-optimal printing parameters. Figure 8-18 depicts a solid square film simulated and printed using drop spacing, printing frequency and standoff distance set to 10 μm , 3.0 kHz and 1.0 mm, respectively. Simulation results show excellent agreement to the CSI measurements of printed sample. A large bulge is predicted at the centre of the film with a thickness of 78.1 μm vs 76.6 μm predicted. The square film sides exceed the target of 1 mm in both simulation and experiments by an average of 350 μm (experiments) vs 320 μm (simulation). X-Z and Y-Z cross sections located at the film centroid show excellent agreement between real and predicted shape, validating our modelling assumptions. The main difference is observed in the surface finish at the centre of the square, which

presents non-smooth ridges due to swaths in the printed sample. Overall, the analytical model simulation predicts the maximum dimensions within 5%, which is consistent with the predictions obtained for single tracks.

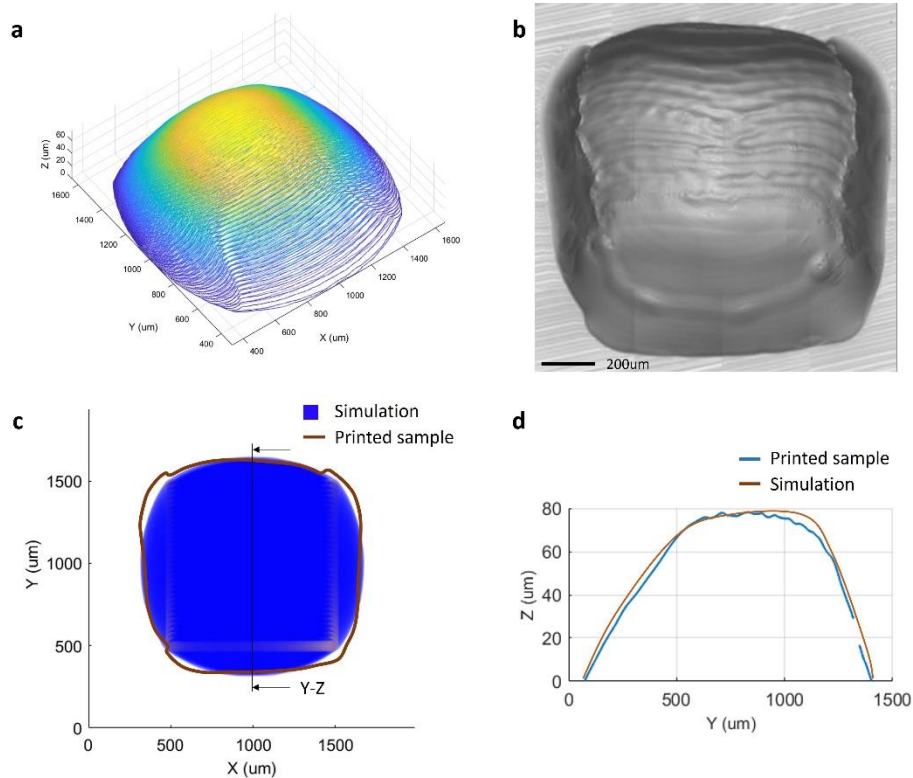


Figure 8-18 Comparison of analytical model simulation of a square film with excessive overflow on pattern boundaries with experiments. a. Simulated morphology, b. Printed sample, c. Footprint overlay plot and d. Y-Z cross-section overlay plot at centroid of film.

Unfortunately, the analytical model simulation cannot build the morphology of films with large drop spacings which typically present discontinuous swaths, voids, and islands. The simulation can only build the morphology of swaths for the single nozzle case which does not reflect the actual location of the break-ups due to the stochastic nature of the droplets size and position. However, the number of film break-ups is statistically determined through Monte Carlo simulations and in this way the printing parameters to avoid discontinuous films can be found. Since the analytical model simulation's purpose is to construct the morphology of continuous films to compare against CSI measurements of printed samples, it is concluded that the model is good enough to fulfil this purpose.

After confirming the capability of the analytical model simulation to build the morphology of a variety of freeform films with single and multiple nozzles and a range of printing parameters, a comparison of the simulated point cloud of a solid square pattern against measurements of printed sample is presented in Figure 8-19. Drop spacing, printing frequency and standoff distance were set to 30 μm , 3 kHz and 1 mm, respectively. The results show a maximum absolute deviation of 75 μm near the bottom left corner of the pattern and a total mean square error of 113 μm . The average error in the thickness direction is in the order of 2.5 μm . A major advantage of the proposed analytical modelling method is that builds the film in tenths of a second, thus providing an extremely fast tool to evaluate the design space for optimisation and multilayer simulation purposes.

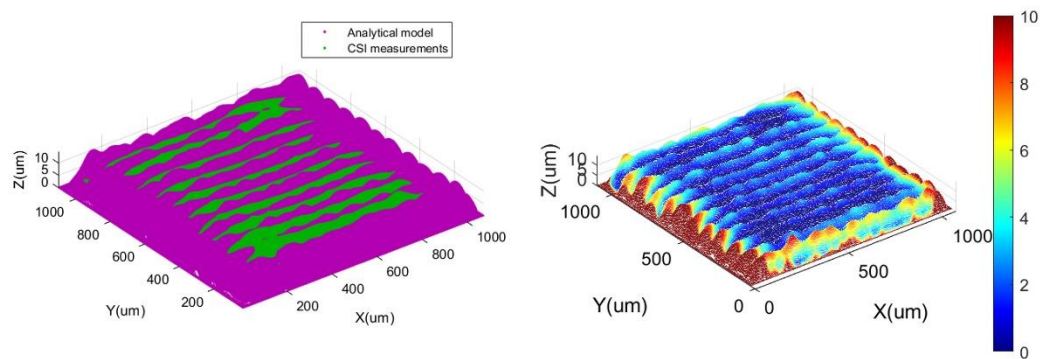


Figure 8-19 Simulated vs real surface morphology overlay and absolute deviation for a solid square film.

Finally, the optimal printing parameters and stability diagrams derived for printing TPGDA on glass and silicon wafer using different printheads (different native droplet volumes) were generated and validated using experiments, as illustrated in Figure 8-20. Stability diagrams provide threshold overlaps for the onset of film break-up and bulging based on the variation introduced by the printer mechanical tolerances. The plot also informs the amount of expected material overflow beyond boundary edges as a function of droplet overlap and the optimal printing parameters to achieve the thinner film. The printed samples were created using the optimal printing parameters for thinner films, except for Figure 8-20d, which employed the optimal printing parameters derived for thicker films ($ds=10 \mu\text{m}$, $pf=9.2 \text{ kHz}$ and $sd=0.7 \text{ mm}$). Overall,

the results demonstrated stable freeform films printed on different substrates, thus validating the proposed stochastic model-based optimisation framework.

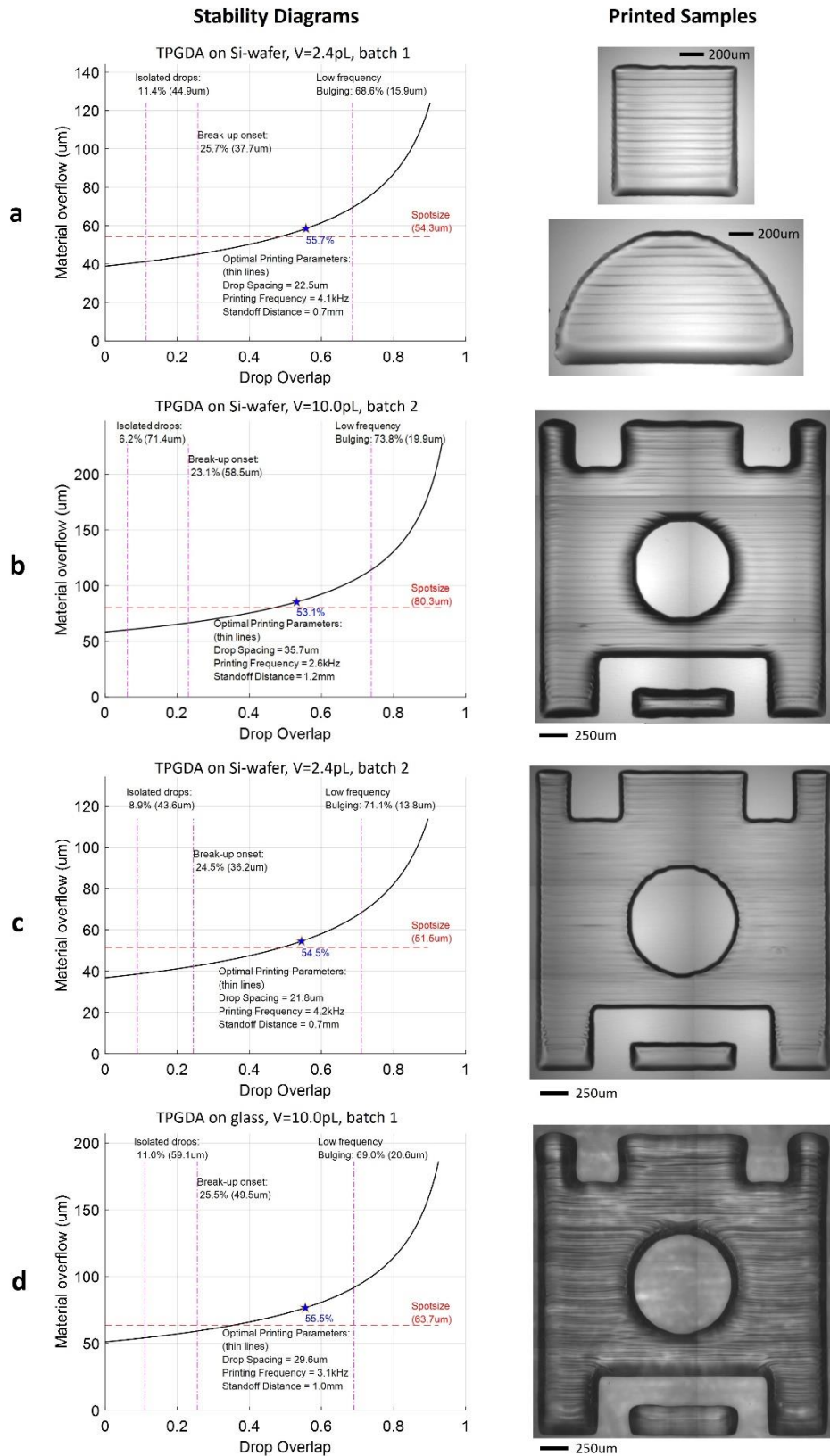


Figure 8-20 Experimental validation of optimal printing parameters using the proposed stability diagrams for: a. TPGDA on Si-wafer, V=2.4 pL, batch 1; b. TPGDA on Si-wafer, V=10 pL, batch 2; c. TPGDA on Si-wafer, V=2.4 pL, batch 2 and d. TPGDA on glass, V=10 pL with optimised parameters for thicker films.

A comparison between target pattern dimensions and the printed sample using optimal printing parameters can be seen in Figure 8-21. A pattern with internal features is chosen to demonstrate the accuracy of the printing process. The pattern was printed on a silicon wafer (a) and on a film of TPGDA (b) to demonstrate the effect of optimal printing parameters on surfaces with different wettability. The maximum absolute deviation observed in the sample printed on the silicon wafer and TPGDA were 83 μm (+3.3% error) and 52 μm (-2% error), respectively. In both samples, all other dimensions showed deviations less than 30 μm . Internal corners have a round shape with an approximate radius of the dot size (64 μm) and internal features follow accurately the intended shape. Overall, printed samples meet target requirements regardless of the different substrate conditions, thus validating the optimal printing parameters derived from our analytical modelling-based optimisation approach.

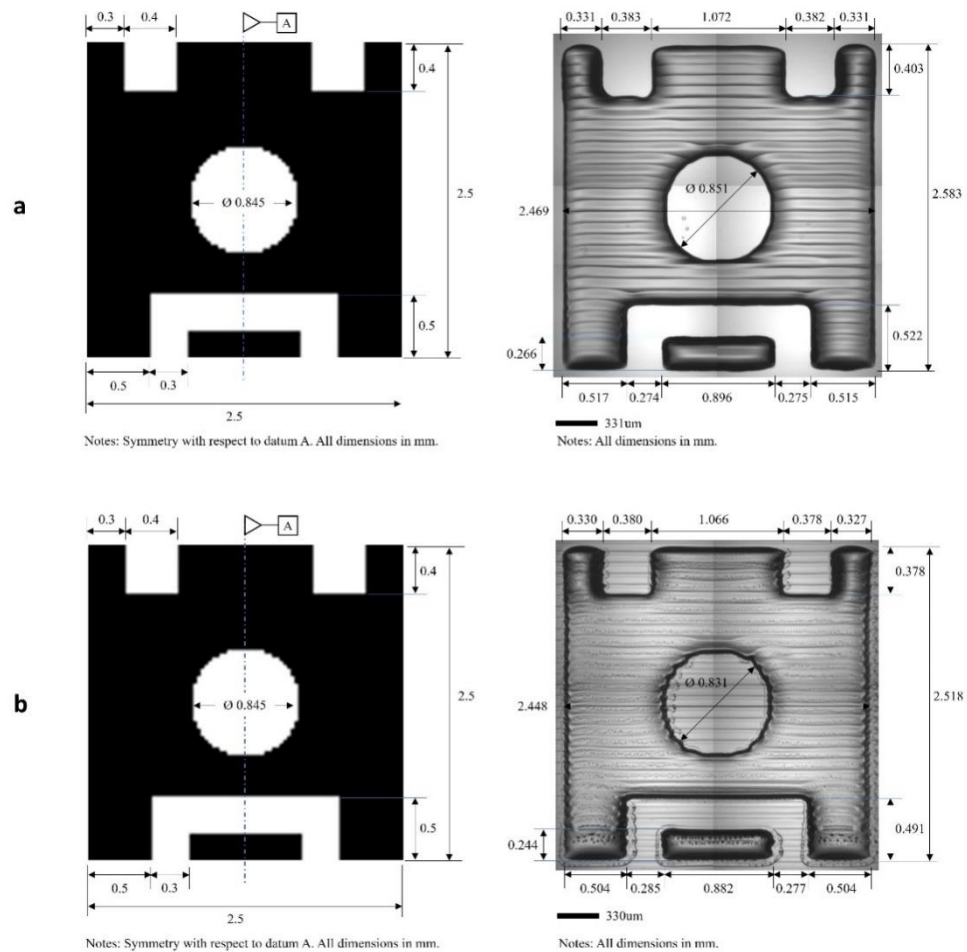


Figure 8-21 Comparison of printed samples with different substrate wettabilities against target dimensions: a. TPGDA printed on Si-wafer and b. TPGDA printed on a film of TPGDA.

In the next section, the analytical model simulation is extended to multilayer printing for the generation of the deformed geometry for inkjet-printed parts and a geometry compensation scheme is introduced to further minimise the error between target and predicted geometries.

8.3.7 Prediction and compensation of the deformed geometry of 3D printed parts.

The results of two methodologies to obtain the deformed geometry of 3D inkjet-printed components are presented in this section. First, the analytical model simulation of the layer-by-layer inkjet process is employed to predict the deformed geometry of the artifacts described in section 3.2.4. Then, an investigation of the effect of inkjet printing on the general dimensions of 3D parts against the target geometry is performed through a series of experiments. Then, the deformed geometry of regular, symmetric patterns such as squares and circles, solid and hollowed, is predicted using the semi-empirical procedure described in section 4.2.2. Simulated and printed samples are generated employing the optimal printing parameters for each layer to isolate the out-of-plane error introduced by the multilayer process. Finally, a geometry compensation scheme is applied if the absolute deviation between prediction and target geometries exceeds 50 μm . This is an optional additional step that can be used to minimise the out-of-plane error and improve the overall quality of the printed part if required.

8.3.7.1 Deformed geometry prediction using stochastic model.

A total of six differently sized and shaped artifacts were simulated and analysed to evaluate the analytical model 3D prediction capabilities. The number of layers used to build the artifacts were 89, 106, 89, 59, 89 and 96 at 8.5 μm layer thickness. The analytical model was calibrated with the corresponding grid analysis results from Section 8.3.1. Drop spacing, printing frequency and standoff distance were set to 30 μm , 3 kHz and 1 mm, respectively. Figure 8-22 shows a comparison of simulation results against the target geometry and footprint of printed samples. The results show good agreement between prediction and target geometry with a maximum absolute deviation of less than 50 μm . For the cage and sensor, the maximum deviation at the

boundaries is approximate 60 μm . The walls of the artifacts show a non-uniform distribution of deviations due to the stochastic nature of film formation. The layer thickness prediction from the analytical model enables fabrication of a 3D object closer to the target height compared to the FE prediction derived in Chapter 7. Although the predicted geometry matches the target well, the 3D printed samples present a larger deviation of external and internal dimensions with respect to target. When the ink is deposited near the edges of previous films, the surface is not flat causing the ink to flow downwards, spreading beyond the target dimensions. Therefore, additional considerations must be investigated to improve the analytical model capabilities to predict 3D parts closer to reality.

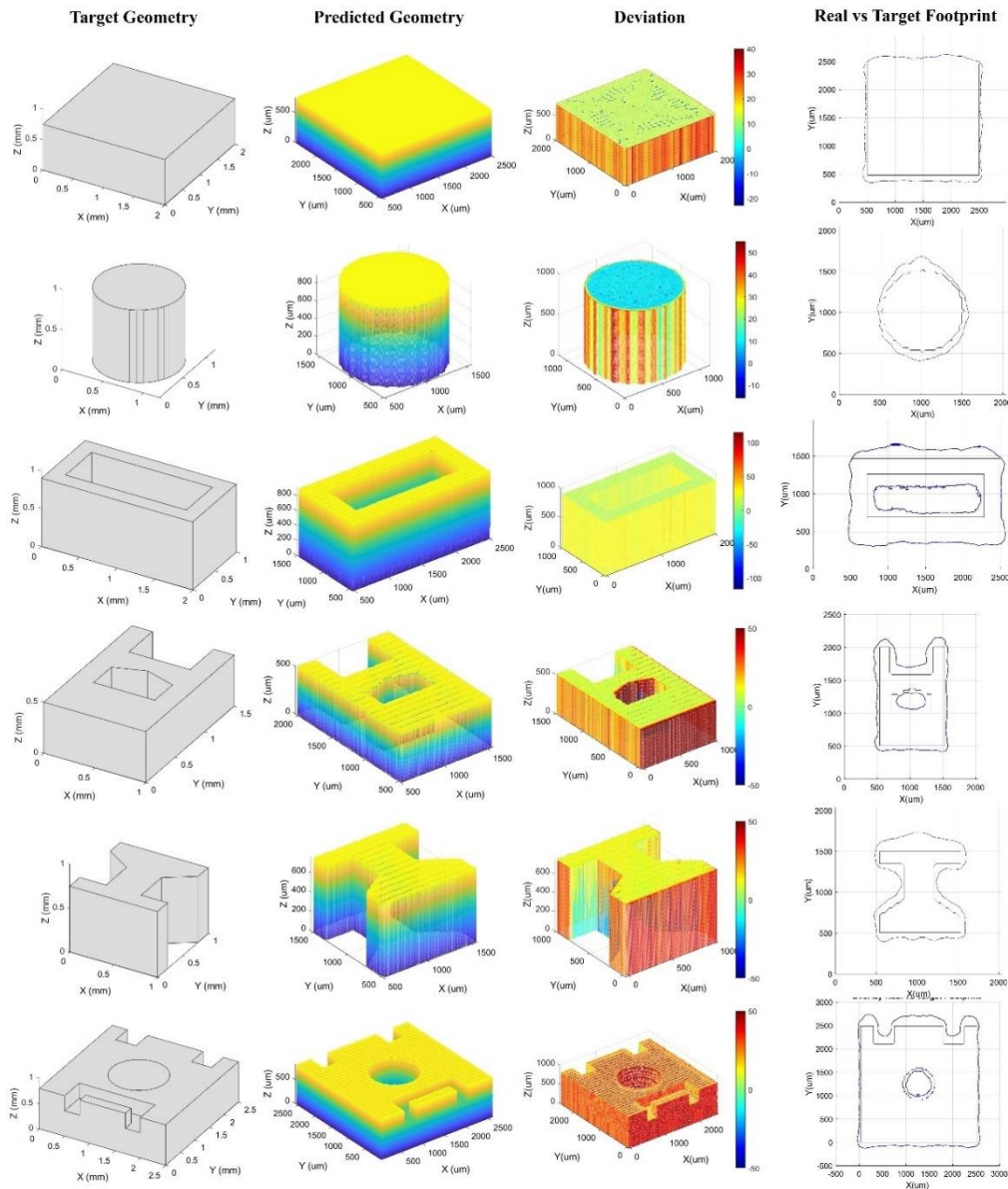


Figure 8-22 Analytical simulation results and comparison to target and printed samples.

8.3.7.2 Deformed geometry prediction using semi-empirical model.

To understand the effect of multi-layered printing on the dimensions of 3D artifacts and improve current model prediction accuracy, a series of experiments printing simple geometries with optimal parameters were performed. Three patterns, a solid square, a hollowed square and a ring were printed on glass using 10 pL cartridge with five layers each, as illustrated in Figure 8-23. The results confirm that using optimal printing parameters, stable features are achieved at every stage of the layer-by-layer process. However, it is noticed that the footprint gradually grows (shrinks for internal patterns) away from the target as layers are deposited on top of each other.

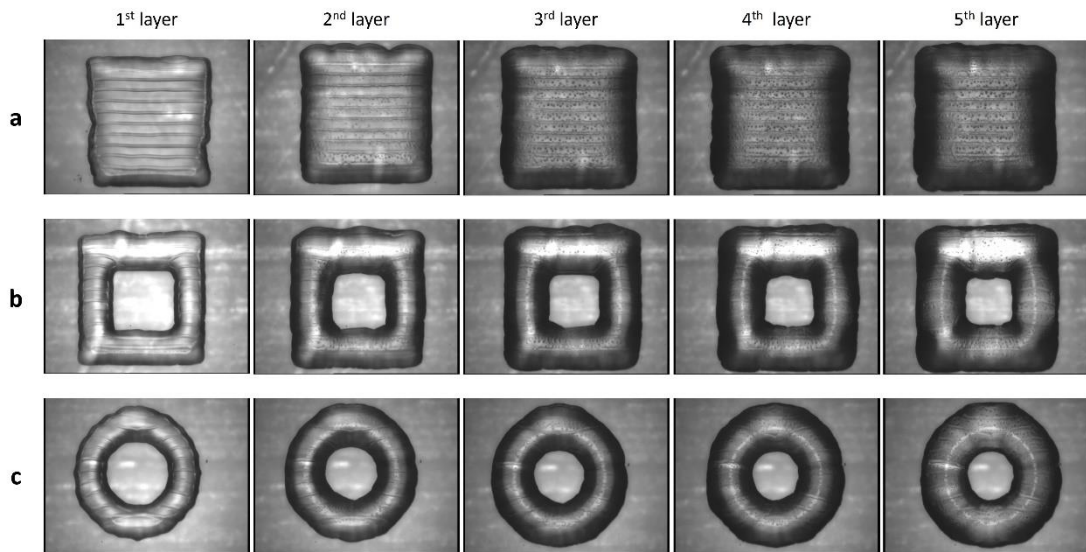


Figure 8-23 Experiments performed to understand the effect of multiple layers on features' dimensions. Three simple patterns are printed with 5 layers each as follows: a. solid square side 1 mm, b. hollowed square side=1 mm, width=0.25 mm and c. ring diameter=1 mm, width = 0.27 mm.

To visualize how much each footprint deviates from target, an overlay plot of the layer edges is presented in Figure 8-24. The first three plots corresponding to (a) solid square, (b) hollowed square (c) ring, demonstrate that the first layers match the target footprint well for both external and internal features. However, plots (d-f) depict how gradually the footprint moves away from the target as layers are overlaid to build the 3D part. The amount of deviation after printing 5 layers is approximately 140 μm and is consistent throughout features. It is also noted that each layer contributes to the total deviation in different proportions and the most significant edge variation is present at the top section of all features.

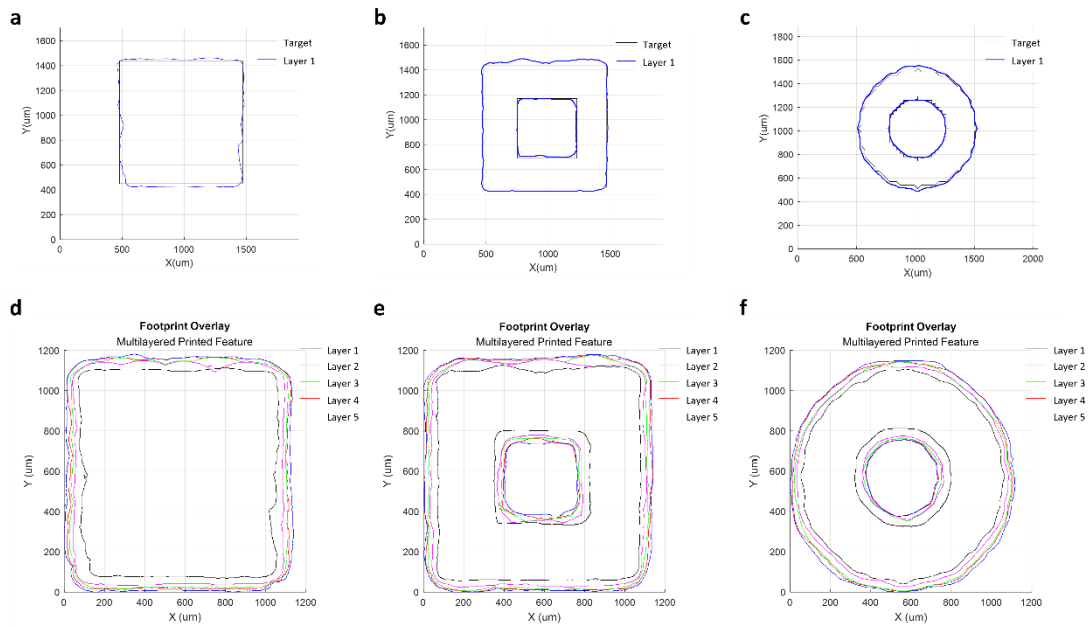


Figure 8-24 Overlay plot of layer footprints to assess the impact of multilayer printing in overall features' dimensions.

A regression analysis was performed to determine the relationship between the multilayer process and the final dimensions of the printed sample. Figure 8-25 shows how the width, length, and thickness of the solid square change as layers are deposited. First, the definition of the measured dimensions is shown in (a). Then, average length and width are plotted as functions of layer number and % of error contribution per layer is included in the secondary axis. It is found that footprint aspect ratio (L/W) is approximate 0.95 and is constant for all footprints; the second layer is the largest contributor to the total error (~45%) and the % contribution to total error per layer gradually reduces with number of layers. It is clearly seen that after 5 layers, length and width exceed target by 103 and 144 μm , respectively. The thickness is modelled using a linear regression in (c) with coefficient of determination of 0.9977 and a layer thickness of 8.25 μm , which validates the prediction of the analytical model (8.5 μm). Finally, width and length deviations from target are plotted as functions of layer number and a logarithmic regression is generated with coefficient of determination 0.9762 and 0.9917, respectively. The same analysis is performed for the hollowed square, where external length and width exceed target by 111 and 145 μm , respectively and layer thickness is calculated as 8.25 μm . Inner width on the hollowed square also exceeds target, by 141 μm , due to the material overflow beyond the inner square boundary. It is important to note that the second layer is the largest contributor to total

error (~43%). Also, an analysis of the internal and external corners of the square start at a radius of the dot size and increase logarithmically with number of layers as illustrated in Figure 8-26. The results of the ring analysis show maximum equivalent diameter deviation from target of 140 μm and layer thickness resulting from linear regression of 7.9 μm . Ring width also exceeds target by 151 μm due to the spreading of material radially inwards. Two main conclusions are drawn from the analysis of these features: compensating the geometry of the second layer automatically cuts the error by almost half and the maximum amount of deviation from target dimensions after depositing 5 layers is consistent regardless of the pattern shape.

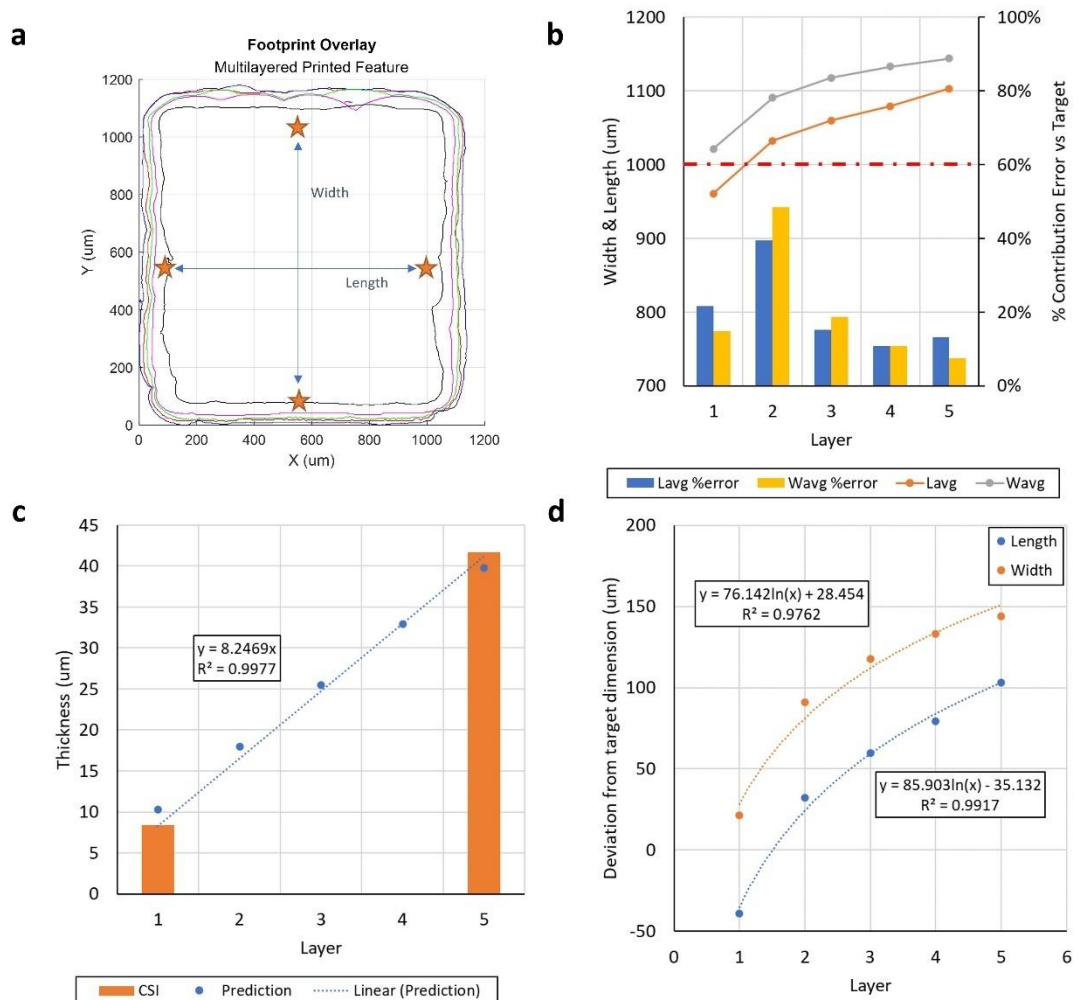


Figure 8-25 Quantitative analysis results for the solid square part. a. Schematic of measured dimensions. b. Effect of multiple layers on length and width. c. Effect of multiple layers on thickness. d. Regression equations to model error on average dimensions.

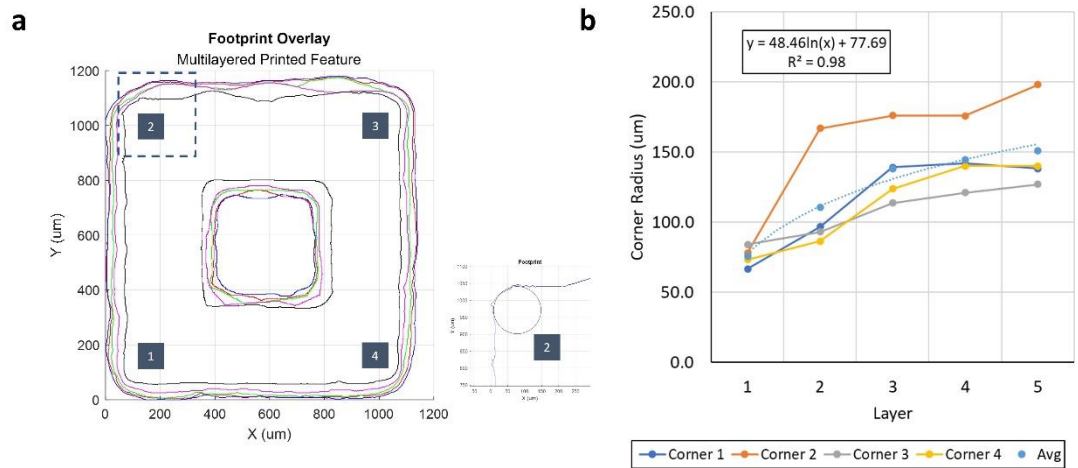


Figure 8-26 Effect of multiple layers on the evolution of corner radii. a. Schematic with corner IDs. b. Regression analysis plot.

With regard to the evolution of corner radii as function of the number of layers, it is observed that the minimum radius is $66.8 \mu\text{m}$ at the bottom left corner, 1) in Figure 8-26a with the first layer. A tighter distribution of corner radii is also achieved with the first layer, then radii variation keeps roughly constant at subsequent layers. Bottom corners (1 & 4) showed much less variation than the top corners (2 & 3) which may be due to less distortion in the previously deposited films. Using optimal printing settings with a 1 mm film size, the minimum achievable corner radius is $75 \pm 7.5 \mu\text{m}$ on a single layer feature. For multilayer printing, the minimum achievable corner radius is $150 \pm 30 \mu\text{m}$ considering only 5 layers. For internal feature with a size of 0.5 mm, the recommended minimum achievable corner radius is $65 \pm 15 \mu\text{m}$ for a single layer and $95 \pm 15 \mu\text{m}$ for multilayer printing. These results shed some light on the maximum resolution that can be achieved in fine features using inkjet printing.

Based on the relationships derived for the error on basic dimensions, a semi-empirical prediction model for simple shapes was developed following the procedure described in Section 4.2.2. A comparison of the feature's morphology between measured data using coherence scanning interferometry and results from the semi-empirical prediction model are illustrated in Figure 8-27. Overall, the prediction results show excellent agreement with printed samples. The spherical cap assumption embedded in the analytical model does an excellent job of predicting the final rounded shape of multi-layered objects. The maximum deviation in all features is kept within $15 \mu\text{m}$ and the mean square errors (MSE) for the solid square, hollowed square and ring are 5.6

μm , $15.1 \mu\text{m}$ and $20.3 \mu\text{m}$, respectively. Larger MSE is observed in the hollowed square and ring parts, due to the lack of measured data obtained from CSI. The maximum thickness of the features is overpredicted by $2 \mu\text{m}$. Using the effect of multiple layers on the general dimensions, an offset of the binary pattern is calculated to predict the final footprint based on the number of layers. This same deviation to target relationship as a function of the number of layers helps in compensating the geometry of binary patterns by offsetting the pattern radially inwards. Therefore, the strategy to compensate the geometry using our machine learning based approach is not needed for this case.

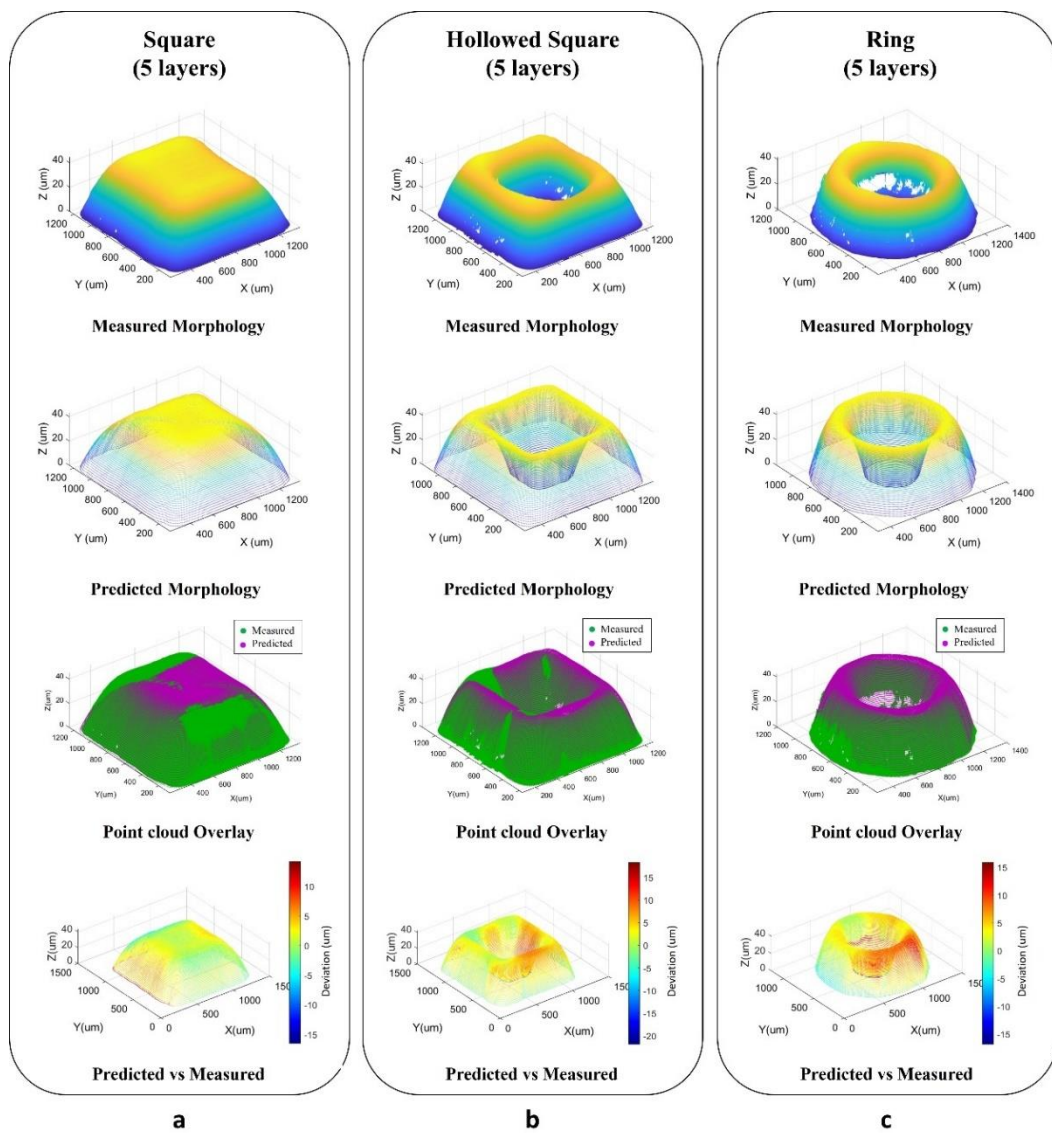


Figure 8-27 Semi-empirical prediction model results comparison with printed samples.

Finally, the graphical user interface that was developed in MATLAB to automate the multiphysics, analytical framework proposed in this chapter is introduced in the next section.

8.3.8 Computational inkjet printing implementation in MATLAB.

To demonstrate how the proposed MPSA framework would be useful for industry or academic environments, a computational inkjet printing process proof of concept (EZInkjet) is implemented in MATLAB, paving the way for real-time process control to improve the quality of inkjet-printed parts. The main code of the graphical user interfaces can be found in Appendix 11.3.

8.3.8.1 Digital image generation module.

The objective of this module is to produce ready-to-print bitmaps of patterns used in electronic packaging applications for any given size and position. The module is capable of reading predefined bitmaps by user and slicing STL files providing the desired resolution and layer thickness. Figure 8-28 illustrates the graphical user interface to create bitmaps of simple shapes (a) and bitmaps from slices of CAD files (b). Predefined patterns are parameterized as functions of the printing location origin and the size and can be selected by the user from three dropdown boxes which categorise patterns in lines, films and special shapes. The lines category includes single pixel horizontal and vertical lines generated by length or number of drops. The films category includes simple shapes used traditionally in electronics packaging applications such as solid and hollowed polygons, circles, corners, junctions, bowtie and Archimedean spiral. The special category includes variable drop spacing films and multiple line patterns. Once the size and location are defined, the pattern is created and displayed for verification purposes. If the pattern is correct, bitmaps are created in a default folder called EZInkjet in the C drive. To slice a CAD geometry in STL format, the GUI enables the user to search and open the file and generate films based on the desired resolution and layer thickness. Slices can be displayed by selecting the slice number from a slider for validation purposes. If slices are correct, bitmaps are created in the default EZInkjet folder. Outputs of the module are saved in a MATLAB

structure and provided as inputs for the prediction module, ensuring efficient communication between modules.

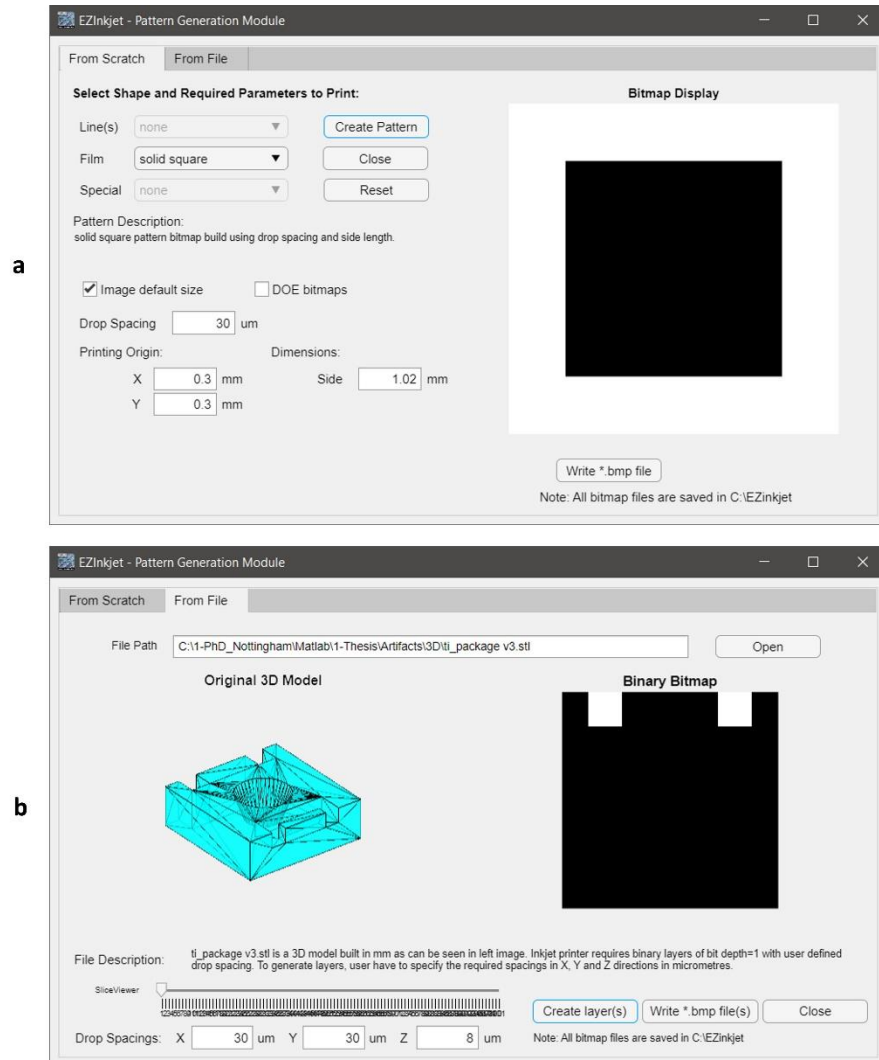


Figure 8-28 Pattern generation module interface. a. Single layer of simple shapes. b. Multiple layers from CAD files.

8.3.8.2 Analytical model prediction module.

The objective of this module is to control the simulation of the inkjet printing process of a selected target layer(s) pattern with given material properties, printing parameters, wetting characteristics, UV curing shrinkage and droplet landing location and size uncertainties using the proposed analytical model. Figure 8-29 depicts the GUI designed to input the simulation parameters, control visualisation of predicted morphology and regulate the contents of results. The interface is divided into three

panels based on the type of parameters to input namely; printing parameters, physical properties and wetting characteristics. The printing parameters panel displays the binary filename and drop spacing of the selected pattern to print and calculates the sabre angle for the Dimatix printer to print in the desired resolution. Printing frequency, standoff distance, number of nozzles, number of layers and position uncertainty are inputs from the user and traverse speed, resolution and estimated layer thickness are calculated automatically. Print mode enables the user to display the overlap map with and without drop position and size uncertainty or build the 3D surface morphology for lines or films. Plot mode enables the user to select between displaying only the results or to visualize the inkjet printing simulation. If the layer count is greater than one, ink to ink wetting characteristics are displayed for user input. The droplet wetting characteristics panel asks for the droplet volume, impact speed, diameter size uncertainty and contact angles. Based on these inputs, in-flight diameter, spot size, droplet height and overlap are calculated. Finally, the physical properties panel is designed to support inks that solidify either by UV curing or evaporation. Currently, only the UV curing mechanism is active and the required physical properties include, density, viscosity, surface tension and shrinkage factor. Dimensionless numbers significant to the inkjet printing process are calculated and the droplet profile is plotted based on the given inputs. Printability and stability diagrams are generated to show if the inputs would achieve printable and stable features.

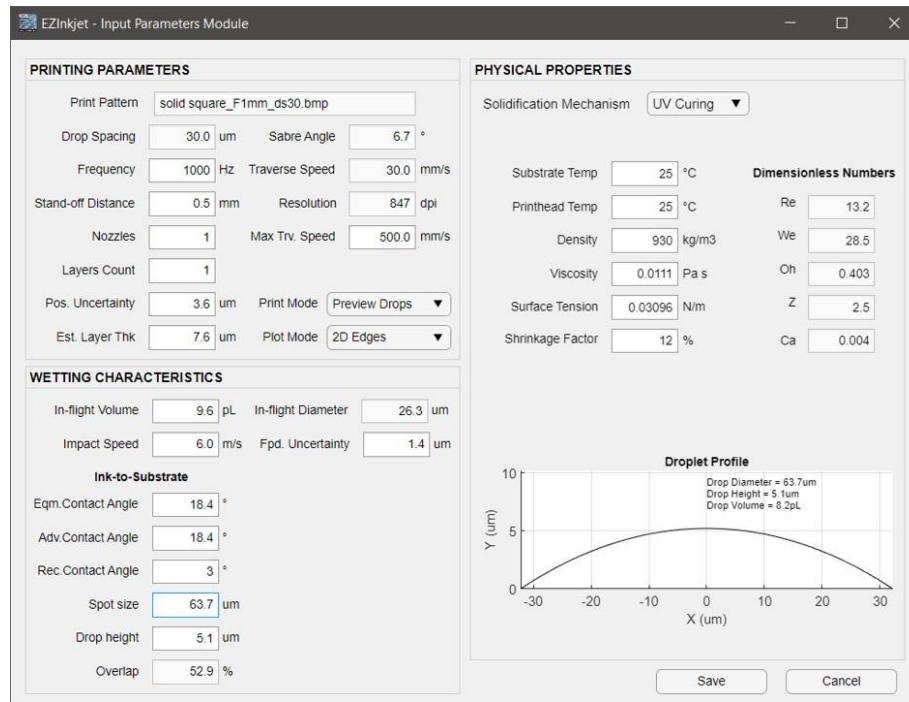


Figure 8-29 Prediction module interface.

It is important to note that the printability diagram limits come from Derby's theory (Derby, 2010) and stability diagram thresholds for bulging and break-up and optimal values for drop spacing, printing frequency and stand-off distance are determined considering droplet location and size uncertainty. Outputs from this module are saved in a MATLAB structure and provided as inputs for the compensation module, ensuring efficient communication between modules.

8.3.8.3 Surrogate model prediction module.

The objective of this module is to build a matrix parametric study based on a response surface design of experiments to create a surrogate model from the results of high-fidelity simulations, shape from shading volume reconstructions or actual measurements of printed features. The module can create an input file to run the simulations in our lattice Boltzmann multiphase flow solver or our finite element chemo-mechanical solver (for lines or small square films only) or a PDE shape from the shading solver (for any shape but constrained to high contrast images). Figure 8-30 illustrates the GUI designed to build an analytical model of the surface morphology of single tracks or films based on selected critical factors of the inkjet printing process.

The interface requests the user to input the number of factors to study, factors maximum and minimum limits and domain discretisation size (e.g., number of equations generated to define the morphology of desired feature). Based on the inputs, width and height cross section plots of the feature are displayed pointing out the locations where response surfaces are to be calculated. The number of experiments is determined based on a central composite design of experiments with 6 centre points for the case of lab experiments and 1 centre point for in silico experiments. Response surfaces are generated automatically and statistical results for each function are available for verification purposes. The module provides detailed descriptive statistics, correlation factors, residuals patterns and main effects for each predicted location, allowing the user to see all locations overlaid on predicted feature morphology using a colour grade (green, yellow, red nomenclature) based on the regression statistical results. Coefficients of determination or residuals can be displayed on the predicted morphology to identify points of poor statistical and practical significance. Outputs from this module are saved in a MATLAB structure and can be provided to the compensation module.

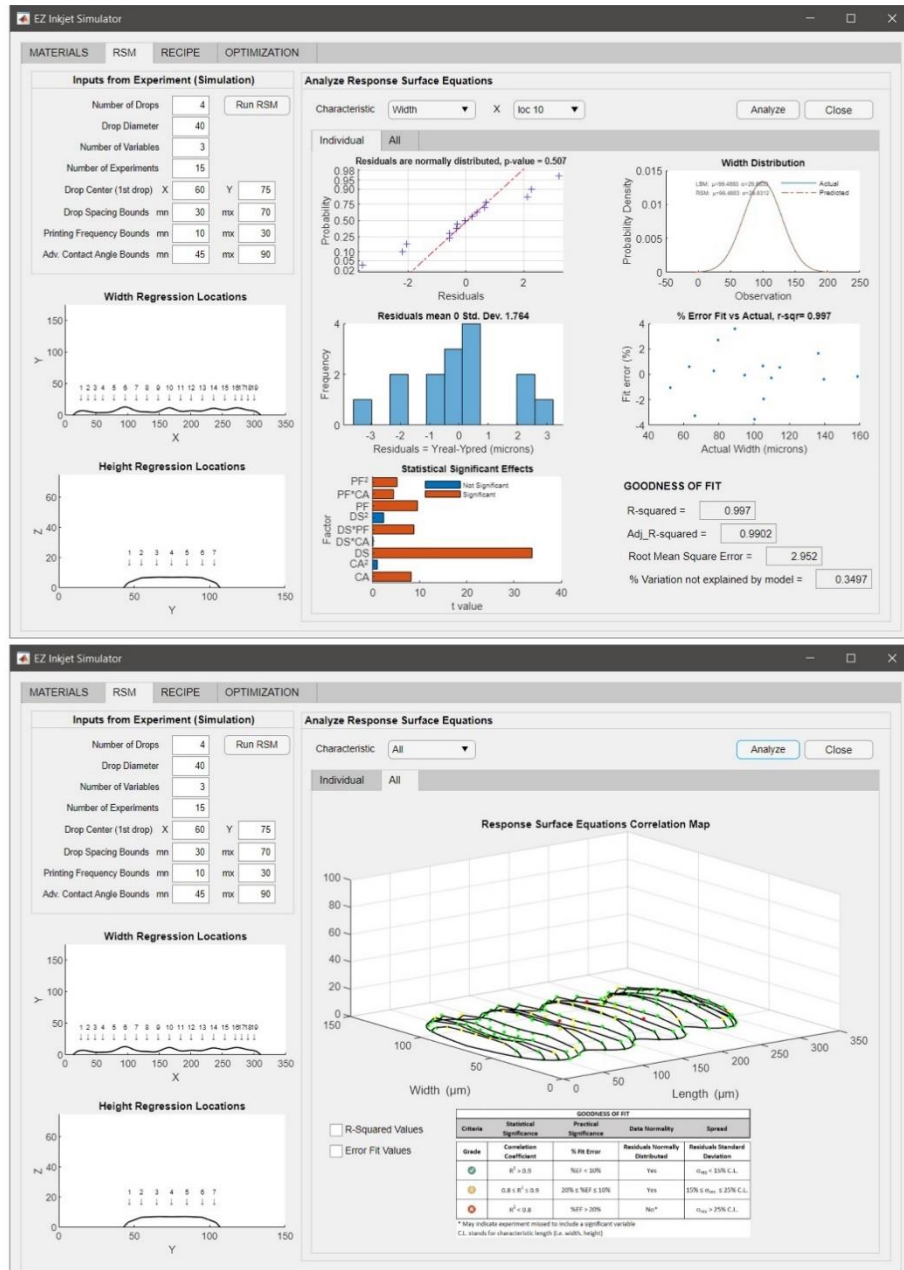


Figure 8-30 Surrogate model prediction module interface. a. Statistical analysis results. b. Predicted surface morphology as function of selected factors.

8.3.8.4 Digital image compensation module.

The objective of this module is to optimise printing parameters and compensate the geometry of binary files to improve the quality of inkjet-printed parts. For the parameter optimisation, the module solves a multi-objective genetic algorithm to simultaneously minimise edge waviness and surface roughness of the desired pattern. The morphology is constructed using the transfer function generated in previous module and parameter space is explored to find the optimal printing parameters. For

the geometry compensation, the module trains a convolutional neural network (CNN) using the x, y and z coordinates of the 3D deformed geometry, which results from either our prediction models or from actual measurements. By providing the target shape coordinates, the CNN calculates the compensation required by the geometry to minimise the error to target shape. The new geometry is sliced and bitmaps for the compensated layer geometry are produced. Figure 8-31 shows the GUI designed to solve in real time the optimisation problem and display the results. The tool allows the user to select if single or multiple objectives are used in the optimisation algorithm. Also, the user has the option to select if the problem is constrained or unconstrained. The constraints are on the feature's edge waviness or surface roughness. The real time genetic algorithm performance plot is displayed to visualize objective function convergence or Pareto front development. Front, side, top and 3D plots of the optimal surface morphology are displayed along with the values of the optimal printing parameters, overlap and dpi resolution. In addition, the overall dimensions of the predicted features are reported, including length, average and maximum width, and thickness. All results are saved in a MATLAB structure and passed to the shape validation module automatically.

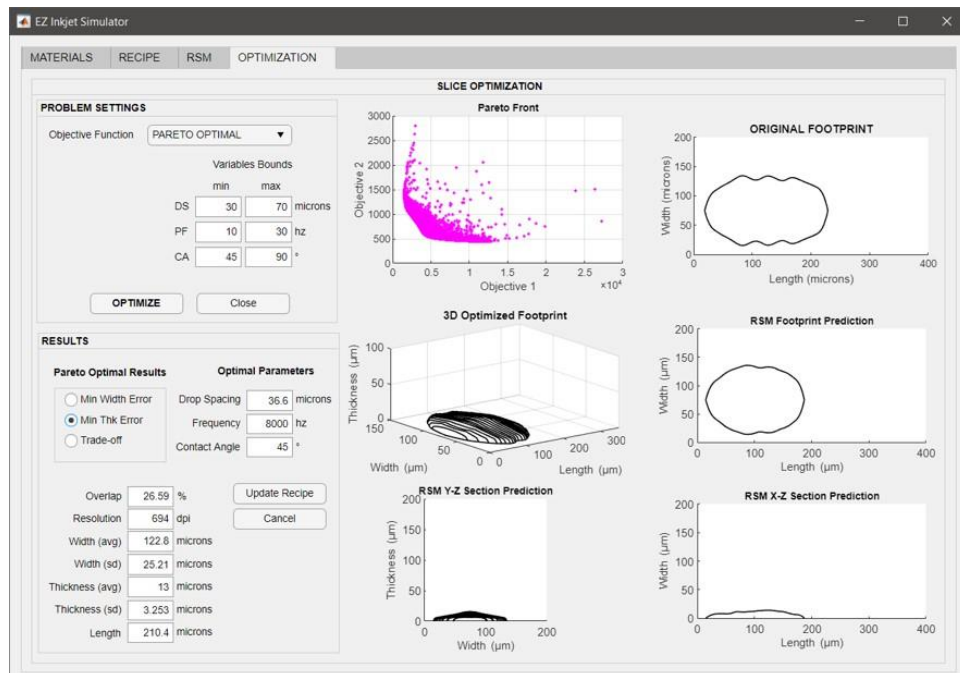


Figure 8-31 Digital image compensation module.

8.3.8.5 *Shape validation module.*

The objective of this module is to provide a set of post-processing tools to compare the results from the model predictions or actual measurements against target 2D patterns and 3D shapes. The tools include the calculation of the mean square error (MSE) and mean absolute deviation between two surfaces, the generation of cross-section images at any given location of a geometry, the overlap and measurement of footprints to evaluate dimensional accuracy, etc. Figure 8-32 illustrates the output from the postprocess tools implemented for this investigation. The volume cross sections viewer (a) generates plots from cross-sections at any location of a printed feature volume defined by its x, y, and z coordinates. It requires as input a text file with 3 columns (x, y, and z) separated by space or CSV file or Excel file with no header, only data located in the first 3 columns. The tool can be used without MATLAB as a standalone program, and it provides the following benefits: easy control of the plotting location using slide bars; fast creation of images at any critical location; accurate plotting of surface morphology dimensions works on any dataset of point coordinates; saves datapoints of edge cross section within a structure in a MATLAB workspace or in a text file if used as a standalone program. The edge overlay tool (b) reads the edges from the target binary file, real Dimatix image file and predictive model results and overlays them for comparison purposes. The tool is extremely useful in the optimisation module to evaluate visually the impact of different printing parameters on printed features and to generate the normalised central geometric moments of aligned images. The surface deviations viewer (c) takes two datasets or geometries, aligns them and calculates the deviations between them. The tool plots the deviations in geometry, pointing out mismatch between geometries. This tool helps to assess the accuracy of the predicted morphology from the methods explored (e.g., surrogate model, volume prediction based on volume conservation assumptions, shape from shading shape reconstruction, analytical model) by comparing datasets against CAD target or CSI measurements. These tools together with the post-processing methods described in Section 4.7 allow the user to reduce the shape validation time from hours to minutes following a standard process.

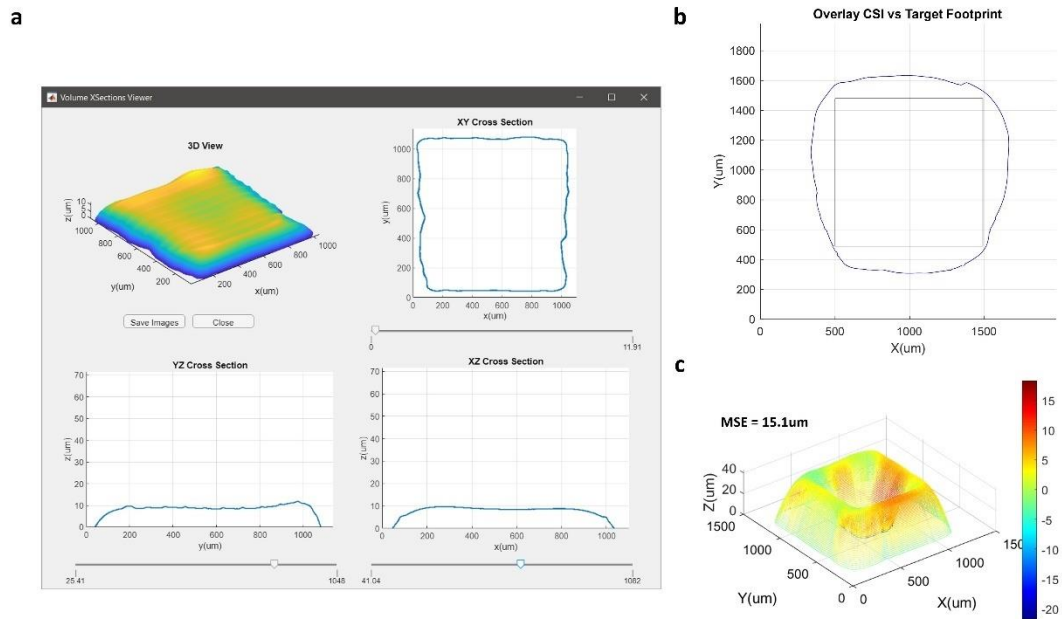


Figure 8-32 Shape validation module interface post processing tools. a. Volume cross-sections viewer, b. Overlay plot and c. Deviations map with maximum deviations and mean square error.

8.4 Conclusions and summary.

In this chapter, a multiphysics analytical model is employed to predict fast and accurately the morphology of inkjet-printed parts for any size and shape considering droplet size and position uncertainty, multi-nozzle printing, UV exposure and chemical shrinkage. Before performing any prediction, the analytical models for material overflow, bulging and break-up size, location and overlap thresholds are analysed and validated through experimental tests. Then, the prediction and optimisation of single tracks using the proposed stability diagram for different substrates and native droplet volumes is performed, confirming the model capability to capture transient effects. Later, simulation of the analytical model to predict film morphology is documented along with experiments to evaluate the accuracy and solution time of the prediction, verifying the appropriateness of the model for parameter optimisation purposes regardless of pattern size and shape. Finally, a multilayer process is simulated to obtain the deformed geometry of complex components and the optimal geometry to counteract the deformation error is determined using a machine learning compensation approach. This work demonstrates three important points: the principle of superposition used to uncouple multiphysics phenomena is able to capture transient effects in a timely manner influencing the

morphology of inkjet-printed features; semi-coupling parameter optimisation with geometry compensation improves the dimensional accuracy and thus the quality of 3D components and computational inkjet printing is feasible through the implementation of a digital twin proof of concept.

Through the implementation of the stochastic, multiphysics analytical model simulation, the interactions between physical properties, printing parameters, droplet characteristics and substrate wettability have been identified. Specific conclusions drawn from the results that have been confirmed with observations from experiments are the following:

- Droplet size and position variation have a significant effect on the threshold values for bulging and break-up defects as well as in the optimal overlap to achieve stable features.
- Overlap map quantification with uncertainty is critical to determine the average number of defects such as bulges and break-ups through Monte Carlo simulation.
- The size of primary and secondary bulges is directly proportional to the advancing contact angle, and the overlap value at which a drastic change in volume happens predicts the onset of bulging in printed features.
- The size and frequency of bulges is drastically reduced as printing frequency increases, which means that stability does not depend purely on drop spacing but also on the rate at which drops are deposited.
- The standoff distance has no significant effect on the size of primary and secondary bulges. However, the frequency of secondary bulges is directly proportional to the standoff distance, suggesting minimal setting of this parameter would improve stability.
- As surface tension increases the size of bulges increases since larger surface tension forces dominate the flow redistribution pulling drops towards bulge. Also, as viscosity increases the frequency of bulges decreases since flow mobility is lower, constraining bulge formation.

- Overall, the stochastic framework provides adequate, consistent and accurate predictions of the average length, width and thickness defining the morphology of printed features, keeping the prediction error less than 10%. Furthermore, the model is capable of building the morphology of any freeform film in tenths of seconds which is critical for multilayer simulation and parameter optimisation.

This investigation revealed new findings that help to understand the role of viscous and capillary forces and timescales and their interaction with printing parameters in the formation of stable, uniform features. The specific conclusions are the following:

- The ratio of momentum diffusivity and capillary diffusivity provides an adequate estimate of the material overflow observed at the boundaries of single tracks and films.
- The ratio of inertia and capillary timescales provides a good estimate of the size of primary bulge and the ratio of capillary and viscous timescales has a significant influence on the frequency of secondary bulges.
- The substrate traverse speed that results from the multiplication of the drop spacing and printing frequency drives the stability of printed features regardless of shape, size, droplet volume and substrate type. For the case of TPGDA deposited on silicon wafer and glass, the optimal velocity is 91.6 mm/s.

9 Discussion.

Recent trends in manufacturing electronics feature digital inkjet printing as a key technology to enable the production of customised and microscale functional devices. However, the mechanical and electrical device performance depends on the accuracy and uniformity of the printed components morphology, which presents significant quality challenges in current applications. Several studies to predict the morphology of printed features have been developed using computationally expensive physics-based simulations or very time-consuming “trial and error” experiments, but little attention has been paid to prediction models suitable for fast production conditions. For this reason, the aim of this thesis is to develop new modelling techniques to predict fast and accurately the surface morphology of inkjet-printed features, enabling the optimisation of process parameters and the compensation of target patterns for better dimensional accuracy of printed electronics devices. To achieve this aim, a series of physics-based, data-driven and hybrid models coupled with machine learning techniques were implemented to predict and optimise the morphology of single tracks (Chapter 5), freeform films (Chapter 6) and 3D components (Chapter 7). Also, an analytical model leveraging learnings from Chapters 5-7 was developed to drive feature’s morphology prediction and optimisation within a computational inkjet printing environment (Chapter 8). The purpose of this chapter is to delve into the meaning, importance and relevance of the results reported in chapters 5-8 and clearly state the contributions of this work to advancing the science behind inkjet printing modelling and optimisation for better quality of printed electronics applications. First, a comparison of the accuracy and speed of prediction models as well as the optimal printing parameters and compensated geometries determined using different predicted morphologies is analysed. Significant contributions and limitations of the proposed frameworks are pointed out along with recommendations of potential improvements. Finally, the benefits of this research to academia and industry are outlined and the novelty of this work is summarised.

9.1 Results discussion summary.

9.1.1 Surface morphology prediction results.

A comparison of the surface morphology prediction of single tracks with the methods developed in this investigation is presented in Figure 9-1. First, a high-fidelity model based on the lattice Boltzmann method was implemented to simulate tracks consisting of four drops as function of drop spacing and contact angle hysteresis. The model was able to predict bulging, uniform and break-up tracks resulting from the variation of the selected parameters. The predicted average width from in silico experiments matched fairly well the theory based on volume conservation assumptions (Stringer & Derby, 2010)(Kang et al., 2010) as well as experiments found in literature (Ledesma, 2018). An example of a line simulated with LBM is illustrated in Figure 9-1a. However, two important limitations of the LBM were identified: the size of the features and the solution time. The maximum number of drops tested was 25 distributed in a 5x5 grid which took 4.5 days to complete simulation. On average, the simulation of single tracks with 4 drops was 6 hours hindering the exploration of parameter space for optimisation purposes. At this point, the first important contribution of this investigation was introduced: a **surrogate modelling framework**. The framework used a sample of LB simulation results to construct transfer functions that define the morphology of the printed feature. The surrogate model built the morphology as function of selected parameters in tenths of seconds, reducing the prediction time 10000x. Good agreement was found between predicted and measured values, with about 95% of data points within 10% error, showing consistent results with Stringer's theoretical model. The predicted morphology using the surrogate model is shown in Figure 9-1b. Furthermore, the proposed framework is not limited to flow dynamics simulations but can be utilized in conjunction with complex multi-physics models or experimental results. For example, a single track printed and measured using coherence scanning interferometry and its corresponding prediction using the surrogate model are shown in Figure 9-1c-d, respectively. As can be seen, the predicted morphology captures the location and size of bulges fairly well from a qualitative standpoint. The absolute deviation of footprint width and feature thickness was within 10 μm and 2 μm , respectively. Again, the time to predict the morphology was in the order of tenths of seconds. The accuracy and speed of the surrogate framework enable the optimal selection of inkjet printing parameters in a reasonable time while capturing

the transient effects from either high-fidelity simulations or lab experiments. However, additional prediction methods were devised with a two-fold objective: first to minimise the high-fidelity model simulation time and second to expand the model capability to include films of any size and shape and different substrate topography. At this point, the second significant contribution of this work was introduced to accomplish this task: a **data-driven Shape from Shading (SFS) approach**. Instead of predicting the morphology of the feature with LBM, the morphology was reconstructed from a single image using the shape from shading inverse problem approach. This approach has been used successfully in the computer vision field to reconstruct the volume of synthetic images by several researchers (Wang et al., 2020)(Durou et al., 2020). However, it is the first time, to the best of author's knowledge, that this is applied to real images coming from inkjet printing cases. To demonstrate the capability of the approach, the reconstructed morphology of a printed track is illustrated in Figure 9-1e. Maximum footprint deviation against experiments was less than 5 μm . The accuracy of the reconstruction (feature thickness) depends on the reflective properties of the material, which for the case of TPGDA printed on glass or silicon wafer, resulted in a prediction error less than 1.5 μm . Overall, the morphology predicted by the shape from shading approach shows very good agreement with printed samples of single tracks. The average time to predict the morphology of single tracks using the Lax-Friedrichs scheme is 3 min. The accuracy and speed of the shape from shading approach is remarkable, especially in terms of the accuracy of the feature's footprint, which is slightly better than surrogate model since the latter employs a low sample of results to fit the morphology. In terms of speed, the surrogate model is two orders of magnitude faster than shape from shading approach, which still hinders the parameter optimisation process in real time using the latter approach. The main limitation of shape from shading lies on the reflective properties of the material used in printed samples, since the morphology is reconstructed based on the grayscale levels defined in the image which ultimately depend on how well frontal light is reflected in a diffusive and specular manner. A potential improvement in the solution speed may be the implementation of fast eikonal solvers (Jeong & Whitaker, 2008) such as higher order Godunov scheme, which does not depend on the adequate selection of the artificial viscosity as in the Lax-Friedrichs scheme. In addition, the use of a Dirichlet boundary condition with a spherical cap shape to guide the solution and avoid convex/concave ambiguity may be beneficial. Overall, the shape from shading

approach enables the accurate morphology reconstruction of printed tracks, avoiding the use of microCT scanning or coherence scanning interferometry and reducing the post-processing time required to clean measured datasets. However, the search of the optimal printing parameters to achieve stable tracks in real time is still not feasible with direct predictions of high-fidelity simulations or surface morphology reconstructions. At this point, the third significant contribution of this investigation was introduced to accomplish this task: an **analytical, multiphysics and stochastic framework (MPSA)**. The framework was based on the theoretical estimation of the average width of single tracks developed by Stringer and Derby, which assumes conservation of volume and a spherical cap shape along the track. Experimental results match the average width predicted by theory (Stringer & Derby, 2010) and are consistent to experiments from literature (Hsiao et al., 2014)(Soltman et al., 2010). This work's contribution is on the estimation of the maximum track width (maximum material overflow) which we claim is a function of the ratio of momentum diffusivity and capillary diffusivity. Experimental results indicate excellent agreement with the prediction of the material overflow using the proposed analytical relationship. In addition, an analytical estimation of the size and frequency of primary and secondary bulges was developed as function of viscous, inertia and capillary timescales, based on lubrication theory (Thompson et al., 2014). Experimental results match the prediction of the primary bulge size and the number of secondary bulges, but the location of secondary bulges could not be accurately predicted. Also, a statistical estimation of the number of break-ups in the feature was devised using a droplet overlap map build considering the uncertainty of droplet position and size and solved using Monte Carlo simulation. Experimental results indicate very good agreement in the average number of break-ups found in a printed feature as function of droplet position and size uncertainty. Furthermore, the MPSA model considers the effect of droplet size and position uncertainty, multi-nozzle printing, UV exposure and chemical shrinkage acting in a semi-independent way, which covers the multiphysics and stochastic part of the model. Figure 9-1f illustrates the prediction of the morphology of a single track using the MPSA framework. As can be seen, the size and frequency of bulges shows very good agreement compared to experimental results. The maximum width and thickness prediction error is less than 10 μm and 3 μm , respectively. The largest prediction error was observed in the length dimension at 22 μm , which represents 2% of the dimension. The average time to predict the

morphology of single tracks is in the order of seconds, which enables the optimisation of printing parameters in real time. The main limitation of the MPSA model is that has only been validated using physical properties of TPGDA at 25°C deposited on glass or nitride-coated silicon wafer. Future short-term work includes the validation of the model with various photocurable inks deposited on rigid and flexible substrates. A long-term model enhancement is to incorporate the physics of evaporation necessary to predict the final shape of solvent-based inks.

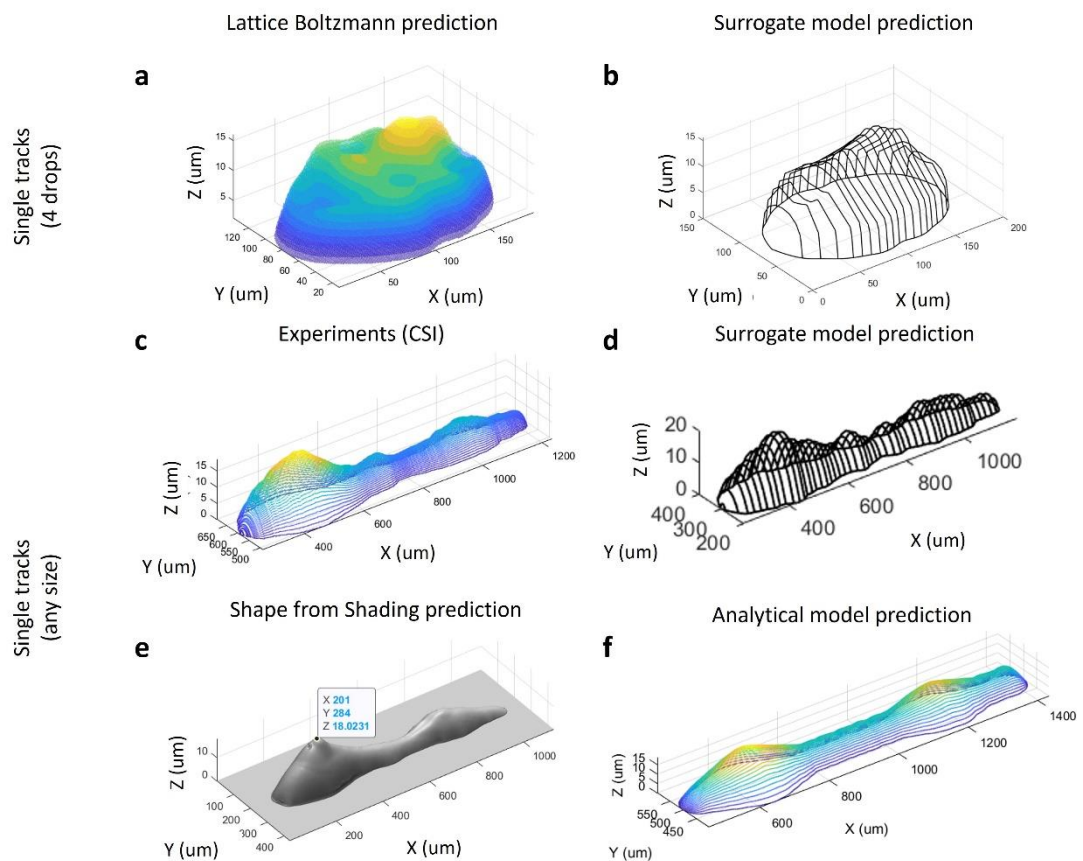


Figure 9-1 Comparison of the surface morphology of single tracks using different prediction models. a. Lattice Boltzmann of a line build from 4 drops. b. Surrogate model built from sample of LBM simulation results. c. Experiments measured using CSI. d. Surrogate model built from experiments. e. Shape from shading prediction built from image. f. MPSA single track prediction.

A comparison of the surface morphology prediction of freeform films with the methods developed in this investigation is presented in Figure 9-2. The capabilities of the prediction models found for freeform films are consistent to the ones observed for single tracks and only particular remarks are included next. Although, LBM simulations of square films showed good capability to capture bulging, uniform and

separated films and compare well with observations found in literature (Zhang et al., 2018)(Cheng et al., 2018) and our own experiments (Section 6.3.1), the excessive computational time required to predict the surface morphology of small patterns prevented the exploration of this method further. Instead, experiments were performed to directly measure the surface morphology of freeform films, as shown in Figure 9-2a, needed for the application of the surrogate modelling strategy. An alternative approach to measuring all printed samples using CSI was introduced and the morphology of the films was reconstructed using the SFS approach. The reconstructed surfaces using SFS showed excellent agreement on the footprint boundaries prediction since the method uses a mask derived from highly accurate image segmentation procedures (e.g., maximum error less than 3 μm). In addition, it was found the SFS approach can build the surface of multiple segments with free-form shapes simultaneously in a timely manner (average build time of 6 minutes). It is important to note that details on the surface roughness caused by printer swaths were lost in the SFS prediction and only smooth surfaces could be reconstructed. Also, it was found that the predicted film morphology is highly influenced by localized specular reflection from the image, which is recommended to be controlled at the imaging process. An example of a film reconstructed using SFS approach is illustrated in Figure 9-2b and a comparison of the reconstructed geometry with the printed sample is shown in Figure 9-2e. The deviations between the reconstructed and measured morphology are within 5 μm and the root mean square error is 2.8 μm , confirming excellent qualitative agreement is achieved. Although, the SFS predicts fairly accurate the morphology of films, the search of the optimal printing parameters to achieve stable films in real time is still not feasible with direct surface reconstructions. Therefore, the surrogate modelling strategy was employed to build the morphology of films as function of printing parameters. Figure 9-2c depicts the film predicted using the surrogate modelling strategy. The prediction error relative to the main dimensions is less than 2.5% and the average root mean square error is 10.3 μm . The increase in the RMSE is likely to be caused by the non-smooth morphology predicted by the surrogate modelling strategy due to low number of sample experiments used in the regression. However, the overall shape of the printed feature was successfully achieved in tenths of seconds, enabling the optimisation of printing parameters. Finally, the predicted morphology of a solid square film using the MPSA model is illustrated in Figure 9-2d. The MPSA was able

to capture the horizontal bands of cured material caused by printing swaths and the thickness reduction due to chemical shrinkage induced by photo-polymerization process in tenths of second. A comparison of the predicted morphology using MPSA model with measurements of printed sample is presented in Figure 9-2f. The results show a maximum absolute deviation of 75 μm near the bottom left corner of the pattern and a root mean square error of 10.6 μm . The average error along the thickness is 2.5 μm , reducing the prediction error for the thickness but yielding a larger error in the footprint length, since MPSA cannot capture adequately the coalescence between swaths, which is the main limitation of the MPSA simulation.

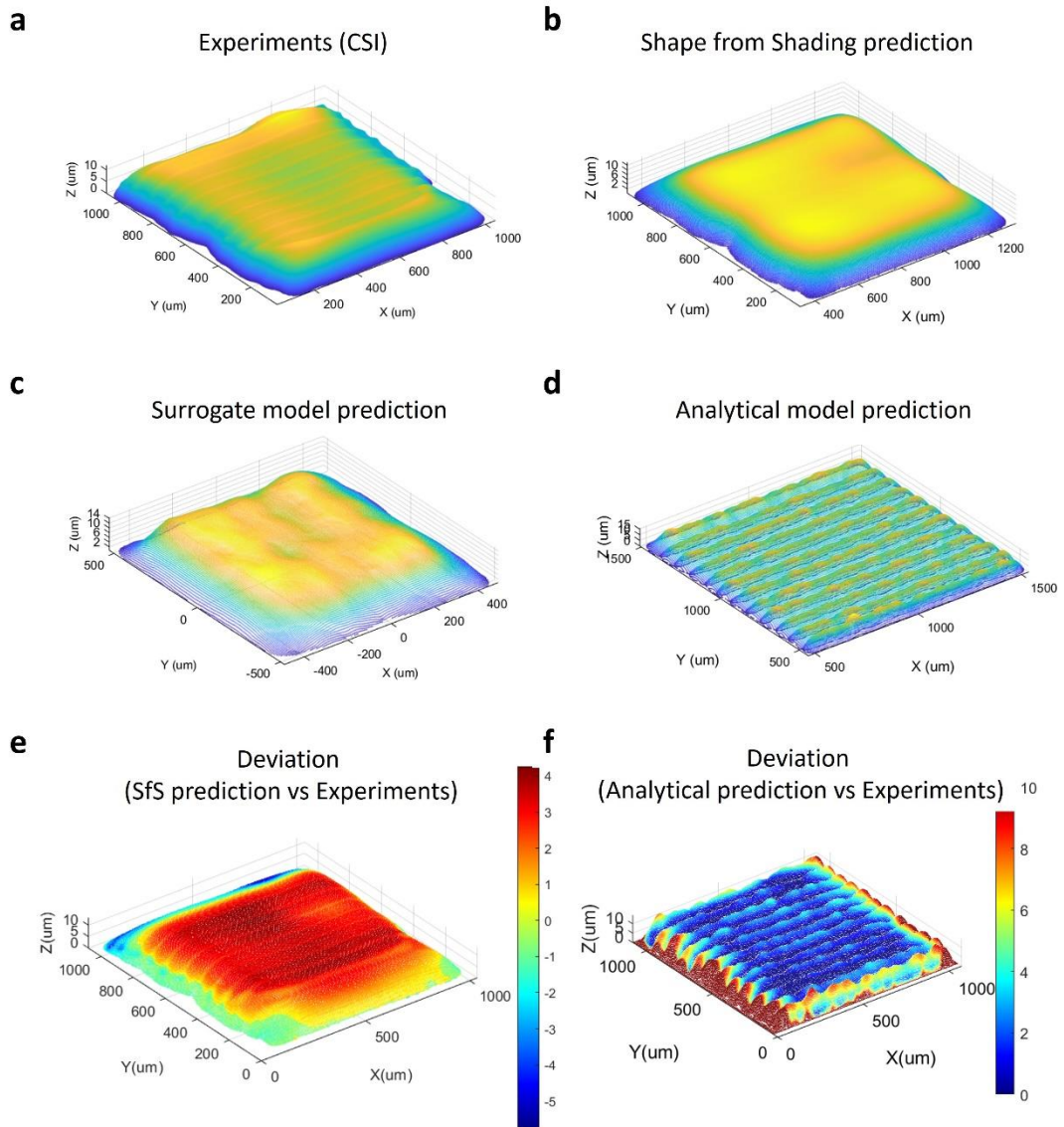


Figure 9-2 Comparison of the surface morphology of solid square films using different prediction models. *a.* Experiments measured using CSI. *b.* Shape from shading prediction built from image. *c.* Surrogate model built from experiments. *d.* Analytical model prediction. *e.* Deviation of SfS prediction from experiments. *f.* Deviation of analytical prediction from experiments.

In summary, various methodologies to predict the surface morphology of single tracks and freeform films as function of printing parameters were evaluated for accuracy and speed of execution. Based on the results, the surrogate modelling framework provides the best trade-off between accuracy and speed to evaluate the design space for parameter optimisation purposes when experiments are available. Otherwise, the MPSA model provides a fast way to predict the morphology of printed features, losing some accuracy in the footprint dimensions, but enabling parameter optimisation. Future work may expand the capability of MPSA model simulation to account for inter-swaths coalescence and improve its accuracy. In the next section, the optimal

printing parameters derived for single tracks and films using the surrogate modelling framework are discussed.

9.1.2 Parameter optimisation results.

Table 9-1 lists the optimal printing parameters derived from various surface morphology prediction models explored throughout this investigation. Four sets of optimal printing parameters were derived targeting feature's stability with minimum thickness and one set targeting stable features with maximum thickness. Analysing the sets focused on minimum thickness, the results show that irrespective of the prediction model used, the optimal printing parameters converged to an approximate drop spacing, printing frequency and standoff distance of 30 μm , 3 kHz and 0.5 mm, respectively, except for the set derived using LBM results. The optimal printing parameters are consistent to the parameters used by Zhao et al. (2021) to achieve stable films. The difference observed in the optimal parameters derived using LBM can be attributed to important process factors not considered in the LBM modelling assumptions such as deformation due to UV curing shrinkage, droplet location and size variation introduced by equipment tolerances and chemically inhomogeneous substrates due to poor cleaning process. More details regarding the observed optimal parameters difference were included in Section 5.3.3. Furthermore, only the MPSA model provided a set of optimal printing parameters for thickest features, since it was revealed by MPSA model that bulge frequency was greatly reduced if the multiplication of printing frequency and drop spacing is approximately 90 mm/s. More details regarding the critical interaction of the drop spacing and printing frequency and its influence in the stability of printed features can be found in Section 8.3.3. In addition, the MPSA model generates a stability diagram based on statistical analysis of an overlap map to obtain the onset of bulging and break up thresholds as well as the recommended optimal parameters considering drop location and size uncertainty. Further details about this novel contribution can be found in Section 8.3.6. Several patterns of different shape and size were printed employing the optimal printing parameters to confirm the fabrication of stable features, as illustrated in Figure 9-3. As can be seen, patterns present minimal footprint waviness and a stable morphology (e.g., no bulges or break-ups, forming a continuous, uniform film). Printing swaths are

noticeable in the surface of the films (e.g., ridges less than 1 μm) in the form of regular horizontal bands, except for the bottom swaths due to partial curing. Overall, experimental data indicates that stable films can be achieved when optimal printing parameters are employed.

Table 9-1 Optimal printing parameters derived from different prediction models.

Parameter	Units	Lines		Films	Lines and Films	
		LBM*	EXP	SFS (exp)	MPSA (thin)	MPSA (thick)
Drop spacing	μm	37.4	31.4	31.0	29.6	10.0
Printing frequency	kHz	M	2.8	3.0	3.1	9.2
Standoff distance	mm	L	0.5	0.5	1.0	0.5

Note: * Printing frequency and standoff distance in LBM simulation were modelled qualitatively and the magnitude of this parameter is reported as low (L), medium (M), or high (H).

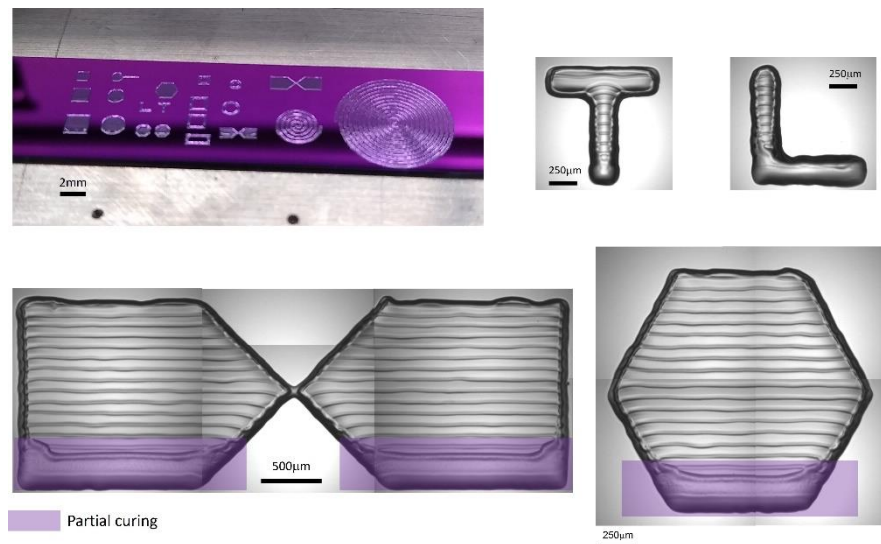


Figure 9-3 Samples printed with optimal printing parameters for validation purposes.

In summary, it has been demonstrated that using a multi-objective genetic algorithm to minimise printed feature's waviness and roughness simultaneously enables robust inkjet printing parameter optimisation. Furthermore, printed sample waviness can be quantified in a fast and accurate way using the normalised central geometric moments of the footprint. It was also shown that printed sample roughness can be quickly calculated from point cloud data of the predicted morphology. The genetic algorithm was able to determine with high accuracy the three key printing parameters: drop spacing, printing frequency and standoff distance from physics-based simulations and experiments. The Pareto front was built in less than 3 min evaluating more than 5000

combinations seeking the global minimum. The results reveal that optimal printing parameters to achieve the best quality of inkjet-printed films (layers) of any size and shape can be derived from single tracks, reducing the time, cost, and complexity of the experiments. The main limitation of the optimisation process lies on the adequate selection of the genetic algorithm hyperparameters such as crossover and mutation rates and convergence criteria. The effectiveness of the algorithm may be further improved by understanding the effect of hyperparameters on the execution time and accuracy of optimal parameters, which demand a wider range of testing values. Although, the parameter optimisation process takes approximately 3 min, it is not fast enough for real-time monitoring and feedback to printer for rapid correction. Therefore, future work may explore analytical methods to constraint parameter space and enable faster determination of optimal parameters. In the next section, the results of the geometry compensation framework using a machine learning approach are discussed.

9.1.3 Deformed geometry generation and compensation results.

In the course of the investigation, observations from experiments revealed that optimal printing parameters derived for single tracks and films do not achieve the most dimensionally accurate 3D inkjet-printed parts, as illustrated in Figure 9-4a. Significant differences between measured data and the CAD model were observed along the width, depth, and height of the printed artifact (e.g., cuboid 2x2x0.75 mm). It was found that first layer matched target footprint fairly well with a maximum deviation of 30 μm ; however, as layers were superimposed the material overflow beyond target footprint was exacerbated. The average deviations in width, depth, and height exceed target in 30 μm , 168 μm and 150 μm , respectively. Therefore, a method to compensate the CAD geometry by counteracting the deviations of the printed geometry introduced by the superposition of layers was developed. It was demonstrated that nodal coordinates from microCT scan measurements together with its corresponding locations in the CAD geometry can train a convolutional neural network (CNN) iteratively until the mean squared error determined from geometry deviations is minimised. The compensated CAD geometry was generated by predicting the location of the original CAD vertices using the CNN, as shown in Figure

9-4b. Results indicate that our machine learning model trained with measured data can compensate the original shape and build a STL file which is vital to obtain binary layers for 3D inkjet printing application. The compensated geometry presents a negative taper on the external faces (e.g., inverted truncated pyramid shape), since the cross-sectional area of the measured artifacts gradually reduces along the part height and away from target. The reduction of the area at bottom section of the compensated geometry is particularly pronounced to control material spreading beyond the target footprint. In addition, there is a clear increase of the height in the compensated geometry to match the target shape dimension. Using a CNN to compensate the deformed geometry predicted by a FE thermo-mechanical model has been used effectively by Chowdhury et al. (2018) in applications where deformed and target geometries have identical meshes. In this work, the registration process of dissimilar meshes was developed by creating a mapping algorithm between point cloud of CAD model surface and the 3D scan of the printed part. The main limitation of this methodology is that requires a thorough statistical analysis to validate the CNN regression. For example, for the cuboid CNN, the coefficient of determination indicate an excellent correlation between predicted and target values (e.g., 0.999), but the magnitude of the residuals is in the order of 100 μm which may not be accurate enough for the prediction. Therefore, the regression models are statistically valid but not accurate enough to approximate the part deformed geometry as a function of the coordinates of its surface points. The most likely cause of the large error in the prediction model is the presence of outliers in the measurement data point clouds. It was found that the mapping algorithm picked points inside the deformed geometry surface that introduce a large variation in the regression model. It is recommended to clean measurement data point clouds so that only points defining the deformed surface are kept for training the neural network and achieve more accurate predictions.

Since the focus of this investigation was to devise novel methodologies to accurately predict the deformed geometry of 3D parts, physics-based and analytical models were developed. We demonstrate that the deformed geometry of 3D inkjet-printed parts can be estimated by a chemo-mechanical FE simulation, a MPSA simulation based on layer superposition and a semi-empirical model based on spherical cap equations, as depicted in Figure 9-4c, Figure 9-4e and Figure 9-4f, respectively. It was found that the only model capable to predict the material overflow and rounded shape observed

in 3D printed part was the semi-empirical model based on spherical cap equations. The chemo-mechanical FE model shows the maximum shrinkage at the top section of the printed artifact where maximum degree of monomer consumption occurs. As the printing progress from top to bottom of the artifact, shrinkage linearly decreases due to the partial curing of the last swaths and higher mobility of the material is expected. This difference in height between top and bottom sections, may explain the propensity of the material to flow towards the top section due to gravity, increasing the thickness of the film as observed in the experiments performed in Chapter 6. Overall, the FE model is capable to predict the magnitude of the maximum thickness shrinkage fairly accurate, which validates the simplified methodology using static restarts instead of transient model and reducing the FE solution time from days to minutes. The FE results are consistent to the work of Tilford et al. (2021). However, the model does not capture the material spreading over the substrate which is typically present in experiments due to the perfect adhesion assumption used at bottom layer and material constitutive modelling assumptions. This is a critical limitation of the FE model to predict accurately the deformed geometry of 3D inkjet-printed parts. A potential improvement to the FE simulation is to incorporate the substrate geometry and model the interface assuming a friction coefficient to enable bottom layer displacement. Future work may incorporate a viscoplastic constitutive model to represent distortion in a more accurate way. Although, the FE model does not capture the behaviour from experiments, the results of the simulation were used to validate our proposed geometry compensation framework with identical meshes. Figure 9-4d illustrates the compensated geometry from FE simulation results. The data indicates that our machine learning compensation framework is capable to compensate CAD model using in silico experiments where the target and deformed geometries have the same number of nodes. Finally, the validation of the compensation framework was performed by direct printing the slices of the compensated geometry. The percentage of reduction in the mean square error due to the compensation strategy for the cuboid artifact is 72%, confirming the effectiveness of the framework.

On the other hand, the MPSA simulation results show good agreement between prediction and target geometry with a maximum absolute deviation of less than 50 μm . The walls of the artifacts show a non-uniform distribution of deviations due to the stochastic film formation. The layer thickness prediction from analytical model

enables to fabricate a 3D object closer to the target height compared to other methodologies. Although the predicted geometry matches target, the MPSA prediction does not represent what actually happens in reality. When the ink is deposited near the edges of previous films, the surface is not flat causing the ink to flow downwards, spreading beyond target dimensions. Therefore, the MPSA model is not capable of capturing the deformed geometry of actual 3D inkjet-printed parts and additional considerations must be implemented to consider the effect of multi-layer printing in the final part geometry. Future work may incorporate empirical correlations relating the amount of deviation from target as a function of number of layers, which follows a logarithmic relationship from experimental observations reported on Section 8.3.7.

Finally, the semi-empirical model based on spherical cap equations show excellent agreement with printed sample, as depicted in Figure 9-4f. The spherical cap assumption embedded in the analytical model suitably predicts the final rounded shape of multi-layered objects. The maximum deviation is less than 15 μm and the mean square error (MSE) for the solid square, is 5.6 μm . The maximum thickness of the features is overpredicted by 2 μm . Using the effect of multiple layers on the general dimensions, an offset on the binary pattern is calculated to predict the final footprint based on number of layers. This same deviation to target relationship as function of the number of layers helps compensating the geometry of binary patterns by offsetting the pattern radially inwards. Therefore, the strategy to compensate the geometry using the machine learning based approach is not needed for this case, reducing the computational prediction time from minutes to tenths of seconds. The semi-empirical model is limited to the prediction of the surface morphology of basic, symmetric shapes such as solid and hollowed polygons. Future work may expand its capability to include more complex shapes and different ink-substrate systems.

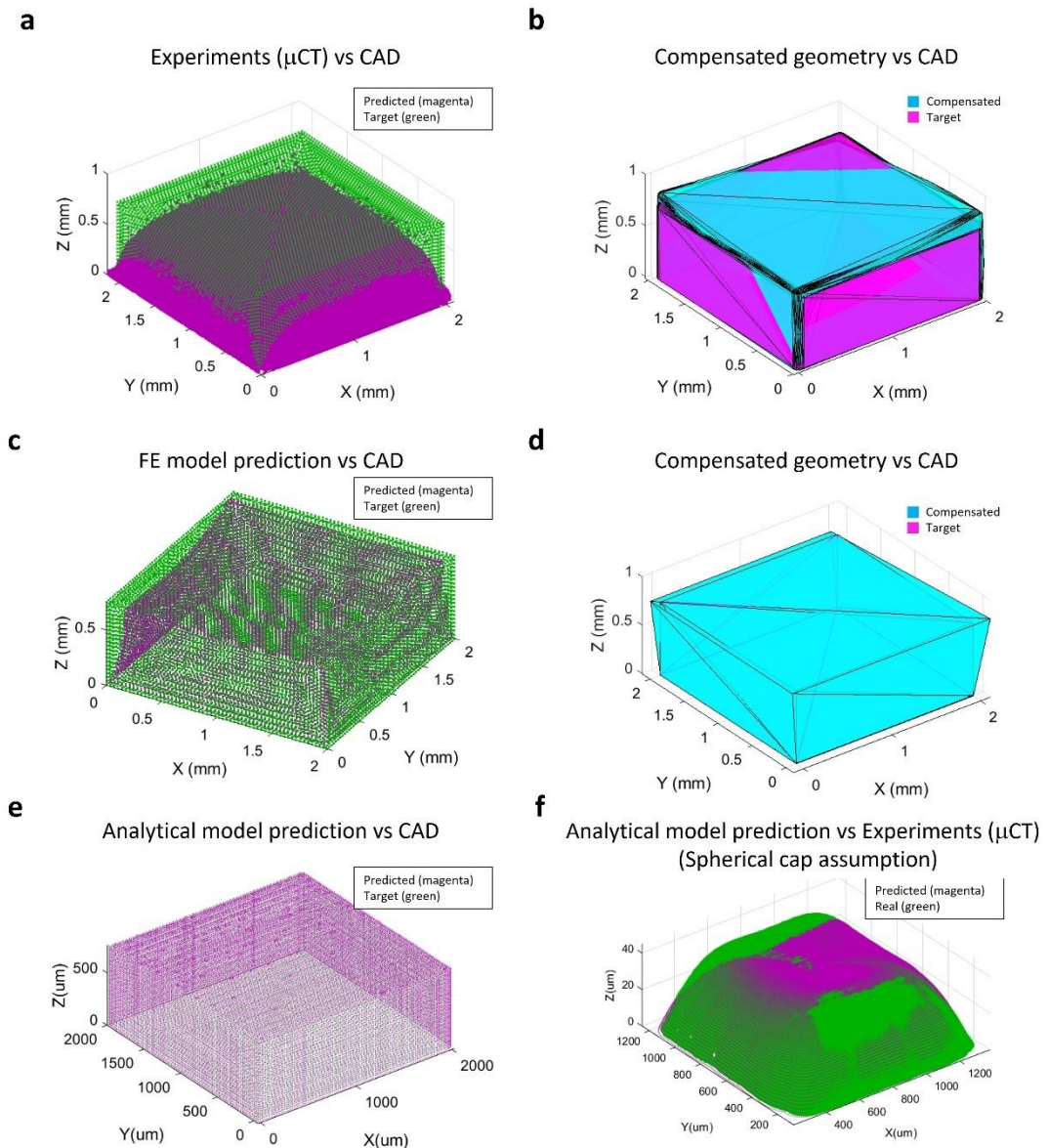


Figure 9-4 Geometry compensation framework results. *a.* Experiments measured using microCT scan. *b.* Target vs compensated geometry using data measurements. *c.* Deformed geometry predicted using FE simulation. *d.* Target vs compensated geometry from FE results. *e.* MPSA model prediction of deformed geometry vs target. *f.* MPSA model prediction with spherical cap assumption for simple 3D features.

The discussion of the results presented in this section provide sufficient evidence to support our research hypotheses and achieve the aims of this investigation. In next section, we identify the benefits of this study to academia and industry and summarize the novelty of the research.

9.2 Benefits of the research to academia.

The outcomes of this investigation are beneficial to the academic community as they contribute to filling the gaps in the literature relative to high throughput models to improve the quality of inkjet-printed parts. For instance, the surrogate model-based optimisation of printing parameters coupled with ML-based geometry compensation approach is a novel and efficient framework focused on producing high quality inkjet-printed parts. Most of research studies from the literature have employed isolated efforts to either optimised AM process parameters (Vaithilingam et al., 2018)(Lanzotti et al., 2015)(Mohamed et al., 2015)(Rahul et al., 2017) or compensate the CAD geometry to counteract the error of printed parts (Chowdhury et al., 2018)(Decker & Huang, 2019)(Jin et al., 2020)(Huang et al., 2020). Whereas the current investigation proposed an integrated framework to produce stable, defect-free parts on a timely manner through the fast and accurate prediction and optimisation of the surface morphology of printed components. Furthermore, the surrogate modelling strategy is highly versatile since can be utilized in conjunction with complex multi-physics models or experimental results to find the optimal printing parameters for any size and freeform patterns considering different materials and substrates or even other AM technologies.

This research is the first to report a multiphysics, stochastic, analytical (MPSA) framework to predict fast and accurately the morphology of inkjet-printed parts for any size and shape considering droplet size and position uncertainty, multi-nozzle printing, UV exposure and chemical shrinkage. The effect of droplet size and position uncertainty is graphically represented using an overlap map of the printed drops to statistically determine film defects such as bulges and voids. No study in the literature has proposed the overlap map concept as a performance indicator of the quality of inkjet-printed features, showing that the literature needed this data for better understanding of the mechanisms behind the generation of film defects. Furthermore, the effect of chemical shrinkage on the film thickness is introduced through the degree of monomer consumption distribution which is a function of the UV exposure time and printing strategy (Zhao et al., 2021). A significant original contribution to this MPSA model is the estimation of the maximum material overflow of single tracks and film edges by correcting the theoretical bead width (Stringer & Derby, 2010) using a factor that results from the ratio between the momentum diffusivity and capillary

diffusivity. The developed equation is valid for TPGDA deposited on glass and nitride coated silicon wafer for 2.4 pL and 10 pL droplet volumes. Through the implementation of the MPSA model simulation, the interaction between physical properties, printing parameters, droplet characteristics and substrate wettability and their effects in the generation of stable printed features is provided. The MPSA framework leverages learnings from the physics-based and data-driven models and integrates creative algorithms and heuristics rules to drive AM part quality optimisation within a computational inkjet printing environment.

9.3 Benefits of the research to industry.

This investigation achieved a number of findings that are of benefit to various industrial sectors interested in inkjet printing of photocurable materials such as the semiconductor and healthcare industries. For example, the surrogate model-based optimisation framework coupled with ML-based geometry compensation method reduces the time devoted to find the optimal printing parameters, enabling the ability to successfully print stable films made of dielectric inks with complex shapes which is paramount for electronic packaging applications. Furthermore, the simplicity of the framework makes it a promising tool for model driven inkjet printing process optimization, including real time process control, paving the way for rapid technology adoption in new fields where dimensional accuracy of the parts is critical. The adaptability of the framework is one of its main advantages since it could also be used to improve mechanical and electrical performance along with dimensional accuracy. This has potential implications in the development of optimal microelectronic devices with tailored performance for applications ranging from flexible electronics to photovoltaic cells.

Practical findings of this investigation show the capability of the inkjet process to generate fine features, establishing resolution limits and providing recommendations on minimum achievable dimensions for corners, channels, and slots using a polymer-based photocurable ink. These recommendations are expected to guide designers in the semiconductor industry on the feasibility of inkjet printing for their applications. Furthermore, the procedures to quantify footprint waviness and surface roughness for optimisation process along with the minimum achievable dimensions for fine features

can support the definition of an inkjet-printing ISO or IPC quality standard focused on polymer-based photocurable inks.

The computational inkjet printing environment (EZInkjet) developed to demonstrate the MPSA model simulation provides a cornerstone step towards the generation of inkjet printing digital twins that would enable predictive maintenance and intelligent feed-forward capabilities to reduce part-to-part variation and enhance machine capability and availability. EZInkjet mimics the operation of the printer, allowing the user to generate bitmap patterns or slice STL files, input physical properties, wetting characteristics, printing parameters and droplet characteristics and simulate the printing operation. EZInkjet outputs the surface morphology based on the inputs and prompts the user if parameter optimisation or geometry compensation or both is required, requesting the necessary inputs to perform the operation. EZInkjet provides a standard workflow for the MPSA framework implementation that shorten processing times and reduce process variability, which represents great value for industry application.

9.4 Novelty of the research.

The novelty of this research lies in the development of a hybrid physics-based and data-driven modelling framework to predict and optimise the surface morphology of 3D inkjet-printed parts as a function of printing parameters, material physical properties and wetting characteristics. The proposed framework introduces for the first time to the best of our knowledge the following features in a single process:

Image Generation App. Produces ready-to-print bitmaps of patterns used in electronic packaging applications for any given size and position. Capable of reading and slicing STL files providing the desired resolution and layer thickness.

Prediction App. Simulates the inkjet printing deposition process of the target layer pattern given material properties, printing parameters, wetting characteristics, UV curing shrinkage and droplet landing location and size uncertainties using an analytical model. Based on the initial inputs, creates a printability diagram illustrating if the system meets droplet formation and impact requirements and produces a stability diagram depicting thresholds for bulging and break-up and optimal values for drop

spacing, printing frequency and stand-off distance depending on the type of feature desired to print such as lines or films.

Optimisation App. Builds matrix parametric study based on a response surface design of experiments to create a surrogate model from the results of high-fidelity simulations, shape from shading volume reconstructions or actual measurements of printed features. Creates an input file to run the simulations in our lattice Boltzmann multiphase flow solver or our finite element chemo-mechanical solver (for lines or small square films only) or our PDE shape from shading solver (for any shape but constrained to high contrast images).

Compensation App. Trains a convolutional neural network (CNN) using the x, y and z coordinates of the 3D deformed geometry, which results from either our prediction models or from actual measurements. By providing the target shape coordinates, the CNN calculates the compensation required by the geometry to minimise the error to target shape. New geometry is sliced and bitmaps with compensated layer geometry are produced.

Validation App. Provides a set of post-processing tools to compare the results from the model predictions or actual measurements against target 2D patterns and 3D shapes. For example, allows the calculation of the mean square error (MSE) and mean absolute deviation between two surfaces, generates cross-section images at any given location of a geometry, overlaps and measures footprints to evaluate dimensional accuracy.

This investigation is significant since it has contributed to the advancement of the understanding of the complex fluid dynamics observed in inkjet printing: Some key contributions derived from this research are:

- An analytical model to predict the material overflow at edges of films employing the ratio of momentum diffusivity and capillary diffusion, which provides an insightful connection between physical properties, printing parameters and wetting behaviour.
- An analytical model to predict the centroid of the layer thickness utilising the ratio of the total volume of ink deposited and the square of the drop spacing,

which offers a fast and accurate way to estimate the layer thickness assuming a spherical cap minimal energy shape.

- An analytical and experimental methodology to determine the droplet landing position and diameter uncertainty inherent to the printer motion system accuracy and precision which are critical to predict edge waviness and therefore, the optimal values of printing parameters.
- An analytical and experimental methodology to identify the size and location of partial curing in printed films, which provides a way to account for its effects in the predicted deformed geometry of layers and 3D printed artifacts.
- An analytical model to calculate the optimal traverse velocity as a function of the ratio between the ejection velocity and the capillary velocity and the contact line velocity, which is critical to determine the printing frequency and stand-off distance required for printing stable tracks and films.
- A droplet overlap map which provides a fast way to quantify statistically the number of defects such as bulges and break ups in tracks and films and helps determining a more realistic footprint edge than traditional simulation methods.
- A film stability diagram which illustrates the onset of bulging and separation for lines and films as well as the optimal drop spacing, printing frequency and stand-off distance considering the uncertainty of the equipment.

10 Conclusions and Future Work.

The purpose of this chapter is to present the conclusions from the investigation and outline recommendations of future work to build upon this research.

10.1 Conclusions.

The main aim of this investigation, to develop new modelling techniques to predict fast and accurately the surface morphology of inkjet-printed features, enabling the optimisation of process parameters and the compensation of target patterns for better dimensional accuracy of printed electronics applications, has been achieved. Physics-based, data-driven and hybrid models coupled with machine learning techniques were implemented to predict and optimise the morphology of single tracks (Chapter 5), freeform films (Chapter 6) and 3D components (Chapter 7). Furthermore, a multiphysics, stochastic, analytical (MPSA) model leveraging learnings from Chapters 5-7 was developed to drive feature's morphology prediction and optimisation within a computational inkjet printing environment (Chapter 8). This thesis demonstrated through the development of hybrid analytical frameworks that model driven inkjet printing process optimisation is feasible, paving the way for better quality devices in the printed electronics industry.

The investigation explored three categories of modelling techniques to predict the surface morphology of inkjet-printed features: physics-based, data-driven and hybrid physics-based and data-driven. Two physics-based numerical models were developed to reproduce the inkjet printing droplet deposition and solidification processes using a lattice Boltzmann (LB) multiphase flow model and a finite element (FE) chemo-mechanical model, respectively. The LB model was limited to the simulation of single tracks and small square films and the FE model was mainly employed for the distortion prediction of multi-layer objects. Alternatively, two data-driven models were implemented to reconstruct the surface morphology of single tracks and free-form films using images from experiments: image analysis (IA) and shape from shading (SFS). IA assumed volume conservation and minimal energy drop shape to reconstruct the surface while SFS resolved the height of the image using a reflection model.

Finally, a hybrid physics-based and data-driven approach (MPSA) was generated which incorporates the uncertainty of droplet landing position and footprint, hydrostatic analytical models, empirical correlations derived from experiments, and relationships derived from physics-based models to predict fast and accurately any free-form layer pattern as a function of physical properties, printing parameters and wetting characteristics.

Depending on the selection of the modelling technique to predict the deformed geometry, further considerations were required. For the purely physics-based and data-driven models, a surrogate model using response surface equations was employed to create a transfer function between printing parameters, substrate wetting characteristics and the resulting surface morphology. The development of a transfer function significantly decreased the computational time required by purely physics-based models and enabled the parameter optimisation using a multi-objective genetic algorithm approach to attain the best film dimensional accuracy. Additionally, for multilayer printing applications, a ML-based geometry compensation approach was achieved utilizing a convolutional neural network trained by the predicted (deformed) geometry to reduce the out of plane error to target shape. The optimal combination of printing parameters and input image compensation helped with the generation of fine features that are traditionally difficult for inkjet, improved resolution of edges and corners by reducing the amount of overflow from material, accounted for varied topography and capillary effects thereof on the substrate surface and considered the effect of multiple layers built up on each other.

Specific conclusions drawn from Chapters 5 and 6 relative to the surrogate modelling framework results that have been confirmed with experimental observations and findings in the current literature are the following:

- Drop spacing is the most critical parameter influencing the surface morphology stability of single tracks and films.
- Advancing contact angle plays a significant role determining the track width.
- Printing frequency and its interaction with drop spacing drives the track thickness uniformity.

- Standoff distance has a minor effect on the footprint waviness, but its interaction with printing frequency has a significant influence on the thickness uniformity.
- Droplet overlap which is a function of drop spacing, contact angle and droplet volume is a key predictor of the stability of printed single tracks.
- A set of full quadratic transfer functions can construct efficiently the surface morphology of printed features as function of the critical printing parameters only requiring a limited number of experiments.
- For single track results, excellent agreement was found between predicted and measured values, with about 95% of data points within 10% error. Maximum absolute deviation of footprint width and feature thickness was within 10 μm and 2 μm , respectively.
- The fast execution of the predictive models allowed the global exploration of the design space to find the optimum printing parameters by minimising the footprint width waviness and feature thickness roughness simultaneously.
- The printing parameters that produce the most stable track representing the best trade-off point of the pareto front are drop spacing, printing frequency and standoff distance equal to 31 μm , 2.8 kHz and 0.5 mm, respectively. The optimum parameters were validated in the Dimatix printer achieving a stable track.
- A significant difference exists in the optimal printing parameters derived from simulations and experiments. The difference is attributed to the UV partial curing, the droplet location and footprint size variation introduced by equipment tolerances and chemically inhomogeneous substrates which are not considered in the high-fidelity simulations.
- Optimal printing parameters to achieve the best quality of inkjet-printed parts printed with TPGDA can be derived using only single-track patterns, reducing the number and complexity of experiments.
- Optimal printing parameters for single tracks can also achieve stable films regardless of size and shape of the pattern for TPGDA material applications.

- Drop overlap rather than single drop spacing (resolution) is key in determining film stability and therefore, the better we understand spot size transient behaviour, the better our ability to predict film stability.
- Important to highlight that footprint shape prediction of single line is consistent to the edge behaviour observed in films simulations for different resolutions.

Specific conclusions draw from Chapter 7 about the FE chemo-mechanical model and the ML-geometry compensation framework results that have been confirmed with experimental observations and findings in the current literature are the following:

- Deformed geometry predicted by FE chemo-mechanical analysis does not capture the material spreading over the substrate which is typically present in experiments due to the perfect adhesion assumption used at bottom layer and material constitutive modelling assumptions. However, the geometry compensation was performed to demonstrate the capability of the method.
- CNN can be trained with measured data and successfully compensate the original shape and build a STL file which is vital to obtain binary layers for 3D inkjet printing applications.
- The registration process of the CAD model surface and the 3D scan of the printed part significantly influences the CNN prediction accuracy. This work contributes with a mapping algorithm that ensures unique pairs are fed to train the network.
- Point cloud cleaning process plays a key role to ensure the CNN is trained accurately and, consequently, an adequate CAD geometry compensation is achieved.
- Overall, the proposed ML-based compensation framework successfully counteracts the deformations resulting from the inkjet printing process, improving the dimensional accuracy (quality) of 3D printing parts in a timely manner.

Specific conclusions drawn from Chapter 8 relative to the MPSA results that have been confirmed with experimental observations from experiments are the following:

- Droplet size and position variation have a significant effect in the threshold values for bulging and break-up defects as well as in the optimal overlap to achieve stable features.
- Overlap map quantification with uncertainty is critical to determine the average number of defects such as bulges and break-ups through Monte Carlo simulation.
- The size of primary and secondary bulges is directly proportional to the advancing contact angle, and the overlap value at which a drastic change in volume happens predicts the onset of bulging in printed features.
- The size and frequency of bulges is drastically reduced as printing frequency increases, which means that stability does not depend purely on drop spacing but also in the rate at which drops are deposited.
- The standoff distance has no significant effect on the size of primary and secondary bulges. However, the frequency of secondary bulges is directly proportional to the standoff distance, suggesting minimal setting of this parameter would improve stability.
- As surface tension increases the size of bulges increases since larger surface tension forces dominate the flow redistribution pulling drops towards bulge. Also, as viscosity increases the frequency of bulges decreases since flow mobility is lower preventing bulge formation.
- The principle of superposition used to uncouple multiphysics phenomena is able to capture transient effects on a timely manner influencing the morphology of inkjet-printed features.
- Semi-coupling parameter optimisation with geometry compensation improves the dimensional accuracy and thus the quality of 3D components.
- Computational inkjet printing is feasible through the implementation of a digital twin proof of concept.

- Overall, the MPSA framework provides fairly accurate predictions of the average length, width and thickness defining the morphology of printed features, keeping the prediction error less than 10%. Furthermore, the model is capable to build the morphology of any freeform film in tenths of seconds which is critical for multilayer simulation and parameter optimisation.

This investigation revealed new findings that help to understand the role of viscous and capillary forces and timescales and its interaction with printing parameters in the formation of stable, uniform features. The specific conclusions are the following:

- The ratio of momentum diffusivity and capillary diffusivity provides an adequate estimate of the material overflow observed on boundaries of single tracks and films.
- The ratio of inertia and capillary timescales provides a good estimate of the size of primary bulge and the ratio of capillary and viscous timescales has a significant influence in the frequency of secondary bulges.
- Data suggests that substrate traverse speed resulting from the multiplication of the drop spacing and printing frequency drives the stability of printed features regardless of shape, size, droplet volume and substrate type. For the case of TPGDA deposited on silicon wafer and glass, the optimal traverse speed is 91.6 mm/s.

The study revealed for the first time to the best of our knowledge the role of the droplet location and footprint diameter uncertainty in the stability and uniformity of printed features. Using a droplet overlap map which was determined critical to assess the effect of printing parameters on pattern geometry, it was shown that reliable limits for break-up and bulging of printed features were obtained. Considering droplet position and diameter size uncertainties, predicted optimal printing parameters improved the quality of printed films on substrates with different wettability. Finally, a stability diagram illustrating the onset of bulging and separation for lines and films as well as the optimal drop spacing, printing frequency and stand-off distance was generated to inform visually the results.

This investigation has developed a predictive physics-based model of the surface morphology of DIJP features on heterogeneous substrates and a methodology to find the printing parameters and compensate the layer geometry required for optimum part dimensional accuracy. The simplicity of the proposed technique makes it a promising tool for model driven inkjet printing process optimization, including real time process control and paves the way for better quality devices in the printed electronics industry.

10.2 Future work.

Although this study has covered several methods to predict and optimise the morphology of inkjet-printed parts, there are still areas of improvement that were impossible to explore within the PhD timeframe. A prioritised overview of recommended studies are presented in this section that would enhance the robustness of the proposed frameworks and build upon this research.

10.2.1 Short term recommendations.

We demonstrate that the surrogate model-based optimisation of printing parameters successfully achieve high quality tracks and freeform films of a polymer-based photocurable ink (e.g., TPGDA) printed on glass and nitride-coated silicon wafer with droplet volumes of 10 pL and 2.4 pL. The next step is to validate the framework using different materials such as SU-8, PVP or PEDOT-PSS deposited on different substrates such as PEN, PET or PI, which are traditionally employed in the printed electronics industry. It is recommended to perform experiments of single tracks adapting the matrix of experiments from Section 3.2.12 with adequate parameters and bounds. Then, follow the procedure described in Sections 4.4.1 and 4.5.1 to build the surface morphology prediction model and to perform the parameter optimisation, respectively. Finally, validate the optimal printing parameters by direct comparison to printed samples of single tracks and freeform films.

We demonstrate that the ML-based geometry compensation framework successfully improve the dimensional accuracy of 3D inkjet-printed parts for six differently sized and shaped artifacts using *in silico* experiments. An 8-layer cuboid made of TPGDA printed on nitride-coated silicon wafer show the compensation scheme greatly reduce

the deviations from CAD model, particularly at the footprint dimensions. The next step is to validate the compensation framework with more complex shapes such as the TI sensor packaging included in Section 3.2.4. The geometry includes vertical slots, channels and coned holes covering a wide range of dimensions (e.g., 0.2 to 2.5 mm) and tolerances. It is recommended to use the optimal printing parameters derived in Section 5.3.2 to achieve stable films. Then, use microCT scanning to measure the printed part following the procedure described in Section 3.2.8. It is critical to clean the point cloud from the scanning process to ensure an accurate compensation of the geometry. Get the compensated CAD model to generate binary files as explained in Section 4.5.2 and determine the geometrical deviation of the printed sample with original CAD model using the post-processing tool from Section 4.7.3.

We demonstrate that the MPSA framework predicts fast and accurately the morphology of inkjet-printed tracks and films for any size and shape considering droplet size and position uncertainty, multi-nozzle printing, UV exposure and chemical shrinkage, using TPGDA printed on glass or nitride-coated silicon wafer (e.g., flat, rigid, non-porous substrate) with two native droplet volumes: 2.4 and 10 pL. To make the MPSA framework more generalisable and robust, it is recommended to perform experiments with a range of polymer-based photocurable materials following the results described in Section 8.3.1. Then, test the recommended optimal printing parameters and confirm stable single tracks and freeform films are achieved. Of particular interest is the experimental validation of the relationships to estimate bulging frequency and volume as well as the models employed to predict average and maximum dimensions of single tracks described in Section 4.3.1.2. If results show good agreement, this potentially will advance the science behind inkjet printing by providing a theoretical way to estimate the maximum overflow of single tracks as function of material physical properties, substrate wetting characteristics and printing parameters.

We highlight that the MPSA framework does not capture accurately the flow dynamics effects introduced by multi-layer behaviour observed in 3D inkjet-printed parts. Further improvements must be implemented to consider the effect of multi-layer printing in the final part geometry. It is recommended to investigate and validate empirical correlations relating the amount of deviation from target as a function of number of layers, which follows a logarithmic relationship from experimental

observations reported in Section 8.3.7. Preliminary results with a simplified MPSA model show excellent agreement with printed samples, but it is limited to the prediction of the surface morphology of basic, symmetric shapes such as solid and hollowed polygons. The next step is to fully deploy experimental results in the MPSA framework to adequately capture the multi-layer effect, enabling the prediction of complex shapes of any size.

10.2.2 Long term recommendations.

The MPSA framework could potentially be extended to include the prediction of the surface morphology of printed features using solvent-based inks, which entails the investigation and modelling of the physics behind evaporation phenomenon. Current framework assumes droplet volume is conserved and printed drops tend towards a spherical cap shape. Additional parameters must be included in the MPSA framework to model the loss of droplet volume and the potential “coffee ring” shape of printed drops due to the evaporation process such as relative humidity, vapor pressure, molar concentration and temperature and surface tension gradients. Preliminary investigations show that a coffee ring shape droplet can be modelled using a Stable distribution which is a function of four parameters. A relationship between the Stable distribution parameters and physical properties, printing parameters and wetting characteristics needs to be investigated. The purpose of this relationship is to enable the droplet profile to change from a spherical cap to a “coffee” ring depending on the Marangoni number driven by temperature or surface tension gradients. Further experimental work is needed to test the model hypothesis and deploy the findings into the MPSA framework.

The inkjet printing parameter optimisation process could potentially be extended to include the jet formation process, ensuring fluid dynamics challenges from the printhead side and the substrate side are tackled simultaneously. Since droplet frequency, velocity and size are critical for the inkjet formation and deposition stages, the optimisation process is very challenging. Current parameter optimisation process only considers the dimensional accuracy of the printed patterns, assuming stable droplets are ejected from nozzle with fixed velocity and size, which behaviour actually depends in the droplet frequency being optimised. Further work is needed to

quantitative understand the effect of waveform parameters and ink physical properties in droplet frequency, velocity, size, and stability. Considering these factors, a more robust and reliable parameter optimisation process can be developed towards faster inkjet printers with smaller droplets, enabling more accurate inkjet-printed parts.

The surrogate model-based optimisation framework could potentially be extended to consider the mechanical and electrical properties (e.g., performance function characteristics) of the printed features as objective functions and find the optimal printing parameters that provide the best trade-off between fit and form characteristics (e.g., dimensional accuracy) and function characteristics of the printed features. In current framework, this can be achieved by measuring mechanical and electrical properties of single tracks and films generated using the matrix of experiments and solve the multi-objective genetic algorithm with three objectives or targeting a single objective with a weighted fitness function. The inclusion of additional objectives in the optimisation process might help design and manufacturing engineers in the development of optimal microelectronic devices with tailored performance.

We demonstrate how the MPSA framework would be useful for industry or academic communities by implementing a computational inkjet printing process proof of concept (EZInkjet) in MATLAB, paving the way for real-time process control to improve the quality of inkjet-printed parts. To fully exploit the capabilities of the software, a hardware interface to automatically measure the droplet position and size variation as described in Section 8.3.1 needs to be developed. With the use of off-the-shelf cameras, small single board computers such as Arduino or Raspberry Pi, and adequate network communication systems, a plug and play hardware interface could be implemented for real time measurements. The droplet variation would be an input to the MPSA framework for calibration purposes, parameter optimisation is performed analytically along with the compensation of the binary files and results are feedbacked to printer to achieve an active control of the inkjet printing process. This inkjet printing digital twin would enable printer self-correction to reduce part-to-part variation and enhance machine capability and availability

References.

- 3DS. (2020). *Simulia PowerFLOW* (online). <https://www.3ds.com/products-services/simulia/products/powerflow/>
- Abdulhameed, O., Al-Ahmari, A., Ameen, W., & Mian, S. H. (2019). Additive manufacturing: Challenges, trends, and applications. *Advances in Mechanical Engineering*, *11*(2), 168781401882288. <https://doi.org/10.1177/1687814018822880>
- Amani, A., Balcázar, N., Naseri, A., & Rigola, J. (2020). A numerical approach for non-Newtonian two-phase flows using a conservative level-set method. *Chemical Engineering Journal*, *385*, 123896. <https://doi.org/10.1016/j.cej.2019.123896>
- Ammar, S., Pernaudat, G., & Trépanier, J. Y. (2017). A multiphase three-dimensional multi-relaxation time (MRT) lattice Boltzmann model with surface tension adjustment. *Journal of Computational Physics*, *343*, 73–91. <https://doi.org/10.1016/j.jcp.2017.04.045>
- Amruth, C., Szymański, M. Z., Łuszczynska, B., & Ulański, J. (2019). Inkjet Printing of Super Yellow: Ink Formulation, Film Optimization, OLEDs Fabrication, and Transient Electroluminescence. *Scientific Reports*, *9*(1), 1–10. <https://doi.org/10.1038/s41598-019-44824-w>
- Antoy, J. (2014). Design of Experiments for Engineers and Scientists: Second Edition. In *Design of Experiments for Engineers and Scientists: Second Edition*. Elsevier. <https://doi.org/10.1016/C2012-0-03558-2>
- Aphinyan, S., Ang, E. Y. M., Yeo, J., Ng, T. Y., & Geethalakshmi, K. R. (2018). Numerical study of surface agglomeration of ultraviolet-polymeric ink and its control during 3D nano-inkjet printing process. In *Journal of Polymer Science, Part B: Polymer Physics* (Vol. 56, Issue 24, pp. 1615–1624). <https://doi.org/10.1002/polb.24749>
- Arjmandi-Tash, O., Kovalchuk, N. M., Trybala, A., Kuchin, I. V., & Starov, V. (2017). Kinetics of Wetting and Spreading of Droplets over Various Substrates.

- Langmuir*, 33(18), 4367–4385. <https://doi.org/10.1021/acs.langmuir.6b04094>
- Ashcroft, I. A. (2020). *Advanced Topic in Additive manufacturing MMME4028–Optimisation*. CfAM. University of Nottingham.
- ASTM. (2012). *Standard Terminology for Additive Manufacturing Technology*.
- Beedasy, V., & Smith, P. J. (2020). Printed electronics as prepared by inkjet printing. *Materials*, 13(3), 1–23. <https://doi.org/10.3390/ma13030704>
- Benzi, R., Biferale, L., Sbragaglia, M., Succi, S., & Toschi, F. (2006). Mesoscopic modeling of a two-phase flow in the presence of boundaries: The contact angle. *Physical Review E - Statistical, Nonlinear, and Soft Matter Physics*, 74(2). <https://doi.org/10.1103/PhysRevE.74.021509>
- Berghout, P., & Van den Akker, H. E. A. (2019). Simulating drop formation at an aperture by means of a Multi-Component Pseudo-Potential Lattice Boltzmann model. *International Journal of Heat and Fluid Flow*, 75(December 2018), 153–164. <https://doi.org/10.1016/j.ijheatfluidflow.2019.01.001>
- Booth, J. C., Whitley, M., Rudd, C., & Kranz, M. (2017). *Material Database for Additive Manufacturing Techniques. TECHNICAL REPORT RDMR-WD-17-64* (Issue December).
- Bowman, C. N., & Kloxin, C. J. (2008). Toward an enhanced understanding and implementation of photopolymerization reactions. *AIChE Journal*, 54(11), 2775–2795. <https://doi.org/10.1002/aic.11678>
- Brünahl, J., Condie, A., Crankshaw, M., Cruz-Uribe, T., & Zapka, W. (2017). Xaar's Inkjet Printing Technology and Applications. In *Handbook of Industrial Inkjet Printing* (pp. 285–312). Wiley-VCH Verlag GmbH & Co. KGaA. <https://doi.org/10.1002/9783527687169.ch15>
- Castrejón-Pita, A. A., Castrejón-Pita, J. R., & Hutchings, I. M. (2012). Breakup of liquid filaments. *Physical Review Letters*, 108(7), 15–19. <https://doi.org/10.1103/PhysRevLett.108.074506>
- Castrejón-Pita, J. R., Betton, E. S., Kubiak, K. J., Wilson, M. C. T., & Hutchings, I. M. (2011). The dynamics of the impact and coalescence of droplets on a solid surface. *Biomicrofluidics*, 5(1). <https://doi.org/10.1063/1.3567099>

- Castrejón-Pita, José Rafael, Martin, G. D., & Hutchings, I. M. (2011). Experimental study of the influence of nozzle defects on drop-on-demand ink jets. *Journal of Imaging Science and Technology*, 55(4), 403051–403057.
<https://doi.org/10.2352/J.ImagingSci.Technol.2011.55.4.040305>
- Chen, J., Jiang, S., Gao, Y., & Sun, F. (2018). Reducing volumetric shrinkage of photopolymerizable materials using reversible disulfide-bond reactions. *Journal of Materials Science*, 53(23), 16169–16181. <https://doi.org/10.1007/s10853-018-2778-2>
- Chen, X., Ashcroft, I. A., Wildman, R. D., & Tuck, C. J. (2015). An inverse method for determining the spatially resolved properties of viscoelastic-viscoplastic three-dimensional printed materials. *Proceedings of the Royal Society A: Mathematical, Physical and Engineering Sciences*, 471(2183).
<https://doi.org/10.1098/rspa.2015.0477>
- Cheng, X., Zhu, Y., Zhang, L., Zhang, D., & Ku, T. (2018). Lattice Boltzmann simulation of droplets coalescence in a film patterning process on nonideal surfaces. *Computers and Fluids*, 176, 68–78.
<https://doi.org/10.1016/j.compfluid.2018.08.026>
- Cho, C. L., Kao, H. ling, Wu, Y. H., Chang, L. C., & Cheng, C. H. (2018). Direct Fabrication of Inkjet-Printed Dielectric Film for Metal–Insulator–Metal Capacitors. *Journal of Electronic Materials*, 47(1), 677–683.
<https://doi.org/10.1007/s11664-017-5832-y>
- Chowdhury, S., Mhapsekar, K., & Anand, S. (2018). Part Build Orientation Optimization and Neural Network-Based Geometry Compensation for Additive Manufacturing Process. *Journal of Manufacturing Science and Engineering, Transactions of the ASME*, 140(3), 1–15. <https://doi.org/10.1115/1.4038293>
- Cook, B. S., Cooper, J. R., & Tentzeris, M. M. (2013). Multi-layer RF capacitors on flexible substrates utilizing inkjet printed dielectric polymers. *IEEE Microwave and Wireless Components Letters*, 23(7), 353–355.
<https://doi.org/10.1109/LMWC.2013.2264658>
- Corrall, J. (2017). Konica Minolta's Inkjet Printhead Technology. In *Handbook of Industrial Inkjet Printing* (pp. 253–284). Wiley-VCH Verlag GmbH & Co.

KGaA. <https://doi.org/10.1002/9783527687169.ch14>

- Cui, T., Marzouk, Y. M., & Willcox, K. E. (2015). Data-driven model reduction for the Bayesian solution of inverse problems. *International Journal for Numerical Methods in Engineering*, *102*(5), 966–990. <https://doi.org/10.1002/nme.4748>
- Davis, S. H. (1980). Moving contact lines and rivulet instabilities. Part 1. The static rivulet. *Journal of Fluid Mechanics*, *98*(2), 225–242. <https://doi.org/10.1017/S0022112080000110>
- de Gennes, P.-G., Brochard-Wyart, F., & Quéré, D. (2004). *Capillarity and Wetting Phenomena*. Springer New York. <https://doi.org/10.1007/978-0-387-21656-0>
- Decker, N., & Huang, Q. (2019). Geometric accuracy prediction for additive manufacturing through machine learning of triangular mesh data. *ASME 2019 14th International Manufacturing Science and Engineering Conference, MSEC 2019*, *1*(June). <https://doi.org/10.1115/MSEC2019-3050>
- Deegan, R. D., Bakajin, O., Dupont, T. F., Huber, G., Nagel, S. R., & Witten, T. A. (2000). Contact line deposits in an evaporating drop. *Physical Review E - Statistical Physics, Plasmas, Fluids, and Related Interdisciplinary Topics*, *62*(1 B), 756–765. <https://doi.org/10.1103/PhysRevE.62.756>
- Denlinger, E. R., & Irwin, J. (2014). *Thermomechanical Modeling of Additive Manufacturing Large Parts*. *136*(December), 1–8. <https://doi.org/10.1115/1.4028669>
- Derby, B. (2010). Inkjet Printing of Functional and Structural Materials: Fluid Property Requirements, Feature Stability, and Resolution. *Annual Review of Materials Research*, *40*(1), 395–414. <https://doi.org/10.1146/annurev-matsci-070909-104502>
- Dugyala, V. R., & Basavaraj, M. G. (2014). Control over coffee-ring formation in evaporating liquid drops containing ellipsoids. *Langmuir*, *30*(29), 8680–8686. <https://doi.org/10.1021/la500803h>
- Duineveld, P. C. (2003). The stability of ink-jet printed lines of liquid with zero receding contact angle on a homogeneous substrate. *Journal of Fluid Mechanics*, *477*. <https://doi.org/10.1017/S0022112002003117>

- Durou, J.-D., Falcone, M., Quéau, Y., & Tozza, S. (2020). *A Comprehensive Introduction to Photometric 3D-Reconstruction* (pp. 1–29).
https://doi.org/10.1007/978-3-030-51866-0_1
- Eral, H. B., Augustine, D. M., Duits, M. H. G., & Mugele, F. (2011). Suppressing the coffee stain effect: how to control colloidal self-assembly in evaporating drops using electrowetting. *Soft Matter*, 7(10), 4954.
<https://doi.org/10.1039/c1sm05183k>
- Fakhari, A., & Bolster, D. (2017). Diffuse interface modeling of three-phase contact line dynamics on curved boundaries: A lattice Boltzmann model for large density and viscosity ratios. *Journal of Computational Physics*, 334, 620–638.
<https://doi.org/10.1016/j.jcp.2017.01.025>
- FAU. (2020). *walBerla – widely applicable Lattice Boltzmann from Erlangen* (online). <https://www.walberla.net/>
- Fernández-Toledano, J. C., Blake, T. D., & De Coninck, J. (2019). Contact-line fluctuations and dynamic wetting. *Journal of Colloid and Interface Science*, 540, 322–329. <https://doi.org/10.1016/j.jcis.2019.01.041>
- Fernandez-Toledano, J. C., Blake, T. D., Lambert, P., & De Coninck, J. (2017). On the cohesion of fluids and their adhesion to solids: Young’s equation at the atomic scale. *Advances in Colloid and Interface Science*, 245, 102–107.
<https://doi.org/10.1016/j.cis.2017.03.006>
- Fernández-Toledano, J. C., Rigaut, C., Mastrangeli, M., & De Coninck, J. (2020). Controlling the pinning time of a receding contact line under forced wetting conditions. *Journal of Colloid and Interface Science*, 565, 449–457.
<https://doi.org/10.1016/j.jcis.2020.01.054>
- Fish, J., Wagner, G. J., & Keten, S. (2021). Mesoscopic and multiscale modelling in materials. *Nature Materials*, 20(6), 774–786. <https://doi.org/10.1038/s41563-020-00913-0>
- Florio, L. A. (2018). Simulation of motion, deformation, break-up and deposition of copper droplets transported in internal compressible flow including phase change effects. *International Journal of Heat and Mass Transfer*, 127, 658–676.
<https://doi.org/10.1016/j.ijheatmasstransfer.2018.08.059>

- FlowKit. (2020). *Palabos-CFD, Complex Physics* (online). <http://www.palabos.org>
- Flusser, J., Suk, T., & Zitová, B. (2016). 2D and 3D Image Analysis by Moments. In *2D and 3D Image Analysis by Moments* (pp. 1–529). John Wiley & Sons, Ltd. <https://doi.org/10.1002/9781119039402>
- Frank, X., & Perré, P. (2012). Droplet spreading on a porous surface: A lattice Boltzmann study. *Physics of Fluids*, *24*(4). <https://doi.org/10.1063/1.3701996>
- Fu, F., Li, P., Wang, K., & Wu, R. (2019). Numerical Simulation of Sessile Droplet Spreading and Penetration on Porous Substrates. *Langmuir*, *35*(8), 2917–2924. <https://doi.org/10.1021/acs.langmuir.8b03472>
- Fukai, J., Ishizuka, H., Sakai, Y., Kaneda, M., Morita, M., & Takahara, A. (2006). Effects of droplet size and solute concentration on drying process of polymer solution droplets deposited on homogeneous surfaces. *International Journal of Heat and Mass Transfer*, *49*(19–20), 3561–3567. <https://doi.org/10.1016/j.ijheatmasstransfer.2006.02.049>
- Gibou, F., Hyde, D., & Fedkiw, R. (2019). Sharp interface approaches and deep learning techniques for multiphase flows. *Journal of Computational Physics*, *380*, 442–463. <https://doi.org/10.1016/j.jcp.2018.05.031>
- Gibson, I., Rosen, D. W., & Stucker, B. (2010). *Additive Manufacturing Technologies*. Springer US. <https://doi.org/10.1007/978-1-4419-1120-9>
- Github. (2020). *Software Development Hosting* (online). <https://github.com/>
- Goldberg, D. E. (1989). Genetic algorithms in search, optimization, and machine learning. In *Choice Reviews Online* (Vol. 27, Issue 02). <https://doi.org/10.5860/choice.27-0936>
- Gongora, A. E., Xu, B., Perry, W., Okoye, C., Riley, P., Reyes, K. G., Morgan, E. F., & Brown, K. A. (2020). A Bayesian experimental autonomous researcher for mechanical design. *Science Advances*, *6*(15). <https://doi.org/10.1126/sciadv.aaz1708>
- Goodfellow, I., Bengio, Y., & Courville, A. (2016). *Deep Learning (Adaptive Computation and Machine Learning series)*. The MIT Press.

- Goodner, M. D., & Bowman, C. N. (2002). Development of a comprehensive free radical photopolymerization model incorporating heat and mass transfer effects in thick films. *Chemical Engineering Science*, *57*(5), 887–900.
[https://doi.org/10.1016/S0009-2509\(01\)00287-1](https://doi.org/10.1016/S0009-2509(01)00287-1)
- Graddage, N., Chu, T. Y., Ding, H., Py, C., Dadvand, A., & Tao, Y. (2016). Inkjet printed thin and uniform dielectrics for capacitors and organic thin film transistors enabled by the coffee ring effect. *Organic Electronics*, *29*, 114–119.
<https://doi.org/10.1016/j.orgel.2015.11.039>
- Grieves, M., & Vickers, J. (2017). Digital Twin: Mitigating Unpredictable, Undesirable Emergent Behavior in Complex Systems. In *Transdisciplinary Perspectives on Complex Systems* (pp. 85–113). Springer International Publishing. https://doi.org/10.1007/978-3-319-38756-7_4
- Guo, Y., Wei, L., Liang, G., & Shen, S. (2014). Simulation of droplet impact on liquid film with CLSVOF. *International Communications in Heat and Mass Transfer*, *53*, 26–33. <https://doi.org/10.1016/j.icheatmasstransfer.2014.02.006>
- Hague, R., Campbell, I., & Dickens, P. (2003). Implications on design of rapid manufacturing. *Proceedings of the Institution of Mechanical Engineers, Part C: Journal of Mechanical Engineering Science*, *217*(1), 25–30.
<https://doi.org/10.1243/095440603762554587>
- Hamad, E. M., Bilatto, S. E. R., Adly, N. Y., Correa, D. S., Wolfrum, B., Schöning, M. J., Offenhäusser, A., & Yakushenko, A. (2016). Inkjet printing of UV-curable adhesive and dielectric inks for microfluidic devices. *Lab on a Chip*, *16*(1), 70–74. <https://doi.org/10.1039/C5LC01195G>
- Han, P. (2017). Additive Design and Manufacturing of Jet Engine Parts. *Engineering*, *3*(5), 648–652. <https://doi.org/10.1016/J.ENG.2017.05.017>
- He, X., Chen, S., & Zhang, R. (1999). A Lattice Boltzmann Scheme for Incompressible Multiphase Flow and Its Application in Simulation of Rayleigh–Taylor Instability. *Journal of Computational Physics*, *152*(2), 642–663.
<https://doi.org/10.1006/jcph.1999.6257>
- He, Y. (2016). *An Investigation of Inkjet Printing of Polycaprolactone Based Inks* By.

- He, Y., Zhang, F., Saleh, E., Vaithilingam, J., Aboulkhair, N., Begines, B., Tuck, C. J., Hague, R. J. M., Ashcroft, I. A., & Wildman, R. D. (2017). A Tripropylene Glycol Diacrylate-based Polymeric Support Ink for Material Jetting. *Additive Manufacturing*, *16*, 153–161. <https://doi.org/10.1016/j.addma.2017.06.001>
- Hernandez, C., Maranon, A., Ashcroft, I. A., & Casas-Rodriguez, J. P. (2013). A computational determination of the Cowper-Symonds parameters from a single Taylor test. *Applied Mathematical Modelling*, *37*(7), 4698–4708. <https://doi.org/10.1016/j.apm.2012.10.010>
- Hoath, S. D. (Ed.). (2016). *Fundamentals of Inkjet Printing*. Wiley-VCH Verlag GmbH & Co. KGaA. <https://doi.org/10.1002/9783527684724>
- Hoath, S. D., Harlen, O. G., & Hutchings, I. M. (2012). Jetting behavior of polymer solutions in drop-on-demand inkjet printing. *Journal of Rheology*, *56*(5), 1109–1127. <https://doi.org/10.1122/1.4724331>
- Hofmann, R. (2017). Polymeric Nonabsorbing Substrates for Industrial Inkjet Printing Applications. In W. Zapka (Ed.), *Handbook of Industrial Inkjet Printing* (pp. 373–390). Wiley-VCH Verlag GmbH & Co. KGaA. <https://doi.org/10.1002/9783527687169.ch20>
- Hsiao, W. K., Martin, G. D., & Hutchings, I. M. (2014). Printing stable liquid tracks on a surface with finite receding contact angle. *Langmuir*, *30*(41), 12447–12455. <https://doi.org/10.1021/la502490p>
- Huang, H., Sukop, M. C. and Lu, X. Y. (2015). *Multiphase lattice Boltzmann methods: theory and applications*. John Wiley & Sons, Ltd.
- Huang, B. C., Chan, H. J., Hong, J. W., & Lo, C. Y. (2016). Methodology for evaluating pattern transfer completeness in inkjet printing with irregular edges. *Journal of Micromechanics and Microengineering*, *26*(6), 65009. <https://doi.org/10.1088/0960-1317/26/6/065009>
- Huang, Q., Nouri, H., Xu, K., Chen, Y., Sosina, S., & Dasgupta, T. (2014). Statistical predictive modeling and compensation of geometric deviations of three-dimensional printed products. *Journal of Manufacturing Science and Engineering, Transactions of the ASME*, *136*(6). <https://doi.org/10.1115/1.4028510>

- Huang, Q., Wang, Y., Lyu, M., & Lin, W. (2020). Shape Deviation Generator-A Convolution Framework for Learning and Predicting 3-D Printing Shape Accuracy. *IEEE Transactions on Automation Science and Engineering*, 17(3), 1486–1500. <https://doi.org/10.1109/TASE.2019.2959211>
- Inkbit. (2020). *Inkbit 3D System*. <https://inkbit3d.com/>
- IPC. (2020). *Institute of Printed Circuits Standards*. <https://www.ipc.org/ContentPage.aspx?pageid=Standards>
- James, G., Witten, D., Hastie, T., & Tibshirani, R. (2013). *An Introduction to Statistical Learning* (Vol. 103). Springer New York. <https://doi.org/10.1007/978-1-4614-7138-7>
- Jang, D., Kim, D., & Moon, J. (2009). Influence of fluid physical properties on ink-jet printability. *Langmuir*, 25(5), 2629–2635. <https://doi.org/10.1021/la900059m>
- Jansen, H. P., Sotthewes, K., Van Swigchem, J., Zandvliet, H. J. W., & Kooij, E. S. (2013). Lattice Boltzmann modeling of directional wetting: Comparing simulations to experiments. *Physical Review E - Statistical, Nonlinear, and Soft Matter Physics*, 88(1), 1–10. <https://doi.org/10.1103/PhysRevE.88.013008>
- JEITA. (2020). *Japanese Electronics and Information Technology Association*. <https://www.jeita.or.jp/english/>
- Jeong, W.-K., & Whitaker, R. T. (2008). A Fast Iterative Method for Eikonal Equations. *SIAM Journal on Scientific Computing*, 30(5), 2512–2534. <https://doi.org/10.1137/060670298>
- Jin, Y., Qin, S. J., & Huang, Q. (2016). Offline Predictive Control of Out-of-Plane Shape Deformation for Additive Manufacturing. *Journal of Manufacturing Science and Engineering, Transactions of the ASME*, 138(12), 1–7. <https://doi.org/10.1115/1.4033444>
- Jin, Y., Qin, S. J., & Huang, Q. (2020). Modeling inter-layer interactions for out-of-plane shape deviation reduction in additive manufacturing. *IISE Transactions*, 52(7), 721–731. <https://doi.org/10.1080/24725854.2019.1676936>
- Jung, S., Hoath, S. D., & Hutchings, I. M. (2013). The role of viscoelasticity in drop impact and spreading for inkjet printing of polymer solution on a wettable

surface. *Microfluidics and Nanofluidics*, 14(1–2), 163–169.

<https://doi.org/10.1007/s10404-012-1034-3>

Kang, Hengyi, Lourenço, S. D. N., & Yan, W. M. (2018). Lattice Boltzmann simulation of droplet dynamics on granular surfaces with variable wettability. *Physical Review E*, 98(1), 1–14. <https://doi.org/10.1103/PhysRevE.98.012902>

Kang, Hongki, Soltman, D., & Subramanian, V. (2010). Hydrostatic optimization of inkjet-printed films. *Langmuir*, 26(13), 11568–11573.

<https://doi.org/10.1021/la100822s>

Kapteyn, M. G., & Willcox, K. E. (2020). *From Physics-Based Models to Predictive Digital Twins via Interpretable Machine Learning*.

<http://arxiv.org/abs/2004.11356>

Katopodes, N. D. (2018). Free-surface flow: Computational methods. In *Free-Surface Flow: Computational Methods*. Elsevier.

<https://doi.org/10.1016/C2017-0-00542-6>

Kim, B., Lee, S., & Kim, J. (2020). Inverse design of porous materials using artificial neural networks. *Science Advances*, 6(1), 1–8.

<https://doi.org/10.1126/sciadv.aax9324>

Kim, C. S., Park, S. J., Sim, W., Kim, Y. J., & Yoo, Y. (2009). Modeling and characterization of an industrial inkjet head for micro-patterning on printed circuit boards. *Computers and Fluids*, 38(3), 602–612.

<https://doi.org/10.1016/j.compfluid.2008.06.003>

Kim, D., Jeong, S., Park, B. K., & Moon, J. (2006). Direct writing of silver conductive patterns: Improvement of film morphology and conductance by controlling solvent compositions. *Applied Physics Letters*, 89(26), 264101.

<https://doi.org/10.1063/1.2424671>

Kim, E., & Baek, J. (2012). Numerical study on the effects of non-dimensional parameters on drop-on-demand droplet formation dynamics and printability range in the up-scaled model. *Physics of Fluids*, 24(8).

<https://doi.org/10.1063/1.4742913>

Krause, M. J., Kummerländer, A., Avis, S. J., Kusumaatmaja, H., Dapelo, D.,

- Klemens, F., Gaedtke, M., Hafen, N., Mink, A., Trunk, R., Marquardt, J. E., Maier, M. L., Haussmann, M., & Simonis, S. (2020). OpenLB—Open source lattice Boltzmann code. *Computers and Mathematics with Applications*, xxx. <https://doi.org/10.1016/j.camwa.2020.04.033>
- Kruger, T., Kusumaatmaja, H., Kuzmin, A., Shardt, O., Goncalo, S., & Viggien, E. M. (2017). The lattice boltzmann method, principles and practice. In *Springer International Publishing* (Vol. 10, Issue 207).
- Kupershtokh, A. L., Medvedev, D. A., & Karpov, D. I. (2009). On equations of state in a lattice Boltzmann method. *Computers and Mathematics with Applications*, 58(5), 965–974. <https://doi.org/10.1016/j.camwa.2009.02.024>
- Kupershtokh, Alexander L., Medvedev, D. A., & Griбанov, I. I. (2018). Thermal lattice Boltzmann method for multiphase flows. *Physical Review E*, 98(2), 1–10. <https://doi.org/10.1103/PhysRevE.98.023308>
- Lanzotti, A., Martorelli, M., & Staiano, G. (2015). Understanding process parameter effects of rewrap open-source three-dimensional printers through a design of experiments approach. *Journal of Manufacturing Science and Engineering, Transactions of the ASME*, 137(1). <https://doi.org/10.1115/1.4029045>
- Ledesma, J. (2018). *Jetting of Multiple Functional Materials by Additive Manufacturing* [University of Nottingham]. http://eprints.nottingham.ac.uk/49373/1/Javier_Ledesma_Thesis.pdf
- Leistner, C., Hartmann, S., Abliz, D., & Ziegmann, G. (2020). Modeling and simulation of the curing process of epoxy resins using finite elements. *Continuum Mechanics and Thermodynamics*, 32(2), 327–350. <https://doi.org/10.1007/s00161-018-0708-9>
- Li, E. Q., & Thoroddsen, S. T. (2015). Time-resolved imaging of a compressible air disc under a drop impacting on a solid surface. *Journal of Fluid Mechanics*, 780, 636–648. <https://doi.org/10.1017/jfm.2015.466>
- Li, Q., Luo, K. H., & Li, X. J. (2013). Lattice Boltzmann modeling of multiphase flows at large density ratio with an improved pseudopotential model. *Physical Review E - Statistical, Nonlinear, and Soft Matter Physics*, 87(5). <https://doi.org/10.1103/PhysRevE.87.053301>

- Li, Z., Kovachki, N., Azzadenesheli, K., Liu, B., Bhattacharya, K., Stuart, A., & Anandkumar, A. (2020). *Fourier Neural Operator for Parametric Partial Differential Equations*. 2016, 1–16. <http://arxiv.org/abs/2010.08895>
- Liang, H., Li, Y., Chen, J., & Xu, J. (2019). Axisymmetric lattice Boltzmann model for multiphase flows with large density ratio. *International Journal of Heat and Mass Transfer*, 130, 1189–1205. <https://doi.org/10.1016/j.ijheatmasstransfer.2018.09.050>
- Liggett, J. A. (1994). Governing Equations for Free Surface Flows. In *Computer Modeling of Free-Surface and Pressurized Flows* (pp. 3–32). Springer Netherlands. https://doi.org/10.1007/978-94-011-0964-2_1
- Lin, J. T., Liu, H. W., Chen, K. T., & Cheng, D. C. (2019). Modeling the Kinetics, Curing Depth, and Efficacy of Radical-Mediated Photopolymerization: The Role of Oxygen Inhibition, Viscosity, and Dynamic Light Intensity. *Frontiers in Chemistry*, 7(November), 1–14. <https://doi.org/10.3389/fchem.2019.00760>
- Linder, N., Criscione, A., Roisman, I. V., Marschall, H., & Tropea, C. (2015). 3D computation of an incipient motion of a sessile drop on a rigid surface with contact angle hysteresis. *Theoretical and Computational Fluid Dynamics*, 29(5–6), 373–390. <https://doi.org/10.1007/s00162-015-0362-9>
- Liu, Y., & Derby, B. (2019). Experimental study of the parameters for stable drop-on-demand inkjet performance. *Physics of Fluids*, 31(3). <https://doi.org/10.1063/1.5085868>
- Lohse, D. (2021). Fundamental Fluid Dynamics Challenges in Inkjet Printing. *Annual Review of Fluid Mechanics*, 54, 349–382. <https://doi.org/10.1146/annurev-fluid-022321-114001>
- Mampallil, D., Reboud, J., Wilson, R., Wylie, D., Klug, D. R., & Cooper, J. M. (2015). Acoustic suppression of the coffee-ring effect. *Soft Matter*, 11(36), 7207–7213. <https://doi.org/10.1039/C5SM01196E>
- Markets & Markets, L. (2020). *Printed Electronics Market with Covid-19 Impact Analysis by Printing Technology (Screen, Inkjet, Gravure), Application (Displays, Sensors, Batteries), Material (Inks, Substrates), End-Use Industry, and Geography - Global Forecast to 2025*. Market Research Report.

https://www.marketsandmarkets.com/Market-Reports/printed-electronics-market-197.html?gclid=EAIaIQobChMIInqbr2O-i7AIV1O3tCh07lgugEAAYASAAEgK76vD_BwE

- McCoul, D., Rosset, S., Schlatter, S., & Shea, H. (2017). Inkjet 3D printing of UV and thermal cure silicone elastomers for dielectric elastomer actuators. *Smart Materials and Structures*, 26(12). <https://doi.org/10.1088/1361-665X/aa9695>
- Meng, W., Liao, L., Chen, M., Yu, C., Li, J., & An, R. (2022). An enhanced CLSVOF method with an algebraic second-reconstruction step for simulating incompressible two-phase flows. *International Journal of Multiphase Flow*, 154, 104151. <https://doi.org/10.1016/j.ijmultiphaseflow.2022.104151>
- Mikolajek, M., Reinheimer, T., Bohn, N., Kohler, C., Hoffmann, M. J., & Binder, J. R. (2019). Fabrication and Characterization of Fully Inkjet Printed Capacitors Based on Ceramic/Polymer Composite Dielectrics on Flexible Substrates. *Scientific Reports*, 9(1), 1–13. <https://doi.org/10.1038/s41598-019-49639-3>
- Mohamad, A. A. (2019). Lattice Boltzmann Method. In *Lattice Boltzmann Method*. <https://doi.org/10.1007/978-1-4471-7423-3>
- Mohamed, O. A., Masood, S. H., & Bhowmik, J. L. (2015). Optimization of fused deposition modeling process parameters: a review of current research and future prospects. *Advances in Manufacturing*, 3(1), 42–53. <https://doi.org/10.1007/s40436-014-0097-7>
- Morrison, N. F., & Harlen, O. G. (2010). Viscoelasticity in inkjet printing. *Rheologica Acta*, 49(6), 619–632. <https://doi.org/10.1007/s00397-009-0419-z>
- Mu, L., Hu, Z., Zhong, Z., Jiang, C., Wang, J., Peng, J., & Cao, Y. (2017). Inkjet-printing line film with varied droplet-spacing. *Organic Electronics*, 51, 308–313. <https://doi.org/10.1016/j.orgel.2017.08.012>
- Mukherjee, S., Zarghami, A., Haringa, C., van As, K., Kenjereš, S., & Van den Akker, H. E. A. (2018). Simulating liquid droplets: A quantitative assessment of lattice Boltzmann and Volume of Fluid methods. *International Journal of Heat and Fluid Flow*, 70(February), 59–78. <https://doi.org/10.1016/j.ijheatfluidflow.2017.12.001>

- Murphy, K. P. (2012). *Machine Learning: A Probabilistic Perspective (Adaptive Computation and Machine Learning series)*. The MIT Press.
- N. Rosario, T. (2017). Concepts and Strategies to Adapt Inkjet Printing to Industrial Application Requirements. In *Handbook of Industrial Inkjet Printing* (pp. 239–252). Wiley-VCH Verlag GmbH & Co. KGaA.
<https://doi.org/10.1002/9783527687169.ch13>
- Nano-Dimension. (2020). *DragonFly LDM System*. <https://www.nano-di.com/dragonfly-ldm-3d-printer>
- Navangul, G., Paul, R., & Anand, S. (2013). Error minimization in layered manufacturing parts by stereolithography file modification using a vertex translation algorithm. *Journal of Manufacturing Science and Engineering, Transactions of the ASME*, 135(3), 1–13. <https://doi.org/10.1115/1.4024035>
- Nguyen, H. A. D., Shin, K., & Lee, C. (2017). Multi-response optimization of R2R gravure printing using orthogonal array and principal component analysis as a weighting factor. *International Journal of Advanced Manufacturing Technology*, 90(9–12), 3595–3606. <https://doi.org/10.1007/s00170-016-9685-y>
- Nguyen, T. A. H., Biggs, S. R., & Nguyen, A. V. (2017). Manipulating colloidal residue deposit from drying droplets: Air/liquid interface capture competes with coffee-ring effect. *Chemical Engineering Science*, 167, 78–87.
<https://doi.org/10.1016/j.ces.2017.04.001>
- NUMECA. (2020). *OMNIS/LB* (online). <https://www.numeca.com/product/omnislb>
- Oñate, E., & Owen, R. (Eds.). (2011). *Particle-Based Methods* (Vol. 25). Springer Netherlands. <https://doi.org/10.1007/978-94-007-0735-1>
- Papalambros, P. Y., & Wilde, D. J. (2017). *Principles of Optimal Design*. Cambridge University Press. <https://doi.org/10.1017/9781316451038>
- Pappas, P. (1980). *UV Curing Science and Technology*. Technology Marketing Corporation.
- Parthier, L., Wiegel, T., Ottermann, C., & Prince, F. (2017). Glass Substrates for Industrial Inkjet Printing Applications. In *Handbook of Industrial Inkjet Printing* (pp. 391–408). Wiley-VCH Verlag GmbH & Co. KGaA.

<https://doi.org/10.1002/9783527687169.ch21>

- Patankar, S. V. (1980). *Numerical heat transfer and fluid flow*. Taylor & Francis.
- Patrick Jansen, H., Sotthewes, K., Zandvliet, H. J. W., & Kooij, E. S. (2016). Potential of lattice Boltzmann to model droplets on chemically stripe-patterned substrates. *Applied Surface Science*, *361*, 122–132.
<https://doi.org/10.1016/j.apsusc.2015.11.120>
- Perelaer, J., de Gans, B.-J., & Schubert, U. S. (2006). Ink-jet Printing and Microwave Sintering of Conductive Silver Tracks. *Advanced Materials*, *18*(16), 2101–2104.
<https://doi.org/10.1002/adma.200502422>
- Piatt, M., Bugner, D., Chwalek, J., & Katerberg, J. (2017). KODAK's Stream Inkjet Technology. In *Handbook of Industrial Inkjet Printing* (pp. 351–360). Wiley-VCH Verlag GmbH & Co. KGaA. <https://doi.org/10.1002/9783527687169.ch18>
- Planchette, C., Marangon, F., Hsiao, W. K., & Brenn, G. (2019). Breakup of asymmetric liquid ligaments. *Physical Review Fluids*, *4*(12), 124004.
<https://doi.org/10.1103/PhysRevFluids.4.124004>
- Poplavko, Y. M. (2019). Dielectrics. In *Electronic Materials* (pp. 287–408). Elsevier.
<https://doi.org/10.1016/B978-0-12-815780-0.00007-4>
- Popov, Y. O. (2005). Evaporative deposition patterns: Spatial dimensions of the deposit. *Physical Review E - Statistical, Nonlinear, and Soft Matter Physics*, *71*(3), 1–17. <https://doi.org/10.1103/PhysRevE.71.036313>
- Pravinraj, T., & Patrikar, R. (2017). Modelling and investigation of partial wetting surfaces for drop dynamics using lattice Boltzmann method. *Applied Surface Science*, *409*, 214–222. <https://doi.org/10.1016/j.apsusc.2017.02.242>
- Rahul, S. H., Balasubramanian, K., & Venkatesh, S. (2017). Optimizing inkjet printing process to fabricate thick ceramic coatings. *Ceramics International*, *43*(5), 4513–4519. <https://doi.org/10.1016/j.ceramint.2016.12.103>
- Raman, K. A., Jaiman, R. K., Lee, T. S., & Low, H. T. (2016). Lattice Boltzmann simulations of droplet impact onto surfaces with varying wettabilities. *International Journal of Heat and Mass Transfer*, *95*, 336–354.
<https://doi.org/10.1016/j.ijheatmasstransfer.2015.11.088>

- Reis, N., & Derby, B. (2000). Ink Jet Deposition of Ceramic Suspensions: Modeling and Experiments of Droplet Formation. *MRS Proceedings*, 625, 117.
<https://doi.org/10.1557/PROC-625-117>
- Reyes-Luna, J. F., Chang, S., Tuck, C., & Ashcroft, I. (2023a). A surrogate modelling strategy to improve the surface morphology quality of inkjet printing applications. *Journal of Manufacturing Processes*, 89(June 2022), 458–471.
<https://doi.org/10.1016/j.jmapro.2023.01.078>
- Reyes-Luna, J. F., Chang, S., Tuck, C. J., & Ashcroft, I. A. (2023b). Material jetting high quality components via an inverse problem framework. *Additive Manufacturing*, 73(March), 103667.
<https://doi.org/10.1016/j.addma.2023.103667>
- Rindler, F. (2018). *Calculus of Variations*. Springer International Publishing.
<https://doi.org/10.1007/978-3-319-77637-8>
- Rodriguez-Rivero, C., Castrejón-Pita, J. R., & Hutchings, I. M. (2015). Aerodynamic effects in industrial inkjet printing. *Journal of Imaging Science and Technology*, 59(4), 1–10. <https://doi.org/10.2352/J.ImagingSci.Technol.2015.59.4.040401>
- Ruffo, M., & Hague, R. (2007). Cost estimation for rapid manufacturing ' simultaneous production of mixed components using laser sintering. *Proceedings of the Institution of Mechanical Engineers, Part B: Journal of Engineering Manufacture*, 221(11), 1585–1591.
<https://doi.org/10.1243/09544054JEM894>
- Ruiz, E., Waffo, F., Owens, J., Billotte, C., & Trochu, F. (2006). Modeling of Resin Cure Kinetics for Molding Cycle Optimization. *The 8 Th International Conference on Flow Processes in Composite Materials (FPCM8)*, July, 10.
http://www.tech.plym.ac.uk/sme/FPCM/FPCM08/FPCM8/papers/FPCM8_18.pdf
- Saleh, E., Woolliams, P., Clarke, B., Gregory, A., Greedy, S., Smartt, C., Wildman, R., Ashcroft, I., Hague, R., Dickens, P., & Tuck, C. (2017). 3D inkjet-printed UV-curable inks for multi-functional electromagnetic applications. *Additive Manufacturing*, 13, 143–148. <https://doi.org/10.1016/j.addma.2016.10.002>
- Sarkar, S., & Lin-Gibson, S. (2018). Computational Design of Photocured Polymers

- Using Stochastic Reaction–Diffusion Simulation. *Advanced Theory and Simulations*, 1(7), 1800028. <https://doi.org/10.1002/adts.201800028>
- Schiaffino, S., & Sonin, A. A. (1997). Formation and stability of liquid and molten beads on a solid surface. *Journal of Fluid Mechanics*, 343, 95–110. <https://doi.org/10.1017/S0022112097005831>
- Schmidt, C., & Scherzer, T. (2015). Monitoring of the shrinkage during the photopolymerization of acrylates using hyphenated photorheometry/near-infrared spectroscopy. *Journal of Polymer Science, Part B: Polymer Physics*, 53(10), 729–739. <https://doi.org/10.1002/polb.23694>
- Sebastian, M. (2008). *Dielectric materials for wireless communication*. Elsevier Science.
- Seo, C., Jang, D., Chae, J., & Shin, S. (2017). Altering the coffee-ring effect by adding a surfactant-like viscous polymer solution. *Scientific Reports*, 7(1), 500. <https://doi.org/10.1038/s41598-017-00497-x>
- Shan, X. (2006). Analysis and reduction of the spurious current in a class of multiphase lattice Boltzmann models. *Physical Review E - Statistical, Nonlinear, and Soft Matter Physics*, 73(4), 6–9. <https://doi.org/10.1103/PhysRevE.73.047701>
- Shanahan, M. E. R., & Sefiane, K. (2010). Kinetics Of Triple Line Motion During Evaporation. *Contact Angle, Wettability and Adhesion, Volume 6*, 19–32. <https://doi.org/10.1163/ej.9789004169326.i-400.12>
- Shi, J., Song, J., Song, B., & Lu, W. F. (2019). Multi-Objective Optimization Design through Machine Learning for Drop-on-Demand Bioprinting. *Engineering*, 5(3), 586–593. <https://doi.org/10.1016/j.eng.2018.12.009>
- Shikhmurzaev, Y. D. (2007). Capillary flows with forming interfaces. In *Capillary Flows with Forming Interfaces*. Chapman & Hall. <https://doi.org/10.1201/9781584887492>
- Simske, S. J. (2017). Hewlett Packard's Inkjet Printhead Technology. In *Handbook of Industrial Inkjet Printing* (pp. 313–334). Wiley-VCH Verlag GmbH & Co. KGaA. <https://doi.org/10.1002/9783527687169.ch16>

- Singh, R., & Ulrich, R. K. (1999). High and low dielectric constant materials. *Electrochemical Society Interface*, 8(2), 26–30.
- Snoeijer, J. H., & Andreotti, B. (2013). Moving contact lines: Scales, regimes, and dynamical transitions. *Annual Review of Fluid Mechanics*, 45, 269–292. <https://doi.org/10.1146/annurev-fluid-011212-140734>
- Soltman, D., Smith, B., Morris, S. J. S., & Subramanian, V. (2013). Inkjet printing of precisely defined features using contact-angle hysteresis. *Journal of Colloid and Interface Science*, 400, 135–139. <https://doi.org/10.1016/j.jcis.2013.03.006>
- Soltman, D., Smith, B., Uorris, S. J. S., & Subramanian, V. (2010). Methodology for inkjet printing partially wetting films. *International Conference on Digital Printing Technologies*, 14(11), 292–296. <https://doi.org/10.1021/la102053j>
- Soltman, D., & Subramanian, V. (2008). Inkjet-printed line morphologies and temperature control of the coffee ring effect. *Langmuir*, 24(5), 2224–2231. <https://doi.org/10.1021/la7026847>
- Sprittles, J. E., & Shikhmurzaev, Y. D. (2012). The dynamics of liquid drops and their interaction with solids of varying wettabilities. *Physics of Fluids*, 24(8), 082001. <https://doi.org/10.1063/1.4739933>
- Stahl, B., Chopard, B., & Latt, J. (2010). Measurements of wall shear stress with the lattice Boltzmann method and staircase approximation of boundaries. *Computers & Fluids*, 39(9), 1625–1633. <https://doi.org/10.1016/j.compfluid.2010.05.015>
- Starov, V., & Velarde, M. G. (2007). *Wetting and spreading dynamics* (C. Press (Ed.); Second). Taylor & Francis.
- Stringer, J., & Derby, B. (2010). Formation and stability of lines produced by inkjet printing. *Langmuir*, 26(12), 10365–10372. <https://doi.org/10.1021/la101296e>
- Su, W., Cook, B. S., Fang, Y., & Tentzeris, M. M. (2016). Fully inkjet-printed microfluidics: a solution to low-cost rapid three-dimensional microfluidics fabrication with numerous electrical and sensing applications. *Scientific Reports*, 6(1), 35111. <https://doi.org/10.1038/srep35111>
- Sussman, M., & Puckett, E. G. (2000). A Coupled Level Set and Volume-of-Fluid

- Method for Computing 3D and Axisymmetric Incompressible Two-Phase Flows. *Journal of Computational Physics*, 162(2), 301–337.
<https://doi.org/10.1006/jcph.2000.6537>
- Tang, C., Qin, M., Weng, X., Zhang, X., Zhang, P., Li, J., & Huang, Z. (2017). Dynamics of droplet impact on solid surface with different roughness. *International Journal of Multiphase Flow*, 96, 56–69.
<https://doi.org/10.1016/j.ijmultiphaseflow.2017.07.002>
- Tehrani, B., Bahr, R., Revier, D., Cook, B., & Tentzeris, M. (2018). The Principles of “Smart” Encapsulation: Using Additive Printing Technology for the Realization of Intelligent Application-Specific Packages for IoT, 5G, and Automotive Radar Applications. *Proceedings - Electronic Components and Technology Conference, 2018-May*, 111–117.
<https://doi.org/10.1109/ECTC.2018.00025>
- Tehrani, B. K., Bahr, R. A., Su, W., Cook, B. S., & Tentzeris, M. M. (2017). E-band characterization of 3D-printed dielectrics for fully-printed millimeter-wave wireless system packaging. *IEEE MTT-S International Microwave Symposium Digest*, 1756–1759. <https://doi.org/10.1109/MWSYM.2017.8058985>
- Tehrani, B. K., Mariotti, C., Cook, B. S., Roselli, L., & Tentzeris, M. M. (2016). Development, characterization, and processing of thin and thick inkjet-printed dielectric films. *Organic Electronics*, 29, 135–141.
<https://doi.org/10.1016/j.orgel.2015.11.022>
- Thompson, A. B., Tipton, C. R., Juel, A., Hazel, A. L., & Dowling, M. (2014). Sequential deposition of overlapping droplets to form a liquid line. *Journal of Fluid Mechanics*, 761, 261–281. <https://doi.org/10.1017/jfm.2014.621>
- Tilford, T., Stoyanov, S., Braun, J., Janhsen, J. C., Patel, M. K., & Bailey, C. (2021). Comparative Reliability of Inkjet-Printed Electronics Packaging. *IEEE Transactions on Components, Packaging and Manufacturing Technology*, 11(2), 351–362. <https://doi.org/10.1109/TCPMT.2021.3049952>
- Tong, K., Joshi, S., & Lehtihet, E. A. (2008). Error compensation for fused deposition modeling (FDM) machine by correcting slice files. *Rapid Prototyping Journal*, 14(1), 4–14. <https://doi.org/10.1108/13552540810841517>

- Tsai, P., Pacheco, S., Pirat, C., Lefferts, L., & Lohse, D. (2009). Drop Impact upon Micro- and Nanostructured Superhydrophobic Surfaces. *Langmuir*, 25(20), 12293–12298. <https://doi.org/10.1021/la900330q>
- Tuck, C. J., Hague, R. J. M., Ruffo, M., Ransley, M., & Adams, P. (2008). Rapid manufacturing facilitated customization. *International Journal of Computer Integrated Manufacturing*, 21(3), 245–258. <https://doi.org/10.1080/09511920701216238>
- Vaithilingam, J., Saleh, E., Wildman, R. D., Hague, R. J. M., & Tuck, C. J. (2018). Optimisation of Substrate Angles for Multi-material and Multi-functional Inkjet Printing. *Scientific Reports*, 8(1), 2–9. <https://doi.org/10.1038/s41598-018-27311-6>
- van den Berg, A. M. J., Smith, P. J., Perelaer, J., Schrof, W., Koltzenburg, S., & Schubert, U. S. (2007). Inkjet printing of polyurethane colloidal suspensions. *Soft Matter*, 3(2), 238–243. <https://doi.org/10.1039/B610017A>
- Vega, E. J., & Castrejón-Pita, A. A. (2017). Suppressing prompt splash with polymer additives. *Experiments in Fluids*, 58(5), 1–8. <https://doi.org/10.1007/s00348-017-2341-y>
- Veltkamp, R. C. (2001). Shape matching: Similarity measures and algorithms. *Proceedings - International Conference on Shape Modeling and Applications, SMI 2001*, 188–197. <https://doi.org/10.1109/SMA.2001.923389>
- Versteeg, H. K., Malalasekera, W., Orsi, G., Ferziger, J. H., Date, A. W., & Anderson, J. D. (1995). An Introduction to Computational Fluid Dynamics - The Finite Volume Method. In *Fluid flow handbook. McGraw-Hill ...* (Second). Pearson Education.
<http://scholar.google.com/scholar?hl=en&btnG=Search&q=intitle:Computational+fluid+dynamics.+The+basics+with+applications#6%5Cnhttp://scholar.google.com/scholar?hl=en&btnG=Search&q=intitle:Computational+Fluid+Dynamics:+The+Basics+with+Applications.+1995%23>
- Viquerat, J., & Hachem, E. (2020). A supervised neural network for drag prediction of arbitrary 2D shapes in laminar flows at low Reynolds number. *Computers and Fluids*, 210. <https://doi.org/10.1016/j.compfluid.2020.104645>

- Wang, G., Zhang, X., & Cheng, J. (2020). A Unified Shape-From-Shading Approach for 3D Surface Reconstruction Using Fast Eikonal Solvers. *International Journal of Optics*, 2020, 1–12. <https://doi.org/10.1155/2020/6156058>
- Wei, B., Huang, H., Hou, J., & Sukop, M. C. (2018). Study on the meniscus-induced motion of droplets and bubbles by a three-phase Lattice Boltzmann model. *Chemical Engineering Science*, 176, 35–49. <https://doi.org/10.1016/j.ces.2017.10.025>
- Westbeek, S., Remmers, J. J. C., van Dommelen, J. A. W., Maalderink, H. H., & Geers, M. G. D. (2021). Prediction of the deformed geometry of vat photo-polymerized components using a multi-physical modeling framework. *Additive Manufacturing*, 40, 101922. <https://doi.org/10.1016/j.addma.2021.101922>
- Wijshoff, H. (2004). Free surface flow and acousto-elastic interaction in piezo inkjet. *2004 NSTI Nanotechnology Conference and Trade Show - NSTI Nanotech 2004*, 2(0), 215–218.
- Wijshoff, H. (2018). Drop dynamics in the inkjet printing process. *Current Opinion in Colloid and Interface Science*, 36, 20–27. <https://doi.org/10.1016/j.cocis.2017.11.004>
- Wu, D., Wei, Y., & Terpenney, J. (2018). Surface roughness prediction in additive manufacturing using machine learning. *ASME 2018 13th International Manufacturing Science and Engineering Conference, MSEC 2018*, 3, 1–6. <https://doi.org/10.1115/MSEC2018-6501>
- Wu, J., Huang, J. J., & Yan, W. W. (2015). Lattice Boltzmann investigation of droplets impact behaviors onto a solid substrate. *Colloids and Surfaces A: Physicochemical and Engineering Aspects*, 484, 318–328. <https://doi.org/10.1016/j.colsurfa.2015.07.043>
- Xia, H., & Kamlah, M. (2022). Modelling Droplet Evaporation with an Improved Coupled Level Set and Volume of Fluid (i-CLSVoF) Framework. *Proceedings of the World Congress on Mechanical, Chemical, and Material Engineering*. <https://doi.org/10.11159/htff22.127>
- Yang, L., Kazmierski, B. K., Hoath, S. D., Jung, S., Hsiao, W. K., Wang, Y., Berson, A., Harlen, O., Kapur, N., & Bain, C. D. (2014). Determination of dynamic

- surface tension and viscosity of non-Newtonian fluids from drop oscillations. *Physics of Fluids*, 26(11). <https://doi.org/10.1063/1.4901823>
- Yarin, A. L. (2006). Drop impact dynamics: Splashing, spreading, receding, bouncing.. *Annual Review of Fluid Mechanics*, 38, 159–192. <https://doi.org/10.1146/annurev.fluid.38.050304.092144>
- Yunker, P. J., Still, T., Lohr, M. A., & Yodh, A. G. (2011). Suppression of the coffee-ring effect by shape-dependent capillary interactions. *Nature*, 476(7360), 308–311. <https://doi.org/10.1038/nature10344>
- Zhang, D., Papadikis, K., & Gu, S. (2014). Three-dimensional multi-relaxation time lattice-Boltzmann model for the drop impact on a dry surface at large density ratio. *International Journal of Multiphase Flow*, 64, 11–18. <https://doi.org/10.1016/j.ijmultiphaseflow.2014.04.005>
- Zhang, F., Tuck, C., Hague, R., He, Y., Saleh, E., Li, Y., Sturgess, C., & Wildman, R. (2016). Inkjet printing of polyimide insulators for the 3D printing of dielectric materials for microelectronic applications. *Journal of Applied Polymer Science*, 133(18), 1–11. <https://doi.org/10.1002/app.43361>
- Zhang, J., Huang, H., & Lu, X. Y. (2019). Pinning-Depinning Mechanism of the Contact Line during Evaporation of Nanodroplets on Heated Heterogeneous Surfaces: A Molecular Dynamics Simulation. *Langmuir*, 35(19), 6356–6366. <https://doi.org/10.1021/acs.langmuir.9b00796>
- Zhang, L., Cheng, X., Ku, T., Song, Y., & Zhang, D. (2018). Lattice Boltzmann study of successive droplets impingement on the non-ideal recessed microchannel for high-resolution features. *International Journal of Heat and Mass Transfer*, 120, 1085–1100. <https://doi.org/10.1016/j.ijheatmasstransfer.2017.12.124>
- Zhang, L., Ku, T., Jia, J., & Cheng, X. (2018). The role of wettability of nonideal nozzle plate: From drop-on-demand droplet jetting to impact on solid substrate. In *AIChE Journal* (Vol. 64, Issue 7, pp. 2837–2850). <https://doi.org/10.1002/aic.16139>
- Zhang, L., Zhu, Y., & Cheng, X. (2017). Numerical investigation of multi-droplets deposited lines morphology with a multiple-relaxation-time lattice Boltzmann

model. *Chemical Engineering Science*, 171, 534–544.

<https://doi.org/10.1016/j.ces.2017.06.014>

Zhao, Peng, He, Y., Trindade, G. F., Baumers, M., Irvine, D. J., Hague, R. J. M., Ashcroft, I. A., & Wildman, R. D. (2021). Modelling the influence of UV curing strategies for optimisation of inkjet based 3D printing. *Materials and Design*, 208, 109889. <https://doi.org/10.1016/j.matdes.2021.109889>

Zhao, Pengbing, Huang, J., Nan, J., Liu, D., & Meng, F. (2020). Laser sintering process optimization of microstrip antenna fabricated by inkjet printing with silver-based MOD ink. *Journal of Materials Processing Technology*, 275(July 2019), 116347. <https://doi.org/10.1016/j.jmatprotec.2019.116347>

Zienkiewicz, O. C., Taylor, R. L., & Nithiarasu, P. (2013). The Finite Element Method for Fluid Dynamics: Seventh Edition. In *The Finite Element Method for Fluid Dynamics: Seventh Edition*. Butterworth-Heinemann.

<https://doi.org/10.1016/C2009-0-26328-8>

11 Appendices.

11.1 Supplemental information on the lattice Boltzmann method.

11.1.1 Mathematical formulation.

The cornerstone of lattice Boltzmann model lies on the fundamental understanding of the particle distribution concept developed in kinetic theory. The continuous Boltzmann transport equation describes the advection of a particle distribution f with microscopic velocity ξ under the influence of external forces controlled by the local redistribution of f due to particle collisions,

$$\frac{\partial f}{\partial t} + \vec{\xi} \cdot \nabla f + \vec{F} \cdot \nabla_{\vec{\xi}} f = \Omega(f) \quad (54)$$

The lattice Boltzmann equation is a discretization of Equation (54) from which the Navier-Stokes equations can be restored,

$$f_i(\vec{x} + \vec{e}_i \delta_t, t + \delta_t) - f_i(\vec{x}, t) = \Omega_i(\vec{x}, t) \delta_t + S_i(\vec{x}, t) \delta_t \quad (55)$$

where f_i is the discrete particle distribution function representing the field density, \vec{x} is the particle position vector, \vec{e}_i is the particle microscopic velocity vector in the i th direction, δ_t is the time step, Ω_i is the collision operator and S_i is the forcing term in velocity space.

$$\begin{aligned} & [\vec{e}_0, \vec{e}_1, \vec{e}_2, \vec{e}_3, \vec{e}_4, \vec{e}_5, \vec{e}_6, \vec{e}_7, \vec{e}_8, \vec{e}_9, \vec{e}_{10}, \vec{e}_{11}, \vec{e}_{12}, \vec{e}_{13}, \vec{e}_{14}, \vec{e}_{15}, \vec{e}_{16}, \vec{e}_{17}, \vec{e}_{18}] \\ & = c \begin{bmatrix} 0 & 1 & -1 & 0 & 0 & 0 & 0 & 1 & 1 & -1 & -1 & 1 & -1 & 1 & -1 & 0 & 0 & 0 & 0 \\ 0 & 0 & 0 & 1 & -1 & 0 & 0 & 1 & -1 & 1 & -1 & 0 & 0 & 0 & 0 & 1 & 1 & -1 & -1 \\ 0 & 0 & 0 & 0 & 0 & 1 & -1 & 0 & 0 & 0 & 0 & 1 & 1 & -1 & -1 & 1 & -1 & 1 & -1 \end{bmatrix} \end{aligned} \quad (56)$$

The multi-relaxation collision operator is calculated as follows,

$$\Omega_i(\vec{x}, t) = -M^{-1} \Lambda M \left(f_i(\vec{x}, t) - f_i^{eq}(\vec{x}, t) \right) \quad (57)$$

where the equilibrium distribution function f_i^{eq} evolves from the second order Taylor expansion of the Maxwellian-Boltzmann distribution function given as,

$$f_i^{eq}(\vec{x}, t) = \omega_i \rho \left[1 + \frac{\vec{e}_i \cdot \vec{u}}{c_s^2} + \frac{(\vec{e}_i \cdot \vec{u})^2}{2c_s^4} - \frac{(\vec{u})^2}{2c_s^2} \right] \quad (58)$$

where the speed of sound $c_s^2 = \frac{c^2}{3} = \frac{1}{3}$, and the weights based on velocity direction are,

$$\omega_i = \begin{cases} 1/3, & i = 0; \\ 1/18, & i = 1 - 6; \\ 1/36, & i = 7 - 18. \end{cases} \quad (59)$$

the macroscopic density and velocity can be obtained as,

$$\rho = \sum_{i=0}^{18} f_i, \quad \rho \vec{u} = \sum_{i=0}^{18} \vec{e}_i f_i + \frac{\vec{F} \delta_t}{2} \quad (60)$$

The transformation matrix M which maps particle distributions from velocity space to moment space is define as,

$$M = \begin{bmatrix} 1 & 1 & 1 & 1 & 1 & 1 & 1 & 1 & 1 & 1 & 1 & 1 & 1 & 1 & 1 & 1 & 1 & 1 \\ -30 & -11 & -11 & -11 & -11 & -11 & -11 & 8 & 8 & 8 & 8 & 8 & 8 & 8 & 8 & 8 & 8 & 8 \\ 12 & -4 & -4 & -4 & -4 & -4 & -4 & 1 & 1 & 1 & 1 & 1 & 1 & 1 & 1 & 1 & 1 & 1 \\ 0 & 1 & -1 & 0 & 0 & 0 & 0 & 1 & 1 & -1 & -1 & 1 & -1 & 1 & -1 & 0 & 0 & 0 \\ 0 & -4 & 4 & 0 & 0 & 0 & 0 & 1 & 1 & -1 & -1 & 1 & -1 & 1 & -1 & 0 & 0 & 0 \\ 0 & 0 & 0 & 1 & -1 & 0 & 0 & 1 & -1 & 1 & -1 & 0 & 0 & 0 & 0 & 1 & 1 & -1 \\ 0 & 0 & 0 & -4 & 4 & 0 & 0 & 1 & -1 & 1 & -1 & 0 & 0 & 0 & 0 & 1 & 1 & -1 \\ 0 & 0 & 0 & 0 & 0 & 1 & -1 & 0 & 0 & 0 & 0 & 1 & 1 & -1 & -1 & 1 & -1 & 1 \\ 0 & 0 & 0 & 0 & 0 & -4 & 4 & 0 & 0 & 0 & 0 & 1 & 1 & -1 & -1 & 1 & -1 & 1 \\ 0 & 2 & 2 & -1 & -1 & -1 & -1 & 1 & 1 & 1 & 1 & 1 & 1 & 1 & 1 & -2 & -2 & -2 \\ 0 & -4 & -4 & 2 & 2 & 2 & 2 & 1 & 1 & 1 & 1 & 1 & 1 & 1 & 1 & -2 & -2 & -2 \\ 0 & 0 & 0 & 1 & 1 & -1 & -1 & 1 & 1 & 1 & 1 & -1 & -1 & -1 & -1 & 0 & 0 & 0 \\ 0 & 0 & 0 & -2 & -2 & 2 & 2 & 1 & 1 & 1 & 1 & -1 & -1 & -1 & -1 & 0 & 0 & 0 \\ 0 & 0 & 0 & 0 & 0 & 0 & 0 & 1 & -1 & -1 & 1 & 0 & 0 & 0 & 0 & 0 & 0 & 0 \\ 0 & 0 & 0 & 0 & 0 & 0 & 0 & 0 & 0 & 0 & 0 & 0 & 0 & 0 & 1 & -1 & -1 & 1 \\ 0 & 0 & 0 & 0 & 0 & 0 & 0 & 0 & 0 & 0 & 0 & 1 & -1 & -1 & 1 & 0 & 0 & 0 \\ 0 & 0 & 0 & 0 & 0 & 0 & 0 & 1 & 1 & -1 & -1 & -1 & 1 & -1 & 1 & 0 & 0 & 0 \\ 0 & 0 & 0 & 0 & 0 & 0 & 0 & -1 & 1 & -1 & 1 & 0 & 0 & 0 & 0 & 1 & 1 & -1 \\ 0 & 0 & 0 & 0 & 0 & 0 & 0 & 0 & 0 & 0 & 0 & 1 & 1 & -1 & -1 & 1 & -1 & 1 \end{bmatrix} \quad (61)$$

through the following relationship,

$$m = M \cdot f, \quad f = M^{-1} \cdot m \quad (62)$$

Λ is a diagonal matrix defining the inverse of the relaxation times towards distribution equilibrium and is given by:

$$\begin{aligned}
\Lambda &= \text{diag}(s_1, s_2, s_3, s_4, s_5, s_6, s_7, s_8, s_9, s_{10}, s_{11}, s_{12}, s_{13}, s_{14}, s_{15}, s_{16}, s_{17}, s_{18}, s_{19}) \\
&= \text{diag}(1, s_e, s_\xi, 1, s_q, 1, s_q, 1, s_q, s_\nu, s_\pi, s_\nu, s_\nu, s_\nu, s_t, s_t, s_t)
\end{aligned} \tag{63}$$

The kinematic viscosity and bulk viscosity can be derived using the following,

$$\nu = \frac{1}{3} \left(\frac{1}{s_\nu} - \frac{1}{2} \right) \tag{64}$$

and

$$\xi = \frac{2}{9} \left(\frac{1}{s_e} - \frac{1}{2} \right) \tag{65}$$

The equilibrium particle distribution in moment space is given by,

$$m^{eq} = \begin{bmatrix} \rho \\ -11\rho + \frac{19}{\rho}(j_x^2 + j_y^2 + j_z^2) \\ 3\rho - \frac{11}{2\rho}(j_x^2 + j_y^2 + j_z^2) \\ j_x \\ -\frac{2}{3}j_x \\ j_y \\ -\frac{2}{3}j_y \\ j_z \\ -\frac{2}{3}j_z \\ \frac{1}{\rho}(2j_x^2 - j_y^2 - j_z^2) \\ -\frac{1}{2\rho}(2j_x^2 - j_y^2 - j_z^2) \\ \frac{1}{\rho}(j_y^2 - j_z^2) \\ -\frac{1}{2\rho}(j_y^2 - j_z^2) \\ \frac{1}{\rho}j_xj_y \\ \frac{1}{\rho}j_yj_z \\ \frac{1}{\rho}j_xj_z \\ 0 \\ 0 \\ 0 \end{bmatrix} \tag{66}$$

where $j_x = \rho u_x$, $j_y = \rho u_y$, and $j_z = \rho u_z$ are components of the mass fluxes.

The improved forcing scheme is introduced as,

$$S_i(\vec{x}, t) = M^{-1} \left(I - \frac{\Lambda}{2} \right) M \vec{F}(\vec{x}, t) + \vec{C}(\vec{x}, t) \quad (67)$$

where $M\vec{F}$ is the forcing term in the moment space corrected for thermodynamic consistency condition derived by (D. Zhang et al., 2014) and given by:

$$M\vec{F}_i(\vec{x}, t) = \begin{bmatrix} 0 \\ 38(u_x F_x + u_y F_y + u_z F_z) + \frac{114\varepsilon \vec{F}^2}{\psi^2(1/s_e - 0.5)} \\ -11(u_x F_x + u_y F_y + u_z F_z) \\ F_x \\ \frac{2}{3} F_x \\ F_y \\ -\frac{2}{3} F_y \\ F_z \\ -\frac{2}{3} F_z \\ 2(2u_x F_x - u_y F_y - u_z F_z) \\ (-2u_x F_x + u_y F_y + u_z F_z) \\ 2(u_y F_y - u_z F_z) \\ (-u_y F_y + u_z F_z) \\ u_y F_x + u_x F_y \\ u_z F_y + u_y F_z \\ u_z F_x + u_x F_z \\ 0 \\ 0 \\ 0 \end{bmatrix} \quad (68)$$

where $\vec{F}^2 = (F_x^2 + F_y^2 + F_z^2)$ and ε is the parameter used to ensure model thermodynamic consistency. Furthermore, to decouple density ratio from surface tension, an additional term derived by (Ammar et al., 2017) to the forcing scheme needs to be included in the following form,

$$C = \begin{bmatrix} 0 \\ \frac{2}{5} s_e (Q_{xx} + Q_{yy} + Q_{zz}) \\ 0 \\ 0 \\ 0 \\ 0 \\ 0 \\ 0 \\ -s_v (2Q_{xx} - Q_{yy} - Q_{zz}) \\ 0 \\ -s_v (Q_{yy} - Q_{zz}) \\ 0 \\ -s_v Q_{xy} \\ -s_v Q_{yz} \\ -s_v Q_{xz} \\ 0 \\ 0 \\ 0 \end{bmatrix} \quad (69)$$

where the tensor \vec{Q} can be obtained from the following equation,

$$\vec{Q} = \frac{\kappa G}{2} \psi(\vec{x}, t) \sum_{i=1}^{18} \omega(|\vec{e}_i|^2) [\psi(\vec{x} + \vec{e}_i \delta_t, t) - \psi(\vec{x}, t)] \quad (70)$$

The fluid-fluid interparticle force F_{int} derived by (Shan, 2006) is expressed as,

$$F_{int} = -G \psi(\vec{x}, t) \sum_{i=0}^{18} \omega_i \psi(\vec{x} + \vec{e}_i \delta_t, t) \vec{e}_i \quad (71)$$

Where G controls the strength of the interparticle force and ψ is the mean field potential which represents the effective mass of the system and can be obtained by the non-ideal equation of state (EOS),

$$\psi(\vec{x}, t) = \sqrt{\frac{2(p - \rho c_s^2)}{G c_s^2}} \quad (72)$$

where the factor G is inserted only to ensure the positivity of the square root.

In this study, the Carnahan-Starling (CS) EOS is employed to achieve high density ratios and numerical stability. The CS equation is given by,

$$p = \rho RT \frac{1 + (b\rho/4) + (b\rho/4)^2 - (b\rho/4)^3}{(1 - b\rho/4)^3} - a\rho^2 \quad (73)$$

Where parameters a , b can be obtained from the values of critical pressure and temperature, using the following equations.

$$a = .4963 \frac{R^2 T_c^2}{p_c^2}, \quad b = .18727 \frac{RT_c}{p_c} \quad (74)$$

The fluid-solid interaction force F_{ads} derived by (Benzi et al., 2006) is,

$$F_{ads} = -G\psi(\vec{x}, t) \sum_{i=0}^{18} \omega_i |\vec{e}_i|^2 |\psi(\rho_w) S(\vec{x} + \vec{e}_i \delta_t, t) \vec{e}_i \quad (75)$$

With the body force F_{body} , the total force F in Equation (68) is given by,

$$\vec{F} = F_{int} + F_{ads} + F_{body} \quad (76)$$

11.1.2 Numerical validation.

11.1.2.1 Evaluation of Thermodynamic Consistency.

For the evaluation of the model's thermodynamic consistency, a flat interface problem was solved numerically to compare coexisting densities with the Maxwell construction rule results. The critical properties for density, pressure and temperature in lattice units are derived as 0.11199, 0.00110 and 0.02358, respectively. Then, by substituting the pressure into the pseudopotential function, the Maxwell construction rule could be derived for a given temperature.

A computational domain using periodic boundary conditions in all directions of size 100x100x100 is initialized with a density field, where W is the initial interface thickness set to 5 lattice units.

$$\rho(x, y, z) = \rho_g + \frac{\rho_l - \rho_g}{2} \left(\tanh\left(\frac{2(z - 25)}{W}\right) - \tanh\left(\frac{2(z - 75)}{W}\right) \right) \quad (77)$$

Maxwell rule coexisting densities are graphed along with corresponding LBM results assuming $\text{Kappa} = 0$ and $\varepsilon = 0.319$ in Fig. 2. Results show excellent agreement between analytical and numerical densities for density ratios up to 870.

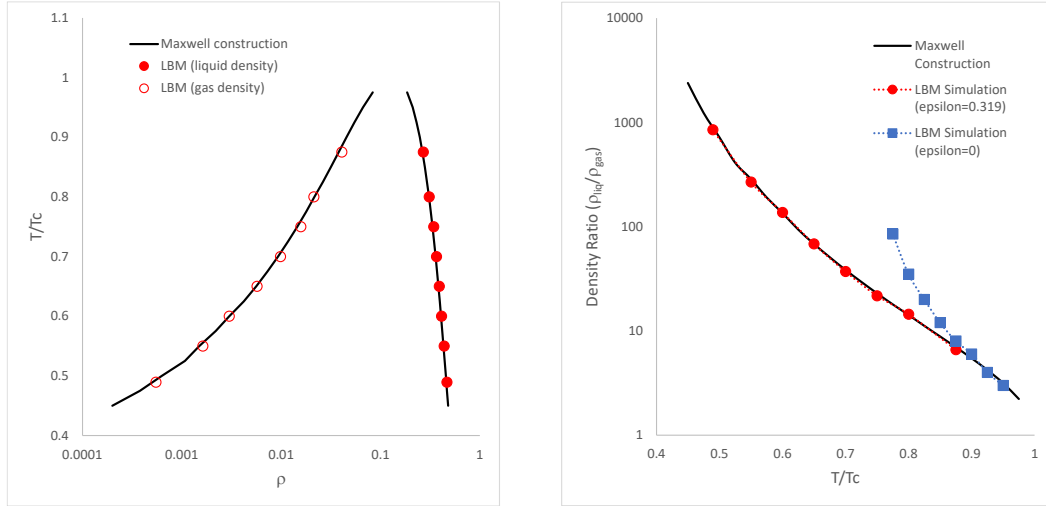


Figure 11-1 Thermodynamic consistency validation.

11.1.2.2 Evaluation of Laplace's Law.

A benchmark test to ensure the lattice Boltzmann simulation is capturing adequately the physics behind surface tension properties is the satisfaction of Laplace's law. For a 3D spherical drop, Laplace's law is given by,

$$p_{in} - p_{out} = \Delta p = \frac{2\sigma}{R} \quad (78)$$

where σ , R , and Δp are the surface tension, droplet radius and pressure difference, respectively. If the pressure difference between the inside and outside of the droplet is proportional to the curvature, then Laplace's law is satisfied.

To assess lattice Boltzmann model, a resting spherical droplet at the centre of a computational domain with periodic boundary conditions applied at all boundaries was prepared. The density field was initialized using Equation (79) where x_0 , y_0 and z_0 represent the droplet centre, R the droplet radius and $W=5$ the initial interface thickness,

$$\begin{aligned} \rho(x, y, z) & \\ &= \frac{\rho_l + \rho_g}{2} \\ &+ \frac{\rho_l - \rho_g}{2} \left(\tanh \left(\frac{2(\sqrt{(x - x_0)^2 + (y - y_0)^2 + (z - z_0)^2} - R)}{W} \right) \right) \end{aligned} \quad (79)$$

The simulation was run using different radius in a cubic domain size of 120 lattice units. The parameter κ was varied to demonstrate the model capability to modify surface tension independently of density ratio. Droplet radius and pressure difference were measured at equilibrium achieved after 20000 timesteps. The pressure difference is calculated between a point at the centre of the droplet and a point furthest away from it in the computational domain. In Figure 11-2, the pressure difference against 2 times the reciprocal of droplet radius is plotted at $\kappa = 0, 0.6, 0.89, 0.95$ with $15 < R < 35$. The droplet radius, pressure difference and calculated surface tension are all in lattice units. The slope of the trendline represents the surface tension which are 0.0166, 0.0081, 0.00175, 0.00078, respectively. The intercept of the linear fit is set to zero for all cases and the coefficients of determination are 0.9998, 0.9993, 0.9991, 0.9982, respectively. The parameter $\kappa = 0.89$ is used in the rest of the study. Results show good agreement between theory and numerical simulation, satisfying Laplace's law and demonstrating model's ability to handle large density ratio with adjustable surface tension.

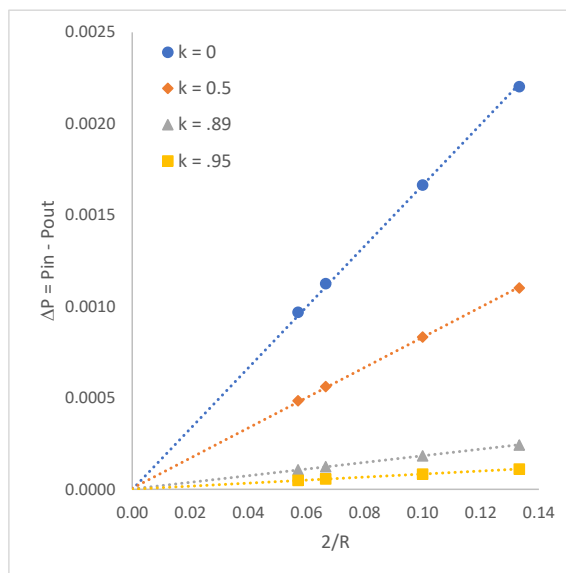


Figure 11-2 Laplace's law validation.

11.1.2.3 Evaluation of spatial accuracy.

Another benchmark test to validate the lattice Boltzmann model is to demonstrate second order accuracy in space, in agreement with derivation assumptions from theory.

Again, a spherical droplet in equilibrium with centre at the cubic computational domain with periodic boundary conditions applied at all boundaries was prepared. The density field was initialized using Equation (79) with initial interface thickness $W=5$. In this case, the ratio between the domain size and droplet radius was kept constant and equal to 4 (i.e., for a grid size equal to 40, the droplet radius is 10). It was assumed that a grid size equal to 160 is the finest mesh and yields accurate results. The CS EOS parameters were fixed at $a=0.25$, $b=4$, $R=1$, parameter $\varepsilon = 0.319$ to satisfy thermodynamic consistency, and reduced temperature $T=0.4898T_c$ to achieve a density ratio=870 with a diffuse interface of 5 lattice units. Parameter κ was set equal to zero to incorporate the largest surface tension value possible using the current model. To assess spatial accuracy, an error measurement defined by the absolute value of the difference between the liquid or gas density at certain grid size level minus the density value obtained at the finer mesh was calculated. In Figure 11-3, the density error against grid size is plotted at grid size = 40, 80, 120. Thick blue line represents exact second order accuracy and results show model is approximately second order accurate in space.

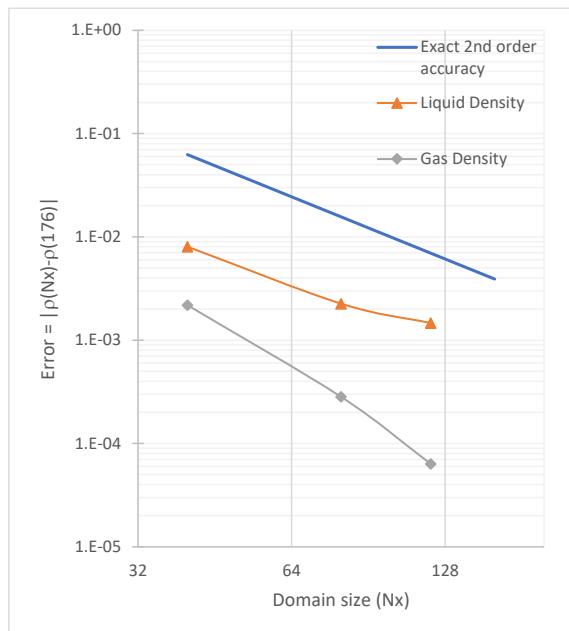


Figure 11-3 Spatial accuracy validation.

11.1.2.4 Evaluation of contact angle.

To adjust wetting characteristics, this work follows the approach developed by (Benzi et al., 2006). The desired contact angle is obtained by setting the parameter ρ_w , which represents a “wall density” to calculate the adhesion force between liquid/gas phase and solid walls. In this benchmark test, a droplet with radius $r=20$ is initially placed on a solid flat surface with half-way bounce back rule at top and bottom boundaries to simulate no-slip condition. Periodic boundary conditions were used in the left and right boundaries in a computational domain size of $100 \times 100 \times 80$. Parameter $\varepsilon = 0.319$ to satisfy thermodynamic consistency, parameter $\kappa = 0.89$ to match desired surface tension and reduced temperature $T = 0.4898T_c$ to achieve a density ratio = 870. A static droplet is obtained after 10000 timesteps. To measure the contact angles from simulation results, an interface tracking method was programmed to get the contact line radius (r) and drop height (h) at profile average density point. Then, the static contact angle is calculated using the following equation,

$$\theta_s = \arctan\left(\frac{2hr}{r^2 - h^2}\right) \quad (80)$$

The relationship between ρ_w and the static contact angle is illustrated in Figure 11-5a. The parameter ρ_w is inversely proportional to the static contact angle and its value ranges between 0.1 and 0.22 achieving a contact angle of 124° and 11° , respectively. Additionally, the simulation was validated by comparing the equilibrium spreading factor against the theoretical spread factor based on volume conservation of the droplet. Contact angles show good agreement with the theoretical values as shown in Figure 11-5b and a 3D representation of droplets with different wetting characteristics is illustrated in Figure 11-4.

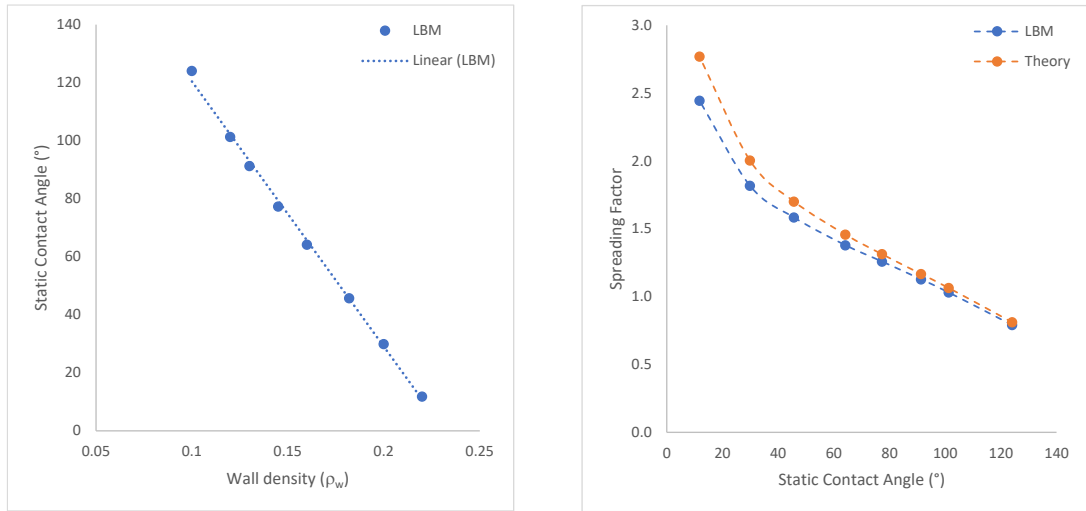


Figure 11-5 (a) Static contact angle vs ρ_w ; (b) Theoretical vs numerical spreading factor comparison.

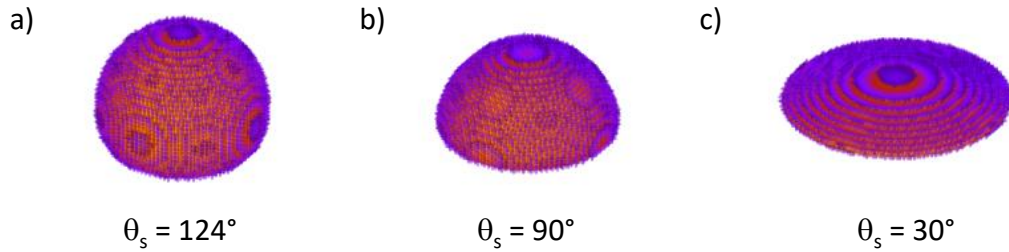


Figure 11-4 (a) Lyophobic surface; (b) Neutral surface; (c) Lyophilic surface.

11.1.2.5 Evaluation of contact line pinning.

For the adequate simulation of multiple sequential drops spreading and coalescing, a wetting model considering contact angle hysteresis and fluid adhesion on the solid surface is required. In this work, we followed the methodology proposed by (J. R. Castrejón-Pita et al., 2011) to simulate contact angle hysteresis. First, the substrate is initialized with a “wall density” parameter that corresponds to the advancing contact angle (θ_a). Once the surface is wetted at a given location, the local static contact angle changes to match the receding contact angle. This is imposed in the code when the density in the node above the wall is greater than a threshold (H_r) given by the following condition,

$$\rho(x, y, z + 1) \geq \rho_g + H_r(\rho_l - \rho_g) \quad (81)$$

On the other hand, when the contact line starts to retract and the surface is dewetted, the local static contact angle reverts gradually from the receding contact angle (θ_r) to

θ_a . This is imposed in the code when the density in the node above the wall is less than a threshold (H_a) given by the following condition,

$$\rho(x, y, z + 1) \leq \rho_g + H_a(\rho_l - \rho_g) \quad (82)$$

In this work, we use linear interpolation to simulate the gradual change from receding to advancing contact angle. In addition, the values used for H_r and H_a are 0.9 and 0.1, respectively. To test the methodology, a simulation of two sequential drops impacting a flat and dry wall was prepared using the physical properties and drop characteristics from table 1. Parameter $\varepsilon = 0.319$ to satisfy thermodynamic consistency, parameter $\kappa = 0.89$ to match desired surface tension and reduced temperature $T=0.4898T_c$ to achieve a density ratio=870. Periodic boundary conditions were used in the left and right boundaries, halfway bounce back in top and bottom, in a computational domain size of 170x140x80. Horizontal drop spacing and vertical drop spacing were set to 50 and 20 lattice units, respectively. Advancing and receding contact angle were set to 70° and 20° , respectively. The purpose is to compare the results of simulation run including wetting model with contact angle hysteresis against model without contact angle hysteresis. Figure 11-6 shows the dynamic contact line modelled by lattice Boltzmann method with and without contact angle hysteresis methodology. The effect of contact angle hysteresis is very apparent: with it, the contact line becomes pinned enabling the formation of a line; without it, all sequential droplets eventually reach a circular footprint and a spherical cap shape. Both simulations were run until equilibrium was achieved at approximately 12000 timesteps.

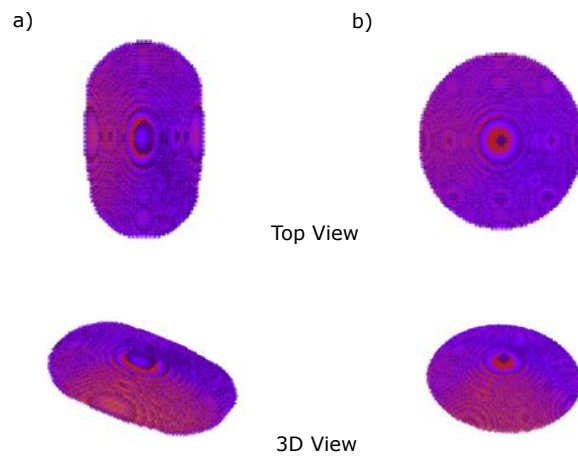


Figure 11-6 Footprint of sequential drops a) with and b) without contact angle hysteresis.

11.2 Supplemental information on the image analysis technique validation for lines and freeform films.

The validation of the image analysis approach employed in this investigation is performed by comparing footprints of single tracks and films extracted from images with feature's measurements using coherence scanning interferometry and optical microscopy.

Seven lines of 1 mm in length are printed on glass with cartridge model 11610 (native droplet volume 10 pL) using printing parameters listed in Table 11-1. Images of the single tracks are taken with Dimatix fiducial camera. Single tracks are measured with coherence scanning interferometry and post processed with in-house MATLAB code following the procedure described in Section 4.7.1. Single track footprints are extracted from the images following the procedure described in Section 4.7.2.

Table 11-1 Printing parameters for single tracks used in image analysis validation.

ID	Drop spacing (μm)	Printing frequency (kHz)	Standoff distance (mm)
1	10	1	0.5
2	40	2.5	1
3	70	2.5	1
4	40	4	1
5	40	2.5	1
6	40	2.5	1.5
7	40	2.5	1

Footprints from image (blue line) and measured data (black line) are compared in Figure 11-7. Overall, the image analysis process to segment and extract edges to assess dimensional accuracy of single tracks matches fairly well the CSI measurements. The main differences are observed in single tracks that are broken (e.g., present more than 1 segment). A potential explanation is that digital images are immediately taken after printing and further expansion of the feature may happen, which is enhanced when multiple segments are present.

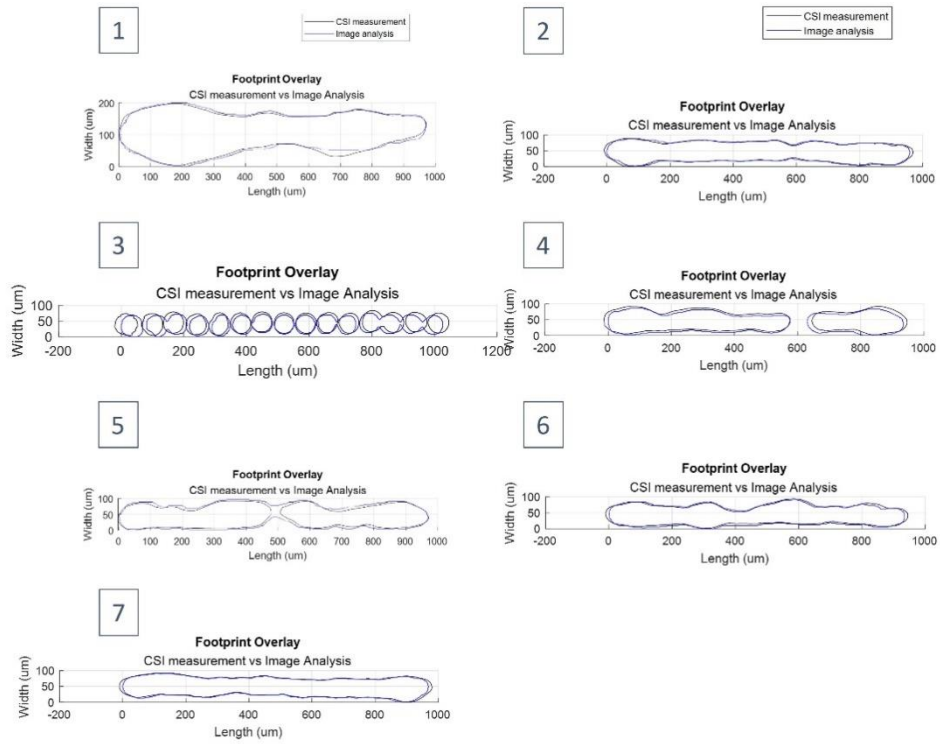


Figure 11-7 Comparison of image analysis vs CSI measurements of the footprints of single tracks.

Bar charts comparing the dimensions of single tracks including length, average width, maximum width, and estimated thickness (Ink Volume/Area assumption) are shown in Figure 11-8. Results from the length comparison reveal that features extracted from images are shorter than measurements, since images are taken immediately after printing and further feature expansion might happen. The maximum length difference is 40 μm and is observed in single track number 3, which corresponds to a line with multiple segments. The average length deviation is 18 μm , which represents 2% error with respect to target dimension. From the average width (b) comparison, it is found that footprints extracted from image analysis are 3% larger than CSI measurements on average. Observation 5 shows a 9.2 μm difference since footprint area measured by CSI shows disconnected line pattern whereas Dimatix image a single feature. It is also observed that average width of stable lines match the average spot size. From the maximum width comparison (c), maximum width difference is less than 5 μm , which represents 4% error with respect to the average of the differences. The maximum difference is 7.5 μm in single track number 5. Finally, from the thickness (d) comparison, the difference between measured and calculated values is less than 0.4

μm , validating our analytical assumptions. Therefore, it is concluded that image analysis is a fast and adequate method to measure the surface morphology of single tracks.

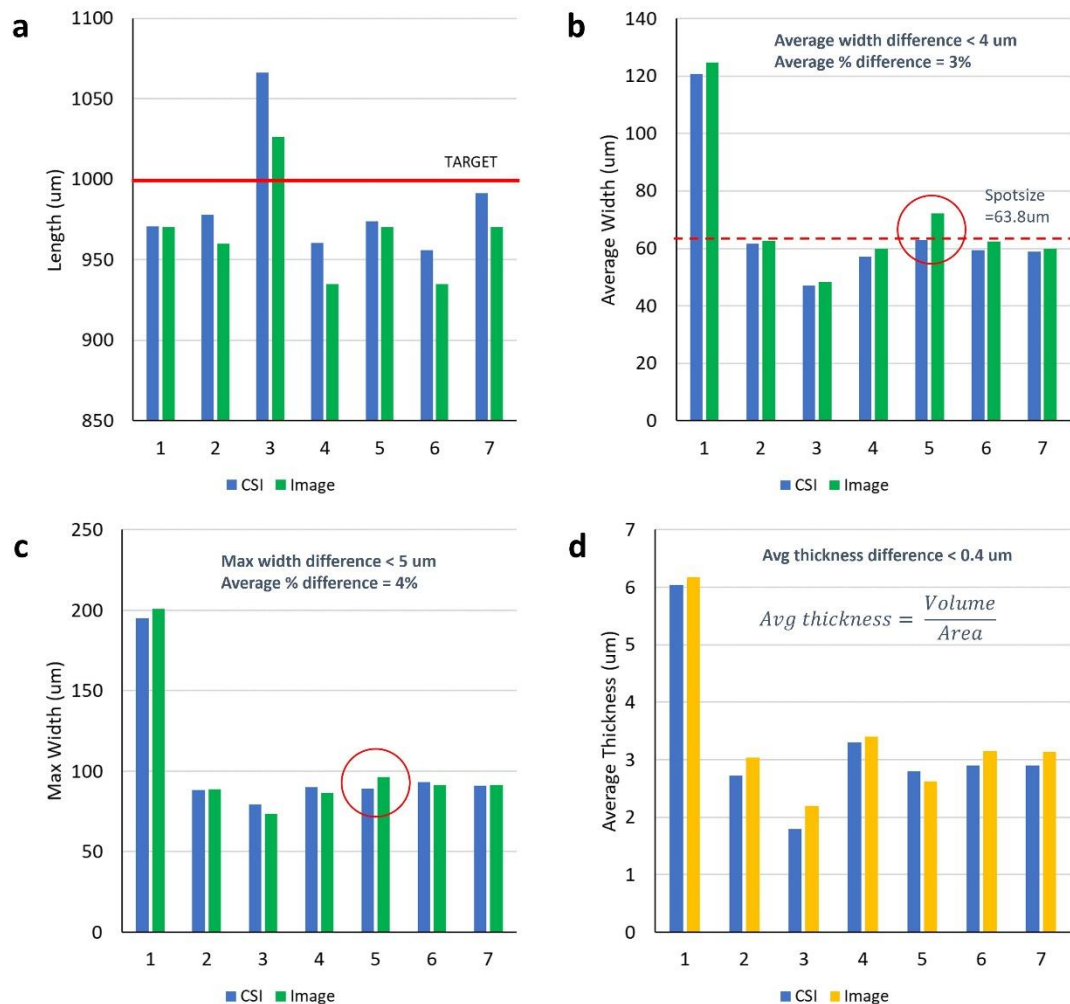


Figure 11-8 Comparison of dimensions measured using image analysis and CSI. a. Length, b. Average width, c. Maximum width and d. Average thickness.

Same quantitative analysis is performed to evaluate the accuracy of the image analysis process to extract footprints of films. Footprints extracted from images (blue line) and from measured data (black line) are compared in Figure 11-9. Overall, the image analysis process to segment and extract edges to assess dimensional accuracy of solid and hollowed films matches fairly well the CSI measurements. For the square patterns, the maximum deviation in average length and width is $25 \mu\text{m}$ and $5 \mu\text{m}$, respectively. For the ring pattern, the maximum deviation in outer average diameter is $13 \mu\text{m}$. The

error with respect to target dimension is less than 2.5% considering all patterns. The time to segment and measure images is in the order of seconds, compared to hours to book and perform measurements using CSI. Therefore, it is concluded that image analysis is a fast and adequate method to measure the surface morphology of solid and hollowed films.

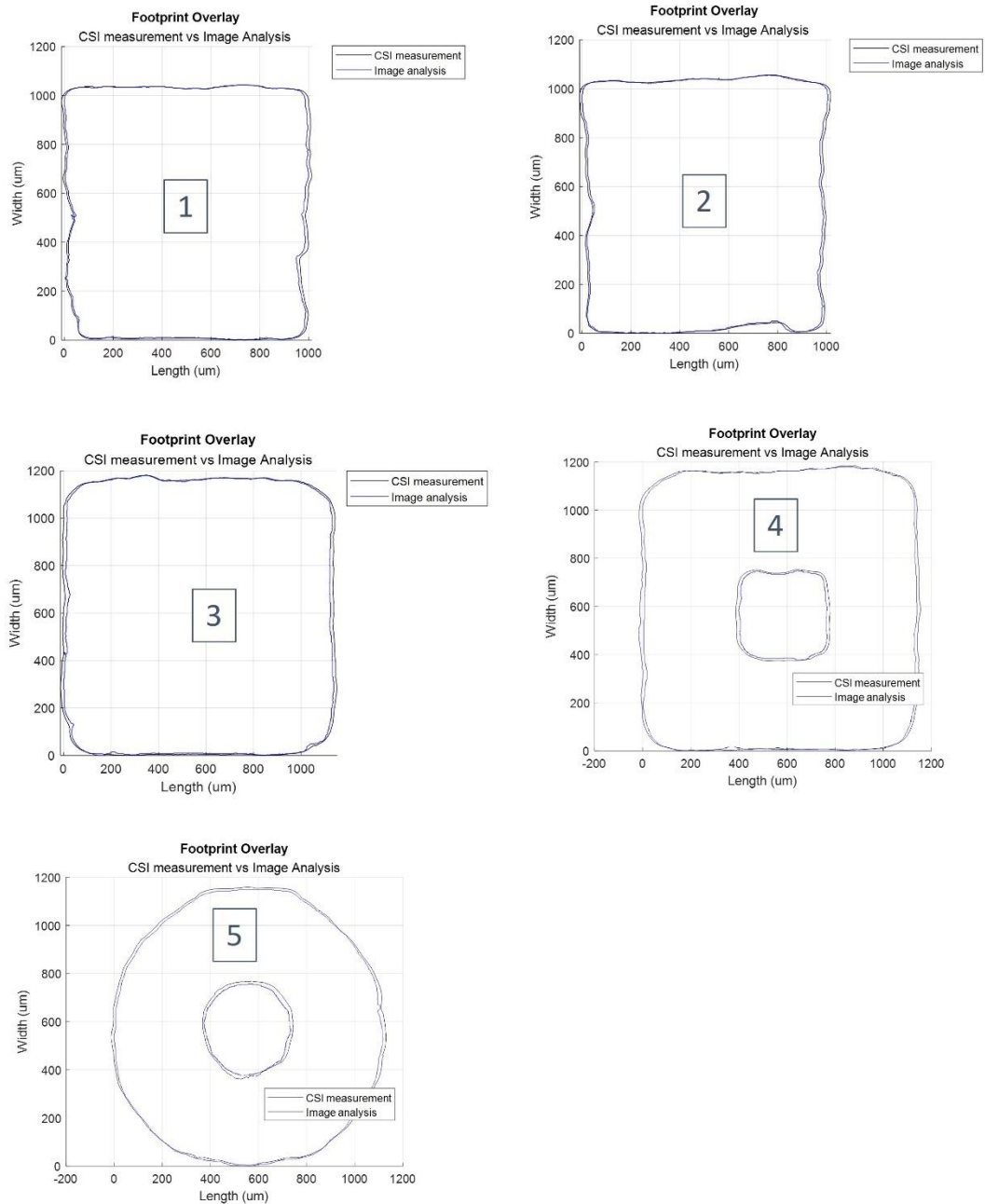


Figure 11-9 Comparison of image analysis vs CSI measurements of the footprints of solid and hollowed films.

11.3 Supplemental information on MATLAB GUI and FORTRAN scripts.

Code used to generate the results in this investigation is available in a University of Nottingham repository (<http://doi.org/10.17639/nott.7332>) and in a GitHub repository (<https://github.com/lunajfr/EZINKJET>) upon request to authors. For further information, please contact Prof. Ian Ashcroft.